THERMAL EVOLUTION OF FORMING PLANETS

ISOTOPE ENRICHMENT, DIFFERENTIATION & VOLATILE RETENTION

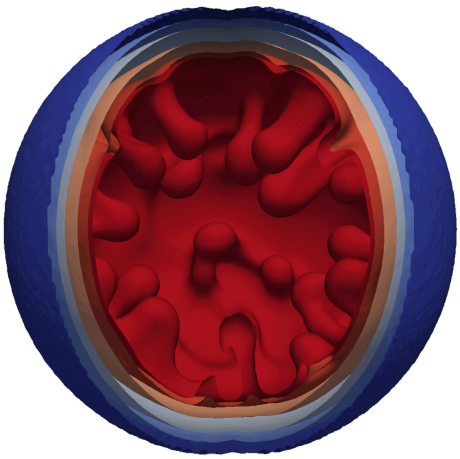

TIM LICHTENBERG

DOCTORAL THESIS, ETH ZURICH

NO 25163

2018

DISS. ETH NO. 25163

THERMAL EVOLUTION OF FORMING PLANETS

ISOTOPE ENRICHMENT, DIFFERENTIATION & VOLATILE RETENTION

A thesis submitted to attain the degree of

DOCTOR OF SCIENCES OF ETH ZURICH

(Dr. sc. ETH Zurich)

presented by

TIM LICHTENBERG

M. Sc. in Physics, Georg-August-Universität Göttingen

born on 22 July 1988, citizen of Germany

accepted on the recommendation of

Prof. Dr. Taras V. Gerya, ETH Zurich, Switzerland (examiner)
Prof. Dr. Michael R. Meyer, University of Michigan, United States (co-examiner)
Prof. Dr. Gregor J. Golabek, University of Bayreuth, Germany (co-examiner)
Dr. Richard J. Parker, University of Sheffield, United Kingdom (co-examiner)
Prof. Dr. Paul J. Tackley, ETH Zurich, Switzerland (co-examiner)
Prof. Dr. Fred J. Ciesla, University of Chicago, United States (co-examiner)

2018

We must know.

We will know.

– *David Hilbert, 1930*

ABSTRACT

Discoveries of extrasolar planets in the last decades raise the question of how common Earth-like worlds with clement surface environments are within the galaxy. Because astronomical observations are ultimately limited in providing a complete picture of the planetary census, a comprehensive understanding of planetary systems' formation and evolution can deliver valuable insights into key physical and chemical properties that cannot be probed by remote sensing alone. In order to understand how terrestrial worlds are formed and distributed, I investigate in this thesis the early evolution of planetary systems and the interior dynamics and volatile retention of rocky protoplanets.

To place the Solar system in the context of the extrasolar planet population, I model the enrichment of protoplanetary disks with short-lived radionuclides, namely ^{26}Al and ^{60}Fe, in typical star-forming environments. I find their distribution to be dichotomous: many planetary systems with zero or negligible abundances, and fewer systems with levels comparable to the early Solar system. Further, I quantify the parametric controls on interior evolution and volatile loss of planetesimals that accrete to form terrestrial planets. I derive the primary thermochemical regimes for the build-up of internal magma oceans, core segregation, chemical differentiation, and volatile retention. Matching planetesimal interior evolution with meteoritic evidence, I constrain the accretion dynamics and reprocessing of planetary materials in the early Solar system, in order to gain a better understanding of planetary assembly. Finally, by extrapolating the derived mechanisms to the exoplanet population, I demonstrate the primary influence of short-lived radionuclides on the efficiency of volatile delivery to terrestrial planets: enriched systems with Solar-like or higher levels tend to form water-depleted planets, while not- or barely-enriched systems dominantly form ocean worlds.

My findings provide a direct link between the star-forming birth environment of planetary systems and the compositional make-up and long-term evolution of rocky planets that form in them. The system-to-system deviations in the abundance of short-lived radionuclides across young star-forming regions qualitatively distinguish planetary systems' formation and evolution, and control the distribution and prevalence of terrestrial planets with Earth-like bulk compositions.

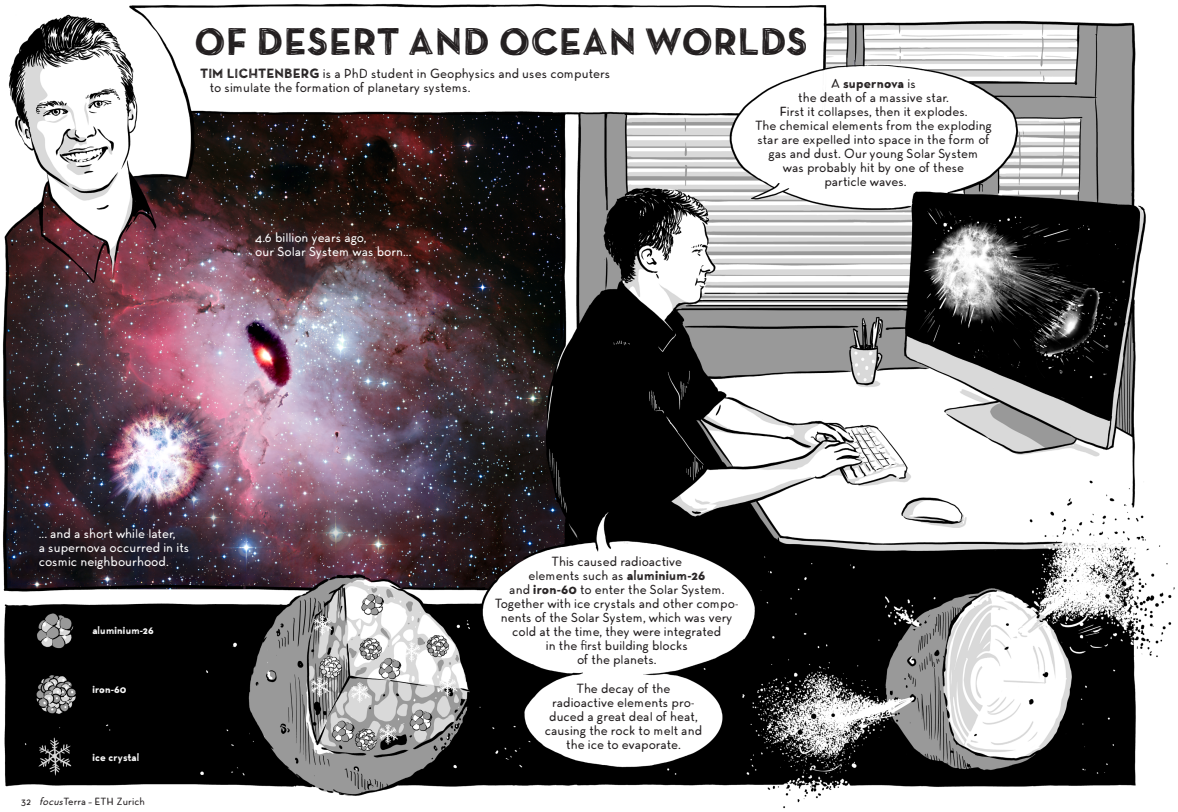

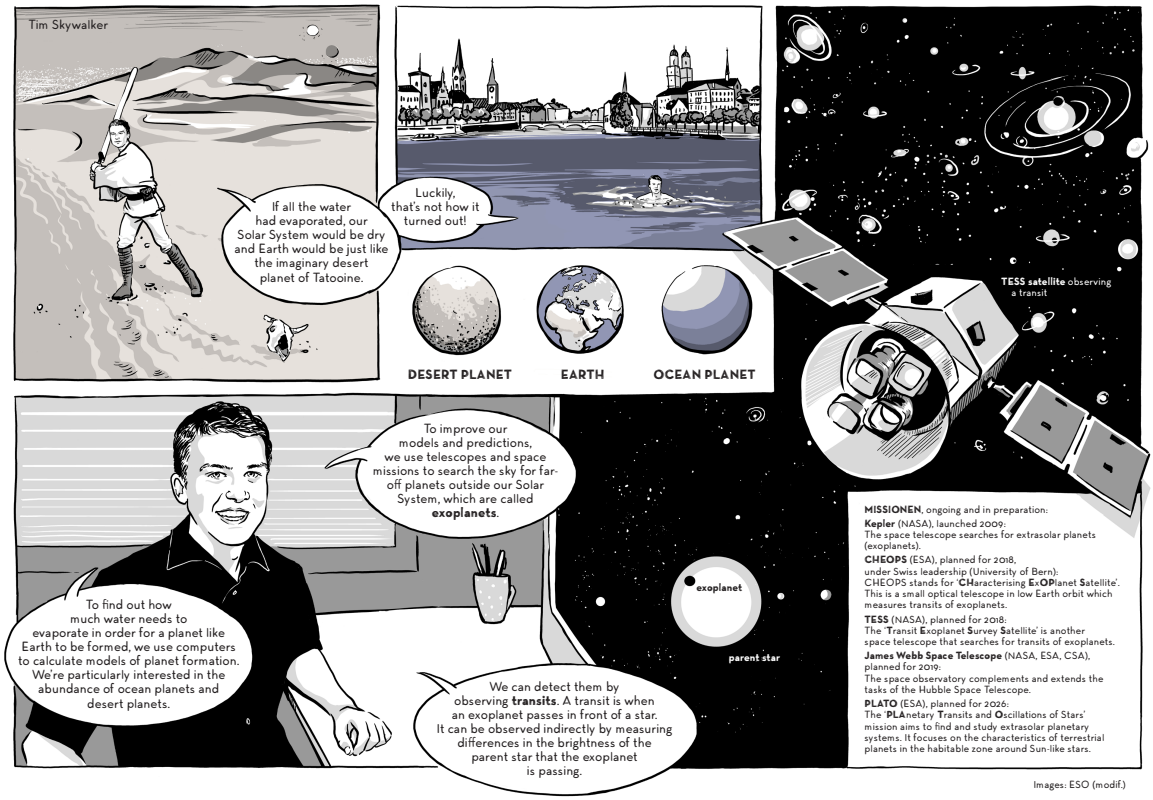

Images: ESO (modif.)

"Expedition Solar System – Join ETH Zurich on a journey into space"; Ulrike Kastrup, Kerstin Fankhauser, Gillian Grün, Jessica Kind, Bettina Gutbrodt, Andrea Dähler; focusTerra, ETH Zurich, 2018

ZUSAMMENFASSUNG

Die Entdeckung von extrasolaren Planeten in den letzten Jahrzehnten wirft die Frage auf, wie häufig erdähnliche Welten in unserer Galaxie auftreten. Da astronomische Beobachtungen nur ein unvollständiges Bild der gesamten Planetenpopulation liefern, können Einsichten in die Entstehung und Entwicklung von Planetensystemen bedeutsame Erkenntnisse über deren wichtigste physikalische und chemische Eigenschaften liefern, welche mit Fernerkundung allein nicht untersucht werden können. Um die Entstehung und Häufigkeit terrestrischer Welten zu verstehen, erforsche ich in dieser Doktorarbeit die frühe Evolution von Planetensystemen, und die interne Dynamik und Beibehaltung volatiler Elemente von gesteinsartigen Protoplaneten.

Um unser Sonnensystem in den Kontext der extrasolaren Planetenpopulation einzubetten, modelliere ich die Anreicherung protoplanetarer Scheiben mit kurzlebigen Radionukliden, insbesondere ^{26}Al und ^{60}Fe, in typischen Sternentstehungsregionen. Ich finde eine dichotome Verteilung vor: Viele Planetensysteme mit keinen oder vernachlässigbaren Isotopenvorkommen und weniger Systeme mit Häufigkeiten vergleichbar mit dem frühen Sonnensystem. In Verbindung dazu quantifiziere ich die Kontrollparameter für die interne Entwicklung und den Verlust von volatilen Elementen von Planetesimalen, und die primären thermochemischen Klassen für den Aufbau interner Magmaozeane, Kernsegregation und chemischer Differenzierung. Indem ich die interne chemische Struktur der Planetesimale mit Anhaltspunkten von Meteoriten abgleiche, schränke ich die Akkretionsdynamik und Weiterprozessierung von planetaren Materialien im frühen Sonnensystem ein, um ein besseres Verständnis der Planetenentstehung zu erhalten. Schlussendlich, indem ich die vorangegangenen Mechanismen in Bezug auf die Exoplanetenpopulation extrapoliere, demonstriere ich den primären Einfluss von kurzlebigen Radionukliden auf die Anreicherung von terrestrischen Planeten mit volatilen Elementen: Vergleichbar mit dem Sonnensystem, tendieren angereicherte Planetensysteme dazu wasserarme Planeten zu formen, während in nicht oder gering angereicherten Systemen Ozeanwelten dominieren.

Meine Erkenntnisse liefern einen direkten Zusammenhang zwischen den Entstehungsgebieten planetarer Systeme und der materiellen Zusammensetzung und langfristigen Entwicklung von Gesteinsplaneten. Die Abweichungen in der Anreicherung mit kurzlebigen Radionukliden in Sternentstehungsgebieten grenzen die Entstehung und den Werdegang von planetaren Systemen voneinander ab und beeinflussen die Verteilung und Häufigkeit von terrestrischen Planeten mit erdähnlicher Zusammensetzung.

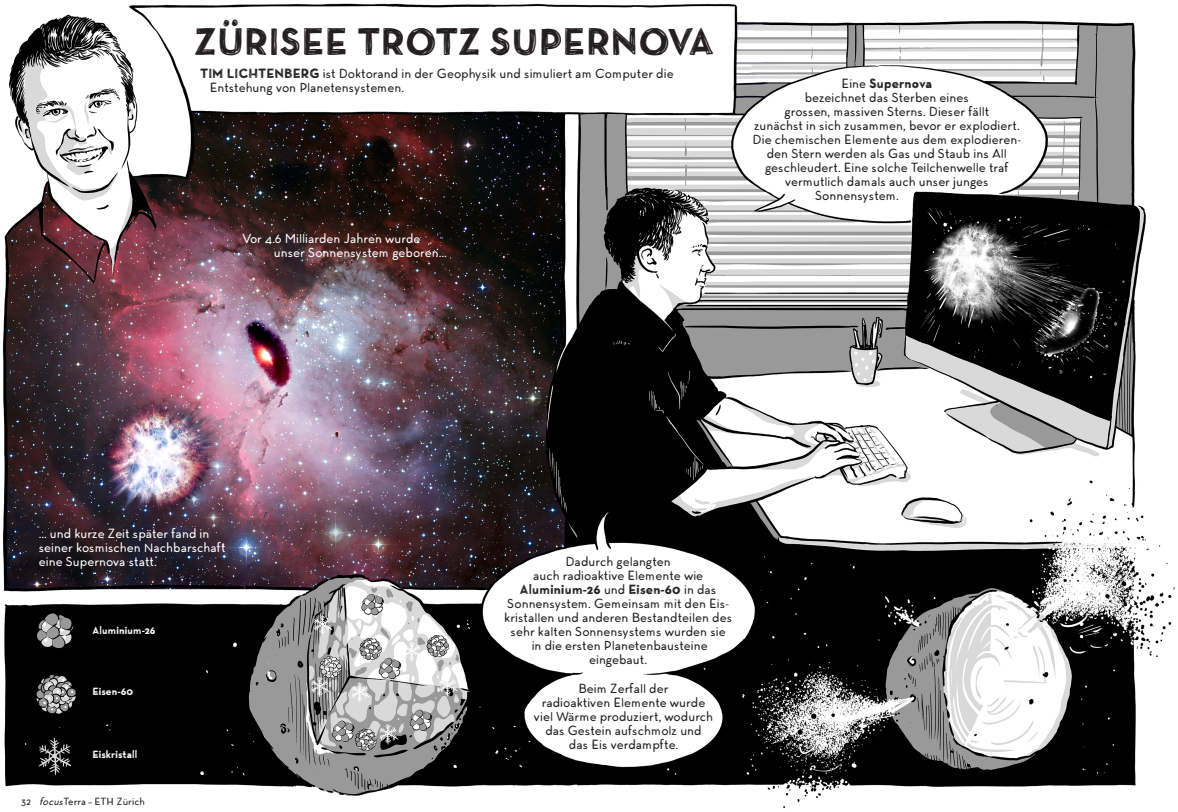

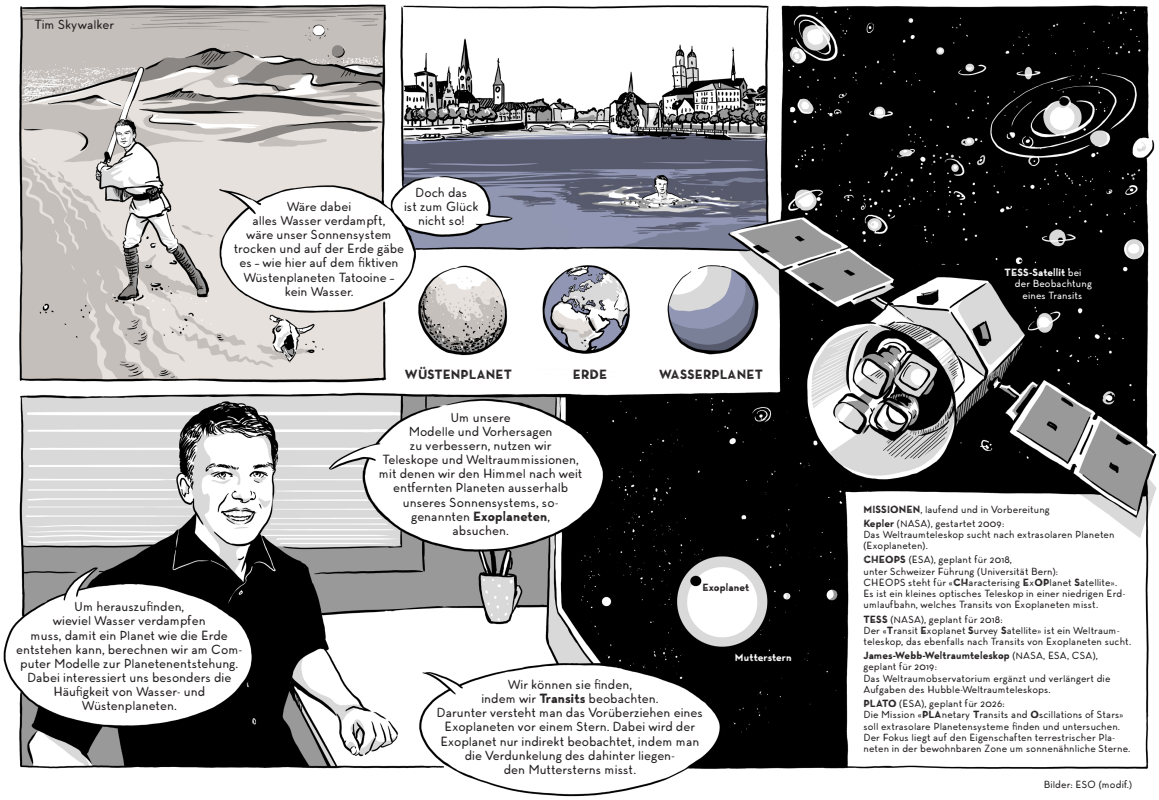

Bilder: ESO (modif.)

"Expedition Sonnensystem – Mit der ETH auf Forschungsreise durchs All"; Ulrike Kastrup, Kerstin Fankhauser, Gillian Grün, Jessica Kind, Bettina Gutbrodt, Andrea Dähler; focusTerra, ETH Zürich, 2018

PUBLICATIONS

Parts of this thesis have appeared previously in the following publications and preprints:

Lichtenberg, T., R. J. Parker, and M. R. Meyer (2016). "Isotopic enrichment of forming planetary systems from supernova pollution." *Monthly Notices of the Royal Astronomical Society* 462, 3979–3992. DOI: 10.1093/mnras/stw1929. arXiv: 1608.01435.

Lichtenberg, T., G. J. Golabek, T. V. Gerya, and M. R. Meyer (2016). "The effects of short-lived radionuclides and porosity on the early thermo-mechanical evolution of planetesimals." *Icarus* 274, 350–365. DOI: 10.1016/j.icarus.2016.03.004. arXiv: 1603.05979.

Lichtenberg, T., G. J. Golabek, C. P. Dullemond, M. Schönbächler, T. V. Gerya, and M. R. Meyer (2018a). "Impact splash chondrule formation during planetesimal recycling." *Icarus* 302, 27–43. DOI: 10.1016/j.icarus.2017.11.004. arXiv: 1711.02103.

Lichtenberg, T., T. Keller, R. F. Katz, G. J. Golabek, and T. V. Gerya (2018b). "Magma ascent in planetesimals: control by grain size." *Earth and Planetary Science Letters, under review*. arXiv: 1802.02157.

Parker, R. J., T. Lichtenberg, and S. P. Quanz (2017). "Was Planet 9 captured in the Sun's natal star-forming region?" *Monthly Notices of the Royal Astronomical Society: Letters* 472, L75–L79. DOI: 10.1093/mnrasl/slx141. arXiv: 1709.00418.

CONTENTS

LIST OF FIGURES

LIST OF TABLES

ACRONYMS

SLR short-lived radioisotope

CAI Ca,Al-rich inclusion

IMF initial mass function of stars

SFD size frequency distribution of planetesimals

FFLOP free-floating planet

olv olivine-like

pxn pyroxene-like

fsp feldspar-like

1 INTRODUCTION

Until the last decade of the 20th century, humanity was aware of only one planetary system around a star in the entire universe – the Solar system. Today in 2018, after roughly 20 years of intensive efforts, there is observational evidence for thousands of planets of all types (Winn and Fabrycky, 2015; Kaltenegger, 2017): gas and ice giants like Jupiter, Saturn, Uranus, and Neptune; or more rocky planets like the four inner Solar system planets Mercury, Venus, Earth, and Mars. Other formerly unknown types of planets that differ qualitatively from the planets in our Solar system are prevalent in the galaxy: *Hot Jupiters* (Mayor and Queloz, 1995), which are gaseous giants orbiting extremely close to their parent star, or *super-Earths* (Valencia, O'Connell, and Sasselov, 2006) that may be either scaled-up versions of Earth, or scaled-down versions of ice giants such as Neptune. Because other stars and their planets are enormously far away from Earth, it is very hard to catch the light they emit. Therefore, indirect observations, such as the transit and radial-velocity methods, which rely on precise measurements of changes in the stars' light, were so far the most successful techniques to detect extrasolar planets. Using extrapolations of the data from all known exoplanets, we think that the frequency of rocky planets per star is high, perhaps approaching 100% (Kaltenegger, 2017). This would be an enormous number by any measure and necessarily provokes the question of how many true Earth-twins are hiding out there in the vast darkness.

However, the available data for extrasolar planets is still sparse and the information that can be obtained is limited to only the very basic characteristics, most often just radius and mass; frequently only one of the two. Therefore, it is incredibly difficult to compare any planet out there to the planets in our Solar system. Figure 1.1 shows the currently available data for planets with radius $R_{\mathrm{P}} \lesssim 4\ R_{\mathrm{Earth}}$ and mass $M_{\mathrm{P}} \lesssim 30\ M_{\mathrm{Earth}}$. Very few known planets are located in close proximity to the Solar system terrestrial planets in mass-radius space, and we therefore, so far, do not know any Earth analogue by even those bulk measures, even though we are getting close (Gillon et al., 2016, 2017).

In addition to mass and radius, the bulk compositional make-up of a planet is of primary importance for its interior structure. Unfortunately, with only these two measures, the bulk chemistry of a planet in major refractory and volatile species is inherently degenerate (Adams, Seager, and Elkins-Tanton, 2008). Figure 1.2 demonstrates how two planets in the rocky regime can be composed of strikingly

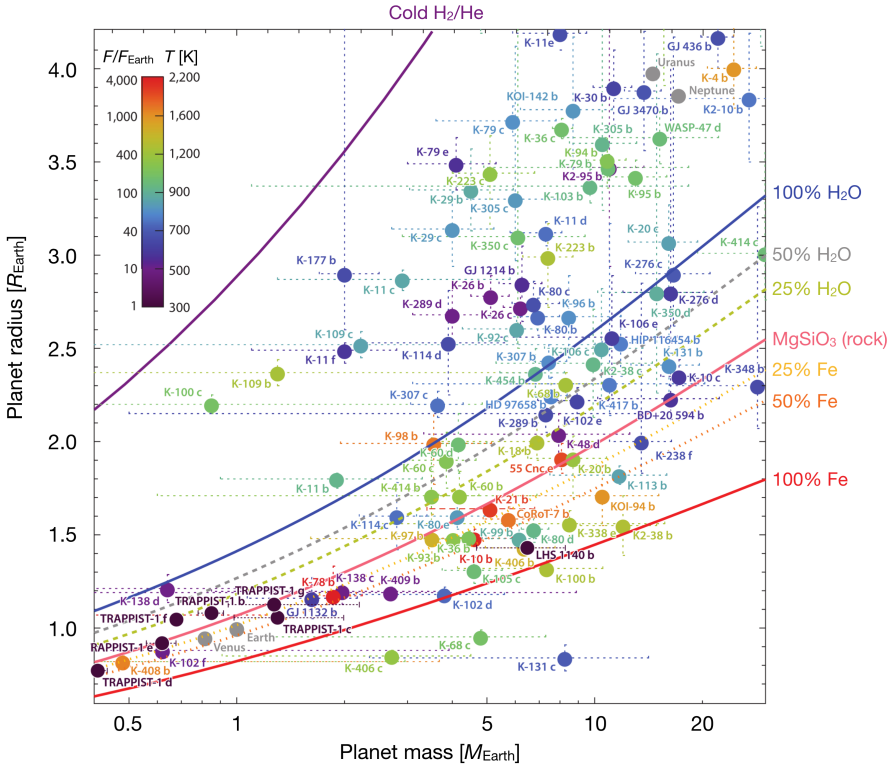

Figure 1.1: Mass-radius relations for various compositional mixtures and data for known extrasolar and Solar system planets below ~ 4 Earth radii and 30 Earth masses (modified from Kaltenegger, 2017). The different colors for exoplanets correspond to the incident stellar flux the planets receive relative to Earth, which can be translated to an estimate of the equilibrium temperature of the planet. For this conversion, Kaltenegger (2017) assumed a bond albedo of zero, perfect heat redistribution in the planet's atmosphere and the absence of a greenhouse effect. The different lines correspond to interior structure curves for a defined compositional mixture of iron, rock, water, and hydrogen/helium.

different materials when mass and radius are the only known parameters. In particular, volatiles like water are much less dense than refractory materials, like silicates or metals, and therefore they can potentially vary by orders of magnitude within the interior.

The amount of volatiles in a rocky planet interior is of fundamental importance for its long-term evolution. Following planet formation, the total amount of water in the mantle of planets with Earth-like bulk abundances controls the cool-down during the magma ocean phase, during which major parts of the rocky mantle are expected to be molten, and influences the chemical composition of the atmosphere (Zahnle, Kasting, and Pollack, 1988; Abe, 1993). In an exoplanetary context, the potential consequences of the bulk water abundance are even more pronounced. First, a planet within a critical orbital distance to its central star is expected to enter a long-

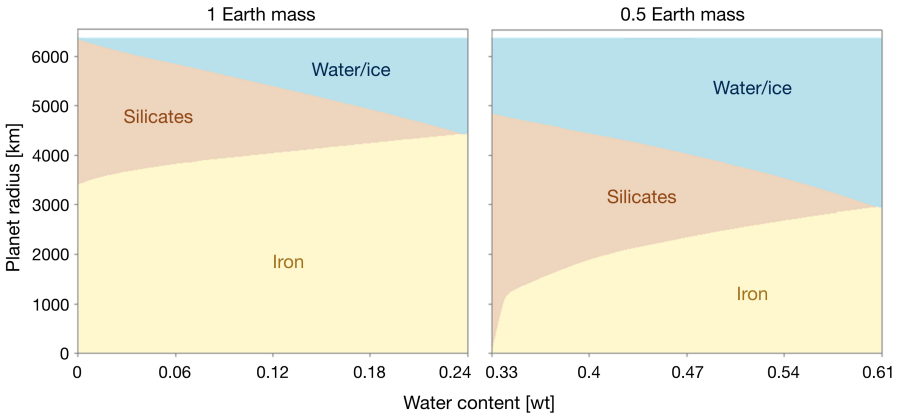

Figure 1.2: Possible interior structures for simplified bulk compositions of a planet with R_{P} = 1 R_{Earth} and M_{P} = 1 or 0.5 M_{Earth}, respectively (modified from Noack, Snellen, and Rauer, 2017). Without additional information besides mass and radius for a measured exoplanet, its composition can vary widely.

term runaway greenhouse phase that can last up to ∼Gyrs (Hamano, Abe, and Genda, 2013). In case the planet is far away enough from its parent star to cool down on a reasonable time scale ($\lesssim$ millions of years), the water will recondense on the planet surface and form surface oceans. However, since the water solubility under the high-pressure conditions in planetary mantles is low (Hirschmann et al., 2012; Peslier et al., 2018), most of the water cannot be mixed into the interior and will remain on the surface. Beyond a certain critical water mass fraction (∼ several wt%, depending on other parameters, such as internal heating and melting processes, Noack, Snellen, and Rauer, 2017), high-pressure ice phases form at the base of such a global water ocean, as depicted in Figure 1.3. These conditions transform any aspiring Earth-twin to something entirely different and render it frozen for potentially the entire stellar main sequence lifetime. Because of the primary control of volatiles on long-term planet behavior, their origin and delivery hold the clue to the surface and atmospheric conditions, which may lead to an origin of life similar to Earth (Elkins-Tanton, 2008; Elkins-Tanton and Seager, 2008; Arney et al., 2016; Pearce et al., 2018).

From studies of Solar system accretion, and theoretical and observational surveys of young star-forming regions, we think that we understand the basic principles of how planets acquire their volatile reservoirs. The general setup for the accretion process around a young star is illustrated in Figure 1.4. When a star forms, its accreting material flattens into a rotating disk-like structure made of gas and ice/-dust species. These *protoplanetary disks* are the birthplace of planets. In the case of terrestrial planets, the dust grains embedded in the disk at first coagulate to form rocky or rock-ice bodies, the so-called *planetesimals* (Morbidelli and Raymond, 2016; Birnstiel, Fang,

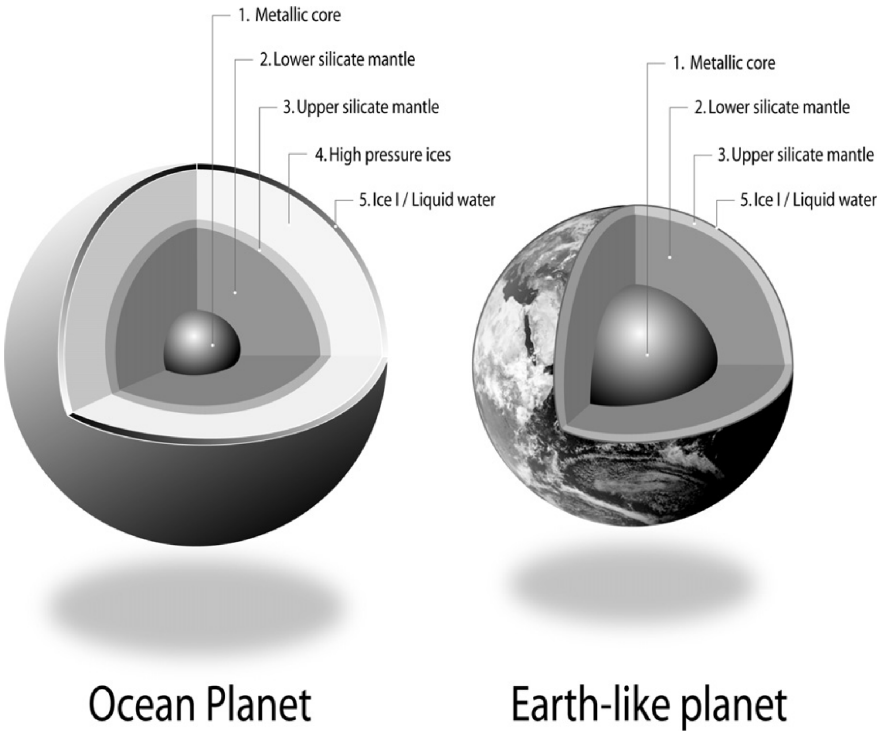

Figure 1.3: Comparison for rocky planets with very high and Earth-like bulk water fractions (from Sotin, Grasset, and Mocquet, 2007). Planets with bulk water fractions in excess of a few wt% exhibit high-pressure ice layers at the base of their global water oceans and suppress any chemical exchange between the interior and atmosphere/surface.

and Johansen, 2016; O'Brien et al., 2018). These then collide with each other and potentially accrete further dust grains to grow into terrestrial planets. As seen in Figure 1.4, the inner parts of the disk are expected to be heated by the star's light and, therefore, are composed of mostly rocky dust grains. Further outside, beyond the *snowline*[1], water ice can condense onto the dust grains (Ciesla and Cuzzi, 2006).

Therefore, a planet forming in the inner part of the disk (like Earth) must acquire some volatile material from outside the snowline. This can happen either by the movement of the snowline as a whole (Sasselov and Lecar, 2000), or by scattering and dynamical mixing of ice-rich planetesimals toward the inside. In the case of the Solar system, it was suggested that the scattering agent was (proto-)Jupiter, which enriched the early Earth with water during its final stages of assembly (Walsh et al., 2011; Raymond and Izidoro, 2017). Now, however, the inner terrestrial planets, in particular Earth, seem to be very water-poor in comparison with the enormous amounts of quantities that are expected to be present beyond the snowline during the proto-

1 For the sake of clarity, I will only speak of the *water* snowline here and neglect the condensation fronts of other chemical species.

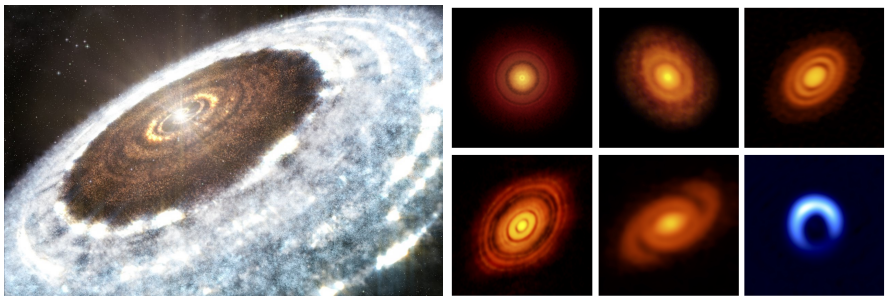

Figure 1.4: *(Left)* Artist's impression of the water snowline around the young star V883 Orionis. (Credit: A. Angelich (NRAO/AUI/NSF)/ALMA (ESO/NAOJ/NRAO)). *(Right)* Gallery of high angular resolution continuum observations of planet forming disks obtained with the Atacama Large Millimeter/submillimeter Array. From left to right and from top to bottom: TW Hya (Andrews et al., 2016), V883 Ori (Cieza et al., 2016), HD 163296 (Isella et al., 2016), HL Tau (ALMA Partnership et al., 2015), Elias 2-27 (Pérez et al., 2016), and HD 142527 (Kataoka et al., 2016). Credits: S. Andrews, L. Cieza, A. Isella, A. Kataoka, B. Saxton (NRAO/AUI/NSF), and ALMA (ESO/NAOJ/NRAO).

planetary disk phase. Based on measurements, Earth holds only a tiny fraction of $\sim$0.1% water by mass (Peslier et al., 2018). In comparison, dust grains and planetesimals beyond the snowline should be composed of roughly similar abundances of rock and ice, based on equilibrium condensation calculations (Lodders, 2003). Therefore, on the grand scale of the extrasolar planet population, the vast majority of material present within planet-forming regions around young stars should be predominantly water-rich. This would render the regions of most planetary systems prone to acquiring excess water mass fractions (in comparison with Earth), populated with ocean worlds as described above.

To resolve this mismatch between the supposedly water-rich compositions beyond the snowline and the apparent water abundances in the terrestrial planets at home, latest Solar system accretion studies argue that an early-forming Jupiter 'fossilized' the water snowline to a position somewhere within the asteroid main belt (Morbidelli et al., 2016), so that ice-rich materials could never reach Earth's orbit directly. Inward-scattering of planetesimals with water fractions similar to the most water-rich meteorites (so-called carbonaceous chondrites) during giant planet migration (Walsh et al., 2011) or steady growth (Raymond and Izidoro, 2017) can then satisfy geochemical constraints for Earth's water delivery (Rubie et al., 2015). However, most stars have been shown to not harbor any giant planet of Jupiter's size (Fischer and Valenti, 2005). This negates any water-shielding functions, which giant planets may serve, for the majority of planetary systems.

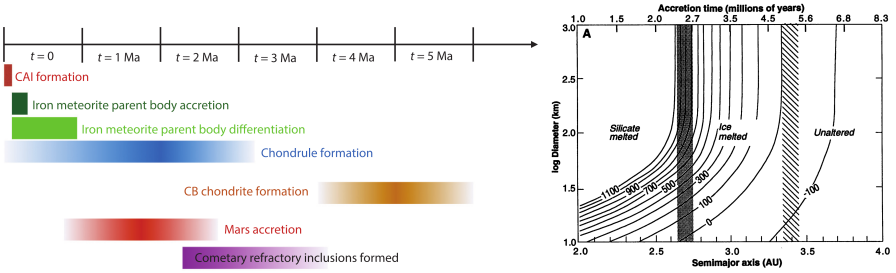

Figure 1.5: *(Left)* Timeline for various physical and chemical processes in the Solar protoplanetary disk as inferred from extraterrestrial samples. Adapted from Nittler and Ciesla (2016), see in there for references of the various ages. *(Right)* Thermal evolution and melting of silicates and water ice within accreting planetesimals from ^{26}Al-heating (from Grimm and McSween, 1993). During the first ∼2 million years the heating from ^{26}Al was energetic enough to melt primordial planetesimals and protoplanets larger than ∼10 km in radius and therefore provided the necessary heat source to differentiate them into a metallic core and silicate mantle.

However, dynamical studies of this process treat water abundances of planetesimals usually as a constant associated with the present-day abundances of water-rich material in meteorites. Moreover, as already expressed in the pioneering works of Grimm and McSween (1989) and Grimm and McSween (1993), early-formed planetesimals in the Solar system were subject to intense radiogenic heating from the presence of ^{26}Al (Lee, Papanastassiou, and Wasserburg, 1976b,a), a short-lived radioisotope (SLR) with a half-life of ∼0.7 Myr, which is comparable to the disk and accretion time scale of protoplanets.

In order to set the anticipated importance of ^{26}Al into context, Figure 1.5 lists the time scale and evidence for various Solar system materials inferred from geo- and cosmochemical studies and compares them with theoretical models of the thermal evolution due to radiogenic heating by ^{26}Al. The heating by radioactive decay in early planetary materials was much stronger than the radiogenic heat sources in the present-day Earth's mantle. Owing to this, early-formed icy planetesimals with high ^{26}Al abundance experienced intense heating that rapidly melted the water ice (Castillo-Rogez and Young, 2017; Monteux et al., 2018), and even the rock itself, transforming the planetesimals into rocky carapaces with large amounts of magma inside that potentially erupted during volcanic activity. Therefore, the presence of ^{26}Al fundamentally altered the compositional inventory of early Solar system materials and must be taken into account if we want to understand the accretion of the planets.

The time scales and ages inferred from matching extraterrestrial samples with the ^{26}Al radiogenic heating enable precise reconstructions of the accretion history of the Solar system. In addition to that, ^{26}Al sets the Solar system into a larger context of the formation of

Figure 1.6: Composite images of two young star-forming regions. *(Left)* The *Flame Nebula*, at a distance of 415 pc from Earth (Meyer et al., 2008) and apparent dimensions 30'×30', with young stars depicted in purple (Getman, Feigelson, and Kuhn, 2014, x-ray: NASA/CXC/PSU/K.Getman, E.Feigelson, M.Kuhn & the MYStIX team; infrared: NASA/JPL-Caltech). *(Right)* Stellar explosion in the Orion nebula (Bally et al., 2017, ALMA, ESO/NAOJ/NRAO).

planetary systems (Adams, 2010). The relative abundance of various SLRs can only be satisfied if the ^{26}Al in our Solar system has an extrasolar source, most likely a massive star that enriched the Solar system material with ^{26}Al early-on (Ouellette et al., 2009; Adams, 2010; Nittler and Ciesla, 2016; Portegies Zwart et al., 2018).

As most stars in the galaxy, the Sun likely formed in the close proximity of dozens to hundreds, or even thousands, of other stars (Lada and Lada, 2003; Bressert et al., 2010; Adams, 2010). Most of them were of similar or lower mass than the Sun, but one or a few of them were likely much more massive. Images of such young star-forming regions are shown in Figure 1.6 and depict the formation of young stellar objects together with the remnants of their parental molecular clouds. Shortly before or during the formation of the Sun, the Solar system material was enriched by additional material from one or more massive stars. The actual abundance of ^{26}Al at the time of Solar system formation, usually defined to be the age of the oldest known solids, the Ca,Al-rich inclusions (CAIs), can then be used to constrain the physics and chemistry within the Sun's parent star-forming region.

THESIS STRUCTURE The former brief introductions to a variety of sub-fields of astrophysics and planetary science serve as the background information for this thesis. I started by introducing the variety of exoplanets observed to date and the difficulties faced to infer their long-term evolution. I connected their evolution to their accretion pathway through their bulk abundances of water and the depen-

dence of the bulk composition on the primary constituents of planets – planetesimals. I introduced heating from short-lived radioisotopes as a potentially primary mechanism to alter the composition of planetesimals and connected the presence of short-lived ^{26}Al in the early Solar system to enrichment mechanisms in the Sun's birth star-forming region.

For the remainder of this thesis, I will invert the order of topics that I have introduced so far and sub-structure them into three different parts. In Part i, I start by quantifying the expected distribution of SLRs, like ^{26}Al, in young star-forming regions and derive prospective radiogenic heating rates for exo-planetesimals (Chapter 2). As a timely addition, I demonstrate how state-of-the-art inferences of the current Solar system architecture can be used in conjunction with cosmochemical constraints and modeling of the star-forming environment of the young Sun to draw conclusions about the history of Solar system objects (Chapter 3).

Part ii focuses on the interior evolution of planetesimals, in particular the high-energy regime where ^{26}Al is energetic enough to melt silicate materials. Even though the models presented in this part are framed within the context of Solar system planet formation, the inferences drawn are generally applicable also to exoplanetary systems. Here, the formation times referenced can be directly converted to initial ^{26}Al values in extrasolar systems at the time of planetesimal formation. Therefore, they can be interpreted as evolution in exo-planetesimals subject to varying degrees of radiogenic heating. To start with, Chapter 4 lays out the general evolutionary regimes of planetesimals in the early Solar system. In particular, it combines the ^{26}Al-heating with the potentially high macro-porosity of planetesimals during assembly, which is relevant for planetesimals that accrete through rapid collapse in the protoplanetary disk. Chapter 5 then digs deeper into the evolution of the silicate melt in planetesimals, focusing on potential volcanic activity due to rapid melt ascent and connects planetesimal evolution to currently ongoing space missions to asteroids and remnant protoplanets in the Solar system.

Part iii then goes beyond the interior models of planetesimals and draws inferences on the accretion dynamics of the Solar system. In particular, Chapter 6 deals with the type of constraints that can be inferred from studies of chondrites and their constituents – chondrules. The cosmochemical record for these types of meteorites that can help guide current models of rocky planet formation are needed to piece together the detailed reconstruction of terrestrial planet accretion. Finally, Chapter 7 circles back to the grand perspective. I connect the time scales and interior evolution models described until then to constrain general features of accretion in planetary systems that apply to the exoplanetary population. In particular, my work introduces SLR-induced dehydration of planetesimals as a major con-

trol on the difference between ocean worlds and water-poor planets, such as Earth. The inferences derived in this chapter are used to make predictions for the exoplanet population in the rocky planet regime that we may be able to probe within a 10 to 20 year time scale with upcoming space telescopes. I suggest that the primary difference between a planetary system with water-poor or ocean worlds may be the ^{26}Al abundance that the system starts out with.

Each part and chapter features its own introduction, where front pages for each part connect the chapters in them to each other. In the very last Part iv, I summarize the advances made in this work as a whole (Chapter 8) and present an outlook (Chapter 9) of ideas and gaps in our current understanding that will be worth exploring in the future.

Part I

STELLAR ENVIRONMENT OF FORMING PLANETARY SYSTEMS

This first part deals with the effects of the star-forming environment on growing planetary systems. The majority of stars in our galaxy are born in intermediate to dense stellar environments, where hundreds or thousands of stars form simultaneously. During that process they interact gravitationally with each other and dynamically excite each others' trajectories in the dispersing cluster. Because stars of various masses are formed close to each other, the most massive stars are thought to dominate the environment. In particular, they explode as supernova(e) after a few million years and may inject freshly fused material into the planet-forming disks of their low-mass siblings, such as the young Sun. By quantifying the efficiency of this mechanism, I derive the anticipated distribution of ^{26}Al and ^{60}Fe, the two most important SLRs for the planet formation process in this context. I find a distribution dichotomy in the abundance of SLRs in young planetary systems – a majority with negligible to zero abundances, and a few per cent to up to tens of per cent of planetary systems that are strongly enriched to levels similar to or higher than the Solar system. Using these quantified enrichment patterns, I calculate the odds that the hypothesized 'Planet 9' in the outer Solar system was captured within the early star-forming environment of the Sun, which yields implications for the dynamic history of the Solar system planets.

2

ISOTOPIC ENRICHMENT OF FORMING PLANETARY SYSTEMS FROM SUPERNOVA POLLUTION

The content of this section was published as: Lichtenberg, T., R. J. Parker, M. R. Meyer (2016). "Isotopic enrichment of forming planetary systems from supernova pollution." Monthly Notices of the Royal Astronomical Society 462, 3979-3992. doi: 10.1093/mnras/stw1929. arXiv: 1608.01435.

ABSTRACT

Heating by SLRs such as ^{26}Al and ^{60}Fe fundamentally shaped the thermal history and interior structure of Solar system planetesimals during the early stages of planetary formation. The subsequent thermo-mechanical evolution, such as internal differentiation or rapid volatile degassing, yields important implications for the final structure, composition and evolution of terrestrial planets. SLR-driven heating in the Solar system is sensitive to the absolute abundance and homogeneity of SLRs within the protoplanetary disk present during the condensation of the first solids. In order to explain the diverse compositions found for extrasolar planets, it is important to understand the distribution of SLRs in active planet formation regions (star clusters) during their first few Myr of evolution. By constraining the range of possible effects, we show how the imprint of SLRs can be extrapolated to exoplanetary systems and derive statistical predictions for the distribution of ^{26}Al and ^{60}Fe based on N-body simulations of typical to large clusters (10^3-10^4 stars) with a range of initial conditions. We quantify the pollution of protoplanetary disks by supernova ejecta and show that the likelihood of enrichment levels similar to or higher than the Solar system can vary considerably, depending on the cluster morphology. Furthermore, many enriched systems show an excess in radiogenic heating compared to Solar system levels, which implies that the formation and evolution of planetesimals could vary significantly depending on the birth environment of their host stars.

2.1 INTRODUCTION

The presence of SLRs during the early stages of planetary formation is of central importance in the view of core-accretion planet formation models. In the Solar system, the radioactive decay of ^{26}Al was the main heat source of the earliest planetesimals and planetary embryos during the first few Myr (Grimm and McSween, 1993) after the formation of CAIs. Their interior thermo-mechanical evolution fa-

cilitated differentiation and thus mineralogical, petrographical and structural evolution (Hevey and Sanders, 2006; Moskovitz and Gaidos, 2011; Lichtenberg et al., 2016) and possibly affected the total volatile budget (Young et al., 1999; Fu and Elkins-Tanton, 2014). Subsequent collisional interactions during runaway growth shaped the core-to-mantle ratio and determined the building material of terrestrial planets like Earth (O'Neill and Palme, 2008; Bonsor et al., 2015). With differing initial abundances of SLRs and thus heating rates many of these mechanisms would change and potentially result in drastically different planetary compositions.

SLR tracers in the meteoritic record additionally provide stringent constraints on the birth environment of the nascent Solar system (Lee, Papanastassiou, and Wasserburg, 1976a). Some of them, like ^{10}Be, can be explained by solar energetic particle irradiation, but others, most importantly ^{26}Al and ^{60}Fe, suggest an external, stellar nucleosynthetic source. To complicate the picture, their concentrations are too elevated to be consistent with galactic background levels (Meyer and Clayton, 2000), with the short half-lives (0.7 Myr for ^{26}Al, 2.6 Myr for ^{60}Fe) implying a late stage enrichment.

Numerous attempts have been made to link the inferred SLR abundance levels to a specific injection channel including triggered collapse of the presolar cloud core (Cameron and Truran, 1977), potentially with former enrichment by the winds of a massive star in a sequential triggering process (Tatischeff, Duprat, and de Séréville, 2010; Gounelle and Meynet, 2012; Young, 2014), or the direct pollution of the circumstellar disk by supernova ejecta (Clayton, 1977; Chevalier, 2000). The difficulties in measuring excess abundances of ^{60}Fe, the strongest argument for a direct supernova injection mechanism, so far failed to converge on a preferred order of magnitude (Tachibana and Huss, 2003; Quitté et al., 2010; Tang and Dauphas, 2012; Mishra, Marhas, and Sameer, 2016). While triggered star formation is a much-debated issue (Dale, Haworth, and Bressert, 2015), we consider intracluster enrichment mechanisms, like direct disk injection from the winds of nearby massive stars or supernova ejecta, to be inevitable to some extent.

Even though the specific enrichment channel of the Solar system is still under much debate (e.g., Davis et al., 2014; Adams, Fatuzzo, and Holden, 2014; Parker et al., 2014b; Schiller, Paton, and Bizzarro, 2015; Boss and Keiser, 2015; Parker and Dale, 2016), attempts are ongoing to extrapolate the predictions by the proposed enrichment channels to extrasolar and even galactic scales (Gounelle, 2015). In the context of the rapidly evolving field of exoplanetary studies (Benz et al., 2014) the injection efficiency and hence distribution of SLRs on larger scales link the geodynamical processes in forming planetary systems to its stellar birth environment.

Although many implications of SLR-dominated heating in planetesimals of sizes greater than $\sim$10 km are now understood (e.g., Hevey and Sanders, 2006; Elkins-Tanton, Weiss, and Zuber, 2011; Elkins-Tanton, 2012; Weiss and Elkins-Tanton, 2013; Golabek, Bourdon, and Gerya, 2014; Lichtenberg et al., 2016), the detailed coupling between interior thermo-mechanical-chemical evolution, collisional growth and subsequent effects on the final planet outcome remains elusive (Fu and Elkins-Tanton, 2014; Gerya et al., 2015; Bonsor et al., 2015; Carter et al., 2015). Nonetheless, with the goal of an observationally consistent theory of planetary assembly in mind, it is crucial to understand the distribution of SLRs on larger, like interstellar or galactic, scales.

Thus, in this work, we derive statistical predictions for the distribution of ^{26}Al and ^{60}Fe, the two main nucleosynthetic SLR heat sources, from the direct pollution of circumstellar disks in young star clusters. The structure of the paper is as follows. In Section 2.2 we describe the N-body simulations and the post-processing calculations, which take into account the dynamical evolution of the star cluster as well as the injection and mixing of supernova ejecta in the disks, as they evolve over time. We present our results in Section 2.3, focusing first on the dynamical evolution of the cluster populations, and secondly the predictions for the SLR distribution in them. We discuss the results and limitations of our study in Section 2.4 and comment on the implications of our study on volatile degassing, planet population synthesis and the enrichment of the Solar system. We draw conclusions in Section 2.5.

2.2 METHODOLOGY

Our method to derive predictions for the SLR abundances in star forming regions is built on a large suite of N-body simulations of stellar clusters from 10^3–10^4 stars. This corresponds to the cluster mass required to form stars massive enough to explode as supernovae during the protoplanetary disk phase (Portegies Zwart, 2009; Adams, 2010), assuming a fully sampled initial mass function of stars (IMF) (Parker and Goodwin, 2007; Weidner, Kroupa, and Bonnell, 2010).

We use N-body simulations with stellar evolution to determine the distances to the supernova(e) of all low-mass stars as a function of the initial conditions of the cluster. We then analyze these simulations using a post-processing routine, which semi-analytically treats details of the pollution mechanism and introduces assumptions about protoplanetary disk lifetimes and isotope mixing. In Section 2.2.1 we present the setup and reasoning of the numerical simulations and explain the post-processing routine in Section 2.2.2.

2.2.1 *Star cluster setup*

Our model clusters initially have either 10^3 or 10^4 stars drawn from the IMF of stars from Maschberger (2013), with a mass range of $M_\star = 0.01 - 50\,M_\odot$. This combines the log-normal approximation from Chabrier (2003) with the Salpeter (1955) power-law slope for stellar masses $> 1\,\mathrm{M}_\odot$. The probability density function for the Maschberger IMF has the form

$$p(m) \propto \left(\frac{m}{\mu}\right)^{-\alpha} \left(1 + \left(\frac{m}{\mu}\right)^{1-\alpha}\right)^{-\beta}, \tag{2.1}$$

with the average stellar mass $\mu = 0.2\,\mathrm{M}_\odot$, the Salpeter power-law exponent $\alpha = 2.3$ for higher mass stars and $\beta = 1.4$ is used to determine the slope of the low-mass part of the distribution.

We adopt two different spatial morphologies for the initial conditions of our star clusters; smooth and substructured. The spatial distribution of stars in older clusters is often observed to be smooth and centrally concentrated. These clusters can often be approximated with a Plummer (1911) or King (1966) profile.

Formally, Plummer spheres are infinite in extent, and are usually described in terms of their half-mass radius. We use Plummer spheres with positions and velocities determined by the prescription in Aarseth, Henon, and Wielen (1974), with initial half-mass radii of 0.3 and 0.4 pc.

Stars are observed to form in filaments (e.g. André et al., 2014), which usually results in a substructured spatial and kinematic distribution for stars in a given star-forming region (Cartwright and Whitworth, 2004; Sánchez and Alfaro, 2009).

We set up star-forming regions with primordial substructure using the fractal distribution in Goodwin and Whitworth (2004). Note that we are not claiming that star-forming regions are fractals (although they may be, Elmegreen and Elmegreen, 2001), but rather that fractals are the most convenient way of setting up substructure because the amount of substructure is set by just one number, the fractal dimension D.

For a detailed description of the fractal set-up, we refer the interested reader to Allison et al. (2010) and Parker et al. (2014a), but we briefly summarize it here. The fractal is built by creating a cube containing 'parents', which spawn a number of 'children' depending on the desired fractal dimension. The amount of substructure is then set by the number of children that are allowed to mature. The lower the fractal dimension, the fewer children are allowed to mature and the cube has more substructure. Fractal dimensions in the range $D = 1.6$ (highly substructured) to $D = 3.0$ (uniform distribution) are allowed. Finally, outlying particles are removed so that the cube from which the fractal was created becomes a sphere; however, the distribution

Setting	$N_\star$	Morphology	$R_{\rm cl}$ or $r_{1/2}$ [pc]
#01	10^3	Fractal	1.0
#02	10^3	Plummer	0.3
#03	10^3	Plummer	0.4
#04	10^4	Fractal	1.0
#05	10^4	Fractal	3.0
#06	10^4	Plummer	0.3
#07	10^4	Plummer	0.4

Table 2.1: Initial settings for all types of N-body simulations, which we follow for 10 Myr in total. All simulations are initialized using $D = 1.6$ and $\alpha_{\rm vir} = 0.5$. From left to right, the columns are the number of stars, $N_\star$, the initial morphology, and either the initial radius of the fractal $R_{\rm cl}$, or the initial half-mass radius of the Plummer sphere $r_{1/2}$. To account for statistical variations we perform 30 simulation runs for each type. The setting identifiers correspond to the ones in Table 2.3 and 2.4.

is only truly spherical if $D = 3.0$. We adopt $D = 1.6$ throughout this paper, and the fractals have initial radii of 1 and 3 pc.

To determine the velocity structure of the cloud, children inherit their parent's velocity plus a random component that decreases with each generation of the fractal. The children of the first generation are given random velocities from a Gaussian of mean zero. Each new generation inherits their parent's velocity plus an extra random component that becomes smaller with each generation. This results in a velocity structure in which nearby stars have similar velocities, but distant stars can have very different velocities. The velocity of every star is scaled to obtain the desired virial ratio of the star-forming region.

The virial ratio, $\alpha_{\rm vir} = T/|\Omega|$, where T and $|\Omega|$ are the total kinetic and total potential energy of all stars in the cluster, respectively. Parker et al. (2014b) found that the amount of enrichment is insensitive to the initial virial ratio in the range $\alpha_{\rm vir} = 0.3$ (bound and initially collapsing) to $\alpha_{\rm vir} = 0.7$ (unbound with some initial expansion). Therefore, all clusters were initialized in virial equilibrium, with $\alpha_{\rm vir} = 0.5$.

Our model clusters are evolved using the KIRA integrator within the STARLAB package (see, e.g., Portegies Zwart et al., 1999, 2001) and we implement stellar evolution using the SEBA code (Portegies Zwart and Verbunt, 1996, 2012), also in STARLAB. The clusters are evolved for 10 Myr, which encompasses the majority of protoplanetary disk lifetimes, stars $\gtrsim 19\,{\rm M}_\odot$ will explode as supernovae and the majority of dynamical interactions that could disrupt disks occur within this time frame.

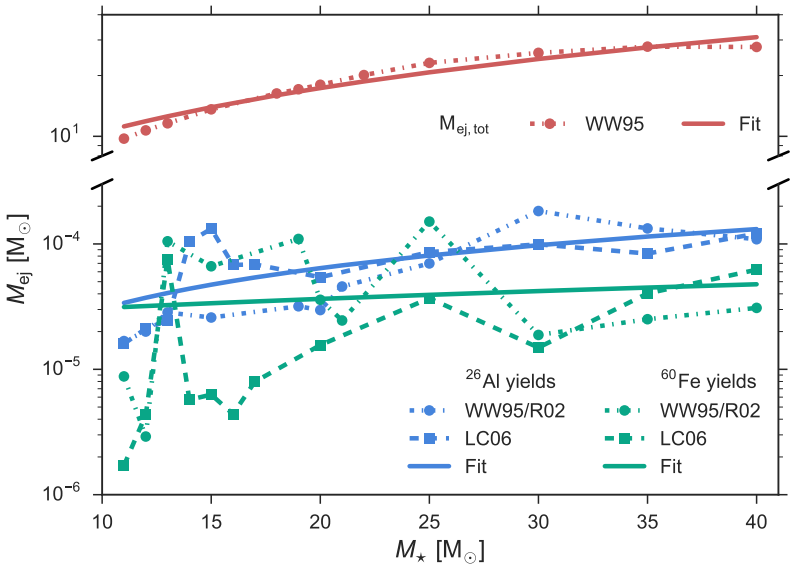

Figure 2.1: Isotopic yields of ^{26}Al and ^{60}Fe per supernova progenitor mass with data from Woosley and Weaver (1995) and Rauscher et al. (2002) (denoted as WW95/R02) and Limongi and Chieffi (2006) (LC02). To achieve a yield function we fit the data linearly. The regressions scale as: $M_{\mathrm{ej,tot}} \propto 0.68 M_\star$, $M_{\mathrm{ej,Al}} \propto 3.4 \times 10^{-6} M_\star$ and $M_{\mathrm{ej,Fe}} \propto 5.6 \times 10^{-7} M_\star$.

To account for the stochasticity inherent in star cluster evolution (Parker and Goodwin, 2012; Parker et al., 2014b), we ran 30 versions of each set of initial conditions, identical apart from the random number seed used to generate the masses, positions and velocities. A summary of the initial settings can be found in Table 2.1. Finally, each simulation was run for 10 Myr, the higher end tail of protoplanetary disk lifetimes and thus the relevant time scale for supernova pollution of circumstellar disks (see, e.g., Haisch, Lada, and Lada, 2001; Lada and Lada, 2003; Mamajek, 2009; Bell et al., 2013; Cloutier et al., 2014).

2.2.2 *Enrichment mechanism*

It is common for young stars to form close together in a cluster and therefore supernova progenitor stars are found in the vicinity of less massive stars (Lada and Lada, 2003). After several Myr of evolution the progenitor(s) explode as core-collapse supernovae, ejecting their SLR-enriched outer shells into the local environment. Parts of the ejecta material are injected into circumstellar disks via cross-section capture, mixed into the disk and subsequently incorporated into forming solid bodies. In the following we describe each physical process from the SLR-ejection of supernova progenitor stars down to the mixing in the disk and present our post-process implementation in order

to derive statistical predictions for the distribution of SLRs in stellar clusters with 10^3– 10^4 stars.

First, we use the N-body simulations to determine the locations of stars when a massive star goes supernova and the relative positions of low-mass stars in the cluster with respect to the supernova. By fitting the supernova yield predictions from Woosley and Weaver (1995), Rauscher et al. (2002), and Limongi and Chieffi (2006) we assign each supernova event to a specific absolute mass of SLR material, as shown in Figure 2.1.

Using the formulation of Ouellette, Desch, and Hester (2007, 2010), the transport and injection physics of supernova yields to a disk can be broken down into 3 parameters: the condensation efficiency of metals in the ejecta shock front, η_{cond}, the cross-section factor of a protoplanetary disk with the ejecta front, η_{geom}, and the injection efficiency into the disk, η_{inj}. Ouellette, Desch, and Hester (2010) discussed the observational constraints of η_{cond} and arrived on a possible parameter range of η_{cond} = 0.01–1. Since then, however, evidence of efficient solid condensation in ejecta fronts has arisen (Matsuura et al., 2011) and it seems indeed possible that η_{cond} is close to $\sim$1. To take a conservative approach and to account for potential variations between different supernova events we chose η_{cond} = 0.5 throughout our analysis. The geometrical cross-section of a random disk with supernova ejecta can be easily calculated (Adams, Fatuzzo, and Holden, 2014) via

$$\eta_{\mathrm{geom}} = \frac{\pi r_{\mathrm{disk}}^2}{4\pi d^2} \cos\theta, \tag{2.2}$$

with r_{disk} the radius of the circumstellar disk (see Section 2.2.3), d the distance between donor and acceptor star and $\theta = 60^\circ$ the average disk alignment with respect to the ejecta for a random distribution. For this purpose we neglected the time interval dt between the supernova outburst and the time of arrival, as average travel times in such a scenario are on the order of $dt \approx 100$ yr (Ouellette, Desch, and Hester, 2010), i.e., negligible in comparison with the evolutionary time scale of the disks, their half-lives and the cluster dynamical time scale.

The injection efficiency η_{inj} is determined by the size distribution of condensed grains in the supernova ejecta, as large grains can be easier injected. For the case of a grain size distribution in accordance with presolar grains of supernova origin, like meteorite grain sizes in the Solar system (Amari, Lewis, and Anders, 1994), the injection efficiency into the disk structures is $\approx$ 0.9 (Ouellette, Desch, and Hester, 2010). However, we assume that the average dust grain size is smaller, $\sim 0.1\mu$m, consistent with the size distribution of interstellar grains (Mathis, Rumpl, and Nordsieck, 1977), in which case $\eta_{\mathrm{inj}} \approx 0.7$ (Ouellette et al., 2009). In general, whenever we had to decide between an approach which would boost final enrichment abundances versus

one which is expected to lower them, we chose the latter, which we see as a conservative way of not overestimating the effects of direct supernova pollution.

When the SLRs are injected into the disk they must be mixed into the disk material on a relatively short time scale as is implicitly assumed when using ^{26}Al as a Solar nebula chronometer in cosmochemical dating methods. From a theoretical perspective, mixing in the disk can occur either via large scale gravitational instabilities or turbulent diffusion on local scales. The first is extremely effective while the disk is massive (e.g., Boss, 2007). The latter demands a very detailed understanding of the actual disk physics and crucially depends on still largely unconstrained disk properties, but can also be efficient when the vertical structure of the disk is considered due to large-scale radial mixing (Ciesla and Cuzzi, 2006; Ciesla, 2007). A detailed review of the mixing processes within the disk is beyond the scope of this paper, for further details see Ouellette et al. (2009). For the Solar system, there is evidence of large-scale ^{26}Al homogeneity (Villeneuve, Chaussidon, and Libourel, 2009), even though the discussion is still ongoing. When the SLRs are mixed into the disk material before planetesimal agglomeration, they will be incorporated into the growing bodies.

2.2.3 *Timing and disk dynamics*

We assumed that every star forms with a disk of initially $M_{\mathrm{disk}} = 0.1\ M_{\star}$, which is expected to be the threshold mass just stable to large-scale gravitational instabilities at the end of the infall phase (Natta, Grinin, and Mannings, 2000; Williams and Cieza, 2011). The initial number of potential planet forming disks was therefore $N_{\mathrm{disk}} = N_{\star}$, depending on the cluster size. As we were interested in the consequences for systems which finally developed fully fledged planetary systems, we subtracted the stars which might have been subject to violent transformation due to either disruption by close-by supernova ($d \leq 0.1$ pc, Adams, 2010), truncation by close encounters with $d \leq 500$ au or photoevaporation from a nearby O star ($d \leq 0.3$ pc for $dt \geq 1$ Myr, Scally and Clarke, 2001; Adams et al., 2004; Alexander et al., 2014). Again, we have chosen these values in a conservative fashion, as not to overestimate SLR abundances. See Section 2.4.4 for a discussion of these issues.

The number of stars/disks not violated by these events was subsequently scaled by a declining distribution, to account for the decreasing number of observed disks with cluster age (Haisch, Lada, and Lada, 2001; Mamajek, 2009). To do so, at the time of each super-

nova event, the number of disks was decreased via the exponential scaling law

$$N_{\mathrm{disk}} = N_{\star} e^{-t/\tau_{\mathrm{disk}}}, \tag{2.3}$$

with mean lifetime $\tau_{\mathrm{disk}} = 5.0$ Myr, corresponding to a disk half-life time of $\tau_{1/2} = \tau_{\mathrm{disk}} \ln(2) \approx 3.47$ Myr. Given that newest observational estimates are consistent with up to $\tau_{1/2} \approx 6.0$ Myr (Bell et al., 2013; Cloutier et al., 2014), this is again a conservative approach.

To achieve a realistic estimate of the mixing ratio of the SLRs with the disk material, we inferred a time-dependent disk model for the evolution of the surface density (Hartmann, 2009) with a flared structure according to

$$T(R) \sim 10 \left(\frac{100\,\mathrm{AU}}{R} \right)^{1/2} \mathrm{K}, \tag{2.4}$$

$$\Sigma \sim 1.4 \cdot 10^3 \frac{e^{-R/(R_1 t_d)}}{(R/R_1) t_d^{3/2}} \left(\frac{M_d(0)}{0.1\,\mathrm{M}_{\odot}} \right) \left(\frac{R_1}{10\,\mathrm{AU}} \right)^{-2} \mathrm{g\,cm^{-2}}, \tag{2.5}$$

$$t_d = 1 + \frac{t}{t_s}, \tag{2.6}$$

$$t_s \sim 8 \cdot 10^4 \left(\frac{R_1}{10\,\mathrm{AU}} \right) \left(\frac{\alpha}{10^{-2}} \right)^{-1} \left(\frac{M_{\star}}{0.5\,M_{\odot}} \right)^{1/2} \left(\frac{T_{100}}{10\,\mathrm{K}} \right) M_{\odot}\,\mathrm{yr}^{-1}, \tag{2.7}$$

with R the distance from the central star, the 'initial' scaling disk radius $R_1 = 10$ au[1], time normalization t_d, scaling time t_s, initial disk mass $M_d(0) = 0.1\,M_{\star}$, disk viscosity parameter $\alpha = 10^{-2}$ and normalization temperature $T_{100} = 10$ K. For a detailed description of this model we refer to Hartmann (2009). Even though newest theoretical and observational estimates of the disk viscosity trend toward lower values, our choice of $\alpha = 10^{-2}$ reflects a compromise between the seemingly low values in observed disks (Alexander et al., 2014; Flaherty et al., 2015) and long disk lifetimes for lower α values in this model.

As the disks became subject to interaction with supernova blast waves and could potentially be truncated from the momentum coupling, we inferred an estimate of the disk truncation radii during the intersection with the ejecta. In a simple analytical estimate Chevalier (2000) stated that two types of mass loss by the interaction with the ejecta must be taken into account. First, matter may be stripped from a disk due to the ram pressure of the ejecta flow, if the time scale of the ejecta interaction is longer than the dynamical time scale of the disk. Then, the disk is stripped if the ram pressure exceeds the gravitational force per unit area

$$P_{\mathrm{grav}} \approx G M_{\star} \Sigma_{\mathrm{disk}} / r_{\mathrm{d}}, \tag{2.8}$$

1 This is *not* a total initial disk radius, compare Figure 2.2.

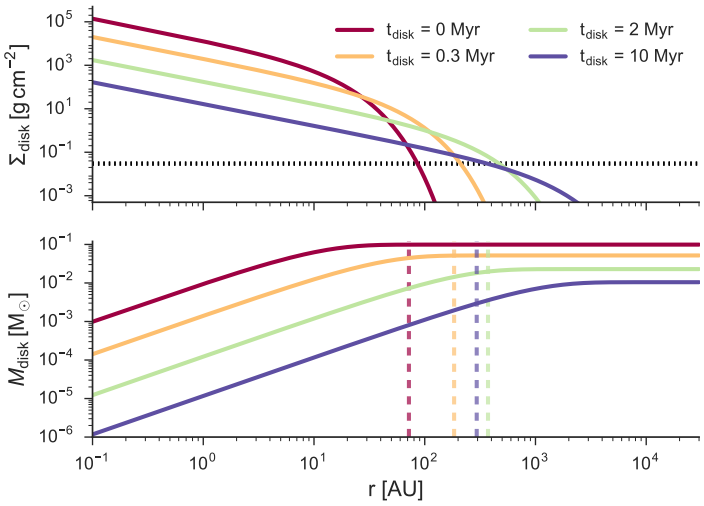

Figure 2.2: time-dependent disk model (Hartmann, 2009) to calculate the truncation radius $R_{\rm disk}$ and total mass $M_{\rm disk}$ for a Solar analog with $M_\star = 1\,M_\odot$. *Upper panel:* Surface density for different times. The horizontal dotted line indicates the cut off density from the density criterion (compare Figure 2.3). *Lower panel:* Disk mass for different times with the truncation radii (again from the density criterion) for different times indicated with vertical dashed lines.

with the gravitational constant G, the surface density of the disk $\Sigma_{\rm disk}$ at distance $r_{\rm d}$. For the case of a constant density supernova with ejection energy $E_{\rm ej}$, Chevalier (2000) found the maximum ram pressure that can be exerted by the ejecta to be

$$P_{\rm ram} = 5E_{\rm ej}/(2\pi d_{\rm SN}^3), \tag{2.9}$$

with the distance to the supernova source $d_{\rm SN}$. Second, in the case of a rapid interaction of the ejecta with the disk, the momentum in the ejecta flow $p_{\rm m,ej}$ can cause disk material to reach escape velocity

$$v_{\rm esc} = (2GM_\star/r_{\rm d})^{1/2}. \tag{2.10}$$

Thus, the momentum stripping criterion becomes

$$p_{\rm m,ej} > p_{\rm m,disk}, \tag{2.11}$$
$$M_{\rm ej}v_{\rm ej}/(4\pi d_{\rm SN}^2) > \Sigma_{\rm disk}v_{\rm esc}, \tag{2.12}$$

with $v_{\rm ej} = (10E_{\rm ej}/3M_{\rm ej})^{1/2}$. However, Ouellette, Desch, and Hester (2007) found that these criteria are too restrictive because disks in interaction with the ejecta become surrounded by high-pressure shocked gas that cushions the disk and deflects gas-phase ejecta around it. The associated bow shock deviates the gas and lowers the effectiveness of momentum stripping and ram pressure by orders of magnitudes. In their model, which is inspired by potential Solar system initial conditions, $d_{\rm SN} = 0.1$ pc, $M_{\rm SN,\star} = 25\ M_\odot$, the gas is stripped beyond the radius with surface density $\Sigma \sim 0.03$ g cm^2 at $\sim$33 au.

Therefore, we employed a semi-analytical, iterative approach to calculate the disk truncation radius for each injection event. We began with a time-dependent disk profile when the supernova explodes and the ejecta hits the disk. An example disk model for the profiles inferred from Equation 2.5 for a Solar analog is shown in Figure 2.2, together with the surface density threshold criterion from Ouellette, Desch, and Hester (2007).

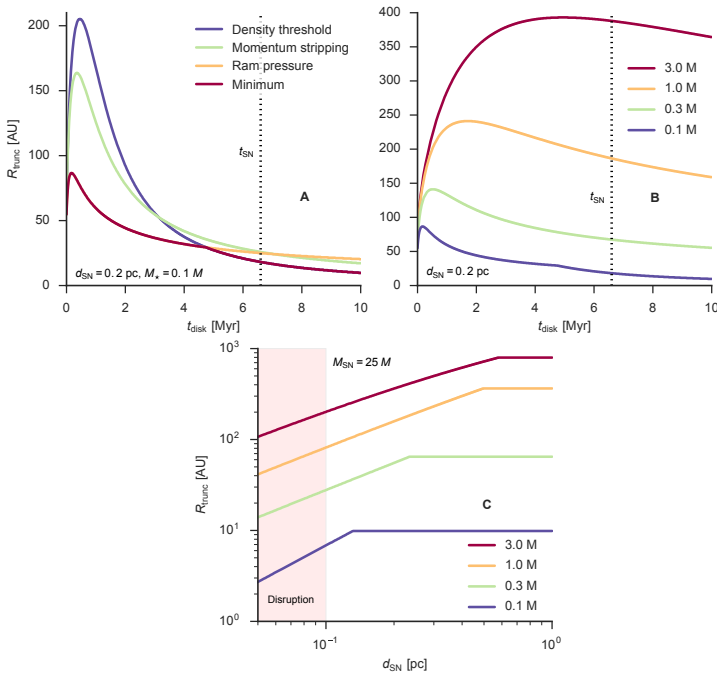

Figure 2.3: Disk truncation radius R_{disk}, calculated from the minimum value of the estimates for momentum stripping, ram pressure and density threshold (compare Figure 2.2). *(A)* Truncation radius for fixed distance from a supernova and mass of the disk host star. During the early evolution of the disk the truncation is determined by the amount of ram pressure, whereas from $\sim$5 Myr onwards momentum stripping and the density threshold become the limiting factors. *(B)* Disk truncation radius for various host star masses. The kink in the slope for a host star of $0.1 M_{\odot}$ results from the transition from ram pressure dominated truncation to density threshold truncation as can be seen in the left image. *(C)* Truncation radii $t = 6.6$ Myr, the explosion time for a supernova with progenitor mass $M_{\mathrm{SN}} = 25 M_{\odot}$. The truncation radii increase with increasing distance to the supernova, as momentum and ram stripping become less rigorous, and are capped from the density threshold criterion.

For this setup we iteratively computed from inside-out the ratio of ejecta and disk momentum $p_{\mathrm{m,ej}} / p_{\mathrm{m,disk}}$ from Equation 2.12, and compared this with the momentum stripping ratio for the parameter combination of Ouellette, Desch, and Hester (2007). For the ram pressure we followed a similar approach and iteratively computed from inside-out the ratio of ejecta ram pressure to the gravitational force per unit

area, and compared this with corresponding ratio calculated from the values in Ouellette, Desch, and Hester (2007). Finally, we chose the minimum truncation radius inferred from the momentum stripping, ram pressure and density cut-off. The disk truncation radius and thus the final mass of the disk were therefore dependent on the specific supernova as well as the disk structure. A demonstration for a subset of parameters is shown in Figure 2.3. The supernova explosion energy $E_{\rm ej} = 1.2 \times 10^{51}$ ergs, as was found for SN 1987A (Rauscher et al., 2002). In principle, this value can vary with progenitor mass, but Ouellette, Desch, and Hester (2007) found that the differences in mass loss rates from different values for $E_{\rm ej}$ are insignificant for the energy range in Woosley and Weaver (1995) and Rauscher et al. (2002).

Finally, to calculate mixing ratios and derive heating values, we assumed Solar-like compositions of all disks, with a dust-to-gas ratio of 0.01, listed in Table 2.2. We calculated the ratios for ^{26}Al and ^{60}Fe, derived the ratios ^{26}Al/^{27}Al and ^{60}Fe/^{56}Fe and from this calculated an initial heating ratio for planetesimals under the assumption of instantaneous homogeneous mixing and planetesimal formation with chondritic compositions (Lodders, 2003). The heating ratio from radioactive decay of SLRs can be computed from (Moskovitz and Gaidos, 2011)

$$Q_{\rm r}(t) = f_{\rm Al,CI} \left[\frac{^{26}{\rm Al}}{^{27}{\rm Al}}\right] \frac{E_{\rm Al}}{\tau_{\rm Al}} e^{-t/\tau_{\rm Al}} + f_{\rm Fe,CI} \left[\frac{^{60}{\rm Fe}}{^{56}{\rm Fe}}\right] \frac{E_{\rm Fe}}{\tau_{\rm Fe}} e^{-t/\tau_{\rm Fe}}, \quad (2.13)$$

with the chondritic abundance of Al or Fe, $f_{\rm Al/Fe,CI}$, the decay energy of ^{26}Al and ^{60}Fe, $E_{\rm Al/Fe}$, and mean lifetime of both radioisotopes, $\tau_{\rm Al/Fe}$, respectively. Note that we have chosen an upper-limit estimate of the initial Solar system ^{26}Al/^{27}Al ratio, as given in Thrane, Bizzarro, and Baker (2006).

If there were more than one supernova event in the simulation, we calculated the remaining SLR material from the former supernova event from the isotopic half-life time and added up the remnant material and the new contribution from the current supernova. For the statistics derived in the results, we accepted the SLR abundance for each individual event with the *maximum* heating rate from the combined effect of ^{26}Al and ^{60}Fe. Therefore, our results reflect the maximum value of SLR abundance each individual system received over the lifetime of the simulation. See Section 2.4 for a discussion of the implications of this.

2.3 RESULTS

In this section we present the results of our study. First, in Section 2.3.1, we describe details of the N-body simulations and discuss the dynamical aspects of the enrichment mechanism. Second, in Section 2.3.2 we present the results from the post-processing of the simula-

Parameter	Symbol	Value	Unit	Ref.
Cluster fractal dimension	D	1.6		(1)
Cluster virial ratio	$\alpha_{\rm vir}$	0.5		
Cluster fractal radius	$R_{\rm F}$	1.0/3.0	pc	
Cluster half-mass radius	$R_{1/2}$	0.3/0.4	pc	
Simulation time	$t_{\rm sim}$	10	Myr	
Number of stars	$N_\star$	$10^3/10^4$		
Supernova explosion energy	$E_{\rm ej}$	1.2×10^{51}	ergs	(2,3)
Dust condensation in supernova ejecta	$\eta_{\rm cond}$	0.5		(4,5)
Ejecta-disk cross-section capture	$\eta_{\rm geom}$	Eq. 2.2		(4,6)
Injection efficiency	$\eta_{\rm inj}$	0.7		(4,6)
Initial disk radius	R_1	10	au	(7)
Initial disk mass	$M_d(0)$	0.1 $M_\star$	$M_\odot$	(7)
Disk alignment	θ	60	$^\circ$	
Disk viscosity	α	10^{-2}		(7,8)
Disk normalization temperature	T_{100}	10	K	(7)
Disk cut-off density	$\Sigma_{\rm out}$	0.03	g cm^{-2}	(2,4)
Disk dust-to-gas ratio		0.01		
Al concentration in CI chondrites	$f_{\rm Al,CI}$	8.5×10^3	μg g^{-1}	(9)
^{26}Al/^{27}Al Solar system[2]	$Z_{\rm Al,SS}$	5.85×10^{-5}		(10)
^{26}Al decay energy	$E_{\rm Al}$	3.12	MeV	(11)
^{26}Al half-life	$t_{1/2,\rm Al}$	7.17×10^5	yr	(11)
^{26}Al radiogenic heating at CAI	$Q_{\rm Al,SS}$	1.7×10^{-7}	W/kg	
Fe concentration in CI chondrites	$f_{\rm Fe,CI}$	182.8×10^3	μg g^{-1}	(9)
^{60}Fe/^{56}Fe Solar system, low	$Z_{\rm Fe,SS}$	1.15×10^{-8}		(12)
^{60}Fe/^{56}Fe Solar system, high		$\sim 10^{-6}$		(13)
^{60}Fe decay energy	$E_{\rm Fe}$	2.712	MeV	(11)
^{60}Fe half-life	$t_{1/2,\rm Al}$	2.60×10^6	yr	(14)
^{60}Fe radiogenic heating at CAI	$Q_{\rm Fe,SS}$	8.325×10^{-11}	W/kg	(15)
Combined radiogenic heating at CAI	$Q_{\rm r,SS}$	1.7×10^{-7}	W/kg	(16)

References: (1) Goodwin and Whitworth (2004), (2) Ouellette, Desch, and Hester (2007), (3) Rauscher et al. (2002), (4) Ouellette, Desch, and Hester (2010), (5) Matsuura et al. (2011), (6) Ouellette et al. (2009), (7) Hartmann (2009), (8) Flaherty et al. (2015), (9) Lodders (2003), Table 3, (10) Thrane, Bizzarro, and Baker (2006), (11) Castillo-Rogez et al. (2009), (12) Tang and Dauphas (2012), (13) Mishra, Marhas, and Sameer (2016), (14) Wallner et al. (2015), (15) based on low ^{60}Fe value, (16) Moskovitz and Gaidos (2011)

Table 2.2: List of physical parameters in the numerical N-body model and analytical post-processing routine. Parameters without reference are further described in Section 2.2.

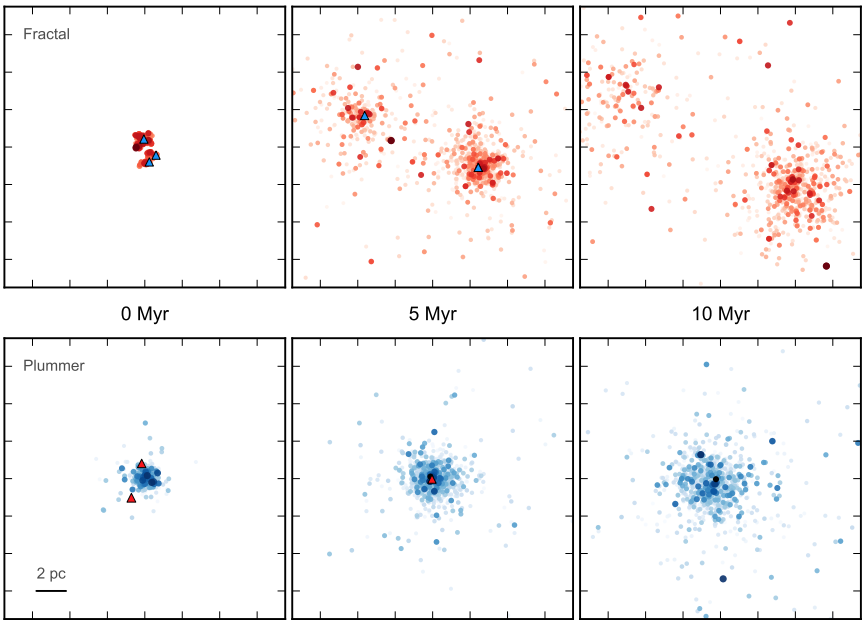

Figure 2.4: Two-dimensional projection of the dynamical evolution of example stellar clusters with 10^3 stars. Stars $\gtrsim 19\ M_\odot$, shown as triangles, explode as supernovae within $t < t_{\rm sim}$ and are therefore gone at $t = 10$ Myr. Smaller stars are shown as circles, with color brightness scaling with stellar mass. *Upper panel:* Fractal simulation with $r_{\rm cl}$ = 1 pc. The initially highly substructured cluster formed two separate sub-clusters after a few Myr of evolution, each containing supernova progenitor stars. *Lower panel:* Plummer simulation with $r_{1/2} = 0.3$ pc. This simulation retained its spherically symmetric morphology and developed a clear mass segregation signature.

tions, deriving predictions for the distribution of ^{26}Al and ^{60}Fe and resulting radiogenic heating rates.

2.3.1 *Star cluster dynamics*

Figures 2.4 and 2.5 illustrate the dynamical evolution of 10^3 and 10^4 simulations with different numbers of stars and cluster morphologies for snapshots at times $t = 0$, 5 and 10 Myr. The supernova progenitor stars were randomly distributed throughout the simulations in the initial conditions. Within 5 Myr most clusters underwent some degree of dynamical mass segregation, such that the massive stars resided at the cluster center or at the center of a sub-cluster structure (as in the fractal simulation in Figure 2.4). At $t = 10$ Myr all of the stars $> 19\ M_\odot$ have exploded as supernovae, losing most of their mass and becoming remnant objects, i.e., a black hole or neutron star. For the enrichment distribution, as presented in Section 2.3.2, it is very important to note that the progenitor stars were not perfectly segre-

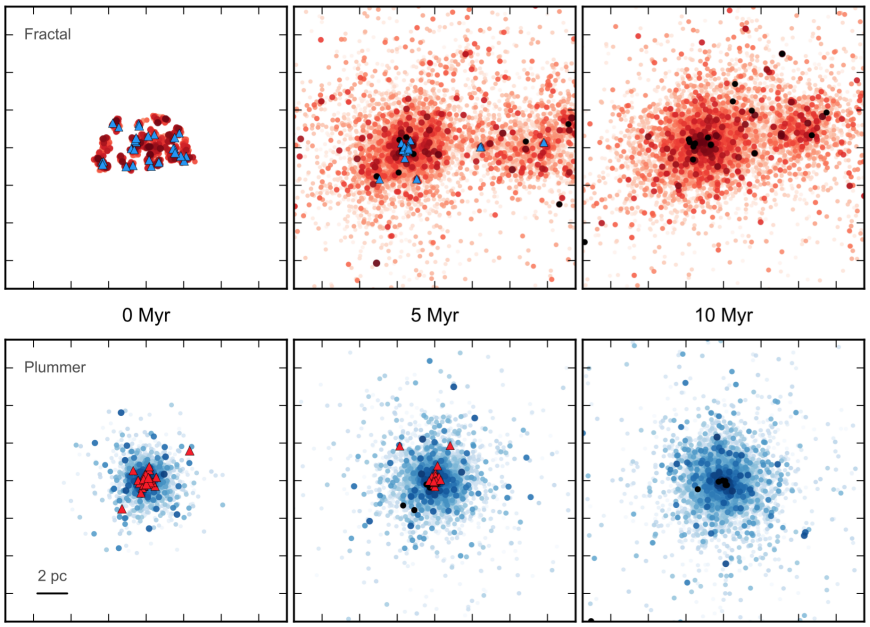

Figure 2.5: Two-dimensional projection of the dynamical evolution of example stellar clusters with 10^4 stars. Stars $\gtrsim 19\ M_\odot$, shown as triangles, explode as supernovae within $t < t_{\rm sim}$ and are therefore gone at $t = 10$ Myr. Smaller stars are shown as circles, with color scaling with stellar mass. *Upper panel:* Fractal simulation with $r_{\rm cl}$ = 3 pc. The initially highly substructured cluster showed a complicated morphology with supernova progenitor stars in very dense and less dense regions. *Lower panel:* Plummer simulation with $r_{\rm M/2}$ = 0.4 pc. Although dynamical mass segregation usually leads to the most massive stars residing in the central region, some massive stars exploded as supernovae in the outskirts of the cluster.

gated into the middle of the cluster. Instead, there were often stars in the outskirts of the cluster, thus enriching stars far away from the cluster center. The fractal simulations often did not form radially symmetric density distributions. Following the erasure of some of the initial substructure they dynamically evolve into association-like complexes with dense subgroups, where the massive stars usually reside approximately at the center of these subgroups (compare Parker et al., 2014a).

Figure 2.6 illustrates the effect of the cluster morphology on the spatial configuration of stars with respect to a supernova progenitor star. In this plot we show the shortest distance $d_{\rm min}$ of each star in the simulations to a supernova event for all timesteps. This supernova event was very likely to determine the enrichment outcome for the specific star as the enrichment cross-section scales with $\sim d^{-2}$ (see Equation 2.2). We highlight the 'disruptive' zone ($d_{\rm SN} < 0.1$ pc) for circumstellar disk evaporation by the shaded red region. If stars were within this distance of the supernova event they were classified as

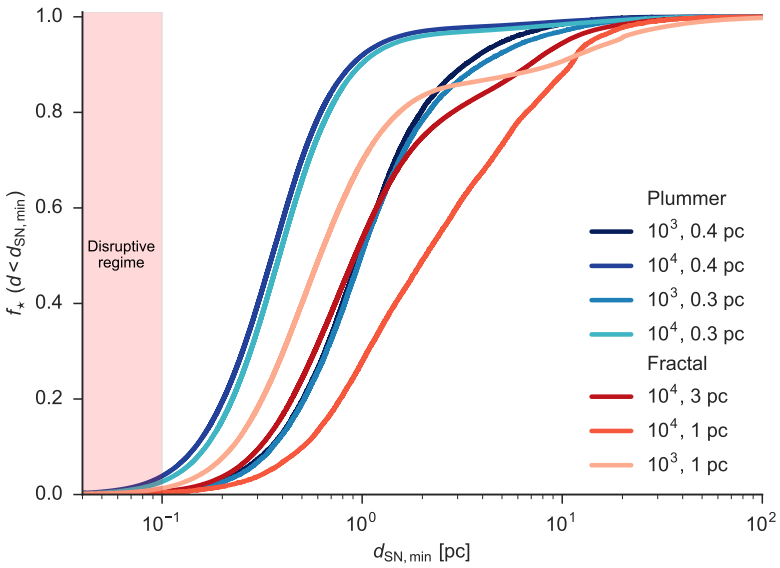

Figure 2.6: Cumulative minimal distances to a supernova event during t_{sim} time for each star in simulations with at least one event. Stars within the red zone were within 0.1 pc of a supernova and could potentially have their disks destroyed, so we subtracted them from the enrichment analysis. On average, stars within 10^4 star-clusters lay closer to supernova progenitors than to stars in 10^3 star-clusters. Furthermore, fractal morphologies increased the average distance in comparison with Plummer-type clusters.

disrupted by the enormous energy injection of the ejecta shock front (Chevalier, 2000). Stars in Plummer-type clusters on average show smaller d_{min} than their fractal counterparts. The reason for this is that a Plummer-sphere relaxes via two-body dynamics only, whereas the fractals initially relax via violent relaxation (Lynden-Bell, 1967), which leads to more drastic expansion (Parker and Meyer, 2012), and therefore higher d_{min} values. In total, $\sim 5-40$ % of stars lie in the expected zone for high pollution efficiencies $0.1 < d_{\mathrm{SN}} < 0.3$ pc (Adams, 2010).

However, the distance to the closest supernova was not enough to derive the enrichment distribution. First of all, as described in Section 2.2.3, the stars may have been subject to other violent interactions, like perturbations by close encounter with other stars or by intense mass loss due to external photoevaporation by nearby O-type stars. We quantify our analysis of these effects in Table 2.3. In the Plummer-sphere simulations, low-mass stars were rarely subject to perturbing close encounters. In the fractals $\sim 3-4$ % of all stars were subject to these interactions.

Photoevaporation by the aggressive radiation fields of O-type stars in the clusters, however, turned out to be an influential mechanism on the survival of disks using our formulation. The fraction of disks subject to potentially evaporative radiation varied from ∼17–79% and

Setting	N_{SN}	N_{disrupt} [%]	N_{perturb} [%]	N_{evap} [%]	N_{destroy} [%]
#01	2.0 ± 1.3	0.6 ± 0.4	3.5 ± 1.6	17.2 ± 8.7	20.3 ± 9.6
#02	1.7 ± 1.2	0.6 ± 0.5	0.1 ± 0.1	26.3 ± 15.6	26.6 ± 15.7
#03	1.7 ± 1.2	0.7 ± 0.7	0.1 ± 0.1	25.1 ± 13.9	25.4 ± 14.1
#04	17.2 ± 4.1	1.5 ± 0.6	4.3 ± 0.9	49.2 ± 8.1	52.3 ± 7.5
#05	18.8 ± 4.4	0.9 ± 0.3	3.2 ± 0.8	30.4 ± 6.0	33.1 ± 5.7
#06	20.1 ± 4.9	2.9 ± 1.0	0.1 ± 0.0	78.8 ± 3.8	79.1 ± 3.7
#07	20.7 ± 4.7	4.1 ± 1.4	0.0 ± 0.0	68.7 ± 3.2	69.2 ± 3.2

Table 2.3: Averaged results of the N-body simulations, with the number of of supernova events during runtime N_{SN}, the number of disks disrupted by supernova N_{disrupt}, the number of disks perturbed by close stellar encounters N_{perturb}, the number of disks potentially violently altered by photoevaporation of near-by O stars N_{evap} and the number of disks subject to at least one these effects N_{destroy}. N_{destroy} could be lower than the sum of the former three values, as a single disk could be subject to more than one effect. Compare with Table 2.1 for the simulation setting identifier.

strongly depended on the initial cluster morphology. Here, stars in fractal clusters tended to be less influenced on average, as they spent less time in photoevaporation zones. Plummer geometries turned out to be more hostile than fractals, because up to 4 out of 5 stars were potentially affected by photoevaporation. It is worth emphasizing that stochastic differences in the dynamical evolution result in a large spread in these values between clusters (see also Parker and Goodwin, 2012; Parker et al., 2014b,a).

The very last column indicates the fraction of disks subject to at least one of the former effects and therefore gives the reverse of the number of disks we considered as *quiescent*, meaning they did not suffer from close encounters, ejecta disruption or photoevaporation effects as defined in Section 2.2.3. These discs could be enriched, if they were not already dispersed 'naturally' (by random drawing from the declining distribution, see Section 2.2.3) by the time of a supernova event. These were the disks for which we derived the enrichment distribution, as described in the next section.

2.3.2 *Enrichment distribution*

In this section we analyze the results for the enrichment distribution for the *quiescent* disks from the former section. Figure 2.7 shows the enrichment distribution for ^{26}Al and ^{60}Fe in terms of the isotopic mixing ratios $\mathrm{Z_{Al}}$ (^{26}Al/^{27}Al) and $\mathrm{Z_{Fe}}$ (^{60}Fe/^{56}Fe), with the Solar system values indicated for comparison. These plots demonstrate various findings. First of all, the ^{26}Al abundance of disks with $\mathrm{Z_{Al}} \gtrsim \mathrm{Z_{Al,SS}}$ varied from $\sim$3–10 % as a function of simulation type. ^{60}Fe abundances,

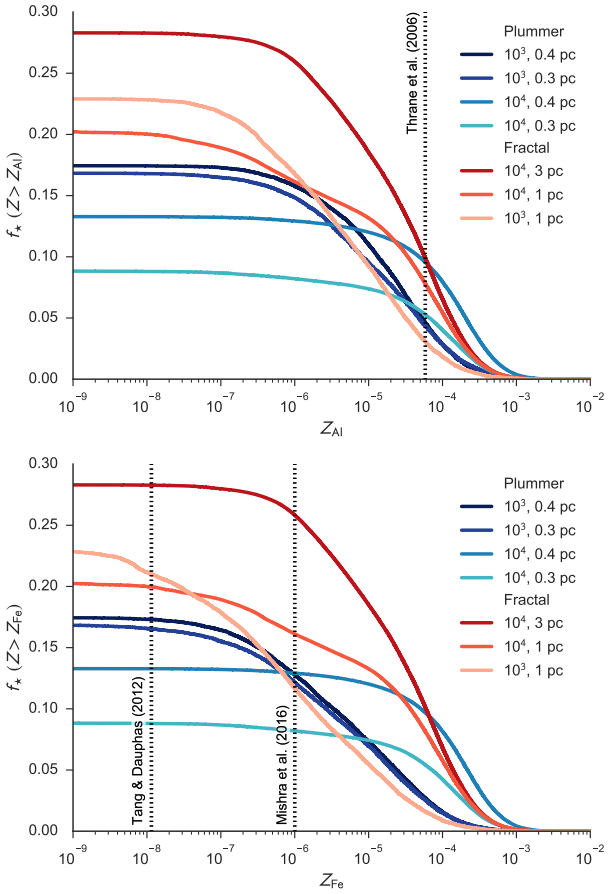

Figure 2.7: Inverse cumulative ^{26}Al and ^{60}Fe yield distributions for stars in clusters, derived in terms of isotopic mixing ratios Z_{Al} (^{26}Al/^{27}Al) and Z_{Fe} (^{60}Fe/^{56}Fe) within disks of initially Solar compositions. The vertical dotted line shows the Solar system values. ∼3–10 % of disks have a similar or higher ^{26}Al abundance than the Solar system. For ^{60}Fe the abundance was typically higher, with ∼8–28 % of disks bearing $Z_{Fe} \gtrsim Z_{Fe,SS}$.

however, showed variations between ∼8–28 % with $Z_{Fe} \gtrsim Z_{Fe,SS}$ for the two end-member simulation types. This was a consequence of our supernova ejecta model, which assumed isotropic expansion and constant ^{26}Al/^{60}Fe ratio in the ejecta, which is higher than the Solar system value (see Section 2.4.3 for a Solar system-focused discussion of this issue). In general, Plummer morphologies show a lower fraction of enriched disks than the fractal geometries. This is mostly because in Plummer simulations the average stellar velocity relative to the cluster center is slower and therefore stars reside longer in the inner regions of the cluster. The fraction of evaporated disks due to photoevaporation is higher and thus fewer disks survive to be enriched. Additionally, clusters with $N = 10^3$ stars show higher abundances than $N = 10^4$ clusters, since in these clusters significantly less O-type stars were present. Although this decreases the enrichment

Setting	f_{enr} [%]	$<Z_{Al}>$ $[10^{-5}]$	$<Z_{Fe}>$ $[10^{-5}]$	$<Q_r>$ $[Q_{r,SS}]$	$f_{Q>SS}$ [%]
#01	22.9 ± 10.1	3.5 ± 10.4	1.8 ± 6.7	1.2 ± 1.0	6.6 ± 4.6
#02	16.8 ± 9.7	6.7 ± 15.8	3.7 ± 10.5	2.3 ± 1.9	9.3 ± 6.2
#03	17.4 ± 10.1	6.1 ± 12.9	3.5 ± 8.2	2.2 ± 1.5	10.1 ± 6.8
#04	20.3 ± 3.4	9.2 ± 17.1	10.1 ± 18.7	5.7 ± 2.0	12.1 ± 2.4
#05	28.3 ± 2.2	8.0 ± 14.7	8.5 ± 16.1	4.8 ± 1.6	16.4 ± 3.2
#06	8.9 ± 1.6	15.7 ± 22.2	17.0 ± 24.2	9.3 ± 2.8	7.0 ± 1.4
#07	13.3 ± 1.6	23.6 ± 30.6	24.8 ± 32.0	13.9 ± 3.9	11.6 ± 1.5

Table 2.4: Enrichment statistics. All values are scaled to the total number of stars at the *beginning* of the simulations. f_{enr} gives the fraction of disks without violent disruption, perturbation or photoevaporation events (compare Table 2.3) *and* did survive until the first supernova event within the specific simulation. The next two columns give the average value of $<Z_{Al}>$ and $<Z_{Fe}>$ and $<Q_r>$ the resulting average heat inside primitive planetesimals. $f_{Q>SS}$ gives the computed fraction of disks with an average heat higher than the Solar system. Compare with Table 2.1 for the simulation setting identifier.

levels, the positive effect of less photoevaporation within the simulations outweighs the negative of the lower number of supernova progenitor stars. Finally, fractal geometries showed a shallower slope toward higher abundance. This can be explained with the higher diversity in evolved clusters at the time when the supernova progenitor stars went supernova. Comparing the morphologies in Figures 2.4 and 2.5 shows that in plummer simulations the stellar density decreased with increasing distance to the cluster center, with the supernova progenitors mostly mass segregated in the center. Fractal geometries could deviate significantly from this, as does the distribution of supernova progenitor stars. As already discussed above, the volume in time subject to photoevaporation is enhanced in comparison with fractal simulations and if mass segregation were perfect, enrichment timing would become a crucial issue. This was one of the central critique points of the supernova pollution model by Williams and Gaidos (2007) and is attenuated by the results of our fractal simulations, where the issue of a star being in the 'right' zone is strongly alleviated.

Table 2.4 summarizes our quantitative results for the enrichment distributions, with f_{enr} the fraction of enriched disks surviving disruption, perturbations, evaporation and dispersion until at least one supernova event has occurred, the average values for Z_{Al} and Z_{Fe} and corresponding heating value in chondritic material $<Q_r>$. $f_{Q>SS}$ indicates the fraction of disks with a higher heating value than the Solar system's initial value (compare Table 2.3). The trends discussed for Figure 2.6 can be confirmed from the average values.

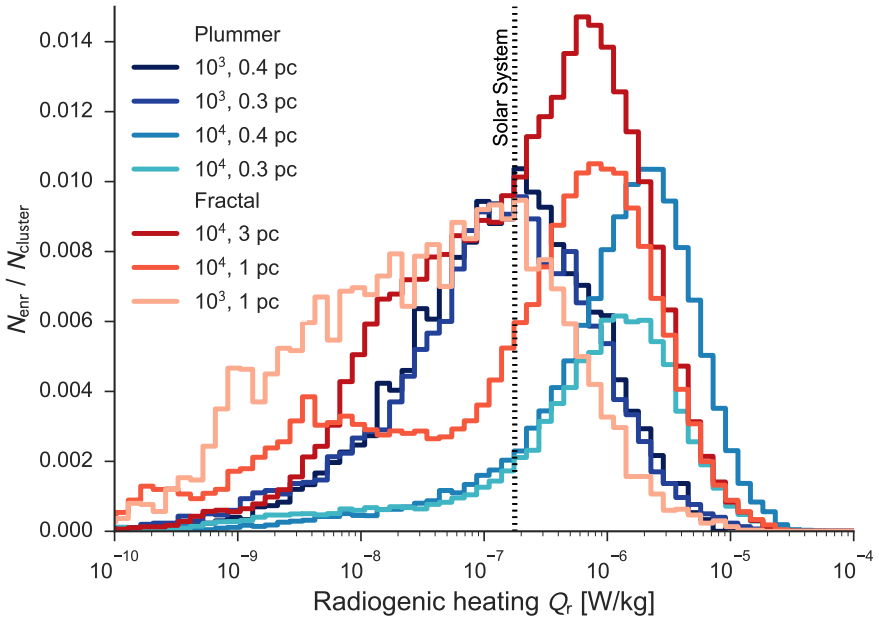

Figure 2.8: Maximum radiogenic heating in planetesimals in enriched systems directly after injection of supernovae ejecta. The vertical dotted line indicates the Solar system value. If a system was enriched via supernova pollution it was likely that planetesimals in there experienced stronger heating than in the Solar system.

The value of Q_r, derived from the combined heating, bridges the gap from the enrichment to the physics of forming planets. Figure 2.8 shows the distribution of initial heating from SLRs among different systems at the time of injection for perfectly effective mixing (no time delay between injection and homogeneous distribution in the system). Two features can be extracted from the histograms. First, 10^3 clusters show median heating rates around the Solar system value. This means, that if a system was enriched, it was most likely to bear similar heating as Solar system planetesimals at CAI formation. Second, 10^4 simulations showed an excess in heating, their peaks are shifted to higher enrichment and thus heating levels. This dichotomy was grounded in the number of supernova events in a simulation. If a system was enriched in a 10^4 simulation, then it was likely to experience multiple enrichment events and from more massive stars, whose ejecta carried more SLRs with them.

2.4 DISCUSSION

In the following we discuss and interpret the outcome of our analysis. In Section 2.4.1 we focus on global aspects of the derived distribution dichotomy, with potential effects on the planet formation process and the global planet population in Section 2.4.2, while in Section 2.4.3 we compare our results with earlier work with regards

to the enrichment mechanism of the Solar system. In Section 2.4.4 we discuss the limitations and uncertainties of our study.

2.4.1 *Enrichment distribution*

As indicated in Section 2.1, the implications of the abundance levels of SLRs are numerous, as they dominated the internal heat budget of planetesimals from ∼10–1000 km in the first few Myr after CAI formation in the Solar system. Our results in Table 2.4 and Figure 2.8 hint on an SLR distribution dichotomy in forming planetary systems. Enriched systems are very likely to bear high concentrations of SLRs and the derived heating value for the early Solar system is by no means the upper limit in those systems. Therefore, if a system is enriched, the heating rate from SLRs, Q_{r}, can be several orders of magnitude higher than in the Solar system. Such extreme heating values are unknown from Solar system studies and the full implications remain elusive. As well as the enriched systems, we find a large fraction of systems with zero enrichment. This is partially based in our simplistic acceptance criteria for disrupted or photoevaporated systems (see Section 2.4.4), but in general agrees with statistical distributions from other studies (Gaidos et al., 2009; Gounelle, 2015).

Given the frequency distribution of star clusters as a function of mass, we expect equal contributions at logarithmic mass intervals to the total mass in stars in the Milky Way galaxy (e.g., Lada and Lada, 2003). In other words, star forming events with richness 10-100 $M_{\odot}$ contribute as much as events with 10^4–10^5 $M_{\odot}$. We expect these smallest events (∼20 % of star forming events) to suffer no SLR enrichment at all. Events 100-1000 M⊙ might contain some stars that experience enrichment. And star clusters 10^4–10^5 M⊙ (∼20 % of Population I star forming events) will certainly produce some stars with even greater SLR enrichment. However we expect the dichotomy we observe here to persist when averaged over all star forming events in the Milky Way: most stars will suffer no enrichment, but the minority that do, will often suffer levels of enrichment much higher than that inferred for our Solar system.

2.4.2 *Implications for planet formation and population synthesis*

A multitude of implications for varying levels of SLRs was already envisioned in the literature. For instance, non-negligible SLR abundances can provide an energy source for ionizing ambient disk material (Cleeves et al., 2013). If the flux from cosmic rays is suppressed by stellar winds, SLRs can in fact be the dominant contribution to the ionization rate present and thus be crucial for the angular momentum transfer via the magnetorotational instability (Balbus and Hawley, 1991). Therefore, disk evolution could be fundamentally different in the two

end-member states of our derived SLR distribution dichotomy, which would affect the internal dynamics and the planet formation process as a whole.

Once accreted, the temperatures in the earliest planetesimals, bearing noteworthy SLR abundances, rise and internally stored volatile species become subject to melting processes. If, however, early Solar system objects transformed substantially due to SLR heating (see Ciesla et al., 2015, and references therein), then planetary systems with much higher SLR concentration would be altered fundamentally, potentially losing a high fraction of internally stored volatile species, such as water in the form of hydrated silicates, by degassing and other mechanisms. Comparable to Gaidos et al. (2009), however due to fundamentally different mechanisms, we find Solar system levels of SLR enrichment were typical for enriched systems. The chemistry and thermo-mechanical evolution of small accreted planetary objects further alters hydration reactions and the formation of serpentinites and thus the synthesis processes of potential seeds for life, such as organic compounds like primitive amino acids (Abramov and Mojzsis, 2011; Cobb and Pudritz, 2014; Cobb, Pudritz, and Pearce, 2015; Lichtenberg et al., 2016).

In addition to the initial abundance of SLRs, the formation time and orbital separation relative to molecular ice lines (e.g., Öberg, Murray-Clay, and Bergin, 2011) likely determine the primordial composition and heat generation within planetesimals. In the Solar system, the initial conditions determined thermal metamorphism, aqueous activity and abundance of volatiles in these bodies (Doyle et al., 2015). Thus, the volatile components of finally assembled planets in the distribution of planetary systems may vary significantly. These species, like water and carbon dioxide, have a disproportionate influence on the processes such as planetary differentiation and habitability (Sotin, Grasset, and Mocquet, 2007; Fu, O'Connell, and Sasselov, 2010; Alibert, 2014). In particular, the initial water content crucially alters the solidification of planetary mantles during the magma ocean phase and degassing pathways, which determines the atmospheric composition and ocean depth to a great degree (Abe and Matsui, 1985; Elkins-Tanton, 2011). Theoretical models show that excess water concentrations could result in extremely volatile rich system architectures (Ciesla et al., 2015; Mulders et al., 2015; Sato, Okuzumi, and Ida, 2016) and would likely alter the conditions for habitability (e.g., Abbot, Cowan, and Ciesla, 2012; Cowan and Abbot, 2014; Schaefer and Sasselov, 2015; Noack et al., 2016). In conclusion, we envisage that our findings indicate a fundamental difference between volatile rich (low initial SLR content) and volatile poor (high initial SLR content) planetary systems with crucial implications for the planetary populations in these systems.

2.4.3 *Solar system enrichment*

Our findings offer new insights into the SLR enrichment channel of the Solar system and can rule out and/or support certain arguments used in the literature for and against specific enrichment channels.

The ^{60}Fe abundance is still a much-debated issue and laboratory experiments diverge by more than two orders of magnitude from $\sim 10^{-8}$–10^{-6} (Tang and Dauphas, 2012; Mishra and Chaussidon, 2014; Mishra, Marhas, and Sameer, 2016). The abundance (or simply, the existence) of ^{60}Fe is, however, of fundamental importance for the enrichment of the Solar system via direct disk pollution (the model featured in this paper) and triggered star formation (as in Gritschneder et al., 2012; Boss and Keiser, 2015) as the ^{26}Al/^{60}Fe ratio in supernova models differs greatly from the ^{26}Al/^{60}Fe ratio in the Solar system. In the formulation used in this paper, we assumed that all supernova yields were transported outwards via isotropic and homogeneous ejecta. This is unlikely, as revealed by observations (e.g., Lopez et al., 2009; Hwang and Laming, 2012) and potential inhomogeneities and anisotropies (for example, via clumps) could have played a fundamental role in enriching young Solar systems (Ouellette, Desch, and Hester, 2010; Pan et al., 2012). Additionally, recent theoretical models of nucleosynthesis in massive stars still suffer from uncertainties in critical nuclear physics (Woosley and Heger, 2007). Therefore, current estimates for the production of SLRs in supernovae and Wolf-Rayet winds must be treated with caution, as the divergence in the models is large enough to account for most of the deviation of Solar system values from the predicted values. Because of these uncertainties, the enrichment by one (Cameron and Truran, 1977) or more (Bizzarro et al., 2007) supernovae by any channel cannot be ruled out.

Chronometric dating of U-corrected Pb-Pb absolute ages of chondrules (Connelly et al., 2012) and paleomagnetic measurements of angrites and Semarkona chondrules (Wang et al., 2015) suggest a lifetime of the Solar protoplanetary disk of ~ 4 Myr. During the earliest stages ($t \leq 0.3$ Myr) the ^{26}Al/^{27}Al ratio was likely heterogeneously distributed (Krot et al., 2009, 2012), but may have rapidly approached the so-called canonical value of ^{26}Al/^{27}Al $\approx 5 \times 10^{-5}$ due to efficient mixing processes, which is often used as an argument for self-enriched molecular cloud models (e.g., Vasileiadis, Nordlund, and Bizzarro, 2013; Kuffmeier et al., 2016).

However, it remains controversial whether such models are consistent with the observed absence of significant age spreads in young star forming regions (Reggiani et al., 2011; Jeffries et al., 2011; Cottaar, Meyer, and Parker, 2012). In general, massive star formation in young star-forming regions is found to be rapid (Elmegreen, 2000), both in simulations (Bonnell, Bate, and Vine, 2003; Dale, Ercolano, and Bonnell, 2012b) and observations (Soderblom et al., 2014). This

underlines the importance for considering intra-cluster enrichment processes.

As we have shown in this study, the likelihood of enriching planetary systems on the level of the Solar system is very common among enriched systems. Additionally, our model results differ from those of Williams and Gaidos (2007) and Gounelle and Meibom (2008), which conclude that supernova polluted systems were a rare event, even when corrected for photoevaporation and co-evolution of low and high mass stars. Moreover, the enrichment levels for ^{26}Al differ by up to one order of magnitude from those in Williams and Gaidos (2007). For this, we identified two main causes. First, in the model by Williams and Gaidos (2007) massive stars were assumed to be entirely mass segregated in the cluster center. Therefore, the enrichment of planetary systems was limited to a very narrow zone around the cluster center, such that timing became a crucial issue. Even though timing played a role in our models as well, the limitations were much less severe, as massive stars could be found in the cluster outskirts as well, due to dynamical evolution and thus the possible volume/zone of enrichment was greatly enhanced. The major effect could be seen in the deviations between fractal and Plummer geometries in our simulations. Second, Williams and Gaidos (2007) used a much smaller disk lifetime, barely in accordance with recent estimates (Cloutier et al., 2014).

In summary, we conclude that the enrichment channel of the Solar system is anything but clarified and needs further investigation. Especially, hints on potential heterogeneities or late-stage injections in ^{26}Al and ^{60}Fe levels in meteorites (like FUN[3] CAIs, which exhibit non-radiogenic isotope abundance anomalies and contained little or no ^{26}Al at the time of their formation; e.g., Thrane et al. (2008)) could open up new ways to derive the enrichment history of the Solar system (Quitté et al., 2007; Makide et al., 2011; Mishra, Marhas, and Sameer, 2016) and need to be synchronized with astrophysical injection mechanism channels, taking into consideration further aspects, like the direct injection of winds from massive stars into protoplanetary disks.

2.4.4 *Limitations*

In this section, we discuss potential limitations of our study. We divide this discussion into two parts: first, we discuss limitations with regards to the simulations and the choices regarding the *stellar* parameters; second, we focus on the disk properties and our assumptions regarding the *planetary* growth process.

3 Fractionation and Unidentified Nuclear isotope properties (Wasserburg, Lee, and Papanastassiou, 1977).

To begin with, we were not able to account for potential age spreads in star formation and cannot investigate triggered star formation scenarios. However, we note that measurements of stellar ages so far are consistent with age spreads up to the order of $\lesssim 2$ Myr (Reggiani et al., 2011; Jeffries et al., 2011; Cottaar, Meyer, and Parker, 2012). These limit the reach of triggered star formation (Pan et al., 2012) and thus triggered enrichment in general (Dale, Haworth, and Bressert, 2015; Parker and Dale, 2016) but in turn could even enhance the likelihood of supernova pollution, when massive stars can be formed earlier than low-mass stars.

Our simulations did not contain any primordial binary stars, whereas the initial binary fraction in star formation could be high (e.g., King et al., 2012; Daemgen et al., 2015). In general, binary stars should be subject to supernova pollution as well. This, however, would demand a much more complicated treatment of the disk dynamics, hence we neglected it in this study.

As discussed in Section 2.4.3, the supernova ejecta were assumed to expand isotropically and homogeneously. This limited our ability to predict the outcome of *specific* planetary system. Thus, we did not derive predictions for single, isolated systems. Instead, we focused on statistical predictions of a large ensemble of stars. As the total mass output for supernova models and the ^{26}Al/^{60}Fe ratio in ejecta are in relative agreement between theoretical models (Rauscher et al., 2002; Limongi, Straniero, and Chieffi, 2000), we argue that the averaging process corrected for the uncertainties in predictions for single systems and thus our averaged predictions in Table 2.4 were not affected. Furthermore, we assumed a dust condensation efficiency of 0.5, which can be subject to changes. However, as discussed in Section 2.2.2, there is recent evidence for very high condensation efficiencies (Matsuura et al., 2011) and hence we believe this estimate to be reasonable.

As found by many authors (Johnstone, Hollenbach, and Bally, 1998; Störzer and Hollenbach, 1999; Scally and Clarke, 2001; Adams et al., 2004) photoevaporation from O-type stars in stellar clusters can severely alter the structures of planet forming disks and potentially even destroy disks completely. Johnstone, Hollenbach, and Bally (1998) give a disk truncation time scale of $\sim 10^6$ yr within $d \sim 0.3$ pc around O-stars, calibrated using θ^1 Ori C in the Orion Nebula Cluster Trapezium system. Recent models have the capability to accurately calculate disk structures and mass outflows from low to mid background radiation fields (Facchini, Clarke, and Bisbas, 2016), which could be used to elaborate on this issue. With the parameters chosen we are confident that the disks left in our enriched ensemble did not suffer massive outflows by photoevaporation.

This leads to the time-dependent evolution of the protoplanetary disks in our models. We chose the classic α viscosity disk model by

Hartmann (2009), which is considered a quasi-standard in the literature and is widely used in observational and theoretical modeling of planet forming disks. Recently, however, doubts about the nature of angular momentum transfer in disks and the physical cause for disk dispersal have arisen (Alexander et al., 2014). An additional caveat closely related is that circumstellar disks in our model dissipate on comparable time scales independent of stellar mass. In fact there is clear evidence that circumstellar disks around higher mass stars dissipate more rapidly than those for lower mass (Hillenbrand et al., 1998; Carpenter et al., 2006). While one is tempted to assume that characteristic disk lifetimes depend linearly on star mass (qualitatively consistent with available evidence) future work will quantify this relationship and enable a more sophisticated population model than assumed here.

The disk disruption and disk truncation due to supernova feedback and momentum stripping and ram pressure by supernova ejecta demand more detailed modeling in future work. The values used in this work were derived with the enrichment of the Solar system in mind (Chevalier, 2000; Ouellette, Desch, and Hester, 2007, 2010) and are therefore not perfectly transferable to other types of disk structures and stellar parameters. We accounted for that by extrapolating these findings to other disk parameters, however, more detailed modeling is necessary to find robust criteria for disk stripping and mass loss by supernova ejecta.

Finally, the derived heating values reflect the maximum enrichment of a single system, which may be asynchronous to solid condensation and thus incorporation into planetesimals and other planetary precursor material. Therefore, the values in Section 2.3.2 can be seen as maximum or 'initial' values for enriched systems. However, this did not affect the number of enriched systems in total and demonstrates that enrichment levels can reach extremely high values in comparison with the Solar system.

2.5 CONCLUSIONS

The supernova pollution of forming planetary systems with SLRs has the potential to crucially alter the growth, interior evolution and volatile budget of terrestrial planets. We have conducted numerous N-body simulations of the evolution of young star clusters of sizes comparable to the Solar birth cluster (10^3–10^4 stars) with varying morphology and realistic stellar evolution. From these we have derived SLR enrichment levels for circumstellar disks struck by supernova ejecta, which are not affected by shock front disruption, dynamical encounters or intense ambient radiation fields. For these system we calculated initial heating values from radioactive decay under the assump-

tion that planetesimals form soon after the enrichment event. Our conclusions can be summarized as follows:

- The potential planetary systems exhibited a wide range in their SLR abundances: ∼10–30% of all systems were enriched, bearing high SLR levels, whereas many systems had negligible or zero abundances.
- Among enriched systems, Solar system SLR enrichment levels were common. However, we do not exactly match the Solar ^{26}Al/^{60}Fe ratio, which is a consequence of our assumption of isotropic and homogeneous supernova ejecta.
- The most extreme heating values could be several orders of magnitude higher than those for the Solar system at CAI formation.

We argue that significant SLR levels can have important influence on the early and long-term evolution of planets by altering interior thermo-mechanical evolution and the volatile budget. These mechanisms may crucially determine exoplanet observables, like atmospheric abundances or radius, and habitability and could be reflected in the global galaxy populations.

Future investigations will improve the link between photoevaporative mass loss with stellar winds and more refined disk models. Furthermore, advanced understanding of melt migration and volatile degassing in planetesimals and planetary embryos with varied radiogenic heating rates is needed to quantify consequences for the terrestrial planetary assembly.

ACKNOWLEDGMENTS

We gratefully acknowledge discussions with Gregor J. Golabek, Maria Schönbächler, Lee Hartmann and Fred J. Ciesla. TL was supported by ETH Research Grant ETH-17 13-1. RJP acknowledges support from the Royal Astronomical Society in the form of a research fellowship. The numerical simulations in this work were performed on the BRUTUS and EULER computing clusters of ETH Zürich. The models were analyzed using the open source software environment MATPLOTLIB[4] (Hunter, 2007). Parts of this work have been carried out within the framework of the National Center for Competence in Research PlanetS supported by the SNSF.

4 http://matplotlib.org

3

WAS PLANET 9 CAPTURED IN THE SUN'S NATAL STAR-FORMING REGION?

The content of this section was published as: Parker, R. J., T. Lichtenberg, S. P. Quanz (2017). "Was Planet 9 captured in the Sun's natal star-forming region?" Monthly Notices of the Royal Astronomical Society Letters 472, L75–L79. doi: 10.1093/mnrasl/slx141. arXiv: 1709.00418.

ABSTRACT

The presence of an unseen 'Planet 9' on the outskirts of the Solar system has been invoked to explain the unexpected clustering of the orbits of several Edgeworth–Kuiper Belt Objects. We use N-body simulations to investigate the probability that Planet 9 was a free-floating planet (FFLOP) that was captured by the Sun in its birth star-formation environment. We find that only 1 – 6 per cent of FFLOPs are ensnared by stars, even with the most optimal initial conditions for capture in star-forming regions (one FFLOP per star, and highly correlated stellar velocities to facilitate capture). Depending on the initial conditions of the star-forming regions, only 5 – 10 of 10 000 planets are captured onto orbits that lie within the constraints for Planet 9. When we apply an additional environmental constraint for Solar system formation – namely the injection of short-lived radioisotopes into the Sun's protoplanetary disc from supernovae – we find that the probability for the capture of Planet 9 to be almost zero.

3.1 INTRODUCTION

One of the outstanding issues in astrophysics is to understand the processes involved in planet formation and to characterize the Solar system within the context of other planetary systems. A recent body of research (e.g. Trujillo and Sheppard, 2014; Batygin and Brown, 2016a,b,b; Holman and Payne, 2016b,a) has suggested that the unusual orbital characteristics of several Edgeworth–Kuiper Belt Objects could be explained by the presence of an unseen/undiscovered $\sim$20 $M_\oplus$ planet – the so-called 'Planet 9' (though see Nesvorný et al., 2017; Shankman et al., 2017, for arguments against this hypothesis). Simulations constrain Planet 9's semi-major axis to between 380 – 980 au, its perihelion to between 150 – 350 au, eccentricity between 0.34 – 0.72 and its inclination to be less than 30 – 60° (Batygin and Brown, 2016a,b,b; Holman and Payne, 2016b,a).

The inherent difficulty of forming a relatively massive planet via core accretion at such a large distance from the Sun has fueled speculation that – if real – Planet 9 may have been captured by the Sun (Li and Adams, 2016), or even "stolen" from another star in the Sun's birth environment (Mustill, Raymond, and Davies, 2016).

The Sun's current location in the Galaxy is a low-density stellar environment, where interactions with passing stars are rare. However, most stars are born in star-forming regions where the stellar density is much higher ($1 - 10^6$ stars pc^{-3}, Lada and Lada, 2003; Porras et al., 2003; Bressert et al., 2010). As planet formation occurs almost immediately after the onset of star formation (Haisch, Lada, and Lada, 2001), then the influence of neighboring stars in the Sun's natal star-forming region cannot be neglected.

Furthermore, several authors have shown that stellar/sub-stellar objects can be readily captured during the evolution and dissolution of relatively dense ($>$100 stars pc^{-3}) star-forming regions (Moeckel and Bate, 2010; Kouwenhoven et al., 2010; Parker and Quanz, 2012; Perets and Kouwenhoven, 2012). In this paper we revisit this question and determine whether a significant fraction of stars can capture free-floating planetary-mass objects (FFLOPs) in their birth star-forming environment with orbital characteristics consistent with the hypothesized Planet 9. We describe our simulations in Section 3.2, we present our results and discussion in Section 3.3 and we conclude in Section 3.4.

3.2 METHOD

We use N-body simulations to model the evolution of star-forming regions containing a population of free-floating planetary mass objects. Observations (Elmegreen and Elmegreen, 2001; Cartwright and Whitworth, 2004; Peretto, André, and Belloche, 2006; André et al., 2010; Henshaw et al., 2017) and simulations (Bonnell, Bate, and Vine, 2003; Dale, Ercolano, and Bonnell, 2012a; Girichidis et al., 2012; Vázquez-Semadeni, González-Samaniego, and Colín, 2017) suggest that stars form in a spatially substructured distribution, with correlated velocities on local scales (Larson, 1981; Kauffmann, Pillai, and Goldsmith, 2013; Hacar et al., 2013). In order to mimic this in our simulations, we use fractal distributions as our initial conditions, using the method described in Goodwin and Whitworth (2004) to determine both the spatial and kinematic properties of our star-forming regions.

In each simulation, the fractal dimension is set to be $D = 1.6$, which corresponds to a high degree of spatial and kinematic substructure in three dimensions. Previous work (Kouwenhoven et al., 2010; Perets and Kouwenhoven, 2012) has shown that spatial and kinematic substructure in star-forming regions facilitates the capture of low-mass

companions and that these objects are more likely to be captured if the amount of substructure is highest.

We then scale the velocities of the objects to a virial ratio, $\alpha_{\rm vir}$ ($\alpha_{\rm vir} = T/|\Omega|$, where T and $|\Omega|$ are the total kinetic energy and total potential energy of the objects, respectively), so the star-forming regions undergo three different phases of bulk motion. Regions with $\alpha_{\rm vir} = 0.3$ have subvirial (cool) velocities and undergo collapse to form a star cluster, whereas regions with $\alpha_{\rm vir} = 0.7$ are mildly supervirial and gently expand. Finally, a third set of regions have $\alpha_{\rm vir} = 1.5$ and are unbound, undergoing rapid expansion. We refer the interested reader to Goodwin and Whitworth (2004) and Parker et al. (2014a) for full details of the set-up of these fractal initial conditions and examples of their dynamical evolution.

In our fiducial simulations, we draw 1000 single stars from a Maschberger (2013) initial mass function of stars (IMF) with stellar mass limits between 0.1 – 50 $M_\odot$. We then add a further population of planetary-mass objects which is equal to the number of stars (i.e. a star-planet ratio of 1:1), apart from one set of simulations where we impose a star-planet ratio of 5:1. The planetary mass objects are all assigned the same mass, which is either Jupiter-mass ($1\,M_{\rm J} = 1 \times 10^{-4} M_\odot$), or ten Earth-masses ($10\,M_\oplus = 3 \times 10^{-5} M_\odot$). Whilst Planet 9's mass has been constrained to $\sim$20 $M_\oplus$, we include the more massive planets to highlight the very slight dependence of the results on planet mass, and to enable a comparison with previous work (Parker and Quanz, 2012; Perets and Kouwenhoven, 2012). We vary the total number of stars (either 150 or 1000) and the initial radius of the star-forming regions (1 or 3 pc), commensurate with observations of nearby star-forming regions (e.g. Lada and Lada, 2003; Pfalzner et al., 2016). These values lead to initial densities that are much higher than the *present day* densities in nearby star-forming regions (Bressert et al., 2010), but these regions (and the Solar system's birth environment) may have been more dense initially.

In our initial conditions, we do not make a direct assumption on the origin of the free-floating planets. However, because they are assigned positions and velocities in the same way as the stars, the implicit assumption is that they form "like stars". That said, planetary mass objects that have been liberated from host stars in simulations of dense star-forming regions often have the same spatial and kinematic distributions as stars (e.g. Parker and Quanz, 2012), so the FFLOPs in our simulations could in principle have two different origins. However we note that FFLOPs produced in planet–planet scattering events can have a different kinematic distribution to those liberated by interactions with passing stars.

We note that the expected number of FFLOPs in the Milky Way is uncertain, with some authors claiming one FFLOP per main sequence star (Sumi et al., 2011) (although this result has been called into ques-

$N_{\rm stars}$	$N_{\rm planets}$	m_p	$\alpha_{\rm vir}$	r_F	$\tilde{\rho}_{\rm ini}$
1000	1000	1 $M_{\rm J}$	0.3	1 pc	5000 – 30 000 $M_\odot$ pc^{-3}
1000	1000	1 $M_{\rm J}$	0.7	1 pc	5000 – 30 000 $M_\odot$ pc^{-3}
1000	1000	1 $M_{\rm J}$	1.5	1 pc	5000 – 30 000 $M_\odot$ pc^{-3}
1000	1000	10 $M_\oplus$	0.3	1 pc	4000 – 20 000 $M_\odot$ pc^{-3}
1000	1000	10 $M_\oplus$	0.7	1 pc	4000 – 20 000 $M_\odot$ pc^{-3}
1000	1000	10 $M_\oplus$	1.5	1 pc	4000 – 20 000 $M_\odot$ pc^{-3}
1000	1000	1 $M_{\rm J}$	0.7	3 pc	200 – 700 $M_\odot$ pc^{-3}
1000	200	1 $M_{\rm J}$	0.3	1 pc	3000 – 15 000 $M_\odot$ pc^{-3}
1000	200	1 $M_{\rm J}$	0.7	1 pc	3000 – 15 000 $M_\odot$ pc^{-3}
150	150	1 $M_{\rm J}$	0.7	1 pc	100 – 800 $M_\odot$ pc^{-3}
150	150	1 $M_{\rm J}$	1.5	1 pc	100 – 800 $M_\odot$ pc^{-3}

Table 3.1: Summary of the initial conditions. The columns show the number of stars, $N_{\rm stars}$, number of planets, $N_{\rm planets}$, the mass of the planet, m_p, the virial ratio, $\alpha_{\rm vir}$, the radius of the star-forming region, r_F, and the median initial local density this mass and radius results in, $\tilde{\rho}_{\rm ini}$.

tion by Raymond et al., 2011; Quanz et al., 2012; Mróz et al., 2017). It is also difficult to pinpoint their origin (either they are an extension of the stellar mass function, or they are planets liberated from orbit around host stars). However, our simulations are designed to deliberately facilitate the capture of FFLOPs and we therefore create a large reservoir of these objects in our simulated star-forming regions.

We evolve our star-forming regions for 10 Myr using the KIRA integrator in the STARLAB environment (Portegies Zwart et al., 1999, 2001) with stellar evolution switched on using the SEBA package (Portegies Zwart and Verbunt, 1996, 2012), also within STARLAB. A summary of the different initial conditions is given in Table 3.1.

3.3 RESULTS

3.3.1 *Fraction of captured planets*

Planets are captured by stars in all three sets of initial conditions for the evolution of our star-forming regions. In Figure 3.1 we show the fraction of captured planets, $f_{\rm cap}$ (the number in a bound orbit around a star, $N_{\rm p,bound}$, divided by the total number of planets in the simulation initially $N_{\rm planets}$), as a function of the initial virial ratio, or bulk motion, of the star-forming region. We have summed together ten realizations of each initial condition, identical apart from the random number seed used to set the positions and velocities of all objects, and the stellar masses.

We find a clear dependence of the fraction of captured planets on the initial virial ratio of the star-forming region. Regions that are subvirial ($\alpha_{\rm vir} = 0.3$), bound and subsequently collapse capture fewer planets than those that are very supervirial ($\alpha_{\rm vir} = 1.5$), unbound and rapidly expanding. This is due to a combination of two effects. Firstly, the unbound supervirial regions never fully dynamically mix, which enables the retention of kinematic substructure and the conditions to facilitate further capture of planets (see also Kouwenhoven et al., 2010; Perets and Kouwenhoven, 2012). The supervirial regions also expand rapidly, lowering the stellar density and preventing planets captured on fragile orbits with low binding energy from being disrupted by interactions with passing stars (Parker et al., 2014a).

The fraction of captured FFLOPs strongly depends on the number of objects in the region initially, with regions with only $N_\star = 150$ (the red points in Figure 3.1) capturing many more planets than our fiducial models ($N_\star = 1000$, $r_F = 1$pc, one FFLOP per star – the black or orange points). This is not simply a density dependence, where lower-density regions can capture and retain more planets on fragile orbits; the blue point shows the capture fraction for an $N_\star = 1000$ region with a comparable stellar density to the $N_\star = 150$ regions ($\sim$100 stars pc^{-3}). Instead, the number of captured systems on wide and fragile orbits has been shown to be independent of the mass of a star-forming region (Moeckel and Clarke, 2011), and so relatively more planets are captured in lower-N star-forming regions of comparable density to higher-N regions.

The fraction of captured FFLOPs is not strongly dependent on the mass of the planets (compare the orange points for simulations with 10 $M_\oplus$ planets to the black points for 1 M_J planets in Figure 3.1), with lower-mass planets being slightly more susceptible to capture.

3.3.2 *Orbital properties of captured planets*

Brown and Batygin (2016) show that Planet 9 is unlikely to be more massive than 20 $M_\oplus$ and we therefore focus on our simulations where the FFLOPs are 10 $M_\oplus$, although the following results do not depend on the FFLOP mass.

In Figure 3.2 we show the orbital parameters for the planets that are captured around a stellar-mass object in our simulations[1]. In each panel in this figure, the cumulative distributions are shown for all three virial ratios in the simulations.

The subvirial (collapsing) star-forming regions are more likely to capture a planet on an orbit with a perihelion distance $r_{\rm peri}$ in the

1 We do not consider planet–planet systems (which can form in this type of simulation, see also Perets and Kouwenhoven, 2012) because we wish to examine systems where the primary-mass object is a star.

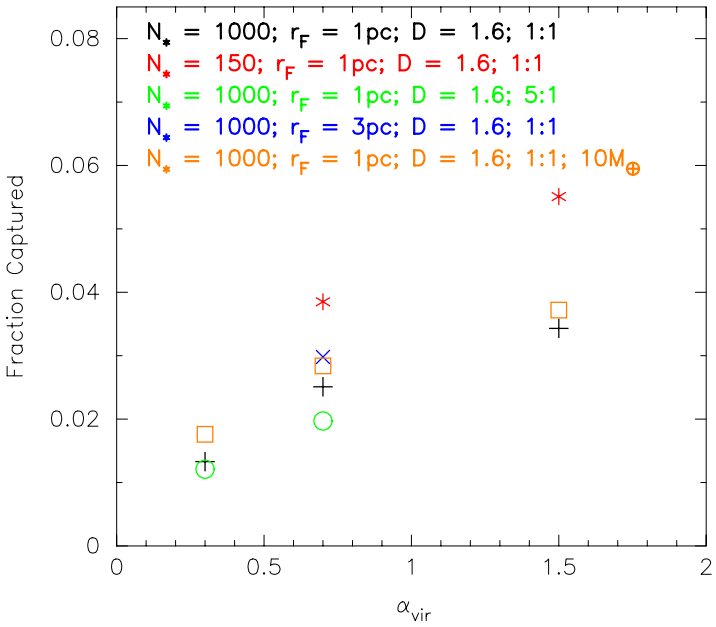

Figure 3.1: The fraction of FFLOPs captured as a function of the initial dynamical state of the star-forming region. $\alpha_{\rm vir} = 0.3$ indicates a collapsing (bound, cool) region, $\alpha_{\rm vir} = 0.7$ is a mildly expanding (supervirial, warm) region and $\alpha_{\rm vir} = 1.5$ is a rapidly expanding (unbound, hot) region. The colored points indicate different initial conditions; $N_\star$ is the number of stars, r_F is the radius of the star-forming region, D is the fractal dimension (amount of substructure) and the ratio of stars to FFLOPs. The FFLOPs are all Jupiter-mass, apart from the simulations shown by the orange points (10 $M_\oplus$).

range of allowed values for Planet 9 than regions with supervirial motion. $r_{\rm peri}$ is defined in the usual way as

$$r_{\rm peri} = a_p \left(1 - e_p\right), \tag{3.1}$$

where a_p and e_p are the semi-major axis and eccentricity of in the captured planet, respectively. The eccentricity distribution is roughly thermal (panel b), which is expected for any binary system that forms via capture (Kroupa, 1995; Kouwenhoven et al., 2010; Perets and Kouwenhoven, 2012). Unlike the perihelion and semi-major axis, there is no dependence of the eccentricity or inclination (panel c) on the virial ratio of the star-forming region.

Whereas a planet is more likely to be captured by a star in an expanding, supervirial star-forming region, a captured planet is more likely to have the required orbital parameters for Planet 9 if it is captured in a subvirial, collapsing star-forming region (Figure 3.2a).

However, the fraction of captured systems have orbital parameters in the range specified for Planet 9 is still extremely small. Summing together ten realizations of the same initial conditions for each simulation, we find that only ∼5–10 out of 10 000 FFLOPs are captured with a perihelion in the range 150 – 350 au, semi-major axis between 380

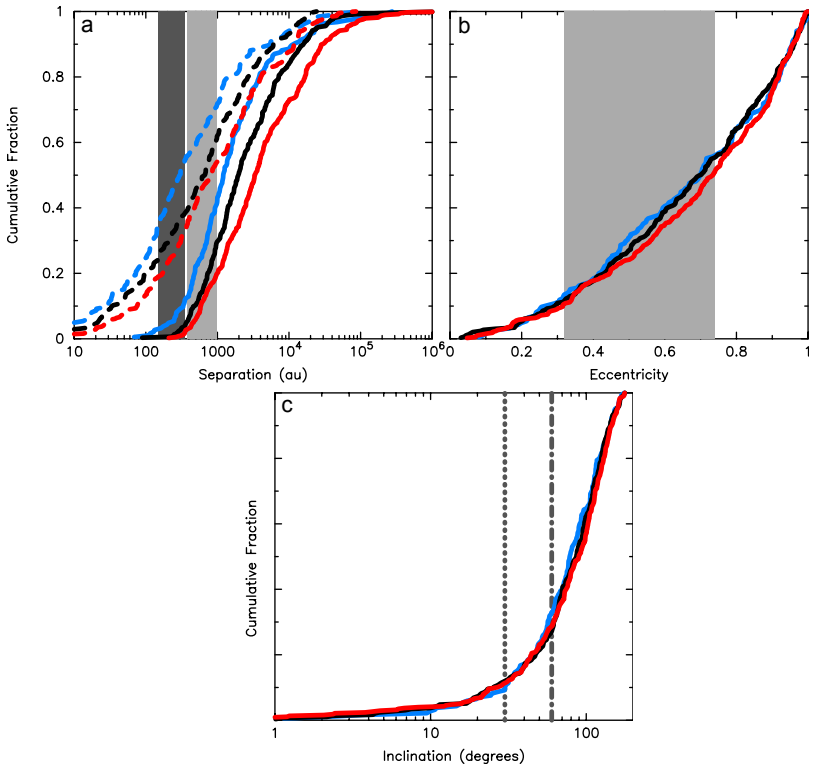

Figure 3.2: Orbital properties of captured FFLOPs in subvirial (collapsing) star-forming regions (blue lines), slightly supervirial (gently expanding) star-forming regions (black lines) and highly supervirial (unbound, rapidly expanding) star-forming regions (red lines). In panel *(a)* we show the perihelia of the captured planets by the dashed lines, and their semi-major axes by the solid lines. The shaded regions in panel *(a)* are limits on perihelion (dark gray) and semi-major axis (light gray) for Planet 9 from Brown and Batygin (2016). In panel *(b)* we show the allowed range of eccentricities for Planet 9s and in panel *(c)* the vertical lines are limits on inclination from Brown and Batygin (2016) and Holman and Payne (2016b,a). Constraints on the orbit of Planet 9 favor inclinations lower than 30°, but higher values ($< 60°$) are not excluded.

– 980 au, eccentricity between 0.34 – 0.72 and an inclination of less than 30 – 60°.

3.3.3 *Planet 9 in the context of Solar system formation*

The possible capture of Planet 9 in the Sun's natal star-forming region is not the only line of argument that the Solar system formed in a dense stellar environment. Many authors have presented evidence that the Sun was either directly enriched by radiogenic isotopes (Adams, Fatuzzo, and Holden, 2014; Lichtenberg, Parker, and Meyer, 2016; Parker and Dale, 2016; Nicholson and Parker, 2017; Telus et al., 2018) or formed from pre-enriched material (e.g. Cameron and Truran, 1977; Gounelle, 2015; Boss, 2017) and both scenarios require

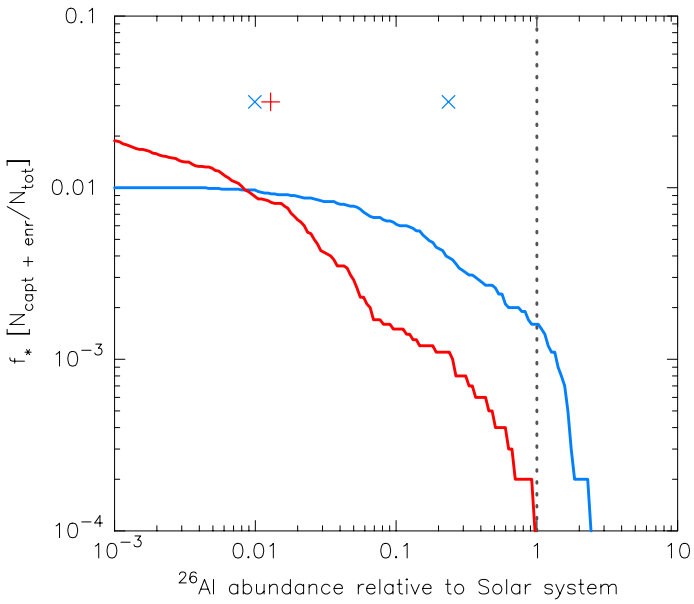

Figure 3.3: Inverse cumulative distribution showing the estimated ^{26}Al abundance relative to the Solar system value for stars in subvirial regions (blue line) and in highly supervirial regions (red line). The distribution is normalized to the fraction of stars that capture a planet *and* are enriched by supernovae ejecta. We also show the ^{26}Al abundance values for stars that capture a planet within the orbital constraints of Planet 9; the red plus sign is for a planet captured in the supervirial simulations, and the blue cross is for planets captured in the subvirial simulations (three in total). All other captured FFLOPs within the allowed Planet 9 parameter space have negligible ^{26}Al abundances.

the Sun to form in reasonably dense stellar environments ($>$100 stars pc^{-3}, Parker and Dale, 2016).

Of these isotopes, the abundance of ^{26}Al is the most robustly measured and can be used to estimate the amount of radiogenic heating during planet formation (Lichtenberg et al., 2016; Lichtenberg, Parker, and Meyer, 2016, and references therein), and to constrain the origin and dynamics of planet-forming material in the Solar system (Kita et al., 2013). Following the methodology in Lichtenberg, Parker, and Meyer (2016), in Figure 3.3 we show the inverse cumulative distribution of the ^{26}Al abundance compared to the Solar system value in either the subvirial (blue) or very supervirial (red) simulations. We show the canonical initial ^{26}Al/^{27}Al ratio (Kita et al., 2013) for the Solar system by the vertical dashed line. The subvirial (collapsing) regions, which retain a higher stellar density throughout the simulations, are more conducive to isotope enrichment than supervirial (expanding) regions, which will likely be too diffuse at the time of the first supernovae (4 – 7 Myr, Parker et al., 2014b,a). The cumulative distribution is normalized to the fraction of stars that capture

a FFLOP and are enriched (at a level $\geq 10^{-3}$ of the Solar value); this is a small percentage of the total number of stars, and only three of these stars capture a FFLOP on an orbit within the constraints of Planet 9 and experience enrichment anywhere near Solar system levels (the crosses/plus symbols in Figure 3.3). A further two stars have ^{26}Al abundances less than 10^{-3} of the Solar value and are not shown. Finally, we note that the three stars that are enriched, and capture a planet, have stellar masses considerably lower than that of the Sun (0.78, 0.12 and 0.24 $M_\odot$, in order of increasing ^{26}Al abundance).

3.4 CONCLUSIONS

We present N-body simulations of the dynamical evolution of star-forming regions with a significant population of free-floating planetary mass objects (FFLOPs). We vary the initial virial ratio of the star-forming regions, so that they are either subvirial (bound) and collapse to form a star cluster, are slightly supervirial and gently expand, or are very supervirial (unbound) and rapidly expand. We vary the number of stars and the initial radii of the star-forming regions and we vary the mass of the FFLOPs, and the number per star in the star-forming regions. Our conclusions are the following:

(i) Between 1 and 6 per cent of planets are captured by stars in star-forming regions with initial conditions optimized for the ensnarement of low-mass objects onto orbits around stars, when these regions contain a significant reservoir of FFLOPs available for capture.

(ii) The fraction of captured planets is a strong function of the initial virial ratio (bulk velocity) of the star-forming region, with FFLOPs twice as likely to be captured in supervirial (unbound) regions undergoing rapid expansion than in subvirial (bound) regions undergoing collapse.

(iii) However, planets captured in star-forming regions that collapse to form a cluster are more likely to have orbits consistent with the allowed parameter space of the proposed Planet 9.

(iv) Convolving the relative numbers of planets in (ii) and (iii), we find the number of planets fulfilling the orbital criteria for Planet 9 is then independent of the initial virial ratio of the star-forming region, and is extremely low (of order 5 – 10 from an initial population of 10 000 FFLOPs).

(v) Finally, we note that the Sun was likely enriched by a supernova explosion in its birth environment. For this to occur, the initial conditions in the Sun's natal star-forming region are likely to have been subvirial in order to facilitate the collapse of the region to form a bound, relatively dense star cluster.

Overall, our results suggest that the fraction of stars that capture a FFLOP onto an orbit consistent with that of the hypothesized Planet 9, and that experience Solar system levels of isotope enrichment, is almost zero. This fraction is lower than that reported in Li and Adams (2016) and Mustill, Raymond, and Davies (2016). This is likely due to differences in the assumed initial velocities of the stars (we adopt quasi-Gaussian kinematic substructure whereas the earlier work assumes a Maxwellian distribution), higher ($\times$10) initial densities (required to facilitate supernova enrichment), and our FFLOPs do not occur as the result of previous planet-planet scattering events.

ACKNOWLEDGMENTS

We thank the referee, Fred Adams, for his helpful comments and suggestions. RJP acknowledges support from the Royal Society in the form of a Dorothy Hodgkin Fellowship. TL was supported by ETH Research Grant ETH-17 13-1. Part of this work has been carried out within the framework of the National Center for Competence in Research "PlanetS", supported by the Swiss National Science Foundation. SPQ acknowledges the financial support of the SNSF.

Part II

THERMOCHEMICAL EVOLUTION OF PLANETESIMALS

In the second part, I connect the abundances of SLRs in planet-forming systems to the growth and build-up of terrestrial planets. To do so, I model the geophysical interior evolution of planetesimals, the fundamental building blocks of terrestrial planets. The heat liberated from decaying SLRs in their interiors, especially from ^{26}Al in the early Solar system, is sufficient to melt these rocky bodies completely, turning their interior into liquid magma that convects vigorously. Thereby, the decay heat from SLRs transforms the structure of the planetesimals from an initially random and homogeneous assembly into a highly substructured and chemically differentiated one. This structural and compositional transformation of planetesimals has implications for the chemical make-up of the terrestrial planets. The end-process of planetesimal evolution can be assessed nowadays by analyzing laboratory samples from meteorites, which are the broken-up pieces of planetesimals. Thereby, the models presented in this chapter represent a crucial step forward in classifying the thermophysical and -chemical regimes in early Solar system planetesimals. They can be interpreted in conjunction with geo- and cosmochemical studies to reconstruct the dynamics and time scales during the accretion of the planets in the Solar system and extrasolar systems that are enriched in SLRs to a varying degree.

4

THE EFFECTS OF SHORT-LIVED RADIONUCLIDES AND POROSITY ON THE EARLY THERMO-MECHANICAL EVOLUTION OF PLANETESIMALS

The content of this section was published as: Lichtenberg, T., G. J. Golabek, T. V. Gerya, and M. R. Meyer (2016). "The effects of short-lived radionuclides and porosity on the early thermo-mechanical evolution of planetesimals." Icarus 274, 350–365. doi: 10.1016/j.icarus.2016.03.004. arXiv: 1603.05979.

ABSTRACT

The thermal history and internal structure of chondritic planetesimals, assembled before the giant impact phase of chaotic growth, potentially yield important implications for the final composition and evolution of terrestrial planets. These parameters critically depend on the internal balance of heating versus cooling, which is mostly determined by the presence of SLRs, such as ^{26}Al and ^{60}Fe, as well as the heat conductivity of the material. The heating by SLRs depends on their initial abundances, the formation time of the planetesimal and its size. It has been argued that the cooling history is determined by the porosity of the granular material, which undergoes dramatic changes via compaction processes and tends to decrease with time. In this study we assess the influence of these parameters on the thermo-mechanical evolution of young planetesimals with both 2D and 3D simulations. Using the code family I2ELVIS/I3ELVIS we have run numerous 2D and 3D numerical finite-difference fluid dynamic models with varying planetesimal radius, formation time and initial porosity. Our results indicate that powdery materials lowered the threshold for melting and convection in planetesimals, depending on the amount of SLRs present. A subset of planetesimals retained a powdery surface layer which lowered the thermal conductivity and hindered cooling. The effect of initial porosity was small, however, compared to those of planetesimal size and formation time, which dominated the thermo-mechanical evolution and were the primary factors for the onset of melting and differentiation. We comment on the implications of this work concerning the structure and evolution of these planetesimals, as well as their behavior as possible building blocks of terrestrial planets.

4.1 INTRODUCTION

During the early stages of planet formation the building material of terrestrial planets like Earth or Mars is distributed within planetesimals with sizes of $\sim 10^1$–10^2 km (Weidenschilling and Cuzzi, 2006). It remains unclear how these bodies assembled from sub-micron grains in a circumstellar disk in detail. First order constraints from the standard collisional model for growth relate the doubling time $t_\mathrm{s} \sim \rho_\mathrm{p} R_\mathrm{p} / (\Sigma_\mathrm{disk} \Omega_\mathrm{K})$ of a growing planetesimal to its size R_p and density ρ_p as well as to the properties of the disk, namely mass surface density Σ_disk and Keplerian frequency Ω_K (Goldreich, Lithwick, and Sari, 2004). This formula, however, essentially a cross-section calculation, ignores gravitational focusing and limits to growth, such as the bouncing barrier (e.g., Zsom et al., 2010) and the radial migration of solids due to gas drag (Weidenschilling, 1977). Nonetheless, there are also complex local processes that can enhance the formation of planetesimals with up to several hundred kilometers radii due to particle collection in vortices, pressure bumps, and other effects (e.g., Johansen et al., 2007; Cuzzi, Hogan, and Shariff, 2008; Morbidelli et al., 2009; Chambers, 2010; Johansen et al., 2015). These point to rapid formation on the time scale of $\sim 10^5$ yr after the formation of CAIs, consistent with findings from geochemical data (Kleine et al., 2009).

Theoretical models to investigate this epoch after the initial assembly of the planetesimals rely on numerical models of internal dynamics. So far, such models were mostly based on 1D studies, focusing on conductive cooling as the main heat transfer mechanism (e.g., Ghosh and McSween, 1998; Hevey and Sanders, 2006; Sahijpal, Soni, and Gupta, 2007). Recent work, however, has shown that more mechanisms need to be taken into account. Firstly, these bodies are supposed to be sufficiently big to become heated by decay of SLRs, most importantly ^{26}Al and ^{60}Fe, which would alter their inner structure and evolution dramatically up to the point of silicate melting. For example, bodies greater than $\sim$ 10 km in radius, formed at the time of CAI formation, are supposed to melt completely (Hevey and Sanders, 2006). Secondly, some meteorite parent bodies seem to have experienced solid-state deformation (Tkalcec, Golabek, and Brenker, 2013; Tkalcec and Brenker, 2014). These points underline the importance of 2D or 3D thermo-mechanical modeling approaches for the evolution of planetesimals to detect effects such as the differences of the surface-to-volume ratio in 1D, 2D and 3D models or non-axisymmetric advection processes. As a further complicating issue, recent work highlights the potentially important role of porous bulk material on the thermal history of planetesimals, by lowering the thermal conductivity of the silicate material and thus to prevent effective heat transport via conduction (Cuzzi, Hogan, and Shariff, 2008; Neumann, Breuer, and Spohn, 2014b).

The initial powdery state of the uncompacted material is however reduced in the inner parts of the planetesimals by cold isostatic compaction due to self-gravity (Henke et al., 2012a), effectively decreasing its influence with increasing size of the body. Another important aspect is the formation time of the body. As outlined above, the accretion time scale of planetesimals is on the order of 10^5 yr, which is roughly an order of magnitude shorter than the evolutionary time scale of the protoplanetary disk and the thermo-mechanical evolution of planetesimals on the order of 10^6 yr. Hence, the quasi-instantaneous formation time sets the limit on the amount of SLRs incorporated into the body.

Additional heat sources for planetesimals can be energy injection during the accretion of the body and later impacts. First, the temperature increase due to the conversion of gravitational energy to heat is low for bodies $<$ 1000 km (Schubert, Spohn, and Reynolds, 1986; Qin et al., 2008; Elkins-Tanton, Weiss, and Zuber, 2011). Second, during runaway growth, the velocity dispersion of planetesimals is set by the equilibrium between self-stirring and gas drag. Impact velocities are therefore comparable or smaller to the escape velocity (Greenberg et al., 1978; Morbidelli et al., 2015), which drastically limits the amount of injected energy. The formation time thus dominates the energy budget for heating and sets the pace of internal dynamic processes, such as core formation, to the order of several ^{26}Al half-lives.

Clearly, the thermo-mechanical evolution of planetesimals needs to be treated adequately to achieve a consistent theoretical understanding of this stage of planetary assembly. In this study we assessed the role of the initial size, formation time and porosity of planetesimals on their thermo-mechanical history via 2D and 3D numerical models. In Section 4.2 we describe constraints from earlier work and outline the most important concepts of our numerical model; in Section 4.3 we present the results obtained from the simulation runs, for which we outline the technically inherent limitations in Section 4.4. In Section 4.5 we discuss the physical implications and draw conclusions in Section 4.6. Supplementary material can be found in 4.7.

4.2 PHYSICAL AND NUMERICAL METHODOLOGY

The physical and numerical methods in this work follow earlier work by Golabek, Bourdon, and Gerya (2014), in which an in-depth analysis of observational constraints on the thermal history for the acapulcoite-lodranite parent body is compiled. In contrast to this study, we focused on the general role of planetesimal evolution and sought to explore the thermo-mechanical regimes before the onset of the giant impact phase in terrestrial planet formation. The most important physical constants used in the model are explained in the following

Parameter	Symbol	Value	Unit	Ref.
Density of uncompressed solid silicates	$\rho_{\mathrm{Si-sol}}$	3500	kg m^{-3}	(1,2)
Density of uncompressed molten silicates	$\rho_{\mathrm{Si-liq}}$	2900	kg m^{-3}	(1)
Temperature of space (sticky air)	T_{space}	290	K	(3,4)
Activation energy	E_{a}	470	kJ mol^{-1}	(5)
Dislocation creep onset stress	σ_0	$3 \cdot 10^7$	Pa	(6)
Power law exponent	n	4		(5)
Latent heat of silicate melting	L_{Si}	400	kJ kg^{-1}	(3,6)
Silicate melt fraction at rheological transition	φ_{crit}	0.4	non-dim.	(7,8)
Heat capacity of of silicates	c_{P}	1000	J kg^{-1} K^{-1}	(6)
Thermal expansivity of solid silicates	$\alpha_{\mathrm{Si-sol}}$	$3 \cdot 10^{-5}$	K^{-1}	(2)
Thermal expansivity of molten silicates	$\alpha_{\mathrm{Si-liq}}$	$6 \cdot 10^{-5}$	K^{-1}	(2)
Thermal conductivity of solid silicates	k	3	W m^{-1} K^{-1}	(9)
Thermal conductivity of molten silicates	k_{eff}	$\leq 10^6$	W m^{-1} K^{-1}	(10)
Minimum thermal conductivity of unsintered solid silicates	k_{low}	10^{-3}	W m^{-1} K^{-1}	(11,12) (12)
Temperature at onset of hot sintering	T_{sint}	700	K	(11)

References: (1) Stolper et al. (1981), (2) Suzuki, Ohtani, and Kato (1998), (3) Ghosh and McSween (1998), (4) Barshay and Lewis (1976), (5) Ranalli (1995), (6) Turcotte and Schubert (2014), (7) Solomatov (2015), (8) Costa, Caricchi, and Bagdassarov (2009), (9) Tarduno et al. (2012), (10) Golabek, Bourdon, and Gerya (2014), (11) Yomogida and Matsui (1984), (12) Henke et al. (2012a)

Table 4.1: List of physical parameters in the numerical model.

sections, all others are listed with their respective references in Table 4.1.

4.2.1 *Fluid flow*

As outlined in Section 4.1 we studied the thermo-mechanical evolution of instantaneously and recently formed planetesimals using the I2ELVIS/I3ELVIS code family (Gerya and Yuen, 2007). The code solves the fluid dynamic conservation equations using the extended Boussinesq approximation, to account for thermal and chemical buoyancy forces, with a conservative finite-differences approach on a fully staggered-grid (Gerya and Yuen, 2003), namely the continuity equation

$$\frac{\partial \rho}{\partial t} + \nabla \rho \mathbf{v} = 0, \tag{4.1}$$

with density ρ, time t and flow velocity $\mathbf{v}$; the Stokes equation

$$\nabla \sigma' - \nabla P + \rho \mathbf{g} = 0, \tag{4.2}$$

with deviatoric stress tensor σ', pressure P and directional gravity $\mathbf{g}$ obtained via the location-dependent Poisson equation

$$\nabla^2 \Phi = 4\pi G \rho, \tag{4.3}$$

with the gravitational potential Φ and Newton's constant G; and finally the energy equation

$$\rho c_{\mathrm{P}} \left(\frac{\partial T}{\partial t} + v_{\mathrm{i}} \cdot \nabla T \right) = -\frac{\partial q_{\mathrm{i}}}{\partial x_{\mathrm{i}}} + H_{\mathrm{r}} + H_{\mathrm{s}} + H_{\mathrm{L}}, \tag{4.4}$$

with heat capacity c_{P}, temperature T, heat flux $q_{\mathrm{i}} = -k\frac{\partial T}{\partial x_{\mathrm{i}}}$, thermal conductivity k, and radioactive (H_{r}), shear (H_{s}) and latent (H_{L}) heat production terms. The energy equation is advanced using a Lagrangian marker-in-cell technique to minimize numerical diffusion and enable an accurate advection of non-diffusive flow properties during material deformation. The staggered-grid finite-differences method permits to capture sharp variations of stresses and thermal gradients with strongly variable viscosity and thermal conductivity. For further details on the code's features we refer to Gerya and Yuen (2003, 2007).

4.2.2 *Heating by short-lived radionuclides*

As discussed earlier, the radiogenic heat source term H_{r} in Equation 4.4 is dominant for early-formed planetesimals. It is driven by the decay of short-lived isotopes ^{26}Al and ^{60}Fe and the long-lived ^{40}K, ^{235}U, ^{238}U and ^{232}Th. Among these ^{26}Al is by far the most important one and therefore drives the internal heating of the young bodies, as the abundance of ^{60}Fe is lower by orders of magnitude (Barr and Canup, 2008; Tang and Dauphas, 2012; Mishra, Marhas, and Sameer, 2016). In this work, we considered time-dependent radiogenic heating by ^{26}Al and the long-lived radioactive isotopes as input for H_{r} in Equation 4.4. For the initial ^{26}Al/^{27}Al ratio we adopted an upper-limit value (Jacobsen et al., 2008) of $5.85 \cdot 10^{-5}$ (Thrane, Bizzarro, and Baker, 2006) at CAI formation.

4.2.3 *Silicate melting model*

For the silicates we assumed a peridotite composition and used the parameterizations by Herzberg, Raterron, and Zhang (2000) and Wade and Wood (2005) (based on data of Trønnes and Frost, 2002) for the solidus and liquidus temperatures T_{sol} and T_{liq}, which determine the silicate melt fraction

$$\varphi = \begin{cases} 0 & : T \leq T_{\mathrm{sol}}, \\ \frac{T - T_{\mathrm{sol}}}{T_{\mathrm{liq}} - T_{\mathrm{sol}}} & : T_{\mathrm{sol}} < T < T_{\mathrm{liq}}, \\ 1 & : T \geq T_{\mathrm{liq}}. \end{cases} \tag{4.5}$$

We took into account both consumption and release of latent heat due to melting and freezing of silicates. Silicate density depends on the melt fraction φ as

$$\rho_{\mathrm{eff}}(P, T, \varphi) = \rho_{\mathrm{Si-sol}}(P, T) - \varphi[\rho_{\mathrm{Si-sol}}(P, T) - \rho_{\mathrm{Si-liq}}(P, T)] \tag{4.6}$$

with solid and liquid silicate densities $\rho_{\mathrm{Si-sol}}$ and $\rho_{\mathrm{Si-liq}}$. For silicate melt fractions $0.1 < \varphi \lesssim 0.4$ the effective viscosity (Pinkerton and Stevenson, 1992) is given as

$$\eta_{\mathrm{eff}} = \eta_{\mathrm{Si-liq}} \cdot \exp\left(\left[2.5 + \left(\frac{1-\varphi}{\varphi}\right)^{0.48}\right] \cdot (1-\varphi)\right). \tag{4.7}$$

Above $\varphi \gtrsim 0.4$ a transition occurs from solid-like structures to low-viscosity crystal suspensions (Solomatov, 2015; Costa, Caricchi, and Bagdassarov, 2009), with $\eta_{\mathrm{Si-liq}} = 10^{-4} - 10^{2}$ Pa s (Bottinga and Weill, 1972; Rubie et al., 2003; Liebske et al., 2005). This effectively increases the Rayleigh number

$$Ra = \frac{\alpha g (T - T_{\mathrm{surf}}) \rho_{\mathrm{eff}}^2 c_{\mathrm{P}} D^3}{k \eta_{\mathrm{Si-liq}}}, \tag{4.8}$$

with thermal expansivity α, surface temperature T_{surf}, depth of the magma ocean D and thermal conductivity k and thus enables an efficient cooling process.

Above melt fractions $\varphi \gtrsim 0.4$ our model is restricted by a lower cut-off viscosity $\eta_{\mathrm{num}} = 10^{17}$ Pa s, which preserves numerical stability, but lies orders of magnitude above realistic values of molten state silicate viscosities. To bypass restrictions of the physical interpretation in this melt regime we employed the soft turbulence model by Kraichnan (1962) and Siggia (1994), and estimated the convective heat flux as

$$q = 0.089 \frac{k(T - T_{\mathrm{surf}})}{D} Ra^{1/3}. \tag{4.9}$$

Using Equation 4.9 we derived an increased effective thermal conductivity

$$k_{\mathrm{eff}} = \left(\frac{q}{0.089}\right)^{3/2} \frac{1}{(T - T_{\mathrm{surf}})^2 \rho_{\mathrm{eff}}} \left(\frac{\alpha g c_{\mathrm{P}}}{\eta_{\mathrm{num}}}\right)^{-1/2}, \tag{4.10}$$

which approximates correct heat flux for a low viscosity magma ocean (Tackley et al., 2001; Hevey and Sanders, 2006; Golabek et al., 2011). For a more detailed discussion on model limitations due to this issue see Section 4.4.

4.2.4 *Porosity*

As already indicated in Section 4.1, the initial porous state of recently accreted planetesimals is thought to decrease due to cold isostatic pressing with pressure and thus depth into a configuration of closer packing (Henke et al., 2012a), via

$$\phi(P) = 0.42 + 0.46 \cdot \left[\left(\frac{P}{P_0}\right)^{1.72} + 1\right]^{-1}, \tag{4.11}$$

PARAMETER	VALUE RANGE	UNIT	VALUE LIST
R_p	20–200	km	20, 50, 80, 110, 140, 170, 200
t_form	0.1–1.75	Myr	0.1, 0.5, [1.0-1.7] in 0.1 steps, 1.75
ϕ_init	0.0–0.75		[0.0–0.5] in 0.1 steps, 0.75

Table 4.2: Value range for the main model parameters.

with $P_0 = 0.13$ bar, which effectively introduces an upper cut-off porosity for depths greater than $\sim 10^2$ m, mostly dependent on the size of the body. Furthermore, the porosity changes the density of the solid material

$$\rho_\mathrm{Si-por}(P,T,\phi) = \rho_\mathrm{Si-sol}(P,T)\cdot(1-\phi), \tag{4.12}$$

and the effective thermal conductivity for porous material

$$k_\mathrm{eff,por} = \begin{cases} k_1 = k\cdot e^{-\phi/\phi_0} & : \phi < 0.2, \\ k_3 = (k_1^4 + k_2^4)^{1/4} & : 0.2 \leq \phi \leq 0.4, \\ k_2 = k\cdot e^{a-\phi/\phi_1} & : \phi > 0.4, \end{cases} \tag{4.13}$$

with constants $a = -1.2$, $\phi_0 = 0.08$ and $\phi_1 = 0.167$, fitting lab experiments (Henke et al., 2012a; Gail, Henke, and Trieloff, 2015). Finally, the material compaction is sensitive to sintering effects via

$$\left|\frac{\partial\phi}{\partial t}\right| = A(1-\phi)\frac{\sigma^{3/2}}{\Re^3}\cdot\exp\left[\frac{-E_\mathrm{a}'}{RT}\right], \tag{4.14}$$

with the effective stress σ, the effective grain size $\Re$, the gas constant R and experimentally determined factors $A = 4\cdot 10^{-5}$ and activation energy $E_a' = 85$ kcal mol^{-1} (Henke et al., 2012a).

4.2.5 *Initial conditions*

The spherical planetesimals in our model box were supposed to be completely composed of silicates. Olivine outrules pyroxene minerals in controlling deformation processes due to its mechanical weakness (Mackwell, 1991). Thus, we apply an olivine rheology (Ranalli, 1995) to be able to follow thermo-mechanical processes, i.e., melting and mixing due to internal heating. Each body was built up by several rheologically identical silicate layers, which could be followed by an internal tracking of the corresponding markers. This enabled us to distinguish different silicate layers and reconstruct their mixing history. Illustrative examples are given in Section 4.3.

As indicated before, the energy release during the accretion phase is only minor for the size of bodies we addressed here (Schubert, Spohn, and Reynolds, 1986). Therefore, we started from a constant temperature distribution all over the model grid in accordance with

values in a typical protoplanetary disk $T_{\mathrm{space}} = 290$ K (Ghosh and McSween, 1998).

The surrounding of the bodies was made up of a so-called sticky-air layer (Schmeling et al., 2008), with near zero density, constant temperature $T_{\mathrm{SA}} = T_{\mathrm{space}}$ and constant viscosity $\eta_{\mathrm{SA}} = 10^{19}$ Pa. Such a layer allows for simulation of free surfaces and serves as infinite reservoir to absorb released heat from the planetesimal (Golabek et al., 2011; Crameri et al., 2012; Tkalcec, Golabek, and Brenker, 2013).

The numerical model boxes had physical dimensions of 500 km in each direction in 2D and 3D, represented by 501^2 grid points in 2D, respectively 261^3 grid points in 3D, which results in physical resolutions of 1 km in 2D and $\sim$ 2 km in 3D.

4.2.6 *Parameter space*

The goal of this work was to assess the combined effect of radiogenic heating by SLRs and initial porosity on the subsequent evolution of planetesimals. Hence, the parameter space was based on varying the planetesimal radius $R_{\mathrm{p}} = 20$–200 km, the instantaneous formation time $t_{\mathrm{form}} = 0.1$–1.75 Myr after CAI formation and the initial porosity $\phi_{\mathrm{init}} = 0.0$–$0.75$, in total a set of 616 2D simulations. A full list of all applied values is given in Table 4.2.

Due to the heavy computational cost of 3D simulations we first analyzed the 2D simulations, categorized them and then performed selected 3D simulations to verify the 2D results.

From our varied parameters, both R_{p} and t_{form} directly influenced the amount of SLRs present in the body. A list of all simulation runs with corresponding parameters and categories is referenced in Section 4.7.

4.3 RESULTS

4.3.1 *Thermo-mechanical evolution*

In this section we analyze the thermo-mechanical outcome of the simulations. In Section 4.3.1.1 we focus on the temporal evolution of the material properties, i.e., solid or molten, and categorize the 2D results accordingly. Each category is then described and examples are given. In Section 4.3.1.2 we investigate the time-dependent maximum temperatures of the bodies and assess the influence of each of the varied parameters on it by constructing R_{p}, t_{form} and ϕ_{init} isolines. Also, we analyze the influence of ϕ_{init} on the temperature profile for fixed formation time and planetesimal size.

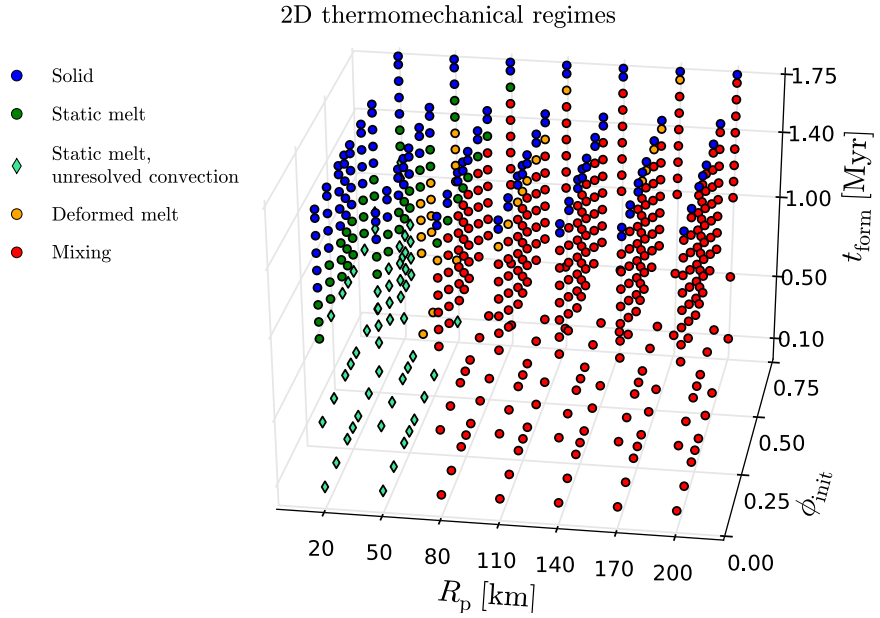

Figure 4.1: 3D parameter space covered by the two-dimensional simulation runs, each dot represents one simulation, with R_{p} in km, ϕ_{init} non-dimensional and t_{form} in Myr. The colors indicate which thermo-mechanical state was reached during the time evolution. *Blue*: all silicates were in solid form during all times (Figure 4.2); *green*: the silicates in the planetesimal were partially or fully molten at some stage during the temporal evolution (Figure 4.3), green simulations with diamonds indicate that the numerical restrictions in our model did not capture fluid motion due to extremely low viscosities, see Section 4.4 for an in-depth discussion of this issue; *orange*: the silicate layers were partially deformed, but the heating was not sufficient for convection (Figure 4.4); *red*: convectional mixing occurs during the temporal evolution of the planetesimal (Figure 4.5).

4.3.1.1 *Material properties*

Figure 4.1 illustrates the thermo-mechanical results of the material properties within each 2D simulation run. Each dot represents a single simulation and color indicates in which kind of regime we categorize the simulation. Each of these regimes is described below and an example, illustrating the state for ϕ, T and ρ at a certain time, is given. Illustrating video files for each of the described regimes below can be found in the supplementary material (see 4.7).

SOLID REGIME The blue rendered simulations in Figure 4.1 build the class of *solid* models. These are models which lacked enough heat production by SLRs to experience any sign of transition from the solid silicate to a partially molten silicate state. An example of this kind is given in Figure 4.2. The upper left image shows all simulation runs of this class. The composition plot illustrates the unperturbed

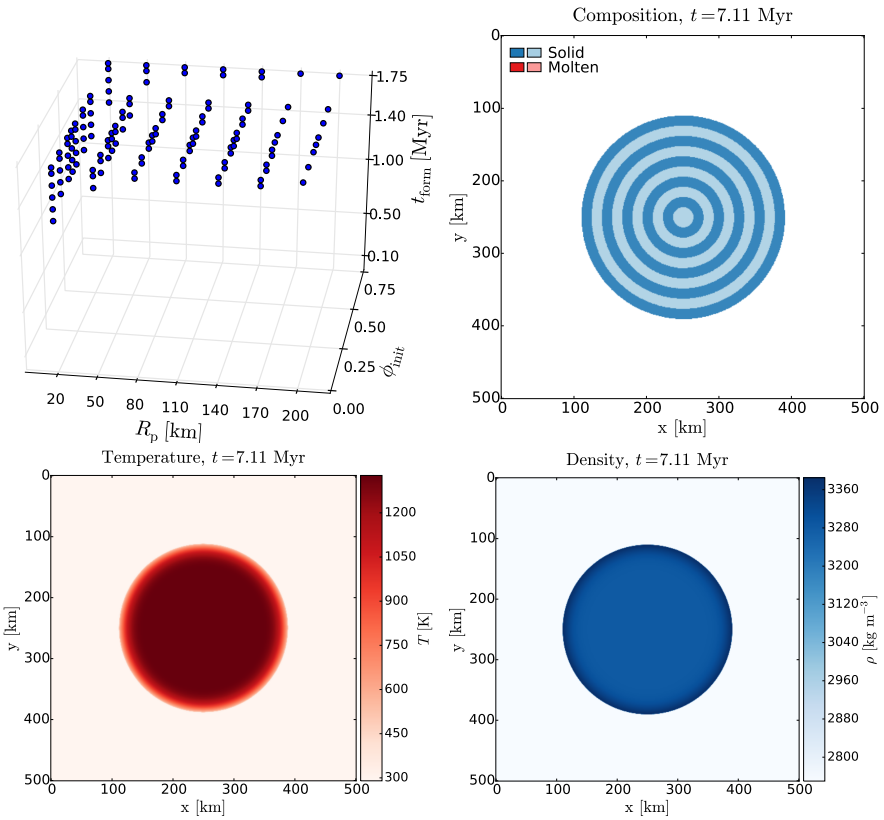

Figure 4.2: Example of a *solid* model, i.e., without any melting throughout the temporal evolution, with $R_{\mathrm{p}} = 140$ km, $t_{\mathrm{form}} = 1.7$ Myr, $\phi_{\mathrm{init}} = 0.5$ at $t = 7.11$ Myr. The all-solid (rheologically identical) layers did not deform throughout the simulation.

layered structure of the silicates it is composed of. Because the body never experienced enough heat, no transition to a molten state occurred and therefore the layers resided with their original ordering. The temperature and density plots illustrate these parameters at the same time during the evolution. Since the body experienced some heat from SLRs it heated up and cooled down to the temperature of the surrounding T_{space} on the order of several tens of Myr. As shown in Figure 4.2 these kinds of models can be found for all tested radii for $t_{\mathrm{form}} \gtrsim 1.7$ Myr, i.e., when the initial amount of ^{26}Al has significantly reduced. Additionally, planetesimals with $R_{\mathrm{p}} = 50$ km already belong to this class for earlier formation times $t_{\mathrm{form}} \gtrsim 1.6$ Myr and for $t_{\mathrm{form}} \gtrsim 1.3$ Myr for bodies with $R_{\mathrm{p}} = 20$ km since they cooled more efficiently. Comparison of figures 4.1 and 4.2 for bodies with $R_{\mathrm{p}} = 20$ km reveals the influence of ϕ_{init}. For $t_{\mathrm{form}} = 1.3$ Myr, the models were *solid* for $\phi_{\mathrm{init}} \leq 0.3$ and *molten* for $\phi_{\mathrm{init}} \geq 0.4$. Hence, the effects of initial porosity only affected this transitional stage for the smallest bodies in our parameter space.

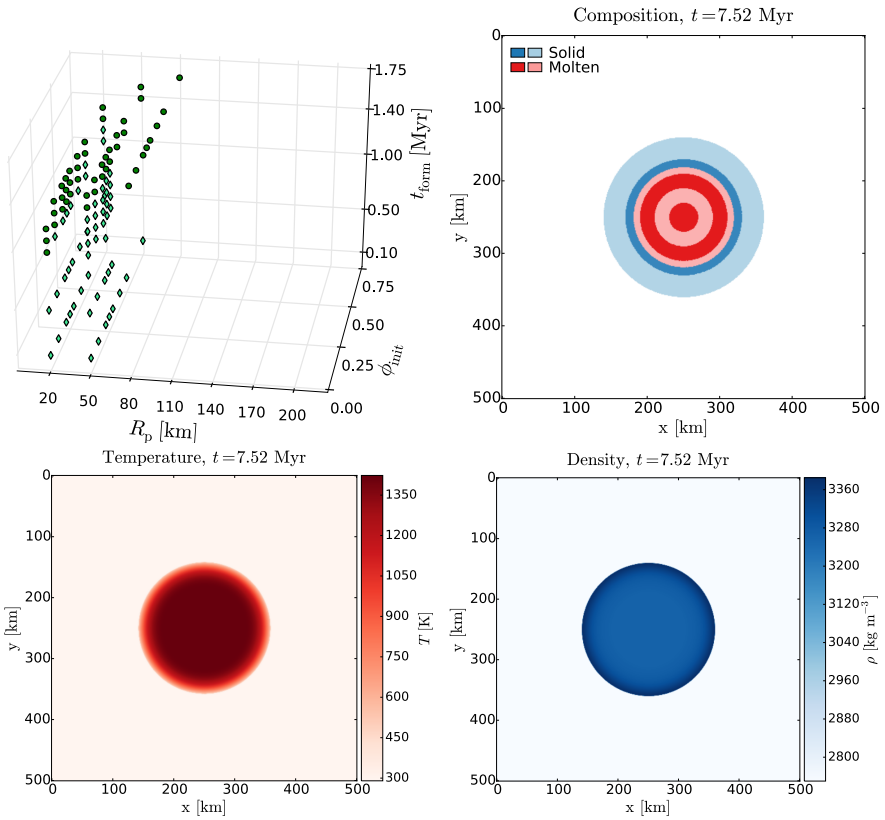

Figure 4.3: Example of a *static melt* model, with $R_{\rm p} = 110$ km, $t_{\rm form} = 1.6$ Myr, $\phi_{\rm init} = 0.25$ at $t = 7.52$ Myr. The molten layers are differently shaded to be able to track the onset of convection (see Figure 4.4). The inner parts were hotter and less dense than the upper layers and the temperatures were high enough to partially melt the silicates for a limited time period.

STATIC MELT REGIME This class of simulations showed characteristics of phase transitions from solid to molten states, indicated with green circles and diamonds in Figure 4.1. For the deviations between these we refer to the discussion of our model limitations in Section 4.4. An example of a *static melt* model is given in Figure 4.3. In the composition Figure we see molten silicate phases shown in red. As the material in the inner parts could not cool as efficiently as the outer parts higher temperatures occurred and thus silicates in this region tended to melt. Hence, the density in the outer shells was higher than in the inner parts. Simulations of this class were dominant for bodies with $R_{\rm p} \leq 50$ km. For $R_{\rm p} = 20$ km the boundary for the transition from solid to melt was $t_{\rm form} \approx 1.3$ Myr, for $R_{\rm p} = 50$ km it was $t_{\rm form} \approx 1.6$ Myr. In bodies with $R_{\rm p} = 80$ km this class could be found solely for $t_{\rm form} = 1.6$ Myr, marking the boundary to the transition from solid models to more dynamic models displaying convection.

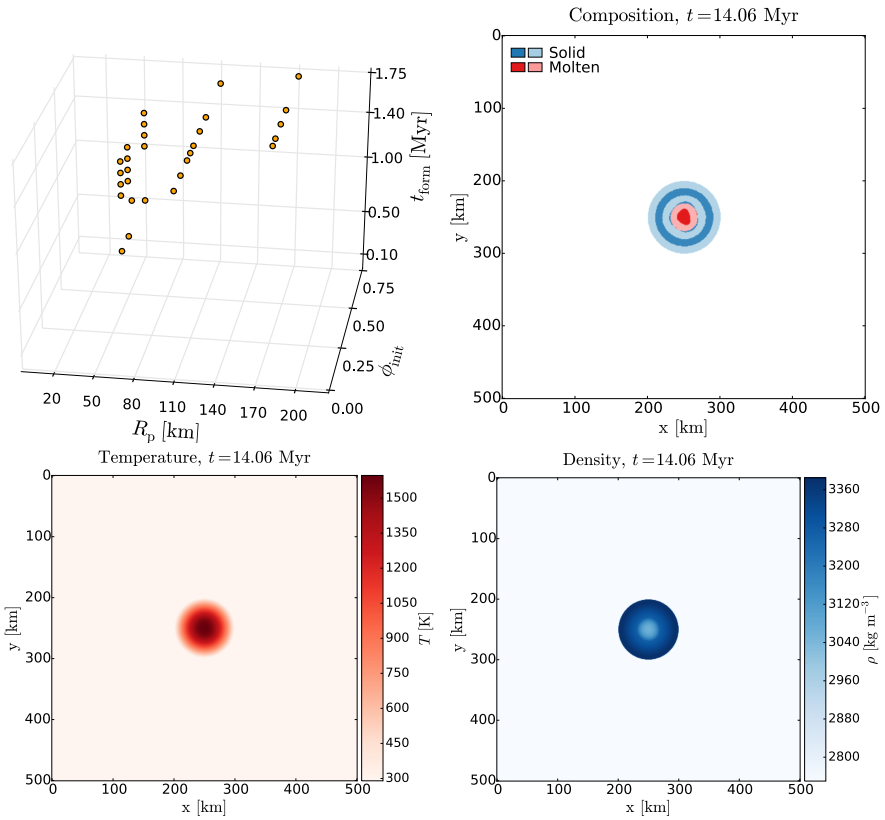

Figure 4.4: Example of a *deformation* model, with $R_{\mathrm{p}} = 50$ km, $t_{\mathrm{form}} = 1.0$ Myr, $\phi_{\mathrm{init}} = 0.75$ at $t = 14.06$ Myr. The temperatures were high enough to initiate the onset of convection but could not sustain these temperatures long enough for mixing to occur.

DEFORMED MELT REGIME This class marked the transition from the *static melt* to the *mixing* regime in the three-dimensional parameter space. A *deformation* example is given in Figure 4.4 for an evolutionary stage with molten silicate phases and deformed layers, which clearly deviated from the initial circular structure. This kind of models reached higher temperatures than their *static melt*-bearing counterparts. Due to the larger density contrast this leaded to the onset of mass segregation within the body. An interesting case is given for $R_{\mathrm{p}} = 50$ km. These bodies were dominated by *deformation* for $\phi_{\mathrm{init}} \geq 0.4$ and $t_{\mathrm{form}} \lesssim 1.3$ Myr. This type is categorized differently as it indicates the restrictions of our model: if the viscosities fell below η_{num}, fluid motions could not always be correctly resolved, in spite of accurately modeling the heat flux. Again, for a more detailed discussion on this issue see Section 4.4.

MIXING REGIME The class of *mixing* models was the most dynamic of all types. An example is given in Figure 4.5, showing the onset of convection due to extreme heating conditions within the body due to high SLR abundances. In these cases the density contrast of inner

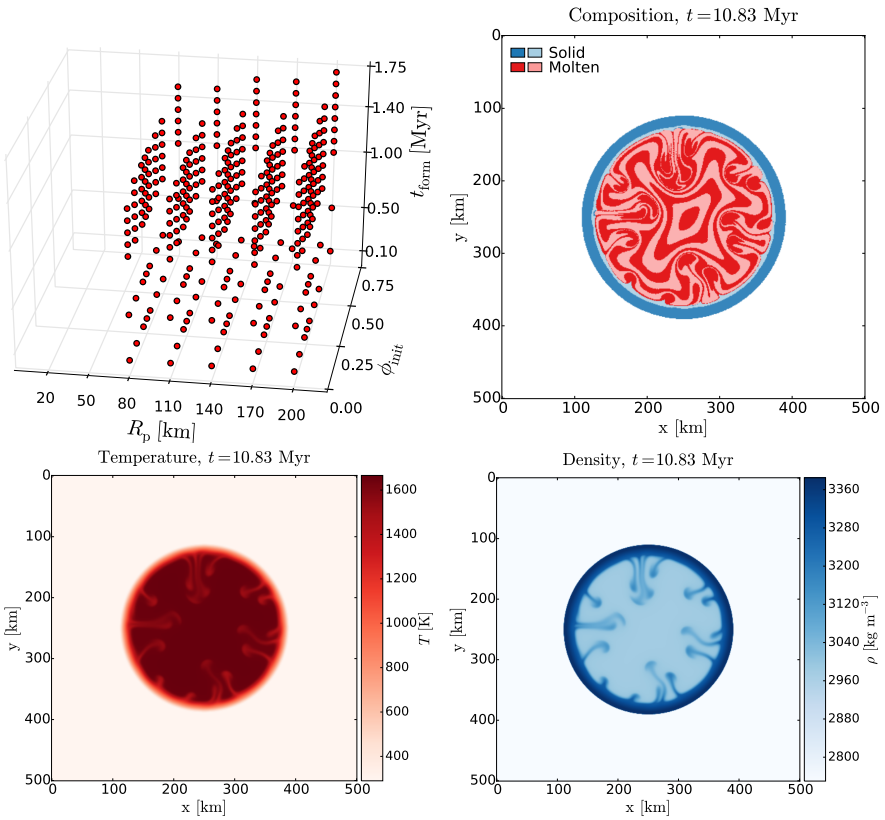

Figure 4.5: Example of a *mixing* model, with $R_{\mathrm{p}} = 140$ km, $t_{\mathrm{form}} = 0.5$ Myr, $\phi_{\mathrm{init}} = 0.4$ at $t = 10.83$ Myr. The density contrast of inner and outer layers drove convection.

and outer layers initiated and drove convectional motion. The subsequent downwellings from the surface layers (cool and dense) to the inner parts (hot and buoyant) are reflected in the composition, temperature and density plots. We will discuss the time evolution of this in Section 4.3.1.2. Models of this kind were only found for bodies with $R_{\mathrm{p}} \geq 80$ km. The formation time is less important than the radius, but showed significant effects by lowering the threshold t_{form} for smaller bodies, i.e., $R_{\mathrm{p}} \leq 140$ km models did not *mix* anymore above $t_{\mathrm{form}} \geq 1.6$ Myr, whereas $R_{\mathrm{p}} \geq 170$ km models did. Even less influential for the qualitative evolution were changes in initial porosity, for which no significant variance was observed.

4.3.1.2 *Heat balance*

This section is devoted to an analysis of the energy reservoir in the bodies over time. To analyze the influence of each of the varied simulation parameters we construct isolines, fixing two of the three parameters (see figures 4.6 and 4.7). The models which are discussed here were among the simulations with the most extreme differences in peak temperature and are therefore best suited to show general trends in the data.

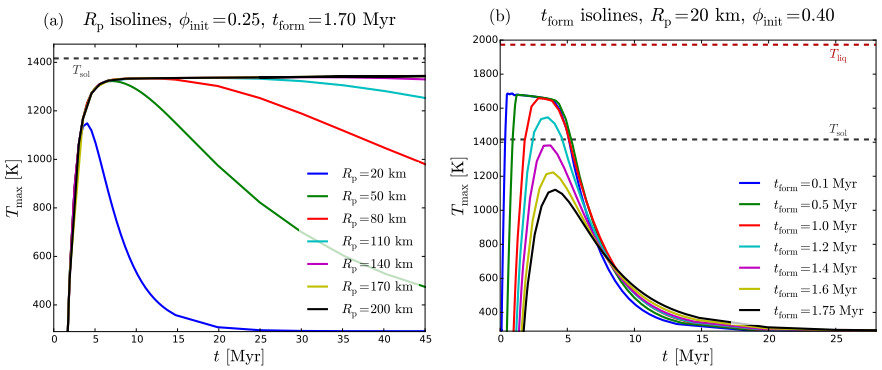

Figure 4.6: Peak temperature inside planetesimal versus time. T_{sol} and T_{liq} represent the solidus and liquidus temperatures, respectively. *(a)* Fixed ϕ_{init}, t_{form} and varying R_p. The cooling time scale is primarily dependent on the size of body. *(b)* Fixed R_p, ϕ_{init} and varying t_{form}. Only models with $t_{form} < 1.4$ Myr reached temperatures high enough for melting processes to occur. The $t_{form} = 0.1/0.5$ Myr models were affected by the soft turbulence model from Section 4.2.3, see Section 4.4 for a discussion of the effect.

INFLUENCE OF PLANETESIMAL RADIUS R_p Figure 4.6a shows the radius isolines for all R_p values for models with $t_{form} = 1.7$ Myr and $\phi_{init} = 0.25$. In general, smaller bodies cooled more efficiently than their larger counterparts, which were prone to reach higher temperatures. This resulted in lower viscosities for the latter and gave them more time to develop deformed structures or convection.

INFLUENCE OF FORMATION TIME t_{form} Figure 4.6b shows the influence of the formation time on models with $R_p = 20$ km and $\phi_{init} = 0.4$. There are two interesting characteristics to note in this plot. Firstly, the bodies with $t_{form} = 0.1/0.5$ Myr showed a steep increase in temperature, compared to all other t_{form} isolines but reached a sudden turning point at $t \approx 7.2 \cdot 10^5$ Myr. These bodies incorporated more ^{26}Al due to its half-life time of $t_{1/2} \approx 7.2 \cdot 10^5$ Myr. When the temperatures increased, the material transitioned to molten states and viscosities $\eta \leq \eta_{num}$ occurred, the soft turbulence model set in and increased the heat flux, which permitted the body to cool at an elevated rate (see Section 4.4). Secondly, simulations with stronger heating sources and therefore higher peak temperatures showed steeper cooling curves than models with later formation time. In practice, the ordering of formation isolines is reverted at $t = 8$ Myr. This can be explained with the higher thermal conductivity of molten silicate states. The models with higher peak temperatures reached higher melt fractions than those with lower peak temperatures, and are therefore able to cool down more efficiently.

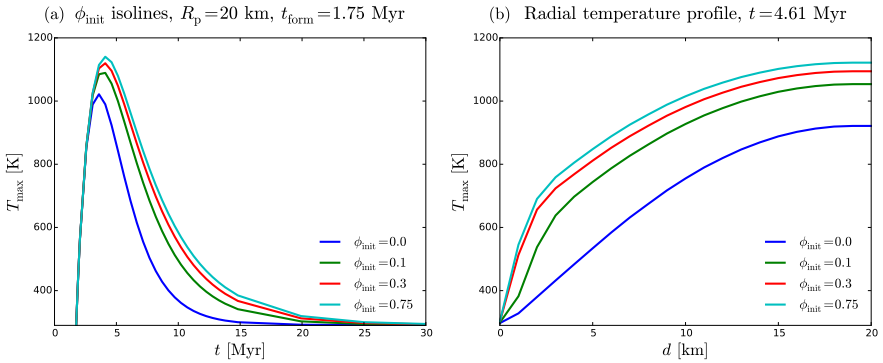

Figure 4.7: *(a)* Peak temperature inside planetesimal versus time with fixed R_{p}, t_{form} and varying ϕ_{init}. The models never reached temperatures high enough for melting processes to occur and the deviations in peak temperature were too small to inherit qualitative changes in the thermo-mechanical behavior of the simulations (compare Figure 4.1.) *(b)* Peak temperature profiles inside planetesimal for time $t = 4.61$ Myr for the same parameters as plot *(a)*. Deviations in peak temperature were more pronounced toward the center of the planetesimal.

INFLUENCE OF INITIAL POROSITY ϕ_{init} Figure 4.7 shows the contribution of initial porosity on peak temperature deviations in bodies with $R_{\text{p}} = 20$ km and $t_{\text{form}} = 1.75$ Myr. In general, higher porosity increases the voids within the granular material, effectively lowering the thermal conductivity. Therefore, models with higher initial porosity sustained their internal heat by SLRs over a longer time period. Figure 4.7a shows an extreme case in the overall parameter range, where the maximum peak temperatures deviated by $\Delta T \approx 120$ K, not enough to achieve qualitative differences, as all peak temperatures were below the melting temperature for silicates.

To check for local variations of the temperature within specific planetesimals, we derive peak temperature profiles by assessing the maximum value from four points at the same distance from the planetesimal center. Therefore, the values in Figure 4.7b represent the maximum temperatures at a certain depth, which does not necessarily imply the same average value for this depth for non-axisymmetric behavior. However, irrespective of a few specific cases these are nearly undistinguishable and certainly not in the range in which these differences affect the long-term thermo-mechanical evolution. Hence, we restrict our discussion to the maximum temperature case. The variations in peak temperature with depth were most importantly effecting small bodies, most remarkably $R_{\text{p}} = 20$ km in our parameter space. Therefore, Figure 4.7b shows the porosity isolines for the simulation with $R_{\text{p}} = 20$ km and $t_{\text{form}} = 1.75$ Myr at time $t = 4.61$ Myr. Going from the surface of the planetesimal to its center the temperature differences increased.

As displayed in both plots of Figure 4.7, in such small planetesimals the peak temperatures were not enough for the onset of *melting*. Thus, the temperature deviations due to porosity changes did not result in qualitative differences between the displayed models. Since the peak temperature differences between porosity isolines decrease for all other parameter combinations the porosity did not have a significant effect on the thermo-mechanical evolution of the planetesimals.

4.3.2 *Porous shells*

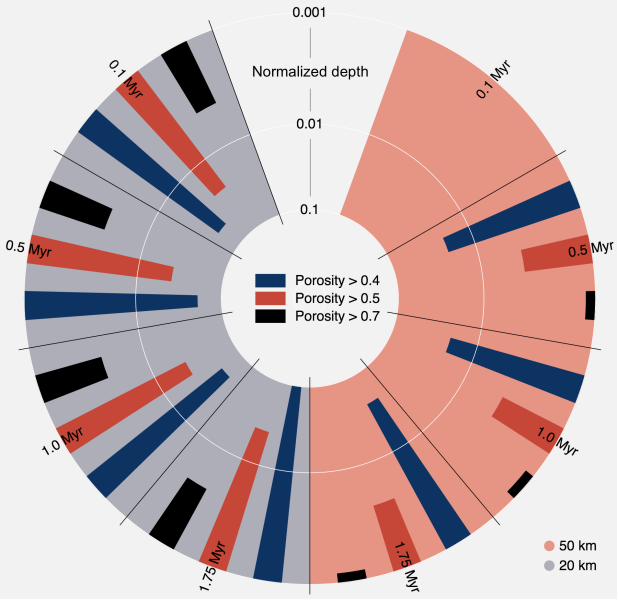

Figure 4.8: Remnant porous shells in evolved planetesimals with $R_\mathrm{p} = 20$ km (gray background) or $R_\mathrm{p} = 50$ km (red background), $\phi_\mathrm{init} = 0.75$ and varying t_form. The tip of each dark blue bar represents the scaled thickness of the remnant porous shell at the end of the thermal evolution, with $\phi > 0.4$ (see Equation 12). As isostatic pressing effects decrease toward the surface, the red and black bars show depths above which the porosity was $\phi > 0.5$ or $\phi > 0.7$, respectively. The white circles represent normalized logarithmic depths within the planetesimal $d_\mathrm{norm} = \log(d/R_\mathrm{p})$ from 0.001 to 0.1. As an example, the red bar for $R_\mathrm{p} = 50$ km, $t_\mathrm{form} = 0.5$ Myr shows that for $d_\mathrm{norm} \lesssim 0.06$ the porosity was $\phi > 0.5$, increasing toward the surface.

In addition to the marginal effect of porosity changes on the peak temperature and the thermo-mechanical evolution, the majority of our models with initial porosity showed a porous shell feature. As illustrated for several models in Figure 4.8, these structures were retained during the thermo-mechanical evolution and formed because of two effects. Firstly, compaction due to self-gravity by cold pressing (Equation 12) lowered the porosity within the body close to $\phi = 0.42$

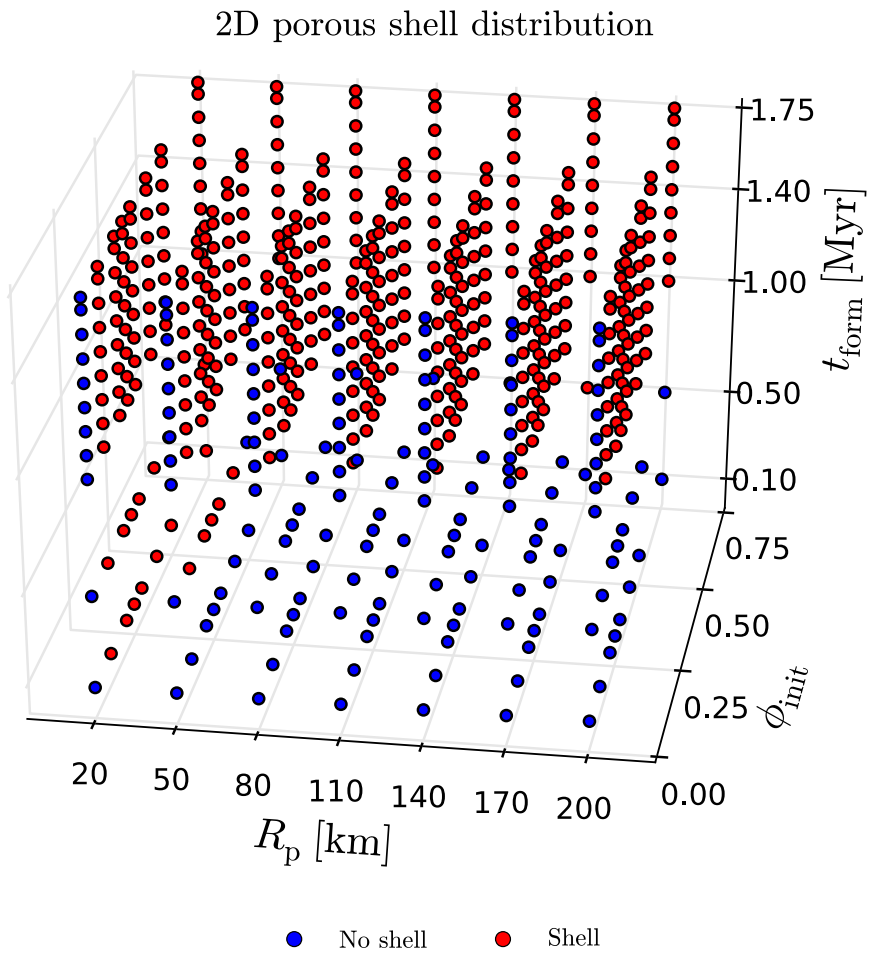

Figure 4.9: 3D parameter space showing the distribution of porous shells, with R_{p} in km, ϕ_{init} non-dimensional and t_{form} in Myr. The retainment of a porous shell depended dominantly on formation time t_{form}.

and consequently increased the density contrast between the outermost layers and the layers deeper inside the body. Secondly, during the temporal evolution of the models the temperatures deep within the planetesimals were by far higher than those close to the surface. The temperatures within the body were high enough for sintering effects, which altered the porosity value according to Equation 15. Because both effects were unimportant closer to the surface, a large subset of the model retained a porous layer throughout their whole evolution. Only the models with the most extreme heating values were hot enough to sinter or melt even their outermost layers. Figure 4.8 shows the combined effects of planetesimal size and formation time on the extent of the porous shells and the porosity change within the shell. Sintering limited the total thickness of the shell (d_{norm}) and compaction determined the increase in porosity toward the surface.

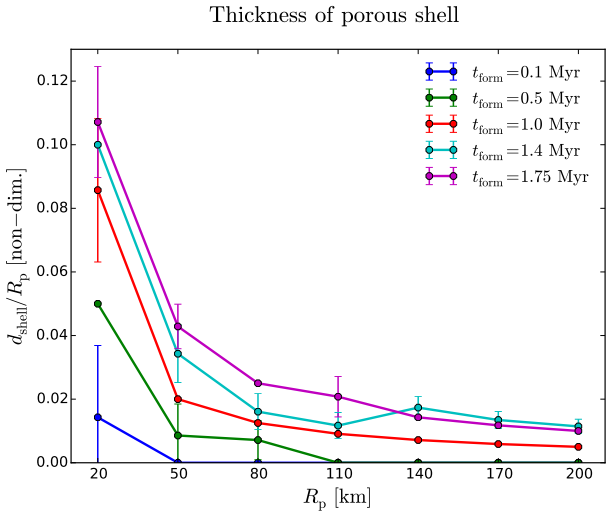

Figure 4.10: Fraction of porous shell versus planetesimal radius after all thermo-mechanical processes have ended. The values represent the arithmetic means over the results for all initial porosities ϕ_{init}, the error bars showing the corresponding standard deviations. The shell fraction decreased with increasing size of the body and with earlier formation time.

Figure 4.9 illustrates the distribution of bodies with and without porous shells. Most notably, the dominant parameter determining the preservation of a porous shell was the formation time: for $t_{\mathrm{form}} \geq 1.0$ Myr all models developed such structures. Aside from the small effects of lithostatic pressure, the material distribution within the upper layers of the body did not depend on its size, since the weight on top of it was unaffected by the overall mass of the body. Therefore, these layers were only minimally affected by cold isostatic pressing. A minor effect regarding the size of the body was still observed, as models with $t_{\mathrm{form}} = 0.5$ Myr and $R_{\mathrm{p}} \leq 110$ km also developed a shell, while bodies with $R_{\mathrm{p}} \geq 140$ km did not.

The distribution of the porous shell structures within the model set remained unaffected by initial porosity ϕ_{init} and was determined by R_{p} and t_{form}. Figure 4.10 shows the thickness of the porous shell as a fraction of the size of the body R_{p} for different formation times t_{form}. The values represent an average over the results for all initial porosity values ϕ_{init}, as this parameter did not affect the final shell depths significantly. The fraction of the shell was larger for smaller bodies and for later formation times. Both vary the amount of heating sources within the body, as later formation times lowered the initial abundances of SLRs and smaller bodies cooled more efficiently and displayed lower temperatures in their interiors. Thus, sintering effects were less important.

4.3.3 *3D analogues*

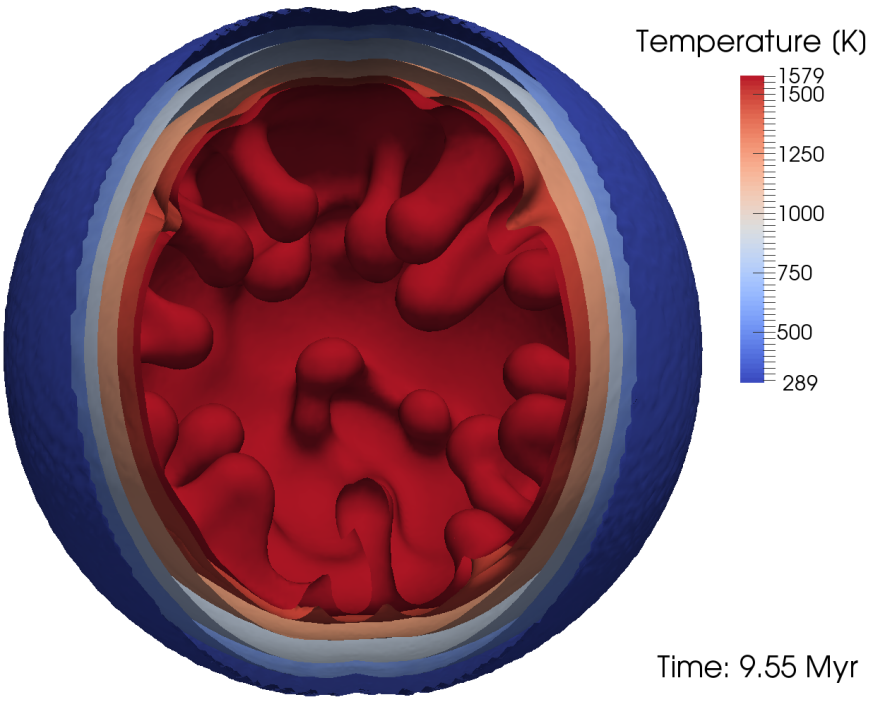

Figure 4.11: Density isocontours in a *mixing* 3D model, with $R_\mathrm{p} = 110$ km, $\phi_\mathrm{init} = 0.25$ and $t_\mathrm{form} = 0.1$ Myr. The density increased from the inside (dark red, $\rho = 3100$ kg m^{-3}) to the outside (dark blue, $\rho = 3385.6$ kg m^{-3}). Therefore, the model experienced buoyancy driven mass movement.

As described in Section 4.2.5 we additionally performed a set of 3D simulations for different parameter combinations to check for possible deviations from the 2D results. All 3D models are referenced in Section 4.7.

In principal, the selected 3D simulations confirmed the general trends we have found in two dimensions before. Smaller bodies with $R_\mathrm{p} \leq 50$ km displayed *solid* or *static molten* type and developed no convection patterns, regardless of their formation time. Larger bodies were more likely to experience convectional mixing, as illustrated in Figure 4.11. Comparable to the 2D simulations the formation time was the dominant parameter for the thermo-mechanical evolution and the onset of melting processes: early formed bodies experienced stronger heating by SLRs. As expected from the 2D results we also found porous shells in the appropriate parameter ranges.

The 3D models, however, did not perfectly match the results from the 2D simulations, as can be seen for model number 624, with $R_\mathrm{p} = 110$ km, $\phi_\mathrm{init} = 0.25$ and $t_\mathrm{form} = 1.7$ Myr, which evolved to a *static molten* state and did not retain a porous shell. Its 2D counterpart

however was *solid* throughout its evolution and we found a shell at the end of its thermo-mechanical evolution. In general, as far as we can conclude from the restricted model set of 3D simulations, they seem to have experienced higher temperatures than their respective 2D analogues and thus the whole parameter space was shifted toward a higher fraction of *static molten*, *deformed molten* and *mixing* models. As already mentioned in the introduction, this result is expected and can be attributed to the lower surface-to-volume ratio of 3D models. Hence, planetesimals in 3D experienced a lower heat flux compared to their increased volume and abundance of SLRs and therefore reached higher internal temperatures.

All in all, our 3D models were capable of reproducing the most important structures, compositional types and porosity features of the 2D models with slightly shifted regime boundaries and therefore verified the main conclusions we have drawn before.

4.4 MODEL LIMITATIONS

The main caveat regarding the evolutionary channels from Section 4.3.1 is the lower cut-off viscosity η_{num}, whereas we expect that the real viscosity at melt fractions above 0.4 drops to values orders of magnitudes smaller than the applied lower cut-off viscosity (see Section 4.2.3 for examples). This especially happened for models with early formation times $t_{\mathrm{form}} = 0.1/0.5$ Myr, i.e., within the first few half-life times of ^{26}Al. As mentioned before these low viscosities cannot be resolved numerically.

To estimate which of our numerical models would have experienced convection, that could not be resolved, we estimate the onset time of convection based on the approach of Howard (1964). Since internal heating was important in the models, we employ the Roberts-Rayleigh number (Roberts, 1967), which can be used to compute the boundary layer Roberts-Rayleigh number

$$Ra_{\delta} = \frac{\alpha g \rho_0 H_{\mathrm{r}} \delta^5}{k \kappa \eta}, \tag{4.15}$$

with reference density ρ_0, boundary layer thickness δ and thermal diffusivity κ. For the latter we use the characteristic diffusion length scale $(\kappa t)^{1/2}$ and assume that the viscosity of the partial melt decreases exponentially from 10^{17} Pa s at $\varphi = 0.4$ to 10^{-2} Pa s at $\varphi = 0.6$. Solving for t we obtain the relation

$$t_{\mathrm{crit}} = \left(\frac{Ra_{\delta} k \eta}{\alpha \rho_0 g H_{\mathrm{r}}} \right)^{2/5} \kappa^{-3/5} \tag{4.16}$$

with $Ra_{\delta} \sim 30$ (Sotin and Labrosse, 1999). We use this relation to compare the time periods $\Delta t_{\eta \leq \eta_{\mathrm{num}}}$, during which the viscosities are

expected to drop below the numerical cut-off viscosity, with the analytical solution. Models with $t_{\mathrm{crit}} \leq \Delta t_{\eta \leq \eta_{\mathrm{num}}}$ are marked in Figure 4.1 (diamonds, *static melt, unresolved convection*). These, together with the *deformed static* class, are models for which we could not properly resolve convection. This drawback, however, did not affect the purely thermal evolution of the models, which was correctly approximated by the soft turbulence approach (as shown in Tackley et al., 2001; Hevey and Sanders, 2006; Golabek et al., 2011) and therefore all other quantities were not affected. Models for which the analytic solution is consistent with pure melting and no convection ($t_{\mathrm{crit}} > \Delta t_{\eta \leq \eta_{\mathrm{num}}}$, circles in Figure 4.1) are additionally referenced in Section 4.7 and are especially found for $t_{\mathrm{form}} \approx 1.1 - 1.5$ Myr and $R_{\mathrm{p}} = 20/50$ km.

Additionally, there are some minor aspects, which could shift the trends of our results, but not crucially change the general regimes. Firstly, all planetesimals were approximated as spherical bodies. Due to accretionary processes in the early formation phase, it is unlikely for planetesimals to be shaped perfectly symmetric. Irregular body structures would result in higher surface to volume ratios, hence enabling a faster cooling of the body (Davison et al., 2013).

Furthermore, as already discussed in Golabek, Bourdon, and Gerya, 2014, a more sophisticated approach for representing melt migration processes, cooling effects via ^{26}Al partitioning (Sahijpal, Soni, and Gupta, 2007) and iron-silicate-separation (Schubert, Spohn, and Reynolds, 1986) would incorporate a two-phase flow model, which was not featured here. Finally we did not consider the effect of melt composition on melt density, which would influence our *melting-mixing* boundary (Fu and Elkins-Tanton, 2014).

4.5 DISCUSSION & IMPLICATIONS

In Section 4.3 we have presented the results from our set of 2D and 3D computational models of the thermo-mechanical evolution of recently formed planetesimals with varied radius, instantaneous formation time and initial porosity to gain a better understanding of the processes in the early stages of terrestrial planet formation. We now discuss the key insights of our results.

Initial porosity of the bodies was only of minor importance for the model set we have run here. Although higher initial porosity tended to lower thermal conductivity and therefore favored higher internal temperatures, the thermo-mechanical evolution was only marginally affected.

As expected, radius of the body and formation time had a strong influence on the evolution of a planetesimal. With increasing radius and decreasing formation time the bodies experienced more heating by SLRs, which resulted in higher peak temperatures and steeper heating curves. Planetesimals displaying *mixing* can be expected to

have experienced iron-silicate separation. The fraction of bodies prone to significant internal silicate melting was consistent with previous work on the thermal histories of planetesimals (Sanders and Taylor, 2005).

With decreasing radius of the body the technical assessment of the numerical model became more important, as a thermo-mechanical regime with partially molten, but non-convectional interior was observed (static melt class in Figure 1). In this regime with $\varphi \lesssim 0.4$ we expect the Stokes velocity $v_{\mathrm{Stokes}} \sim g/\eta$ for iron droplets to be small, such that the time scale for differentiation is high. These melt-bearing but undifferentiated planetesimals are a potentially important link for impact splash models of chondrule formation (see, e.g., Sanders and Taylor, 2005; Sanders and Scott, 2012; Dullemond, Stammler, and Johansen, 2014). For a more stringent analysis of the importance of these models and corresponding parameter ranges we will further evaluate this connection in future work.

A subset of our models evolved to a state with highly porous outer layers, which altered the cooling history of the planetesimal. These shells occupied a larger fraction of the planetesimal radius with later formation time and smaller radius of the body. Hence, smaller and later formed objects were the most porous bodies, which can have implications on their dynamical behavior during impact processes, as investigated by Jutzi, Benz, and Michel (2008) and Jutzi et al. (2009). The larger planetesimals in our dataset can either be subject to catastrophic impact events with similar-sized bodies or subject to impacts by smaller bodies. For both cases the state of the material is important for the interaction with the encountered body. All in all these effects tend to influence the dynamical history of the accretion phase of terrestrial planets and cannot be neglected for investigations of collisional growth. Additionally, the thickness of the shells could be used to relate the structure of pristine bodies in the Solar system, which did not experience catastrophic impact events after their rapid formation, to their formation time.

Many of our models reached elevated temperatures, potentially high enough to outgas existing volatile elements. When these models reached a specific boundary the resulting bodies might end up as dry bodies, unable to deliver volatile elements to the forming planets via impacts. Thus, future studies will investigate the effect of SLR heating and initial porosity on the outgassing of volatiles in small bodies and therefore might have implications for the habitability of planetary systems, when related to the delivery to accreting terrestrial planets (e.g., Elser, Meyer, and Moore, 2012; Ciesla et al., 2015).

The more moderate models still showed temperatures high enough for hydration and metamorphic transformation processes, potentially creating serpentinites via an exothermic reaction. As discussed in Abramov and Mojzsis (2011) such reactions can provide energy for

non-volcanic hydrothermal activity. Within certain depths of onion shell structured planetesimals, which are in accordance with our models and previous work (Weiss and Elkins-Tanton, 2013, and references therein), the energy output might be in the right regime for the synthesis of primitive organic compounds, such as basic amino acids (Cobb and Pudritz, 2014). Their synthesis is dependent on the ammonia and water content of the corresponding planetesimal and can also change with radial distance to the central star (Cobb, Pudritz, and Pearce, 2015). Therefore, future studies can be directed to couple interior evolution to exterior formation conditions, i.e., the region in the protoplanetary disk and the appropriate formation time for various size classes, to gain a better understanding of the geological environment of early biological processes in our Solar system.

4.6 CONCLUSIONS

The initial state of planetesimals in the early Solar system crucially affected their thermo-mechanical evolution, which yields implications for terrestrial planet formation theories. We have conducted numerous 2D and 3D finite-difference fluid dynamics simulations of planetesimals with varying radius, formation time and initial porosity. From these we have determined the parameter space for various thermo-mechanical regimes and the influence of initial porosity. Our conclusions are the following.

- Typically, planetesimals with large size, early formation time and high initial porosity tended to develop convection. Small radii, late formation times and low porosities led to bodies which did not experience silicate melting.
- A third thermo-mechanical regime with largely molten bodies without convectional mixing existed for an intermediate parameter range with a trend toward small bodies and formation times $t_{\mathrm{form}} \approx$ 1.1–1.5 Myr after CAI formation.
- The effects of initial porosity were by far outweighed by those of planetesimal size and formation time, scarcely affecting the qualitative evolution of a planetesimal.
- A majority of models retained a shell of highly porous material in their outer layers, which was not affected by melting and sintering processes inside the bodies. The depth of these shells increased with later formation times and decreased planetesimal size.

With our models we were able to constrain stringent parameter ranges for the major thermo-mechanical regimes and to show that

porosity is not a primary factor for the evolution of planetesimals. Future investigations will link these results to specific aspects of terrestrial planet formation, like volatile degassing and chondrule formation. Moreover, connecting these results with SLR enrichment mechanisms in stellar clusters (e.g., Parker et al., 2014b; Parker and Dale, 2016), and thus probably strongly varying abundances of SLRs, would be beneficial for a comprehensive theory of planetary assembly and habitability on interstellar or galactic scales.

4.7 SUPPLEMENTARY MATERIAL

Supplementary materials associated with this section, containing lists of the simulations, can be accessed online, in the journal (10.1016/j.icarus.2017.11.004) or arXiv version (arXiv:1603.05979).

ACKNOWLEDGMENTS

We thank the referee, Stephen J. Mojzsis, for a thorough and constructive review, which considerably helped to improve the manuscript. We thank the NCCR PlanetS and the PlanetZ platforms for an inspiring and collaborative scientific environment and Richard J. Parker and Cornelis P. Dullemond for stimulating discussions. TL was supported by ETH Research Grant ETH-17 13-1. The numerical simulations in this work were performed on the BRUTUS and EULER computing clusters of ETH Zürich. The models were analyzed using the open source software environments MATPLOTLIB[1] (Hunter, 2007), BOKEH[2] and PARAVIEW[3] (Ahrens, Geveci, and Law, 2005).

1 http://matplotlib.org
2 http://bokeh.pydata.org
3 http://www.paraview.org

5

MAGMA ASCENT IN PLANETESIMALS: CONTROL BY GRAIN SIZE

At the time of writing, June 19, 2018, the content of this section is under review for publication in Earth and Planetary Science Letters as: Lichtenberg, T., T. Keller, R. F. Katz, G. J. Golabek, and T. V. Gerya (2018). "Magma ascent in planetesimals: control by grain size." arXiv: 1802.02157.

ABSTRACT

Rocky planetesimals in the early Solar system melted internally and evolved chemically due to radiogenic heating from ^{26}Al. Here we quantify the parametric controls on magma genesis and transport using a coupled petrological and fluid mechanical model of reactive two-phase flow. We find the mean grain size of silicate minerals to be a key control on magma ascent. For grain sizes larger than $\sim$1 mm, melt segregation produces distinct radial structure and chemical stratification. This stratification is most pronounced for bodies formed at around 1 Myr after Ca,Al-rich inclusions. These findings suggest a link between the time and orbital location of planetesimal formation and their subsequent structural and chemical evolution.

According to our models, the evolution of partially molten planetesimal interiors falls into two categories. In the *global magma ocean* scenario, the whole interior of a planetesimal experiences nearly complete melting, resulting in turbulent convection and core-mantle differentiation by the rainfall mechanism. In the *magma sill* scenario, segregating melts gradually deplete the deep interior of the radiogenic heat source. In this case, magma may form melt-rich sills beneath a cool and stable lid, while core formation would proceed by percolation. Our findings suggest that grain sizes prevalent during the internal-heating stage governed magma ascent in planetesimals. Regardless of whether evolution progresses toward a global magma ocean or segregated magma sills, our models predict that temperature inversions due to rapid ^{26}Al redistribution are limited to bodies formed earlier than $\sim$1 Myr after CAIs. We find that if grain size was smaller than $\sim$1 mm during peak internal melting, only elevated solid-melt density contrasts (such as found for the strongly reducing conditions in enstatite chondrite compositions) would allow substantial melt segregation to occur.

5.1 INTRODUCTION

At the time of planet formation, the inner Solar system was populated by rocky planetesimals with radii ranging from a few to some hundreds of kilometers. Within a few million years, the largest of these seeded today's terrestrial planets through dynamical accretion of many smaller bodies (Goldreich, Lithwick, and Sari, 2004). The internal evolution of planetesimals was influenced by radiogenic heating from the short-lived radionuclide ^{26}Al (Hevey and Sanders, 2006). For planetesimals larger than $\sim$10 km, and depending on the amount of ^{26}Al incorporated upon formation, the released energy was sufficient to cause significant silicate melting and release of volatiles like water (Castillo-Rogez and Young, 2017; Monteux et al., 2018). For initial ^{26}Al abundances and planetesimal radii exceeding certain critical values, the degree of silicate melting likely surpassed the rheological transition from solid-state creep to disaggregation and melt-dominated deformation at melt fractions of 0.4–0.6, resulting in interior magma oceans. In comparison with solid or partially molten interiors, which lose heat by conduction and/or laminar convection, disaggregation results in significantly increased heat flux by turbulent convection and an efficient metal-silicate differentiation by raining out of iron droplets (Stevenson, 1990).

The interior evolution of early Solar system planetesimals has broad implications for the formation of rocky planets as well as the main-belt asteroid populations, the most-direct remnants of the accretion process. Meteorites, the broken-up pieces of asteroids, are currently our only direct source of evidence from the early Solar system. Therefore, our understanding of planetary growth and evolution is fundamentally limited by our ability to reconstruct the thermochemical evolution of planetesimals as evidenced by meteorites. Achondritic meteorites, which are thought to originate from differentiated planetesimals, show a remarkable diversity and likely originate from more than 50–100 parent bodies (Wasson, 1990). However, spectral properties of asteroids do not match this diversity, as most known asteroids with an achondritic surface were reconstructed to be the debris of only a few parent bodies (Burbine et al., 2017). This apparent lack of achondritic asteroids is at odds with the available meteorite record.

A possible solution to this conundrum is that internally differentiated planetesimals can retain their primitive, chondritic surfaces if magma remains confined to the interior instead of being erupted by volcanism (Elkins-Tanton, Weiss, and Zuber, 2011; Weiss and Elkins-Tanton, 2013). Some paleomagnetic studies on CV and CM meteorites suggest their parent bodies, at some stage, had magnetic core dynamos, which would be consistent with this hypothesis (Carporzen et al., 2011; Cournede et al., 2015). Furthermore, data from the Rosetta

spacecraft indicates that 21 Lutetia features a carbonaceous or enstatite chondrite surface contrasting with a density of $\sim$3400 kg m^{-3} (Sierks et al., 2011; Pätzold et al., 2011), higher than known chondrites, but consistent with past compaction of the interior due to partial melting beneath a primitive, chondritic crust (Weiss et al., 2012; Neumann, Breuer, and Spohn, 2013).

Based on the available evidence, most current theoretical models propose a *magma ocean* scenario for planetesimal evolution, where an internal magma ocean, often confined beneath a relatively thin ($\sim$ 10 km) primitive crust, dominated the thermal and chemical evolution of planetesimals. This hypothesis implies a temperature structure with an adiabatic convective profile in the interior and a linearly conductive profile in the lid. Efficient silicate-metal separation in the magma ocean would have enabled rapid core formation, while sequential crystallization could have resulted in a layered silicate mantle forming from an initially well-mixed magma ocean. Recent modeling studies that have investigated this scenario have relied either on thermal modeling with parameterized melting (e.g., Hevey and Sanders, 2006; Elkins-Tanton, Weiss, and Zuber, 2011), or on one-phase convection models (e.g., Golabek, Bourdon, and Gerya, 2014; Lichtenberg et al., 2016) that capture the collective flow and thermochemical evolution of partially molten rock or partly crystalline magma.

However, two-phase theory of partially molten systems (e.g., McKenzie, 1984) suggests that silicate melts may buoyantly ascend relative to the ambient rock matrix. Depending on the compositional and rheological properties of silicate minerals and their melts, this segregation may have been rapid with respect to internal heating and melt generation. In that scenario, planetesimals could have become depleted of melt in their interior, thus protracting, or even precluding, the generation of internal magma oceans. Ascending melts would instead have accumulated to form melt-rich layers, so-called magma sills (Wilson and Keil, 2017), beneath the primitive lid. This *magma sill* hypothesis implies a potentially significant redistribution of ^{26}Al, which is a moderately incompatible element and preferentially partitions into silicate melts. The transfer of the major heat source into shallow magma sills might then result in a transient inverted temperature profile with a peak temperature around the sill overlaying a cooler interior. Hence, this model posits that a subset of planetesimals, for which the chemical and rheological criteria for rapid melt ascent were met, could have experienced a thermal evolution and chemical differentiation significantly different from the *magma ocean* hypothesis. To date, only few theoretical studies have investigated the coupled mechanical and thermochemical evolution of partially molten planetesimals. These were either based on parameterized melt transport models with approximated melt ascent velocities

(Moskovitz and Gaidos, 2011; Wilson and Keil, 2012; Mandler and Elkins-Tanton, 2013; Neumann, Breuer, and Spohn, 2013, 2014a), or focused on metal-silicate differentiation and core formation without addressing silicate differentiation or the redistribution of ^{26}Al (Šrámek et al., 2012).

The efficiency of melt transport in planetesimals depends on various parameters. The presence of primordial volatiles like H_2O and CO_2 would strongly favor rapid segregation by increasing the buoyancy and lowering the viscosity of magmas. However, if volatiles are exsolved before the onset of silicate melting, Fu and Elkins-Tanton (2014) argue that the segregation rate of dry melt is mostly controlled by the oxygen fugacity and the degree of melting. Bulk oxygen fugacity may span a wide range across different meteorite classes, from IW+2 for angrites to IW-2.5 for enstatites (Brett and Sato, 1984), where IW represents the iron-wüstite buffer. The oxygen fugacity controls the relative abundance of FeO versus Fe-FeS in the primordial rock, with parts of the latter possibly lost to the core by percolation before the onset of major silicate melting (Bagdassarov et al., 2009b; Cerantola, Walte, and Rubie, 2015). Higher oxygen fugacity may therefore result in silicate melts richer in iron with reduced (or even inverted) density contrast relative to the host rock. Lower oxygen fugacity, in contrast, may produce iron-poor, buoyant melts that ascend rapidly.

In this study, we assess the effects of melt segregation on the thermal evolution and chemical differentiation of early Solar system planetesimals. We focus on the melting and partitioning of the major lithophile phases in primitive planetesimals and investigate the potential for melt accumulation and heat source redistribution. We employ a computational model of coupled fluid dynamics and thermochemical evolution that combines multi-component petrological reactions with a two-phase magma transport model. We quantify the leading controls on melt segregation in planetesimals using theoretical considerations and numerical calculations of idealized planetesimal evolution. Our results show that both the *magma ocean* and *magma sill* hypotheses are realized within a relevant parameter space. We will focus our discussion on the latter case, where melt segregation is most important.

In Section 5.2, we introduce basic concepts using scaling relations for melt transport by porous flow. In Section 5.3, we discuss the major silicate components of primitive planetesimals and calibrate the reactive melting model. We briefly review the method for thermochemically coupled reactive two-phase flow and its application to planetesimal interiors. We present results in Section 5.4 and discuss their implications in Section 5.5, before presenting conclusions in Section 5.6.

5.2 MELT SEGREGATION SCALING

To gain a leading-order understanding of silicate melt ascent in ^{26}Al-heated planetesimals, we consider the characteristic time scale of melt transport in partially molten bodies. Two-phase flow theory describes melt segregation as porous flow through a deformable and compactable matrix (McKenzie, 1984, see model equations in Section 5.3.2). In this formulation, the characteristic speed at which buoyant melt migrates relative to the surrounding rock matrix in a planetesimal is given by the Darcy velocity

$$w_0 = k_\varphi \Delta\rho g / \mu \,, \tag{5.1}$$

with the solid-melt density contrast $\Delta\rho$, gravity g, melt viscosity μ, and rock permeability

$$k_\varphi = \frac{a_0^2}{b} \frac{\varphi^{\mathrm{n}}}{(1-\varphi)^{\mathrm{m}}} \,, \tag{5.2}$$

with mean grain size a_0, geometric factor b, melt fraction φ[1], permeability exponent n and solid fraction exponent m. In primordial, homogeneous planetesimals, gravity increases with radius $g(r) = g_0 r / R_\mathrm{P}$, until it reaches the full magnitude g_0 at the surface. The first silicate melts in sufficiently large planetesimals form in an adiabatic zone stretching from the center, where gravity is close to zero, to below the upper conductive lid (Hevey and Sanders, 2006; Lichtenberg et al., 2016). As melting progresses, the permeability increases and melts in shallower regions of the planetesimal, where gravity is highest, begin to segregate from the residual rock.

To estimate the importance of melt ascent for planetesimal evolution, we define the *melt segregation time scale*, τ_segr, as the characteristic time of melt migration,

$$\tau_\mathrm{segr} = R_\mathrm{P} / w_0 \,, \tag{5.3}$$

with R_P the radius of the planetesimal, and w_0 calculated at the surface gravity. In order to achieve a substantial redistribution of melt present in a planetesimal, the rate of melt transport speed must exceed the rate of melt generation in the interior, which is controlled by the rate of internal heating. We thus define the *heating time scale*, τ_heat, of a planetesimal

$$\tau_\mathrm{heat} = c_\mathrm{p} \Delta T_0 / H_{0,^{26}\mathrm{Al}} \,, \tag{5.4}$$

1 In this chapter, φ represents the silicate melt fraction, also denoted 'porosity'. This notation may not be confused with the *macroporosity* ϕ, voids in the silicate matrix inherited from the gravitational collapse during planetesimal formation, in chapters 4 and 6.

with the specific heat of silicates, $c_\mathrm{p} = 1100$ J kg^{-1} K^{-1}, the temperature difference between the initial temperature and the silicate solidus, $\Delta T_0 \sim 1100$ K, and the decay power of ^{26}Al,

$$H_{^{26}\mathrm{Al}}(t) = f_\mathrm{Al} \cdot \left[\frac{^{26}\mathrm{Al}}{^{27}\mathrm{Al}}\right]_0 \cdot \frac{E_{^{26}\mathrm{Al}}}{\tau_{^{26}\mathrm{Al}}} \cdot \mathrm{e}^{-t/\tau_{^{26}\mathrm{Al}}}, \tag{5.5}$$

evaluated at $t = t_\mathrm{form}$, the formation time of a planetesimal relative to the formation of Ca,Al-rich inclusions (CAI, $t = 0$). Here, f_Al is the chondritic abundance of aluminum (Lodders, 2003), $\left[\frac{^{26}\mathrm{Al}}{^{27}\mathrm{Al}}\right]_0 = 5.25 \times 10^{-5}$ (Kita et al., 2013) is the canonical ratio of ^{26}Al to ^{27}Al at CAI formation, $E_{^{26}\mathrm{Al}} = 3.12$ MeV is the decay energy, and $\tau_{^{26}\mathrm{Al}} = t_{1/2,^{26}\mathrm{Al}}/\ln(2) = 1.03$ Myr is the mean lifetime of ^{26}Al.

Using the heating and segregation time scales, we define the non-dimensional *melt segregation number*, which quantifies the propensity of a planetesimal to undergo substantial melt segregation, as a function of the key model parameters,

$$R_\mathrm{seg} = \log_{10}\left(\frac{\tau_\mathrm{heat}}{\tau_\mathrm{segr}}\right) = \log_{10}\left(\frac{k_\varphi \Delta\rho g_0 c_\mathrm{p} \Delta T_0}{R_\mathrm{P} \mu H_{0,^{26}\mathrm{Al}}}\right). \tag{5.6}$$

To assess the expected melt segregation regimes in planetesimals, we calculate R_seg for a reasonable range of melt fractions below the rheological transition ($\varphi_\mathrm{crit} \sim 0.4$), ($\varphi = [0, \varphi_\mathrm{crit}]$), formation times ($t_\mathrm{form} = [0, 4]$ Myr), grain sizes ($a_0 = [10^{-5}, 10^{-2}]$ m) and melt-rock density contrasts ($\Delta\rho = [120, 1200]$ kg m^{-3}). Figure 5.1 shows that a growing melt fraction increases the melt segregation number through its effect on permeability. Larger grain sizes and higher density contrasts also significantly enhance segregation, but the effect of the latter is less pronounced than the former. For a fixed melt fraction, the heating rate decreases with time, which again serves to favor melt segregation relative to melt production.

From this scaling analysis, we conclude that melt segregation can in principle occur on a time scale that is relevant compared to the internal heating by ^{26}Al in planetesimals (10^5–10^6 yr, Lichtenberg et al., 2016, 2018). However, it crucially depends on the dynamic evolution of the melt fraction, which is controlled by the fluid mechanics of melt transport in a deforming rock matrix, and the thermochemical evolution of the body. This scaling analysis does not capture any of these, including the potential formation of magma sills beneath a primitive lid and the redistribution of the heat source by transport of aluminum in the melt. In order to assess these dynamic processes we require a time-dependent evolution model, which will be introduced in the next section.

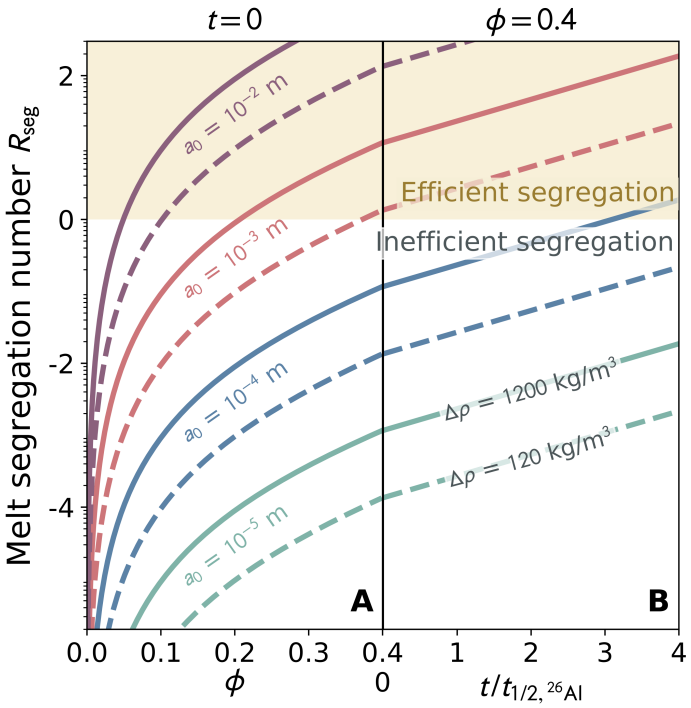

Figure 5.1: Scaling analysis of melt segregation propensity, with melt segregation number $R_{\text{seg}} = \log_{10}(\tau_{\text{heat}}/\tau_{\text{mt}})$. (A) At t = 0 Myr (CAI formation) and with rising melt fraction φ, the migration velocity increases, and so the system is more likely to become segregated. For $\varphi > 0.4$, the magma ocean regime is reached and the system would be dominated by turbulent convection. (B) For fixed melt fraction $\varphi = 0.4$ and later times (= weaker radiogenic heating) the melt segregation number rises further.

5.3 METHOD

5.3.1 *Melting and heat source partitioning*

Studies of primitive meteorites (McSween, Bennett, and Jarosewich, 1991; Dunn et al., 2010) and equilibrium condensation sequence calculations (Ebel and Grossman, 2000) both suggest that the main rock-forming mineral phases in Solar system planetesimals are olivine (mostly forsterite, Mg_2SiO_4), pyroxene (mostly enstatite, $MgSiO_3$) and feldspar (mostly anorthite, $CaAl_2Si_2O_8$). Ignoring minor contributions from CAIs and trace minerals, feldspar represents the major host phase of ^{26}Al in rocky planetesimals. In addition to the timing of accretion and size of a planetesimal (Lichtenberg et al., 2016, 2018), magma genesis depends on the relative abundance of these phases. Furthermore, the concentration of volatiles has a major effect on incipient silicate melting. However, to avoid further complexity, we will consider only dry melting here, which is justified if volatile degassing during accretion is efficient (Castillo-Rogez and Young, 2017; Fu et al.,

2017). We therefore formulate a model for melting and melt-rock partitioning of these major mineral phases.

We employ the R_DMC method of Keller and Katz (2016) to calculate idealized thermodynamic equilibrium at given temperature, pressure, and bulk composition, and linear kinetic reaction rates for a multi-component system. To do so, we define three compositional pseudo-components and their mass-concentrations in the solid (rock), c_s^i, and liquid phases (melt), c_ℓ^i, which capture the collective behavior of classes of minerals grouped by similar melting points and partitioning behavior: olivine-like (olv), pyroxene-like (pxn), and feldspar-like (fsp). The mass fraction of all three components must sum to unity in both phases.

Using a simplified form of ideal solid solution theory (Rudge, Bercovici, and Spiegelman, 2011), we determine the component partition coefficients at given P, T-conditions,

$$K^i = \frac{c_s^{i,\mathrm{eq}}}{c_\ell^{i,\mathrm{eq}}} = \exp\left[\frac{L^i}{r^i}\left(\frac{1}{T} - \frac{1}{T_\mathrm{m}^i(P)}\right)\right], \tag{5.7}$$

which are the ratios of solid, $c_s^{i,\mathrm{eq}}$, to liquid, $c_\ell^{i,\mathrm{eq}}$, component concentrations defined in equilibrium. The latent heat of pure-component fusion,

$$L^i = \Delta S T_{\mathrm{m},0}^i\,, \tag{5.8}$$

is given by the entropy gain of fusion ΔS and the pure-component melting temperatures at zero pressure, $T_{\mathrm{m},0}^i$. Curvature coefficients r^i adjust the temperature dependence of partition coefficients. The pressure-dependent pure-component melting points are parameterized as

$$T_\mathrm{m}^i(P) = T_{\mathrm{m},0}^i + B^i P\,, \tag{5.9}$$

with B^i the linear slopes.

At a given phase-volume-averaged bulk composition (lever rule)

$$\bar{c}^i = (1-\varphi)c_s^i + \varphi c_\ell^i\,, \tag{5.10}$$

we numerically determine the equilibrium melt fraction φ^eq that satisfies the partitioning coefficients K^i by combining the lever rules with the unity sum constraint on all components

$$\sum_{i=1}^{n} \frac{\bar{c}^i}{\varphi^\mathrm{eq}/K^i + (1-\varphi^\mathrm{eq})} = \sum_{i=1}^{n} \frac{\bar{c}^i}{\varphi^\mathrm{eq} + (1-\varphi^\mathrm{eq})K^i}. \tag{5.11}$$

Then, using the equilibrium melt fraction we can calculate the equilibrium phase compositions for solid and melt,

$$c_s^{i,\mathrm{eq}} = \frac{\bar{c}^i}{\varphi^{\mathrm{eq}}/K^i + (1-\varphi^{\mathrm{eq}})}\,, \tag{5.12a}$$

$$c_{\mathrm{liq}}^{i,\mathrm{eq}} = \frac{\bar{c}^i}{\varphi^{\mathrm{eq}} + (1-\varphi^{\mathrm{eq}})K^i}\,. \tag{5.12b}$$

Any dynamic changes in pressure, temperature or bulk composition over time creates disequilibrium. The mass transfer of component i from solid to liquid that drives the system back toward equilibrium is assumed to occur according to linear kinetic reaction rates,

$$\Gamma^i = \mathcal{R}\left(\varphi^{\mathrm{eq}} c_\ell^{i,\mathrm{eq}} - \varphi c_\ell^i\right)\,, \tag{5.13}$$

with a rate factor $\mathcal{R} = \rho_0/\tau_\Gamma$, which enforces equilibration over time τ_Γ at reference density ρ_0. The sum of all component reaction rates is the total melting rate $\Gamma = \sum_i \Gamma^i$. All parameter values are given in Table 5.1.

Before coupling this reactive melting model to a dynamic transport model, we consider the aluminum partitioning behavior in a closed system with increasing temperature ($P = 0$). For consistency with earlier work (Tkalcec, Golabek, and Brenker, 2013; Golabek, Bourdon, and Gerya, 2014; Lichtenberg et al., 2016; Monteux et al., 2018; Lichtenberg et al., 2018; Hunt et al., 2018), we choose the lowest component melting point, that of fsp, to conform with previous estimates of the silicate solidus. To test different partitioning behaviors, we vary the relative temperature difference between the melting points for the ^{26}Al-hosting fsp and the pxn components, $\Delta T_{\mathrm{m}} = T_{\mathrm{m},0}^{\mathrm{pxn}} - T_{\mathrm{m},0}^{\mathrm{fsp}}$, with $T_{\mathrm{m},0}^{\mathrm{pxn}} = [1400, 1600]$. The resulting rock and melt compositions in the ternary system olv-pxn-fsp are shown in Figure 5.2. Depending on the difference between fsp and pxn melting points, the incipient melt may be strongly enriched in fsp, and thus ^{26}Al. As the degree of melting increases with temperature, more pxn is dissolved into the melt. Finally, the melt composition converges toward the bulk composition as the system approaches complete melting. A larger difference in melting points increases the initial enrichment of aluminum in the melt. At our chosen reference calibration, the melt initially comprises $\sim 80\%$ fsp, but becomes relatively enriched in pxn by the time the melt fraction reaches φ_{crit}.

5.3.2 *Two-phase, multi-component fluid model*

As partial melts segregate from their residual rock, the interior will be gradually depleted of its ^{26}Al content and thus its heat source. To model this dynamic process, we couple the multi-component melt-

Parameter	Symbol	Unit	Value/Range
Geometric factor	b	non-dim.	100
Melt fraction exponent	n	non-dim.	3
Solid fraction exponent	m	non-dim.	2
Melt shear viscosity	μ	Pa s	1
Thermal expansivity	α	K^{-1}	3×10^{-5}
Specific heat capacity	c_p	J kg^{-1} K^{-1}	1100
Thermal diffusivity	κ	m^2 s^{-1}	1.14×10^{-6}
olv initial mass fraction	$\bar{c}^{olv}$	wt %	50
pxn initial mass fraction	$\bar{c}^{pxn}$	wt %	35
fsp initial mass fraction	$\bar{c}^{fsp}$	wt %	15
olv melting point	$T^{olv}_{m,0}$	K	2050
pxn melting point	$T^{pxn}_{m,0}$	K	1500
fsp melting point	$T^{fsp}_{m,0}$	K	1350
Entropy gain of fusion	dS	J K^{-1}	320
Curvature coefficients	r^{olv}, r^{pxn}, r^{fsp}	J kg^{-1} K^{-1}	50, 20, 10
Linear P-coefficients	B^{olv}, B^{pxn}, B^{fsp}	K GPa^{-1}	60, 100, 120
Reference rock density	ρ_0	kg m^{-3}	3200
Reference rock viscosity	η_0	Pa s	10^{19}
Shear viscosity cut-off	η_{min}	Pa s	10^{16}
Compaction viscosity cut-off	ζ_{min}	Pa s	10^{17}
Initial temperature	T_{init}	K	290
Surface temperature	T_{space}	K	290
Planetesimal radius	R_P	km	60
Grain size	a	m	$[10^{-5}, 10^{-2}]$
Formation time	t_{form}	Myr	[0, 4]
Melt-rock density contrast	$\Delta\rho$	kg m^{-3}	[120, 1200]

Table 5.1: Scaling quantities, definitions and parameter values introduced in the scaling analysis, R_DMC and two-phase flow models. Varying model parameters are named in the text and figures. Parameters not listed here are as given in Table 1 in Keller and Katz (2016).

ing model above to the two-phase reactive transport model fully described in Keller and Katz (2016). The fluid mechanics part of the model is based on the seminal work of McKenzie (1984), and the thermochemical evolution model on Rudge, Bercovici, and Spiegelman (2011). Here, we give a brief summary of the governing equations and constitutive relations.

The physical model is derived from statements for the conservation of phase and component mass, phase momentum, and total energy. We consider the model in a cartesian coordinate system with gravity pointing down the vertical coordinate, $\mathbf{g} = -g\hat{\mathbf{z}}$. The governing equations are formulated in the geodynamic limit (liquid viscosity $\mu \ll$ rock viscosity η), using the extended Boussinesq approximation

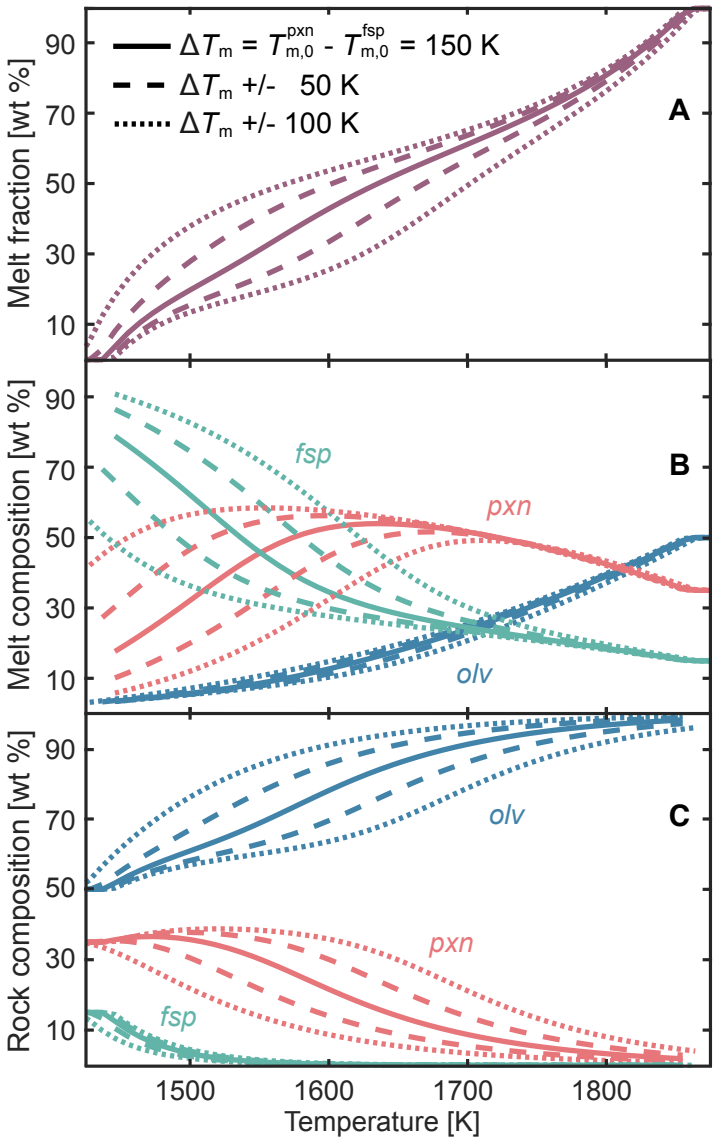

Figure 5.2: Temperature dependence of melt fraction (A), melt (B) and rock (C) composition, with varying melting point difference between fsp and pxn, ΔT_m = $T_\mathrm{m}^\mathrm{pxn}$ - $T_{\mathrm{m},0}^\mathrm{fsp}$, which changes the partitioning coefficient of fsp and the composition of the earliest melts. If the fsp melting point is close to the one of pxn, the initial melt composition is close to a 50-50 mixture. For higher melting point difference, the first melts are dominated by fsp, and thus the heating component (^{26}Al) of the system preferentially follows the dynamics of the earliest melts. When the absolute temperature of the system further rises and approaches the olv melting point, the composition converges toward the initial pure solid setting.

(densities $\rho_s = \rho_\ell = \rho_0$ taken equal and constant except when multiplying gravity). The fluid mechanics governing equations are,

$$\nabla \cdot 2\eta \mathbf{D}(\nabla \mathbf{v}_s) - \nabla P_\ell + \varphi \Delta\rho \mathbf{g} = \nabla P_\mathrm{C}\,, \tag{5.14a}$$

$$-\nabla \cdot \mathbf{v}_s = \nabla \cdot \mathbf{v}_\mathrm{D}\,, \tag{5.14b}$$

$$\mathbf{v}_\mathrm{D} = \varphi(\mathbf{v}_\ell - \mathbf{v}_s) = -\frac{k_\varphi}{\mu}\left(\nabla P_\ell + \Delta\rho \mathbf{g}\right)\,, \tag{5.14c}$$

$$P_\mathrm{C} = (1-\varphi)(P_s - P_\ell) = -\zeta \nabla \cdot \mathbf{v}_s\,. \tag{5.14d}$$

They are posed in four independent variables, the dynamic pressures and velocities of the solid and liquid phases, P_s, P_ℓ, $\mathbf{v}_s$, and $\mathbf{v}_\ell$. Two dependent variables, the Darcy segregation velocity, $\mathbf{v}_\mathrm{D}$, and the compaction pressure, P_C, express the mechanical interactions between the phases. If these vanish, the equations become identical with the Stokes system. The deviatoric operator $\mathbf{D}(\cdot) = \frac{1}{2}([\cdot] + [\cdot]^T) - \frac{1}{3}\mathrm{tr}[\cdot]\mathbf{I}$ acts on the velocity gradient tensor. Assuming a diffusion creep rheology with melt-weakening, the shear viscosity of the rock matrix is given by

$$\eta = A_0\, a_0^3 \exp\left(\frac{E_\mathrm{a} + PV_\mathrm{a}}{RT} - \lambda\varphi\right), \tag{5.15}$$

with prefactor A_0, activation energy, E_a, and activation volume V_a as in Hirth and Kohlstedt (2003) and Mei et al. (2002); R is the universal gas constant, and $\lambda \approx 30$ the melt-weakening factor (Keller and Katz, 2016; Keller, Katz, and Hirschmann, 2017). Permeability is set by the Kozeny-Carman relation (Equation 5.2), with powerlaw exponents $n = 3$, $m = 2$ for the melt and solid fractions, respectively. The compaction viscosity $\zeta = r_\zeta \eta/\varphi$, with $r_\zeta \approx 5$ the shear to compaction viscosity ratio.

To these equations we add thermochemical evolution equations for temperature, T (assuming thermal equilibrium between the phases), melt fraction, φ, and pseudo-component concentrations in the solid and liquid phases, c_s^i and c_ℓ^i:

$$\frac{\bar{\mathrm{D}}T}{\mathrm{D}t} = \kappa\nabla^2 T - \sum_{i=1}^{n} \frac{L^i\Gamma^i}{\rho_0 c_\mathrm{p}} + \frac{\Psi}{\rho_0 c_\mathrm{p}} + \frac{H_{^{26}\mathrm{Al}}}{c_\mathrm{p}} + \frac{\alpha T}{c_\mathrm{p}} g w_z\,, \tag{5.16a}$$

$$\frac{\mathrm{D}_s\varphi}{\mathrm{D}t} = (1-\varphi)\nabla\cdot\mathbf{v}_s + \Gamma/\rho_0\,, \tag{5.16b}$$

$$\frac{\mathrm{D}_\ell c_\ell^i}{\mathrm{D}t} = \frac{\Gamma^i - c_\ell^i\Gamma}{\varphi\rho_0}\,, \tag{5.16c}$$

$$\frac{\mathrm{D}_s c_s^i}{\mathrm{D}t} = -\frac{\Gamma^i - c_s^i\Gamma}{(1-\varphi)\rho_0}\,. \tag{5.16d}$$

Temperature evolves through advection, thermal diffusion, latent heat exchange of reactions, heating by viscous dissipation Ψ and internal heating $H_{^{26}\mathrm{Al}}$, and adiabatic decompression. Melt fraction evolves through advection, compaction and reactions, and composition by advection and reaction. The material derivative of the two-phase mixture is $\bar{\mathrm{D}}/\mathrm{D}t = (1-\varphi)\mathrm{D}_s/\mathrm{D}t + \varphi\mathrm{D}_\ell/\mathrm{D}t$, with $\mathrm{D}_s/\mathrm{D}t = \partial/\partial t + \mathbf{v}_s\cdot\nabla$, and $\mathrm{D}_\ell/\mathrm{D}t = \partial/\partial t + \mathbf{v}_\ell\cdot\nabla$. κ is the thermal diffusivity, $w_z = ((1-\varphi)\mathbf{v}_s + \varphi\mathbf{v}_\ell)\cdot\hat{\mathbf{z}}$ the vertical speed, and α the thermal expansivity.

The governing equations for the fluid mechanics (Equations 5.14a–5.14d) and thermo-chemistry (Equations 5.16a–5.16d) are discretized using the finite difference method on a rectangular, staggered grid

and solved by two coupled Newton-Krylov solvers. The simulation software uses parallel data structures and robust solvers provided by PETSc (Balay et al., 1997; Katz et al., 2007). Nonlinearities between the fluid mechanics and thermochemical sub-problems are resolved using a Picard fixed-point iterative scheme. During every iteration, Equation 5.11 is solved using Newton's method to update the equilibrium melt fraction. The adopted model is strictly valid only for melt transport by porous flow below the disaggregation threshold. However, we cannot avoid models producing regions with higher melt content. To ensure that the equations do not produce disruptive solutions in these regions, we apply lower viscosity cut-offs to the shear viscosity ($\eta_{\mathrm{num}} = \eta + \eta_{\mathrm{min}}$) and compaction viscosity ($\zeta_{\mathrm{num}} = \zeta + \zeta_{\mathrm{min}}/(1-\varphi)$). The effect of this regularization is to dampen out the segregation velocity and compaction pressure at elevated φ. As a result, our model will produce stable solutions above the rheological transition, but will underestimate chemical mixing and heat transport by rapid flow in the crystal-bearing suspensions that characterize this limit.

5.3.3 *Model setup and parameter space*

We model magma genesis and transport along a 1D Cartesian column from the center to the surface of an initially homogeneous and isothermal body. We focus our analysis on bodies of 60 km radius. Planetesimals of this size are qualitatively representative of the interior evolution of planetesimals of $R_{\mathrm{P}} \gtrsim 50$ km, because the effect of size is limited by the thermal diffusivity and the ^{26}Al decay rate (Castillo-Rogez and Young, 2017). In other words, planetesimals with radii $\gtrsim 50$ km are dominated by a relatively large adiabatic interior and a thin ($\lesssim 10$ km) conductive lid, whereas the relative dimensions of these domains vary significantly for planetesimal radii $\lesssim 50$ km (cf. Lichtenberg et al., 2018; Hunt et al., 2018). The computational domain has a size of 500 grid cells with a spatial resolution of 120 m. The surface boundary is isothermal at $T_{\mathrm{space}} = 290$ K, while the center boundary is insulating, $\partial T/\partial z = 0$. We assume the accreted body is initially at ambient temperature, $T_{\mathrm{init}} = T_{\mathrm{space}}$, and subsequently heats up due to ^{26}Al decay. As noted above, gravity decreases linearly from the surface gravity down to zero at the center.

Magma and rock composition are modeled in the three-component compositional space of olv, pxn and fsp described in Section 5.3.1. We use the melting points for the components as in Figure 5.2 (solid lines). The solid-melt density contrast $\Delta\rho$ is varied from 200–1200 kg m^{-3} between runs to reflect changes in FeO content and thus density of the melt due to the oxygen fugacity of the host planetesimal (Fu and Elkins-Tanton, 2014; Wilson and Keil, 2017). Grain size a_0, which controls both the permeability and rock viscosity, is held constant during each calculation, but we consider values from 10 μm to 1 cm,

i.e., from chondrite matrix-like dust to pallasite-like crystal sizes (see Figure 5.1). ^{26}Al is contained solely in the fsp component. Any redistribution of this component will hence affect the local heating rate. The initial heating rate at t_{form}, $H_{0,^{26}\mathrm{Al}}$, is varied from 1.52×10^{-7} W kg^{-1} to 1.91×10^{-8} W kg^{-1}, and decreases with progressing simulation time according to Equation 5.5. The top value is calculated (Moskovitz and Gaidos, 2011; Lichtenberg, Parker, and Meyer, 2016) from the canonical ^{26}Al/^{27}Al ratio of 5.25×10^{-5} (Kita et al., 2013), the latter represents the decay power after three half-lives ($t_{1/2} = 0.717$ Myr) of ^{26}Al, after which it no longer causes significant silicate melting. To avoid further model complexity, we ignore the potential heat contribution from ^{60}Fe (see, e.g., Tang and Dauphas, 2015; Lichtenberg, Parker, and Meyer, 2016, for discussions of ^{60}Fe inheritance).

5.4 RESULTS

5.4.1 *Parameter study*

We find that the model results across the tested parameter range fall into three qualitative categories. Some models show no substantial melt formation or segregation; we will not further discuss these *undifferentiated* models here. The time evolution of the latter two categories are shown in Figure 5.3. Both show the same general evolution: rapid initial heating leads to substantial melt production, which is followed by some degree of melt segregation, before ending with slow cooling from the top down. One category of models, which we identify with the *magma ocean* end-member (red), evolve to where most of the interior is above the disaggregation threshold, whereas the other, the *magma sill* end-member (blue), result in a melt-depleted interior along with melt-enriched sills beneath the lid (Fig. 5.3A–E). The latter show clear signatures of a thermal inversion (Fig. 5.3F–J) related to segregation of fsp into enriched layers beneath the lid (Fig. 5.3K–O).

The scaling analysis above predicts that grain size, a_0, and density contrast, $\Delta\rho$, are pertinent controls on melt segregation. Figure 5.4 shows the results of a detailed study of that parameter space. To quantitatively analyze the results, we introduce three metrics measuring the degree of

- melt segregation: $\Delta\varphi = \varphi_{\mathrm{max}} - \varphi_{\mathrm{ctr}}$,
- temperature inversion: $\Delta T = T_{\mathrm{max}} - T_{\mathrm{ctr}}$,
- fsp differentiation: $\Delta c_{\mathrm{fsp}} = \mathrm{fsp}_{\mathrm{max}} - \mathrm{fsp}_{\mathrm{ctr}}$.

Here, $(\cdot)_{\mathrm{max}}$ denotes the maximum value in the computational domain, and $(\cdot)_{\mathrm{ctr}}$ denotes the value at the base of the domain, i.e., the planetesimal center. The metric is calculated at the time of maximum melt volume in the domain before cooling sets in. With these

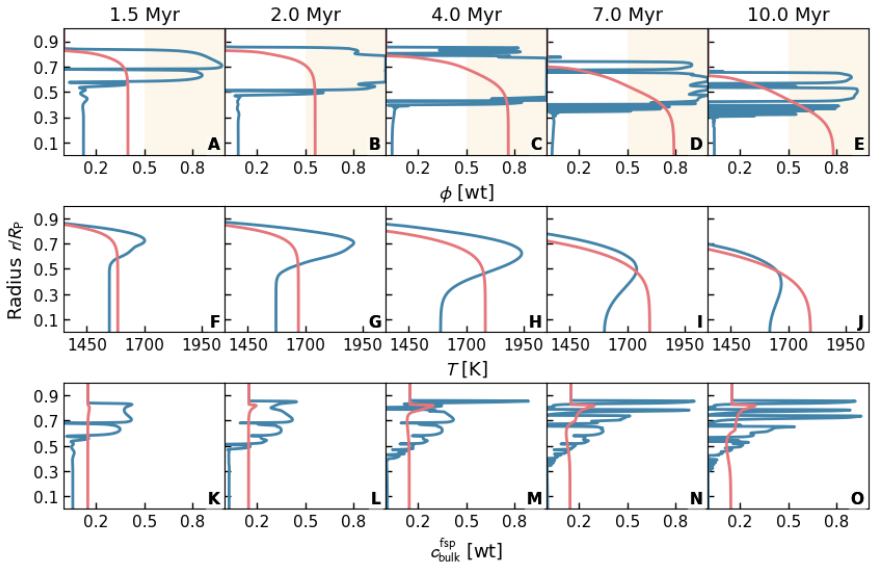

Figure 5.3: Time evolution of melt fraction (A–E), temperature (F–J) and fsp bulk composition (K–O) for two end-member models with radii R_P = 60 km and formation time t_{form} = 1.25 $t_{1/2,^{26}Al}$ = 0.90 Myr after CAIs. Red lines show a *magma ocean* model with $\Delta\rho$ = 200 kg m^{-3} and $a_0 = 10^{-4}$ m, blue lines a *magma sill* model with $\Delta\rho$ = 800 kg m^{-3} and $a_0 = 10^{-3}$ m. Upon progressive heating, the *magma sill* model builds up melt deposits below the cold upper lid, depleting the center of the planetesimal of silicate melts. High melt fractions $\varphi > \varphi_{crit}$ = 0.5 (yellow areas) are only reached in the sub-lid sills. fsp enrichment in the sill structure leads to a temperature inversion of ~400 K at peak melting. The *magma ocean* model, in contrast, shows a near-isothermal internal temperature and thus melt fraction structure in the interior. The fsp component shows notable deviations from the initial bulk composition only after $t \geq 2$ Myr, when most of the ^{26}Al has already decayed. A video showing the time evolution of the major thermochemical parameters and composition is referenced in the Supplementary material.

metrics, we quantify the deviation from an interior structure with near-constant melt fraction, temperature, and bulk composition, as it would be expected in the absence of significant segregation.

Figure 5.4 shows the three metrics across a range of a_0 = [10^{-5}, 10^{-2}] m and $\Delta\rho$ = [200, 1200] kg m^{-3}. We find that grain size strongly influences the interior evolution of the planetesimals. If grain size remains below $a_0 < 10^{-4}$ m, melt density contrasts of < 500 kg m^{-3} are not sufficient to drive significant segregation. For density contrasts > 1000 kg m^{-3} and for larger grain sizes, melt segregation becomes significant, as evidenced by a step-increase in each of the three metrics. However, we find that since initially fsp-enriched melts migrate on time scales comparable or longer than $t_{1/2,^{26}Al}$, the temperature inversion effect remains minor throughout (Figure 5.4, panels B & F).

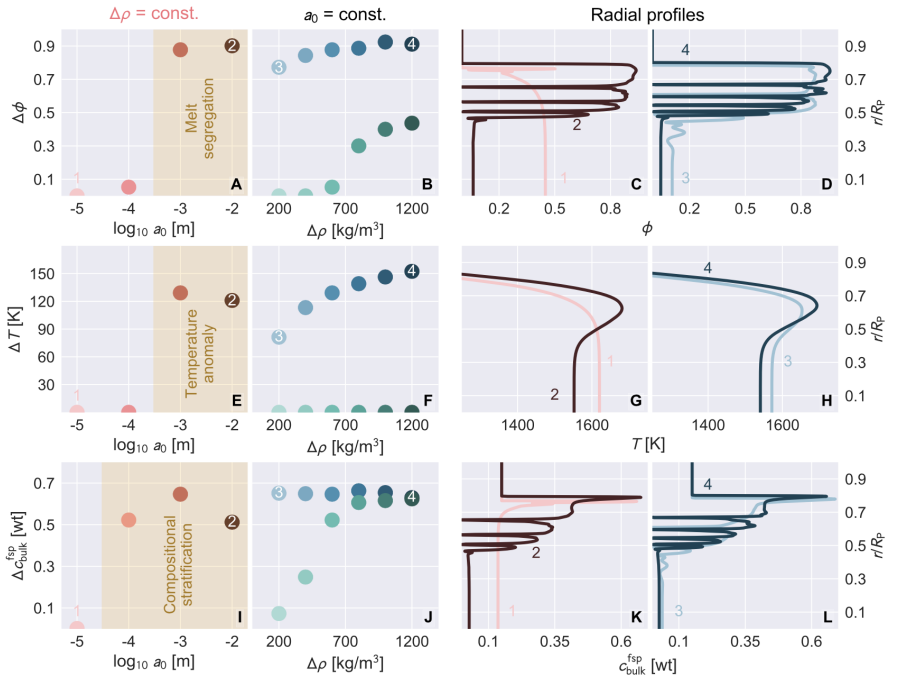

Figure 5.4: Parameter study of the influence of grain size a_0 and density contrast $\Delta\rho$ on melt segregation $\Delta\varphi$, temperature inversion ΔT and compositional stratification Δc_{fsp}, for planetesimals with R_{P} = 60 km, t_{form} = 1.5 $t_{1/2,^{26}\mathrm{Al}}$. Panels (A,E,I) show the metric deviation for constant density contrast $\Delta\rho$ = 600 kg m^{-3} and varying grain size a_0, indicating a steep gradient between grain sizes of 10^{-4} m and 10^{-3} m. For these two values fixed (blue: a_0 = 10^{-3} m, green: a_0 = 10^{-4} m), panels (B,F,J) display the metric deviations for varying $\Delta\rho$. Here, changes in density contrast are outweighed by the grain size. Models with a_0 = 10^{-3} m feature notable melt segregation, temperature inversions, and compositional differentiation. Models with a_0 = 10^{-4} m only do so toward the high-end range of density contrasts, $\Delta\rho \gtrsim$ 700 kg m^{-3}. Panels (C/D, G/H, K/L) show the radial profiles for the end-member models of the variations from (A/B, E/F, I/J). In general, variations in grain size a_0 outweigh effects from increasing density contrast $\Delta\rho$. *Magma sill* structures only form for grain sizes $a_0 > 10^{-4}$ m.

5.4.2 *Silicate differentiation*

As the planetesimals cool and crystallize, *magma sill* end-member cases exhibit a silicate differentiation trend toward compositional layering. In Figure 5.5, we compare a representative *magma ocean* with a *magma sill* model outcome. *Magma ocean* models evolve toward a global interior magma ocean, with melt fractions above the rheological transition $\varphi > \varphi_{\mathrm{crit}}$ and cool relatively unsegregated, such that the bulk concentrations of the fsp, pxn and olv components remain similar to the initial composition (Figure 5.5A). However, in *magma sill* models, the shallow magma sills above a low-melt-fraction inte-

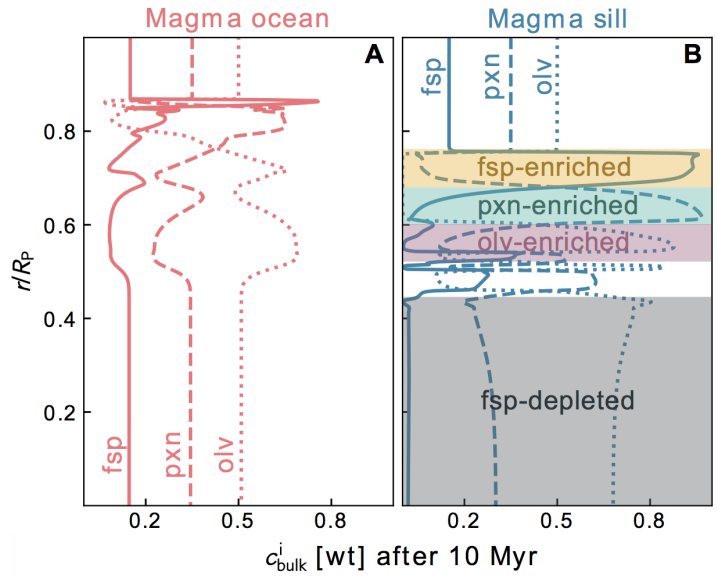

Figure 5.5: Compositional stratification after cooling and crystallization of magma beneath the primordial lid for *magma ocean* (A) and *magma sill*-type (B) models. *Magma sill* cases with intermediate temperatures and thus high concentrations of fsp in the upper layers produce this signature.

rior crystallize into distinct layers enriched in fsp, pxn and olv. This stratification reflects the component melting points ($T_\mathrm{m}^\mathrm{fsp} < T_\mathrm{m}^\mathrm{pxn} < T_\mathrm{m}^\mathrm{olv}$, Figure 5.5B). The melt-depleted central parts of the planetesimal are strongly depleted in fsp and also in pxn, the latter to a lesser degree. In general, such compositional layering forms during the cooling stage and is therefore not correlated with substantial temperature inversion. The densities of the minerals represented by the pseudo-components suggest that such layering would be dynamically stable.

5.4.3 *Magma dynamics regimes*

Figure 5.6 shows the regimes of melt segregation and compositional stratification we identify for different formation times, t_form, and melt segregation numbers, R_seg. We quantify the boundaries separating the three characteristic regimes as follows.

(I) *Magma ocean* regime: $\varphi_\mathrm{ctr} > \varphi_\mathrm{crit} = 0.5$, where the whole interior melts to above the disaggregation threshold;

(II) *magma sill* regime: $\Delta\varphi > \varphi_\mathrm{crit} = 0.5$, where melt segregation generates a magma sill beneath the lid and depletes the interior from melt;

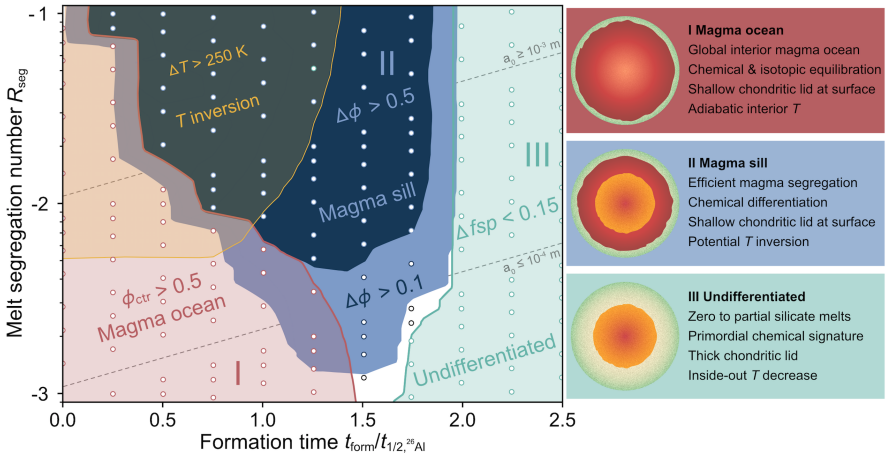

Figure 5.6: Evolution of silicate melt segregation with formation time t_{form} versus melt segregation number R_{seg}. Values are given for the peak mean melting time of each model (circles). We identify three primary melt dynamics regimes. (I) *Magma ocean* models, where melting occurs more rapidly than melt migration, feature high melt fractions above the rheological transition in their center $\varphi_{\mathrm{ctr}} > \varphi_{\mathrm{crit}}$ = 0.5. *Magma ocean*-type evolution is preferred for early t_{form} and low R_{seg}, i.e., small a_0 and $\Delta\rho$. (II) *Magma sill* models feature efficient melt segregation, with additional compositional stratification toward cooling-down of the planetesimals (cf. Figure 5.5). *Magma sill* type evolution is preferred for intermediate $t_{\mathrm{form}} \sim$ 1–1.5 Myr, and high R_{seg}. (III) *Undifferentiated* models never show melt fractions $\varphi_{\mathrm{ctr}} > \varphi_{\mathrm{crit}}$ = 0.5, and never experience substantial compositional redistribution. They are preferred for late formation times $t_{\mathrm{form}} \gtrsim$ 2.0 Myr. In addition to these three regimes, we show the region of increasing temperature inversion in yellow.

(III) *undifferentiated* regime: $\Delta c_{\mathrm{fsp}} < c^{\mathrm{fsp}}_{\mathrm{bulk},0}$ = 0.15, where melting and melt segregation do not redistribute a substantial amount of fsp.

In addition to these segregation and differentiation criteria, we show which models are most affected by substantial *temperature inversions*, $\Delta T >$ 250 K. These inversions occur both for *magma sill* and *magma ocean* models and reflect rapid magma ascent on time scales shorter than $t_{1/2,^{26}\mathrm{Al}}$. We find that the *magma sill* regime generally occurs at higher segregation numbers—at larger grain sizes or elevated density contrasts—and formation times less than 2 Myr after CAI, with a peak at around 1 Myr after CAI. Very early formation time, $t_{\mathrm{form}} \leq$ 1 Myr, or lower melt segregation number, $R_{\mathrm{seg}} \lesssim$ -1.4, favor *magma ocean*-type evolution. Formation later than 2 Myrs after CAI leads to *undifferentiated* planetesimals that barely melt at all. *Temperature inversions* occur for $t_{\mathrm{form}} \leq$ 1 Myr, and $R_{\mathrm{seg}} \gtrsim$ -2.5.

5.5 DISCUSSION

The question of whether early Solar system planetesimals were dominated either by global interior *magma oceans* or *magma sills* is of direct concern for the mechanisms of core formation, silicate differentiation and redistribution of planetary materials during accretion. The relative time scales of these mechanisms determine the compositional inventory of terrestrial planets and the remnants we observe today in the form of the asteroid belt and the meteorite collection.

5.5.1 *Parametric controls on magma segregation*

The models above present thermochemically consistent two-phase flow calculations that directly resolve the partitioning of the major rock-forming components and the reactive transport of magma. Using this method, we show that magma segregation in planetesimals that formed within 2 Myr of CAIs was potentially significant if magma ascent was rapid with respect to the rate of melt production controlled by ^{26}Al decay. Expressed in terms of the melt segregation number R_{seg}, *magma sill* models were produced for $R_{\mathrm{seg}} \geq$ -2.5. This requires that (i) grain sizes in these planetesimals were comparable to or larger than chondrules, on the order of $a_0 \geq 10^{-3}$ m, or (ii) in reducing environments (IW-2.5, $\Delta\rho \sim$ 1200 kg m^{-3}, Brett and Sato, 1984; Fu and Elkins-Tanton, 2014) at $a_0 \geq 10^{-4}$ m. Moreover, we find that even in the case of significant magma redistribution into shallow sills, the segregation time scale is comparable to the evolutionary time scale of the protoplanetary disk and thus the accretion time scale. Therefore, ^{26}Al-hosting phases release at least part of the ^{26}Al decay energy in the deeper region of planetesimals, and substantial temperature inversions on the order of a few hundred K are only observed for extreme cases with $R_{\mathrm{seg}} \gtrsim$ -1, or early formation times $t_{\mathrm{form}} \lesssim$ 1 Myr with $R_{\mathrm{seg}} \gtrsim$ -2.

Melt-rock density contrast is thought to be controlled by the oxidation state of the body. The chemical composition of accreting planetesimals is inherited from the oxidation gradient in the protoplanetary disk. Hence, the time and place of formation is expected to influence the subsequent interior evolution as it relates to the effects of melt segregation. For example, planetesimals primarily accreted toward inner parts of the disk may feature lower oxygen fugacities and therefore higher $\Delta\rho$, compared to planetesimals accreted further out (Rubie et al., 2015). In our models, we find that the effect of density contrast on magma segregation is of secondary importance. If grain sizes were not sufficient to allow for a critical permeability, variations in density contrast would have produced no significantly different outcomes. This is in contrast to previous studies (Moskovitz and Gaidos, 2011; Wilson and Keil, 2012; Šrámek et al., 2012; Fu and Elkins-

Tanton, 2014; Wilson and Keil, 2017; Fu et al., 2017), which did not consider magnitude variations in grain size or mechanisms of growth inhibition and grain destruction (Neumann, Breuer, and Spohn, 2013, 2014a).

5.5.2 *Implications for the role of grain size*

A main conclusion from our models is that the grain size a_0 is the dominant parameter controlling the magma transport rate inside planetesimals. There are two main mechanisms that can alter the grain size relevant for planetesimal evolution. First, the grain sizes may differ depending on the orbital location and mineralogical composition (van Boekel et al., 2004) of the dust that agglomerates to form the planetesimals. Coagulated dust aggregates on the order of $a_0 \geq 10^{-4}$ m are in the critical size regime for fast radial drift toward the protostar, depending on orbital location and evolutionary state of the protoplanetary disk. However, these sizes may facilitate planetesimal formation from local dust-gas interactions (Johansen et al., 2015; Birnstiel, Fang, and Johansen, 2016) and can trigger planetesimal formation at various orbital separations and times (Drążkowska and Alibert, 2017) with varying dust particle distributions within newly-formed bodies (Wahlberg Jansson and Johansen, 2017). Second, grain sizes may evolve during the heating and melting in the planetesimal interior after accretion. In this process, the grain size is influenced by competing mechanisms for growth and destruction (Rozel, Ricard, and Bercovici, 2011). Grain growth by either normal grain growth before the first melts arise, or Ostwald ripening during partial melting in a solid-liquid aggregate, is generally driven by the reduction of interfacial energies and competes with size reduction due to the presence of secondary solid phases (Hiraga et al., 2010), and mechanical work due to deformation (Tkalcec, Golabek, and Brenker, 2013).

As a comparison, grain sizes of meteorite classes span a wide range, from μm-sized dust to pallasite-like, cm-sized phenocrysts (Hutchison, 2004). Chondrites, generally regarded to be the most pristine rock samples from the early Solar system, display a bimodal size distribution, split between μm-sized dust ('matrix') and chondrules, which vary in size from 10^{-4} m to 10^{-3} m, with drastically differing internal texture and grain sizes. The relative amount of chondrules to matrix varies strongly between different chondrite groups, resulting in complex mixtures and average grain size distributions. Meteorites that likely underwent partial melting ('primitive achondrites'), like Acapulcoite-Lodranites, Winonites and Brachinites, display grain sizes around 10^{-4} m (Hutchison, 2004; Wilson and Keil, 2017). Ureilites, Aubrites, and Angrites, which come from bodies with more extensive, or even large-scale silicate melting feature larger grains, on the order of 10^{-3} m. However, these textures are the end result of a

million-year long evolutionary processes, and may have undergone repeated accretion and reaccretion cycles, that reset their thermal histories and textures (Lichtenberg et al., 2018). Therefore, we cannot yet assess the grain size evolution in the interiors of planetesimals on time scales relevant to interior melting processes based on the grain sizes observed in meteorites.

Interpretation of our results in this context suggests that the planetesimal interior evolution and the redistribution of chemical and isotopic heterogeneities during planetary accretion can be influenced by the planetesimal formation mechanism, its accretion location, and the local compositional distribution of grains in the protoplanetary disk. Further high-resolution studies of the planetesimal formation mechanism and mineralogical inventory, as e.g., during rapid gravitational collapse (Wahlberg Jansson and Johansen, 2017) or more gradual growth (Kataoka et al., 2013), are needed to determine the local grain-size distribution within planetesimals to be able to link the formation mechanism to the subsequent geophysical evolution of these bodies. Also, further accretion, for instance due to subsequent pebble accretion (Visser and Ormel, 2016) will influence if the magma can eventually reach the surface through fractures.

5.5.3 *Implications for chemical differentiation*

Recently, it was shown that percolation of Fe,Ni-FeS phases in primordial planetesimals will not be complete and at least some material remains trapped in the rock matrix until the disaggregation threshold is reached (Bagdassarov et al., 2009b; Cerantola, Walte, and Rubie, 2015). Beyond the disaggregation threshold, the remaining metal droplets will rain out rapidly toward the forming core (Lichtenberg et al., 2018). Therefore, even though the models in this study do not include a metal phase, they allow some leading order predictions on the implications for core formation.

In the case of a global *magma ocean*, we expect core formation to be rapid, with nearly complete loss of metals to the core. In the case of a shallow *magma sill*, an interesting two-step process may occur. First, a small, inner core may form from incomplete percolation. Then, after the formation of the sill structure, the remaining metal from this region may rain out and accumulate at the interface between the deep partial melt zone and the magma sill zone. This forming metal ring may segregate downwards or form diapirs sinking through the mechanically weakened partially molten rock if the viscosity is low enough to allow for Rayleigh-Taylor instabilities to form on timescales while the interior is still warm and it viscosity is reduced. The thermo-mechanical evolution of such a two-step process needs to be tested by taking into account metal phases in self-consistent multi-phase flow models, in order to make robust predic-

tions that can be compared to laboratory studies of the core formation process.

The limited melt segregation toward shallow layers in our non-segre-gated models may offer an explanation for the absence of remnant differentiated materials in the asteroid belt (Weiss et al., 2012; Mandler and Elkins-Tanton, 2013). Conversely, chemical stratification resulting from melt segregation may help to explain the paucity of olivine-rich deposits on 4 Vesta's surface (Clenet et al., 2014; Consolmagno et al., 2015). Furthermore, the *magma sill* models we present here are consistent with earlier work by Neumann, Breuer, and Spohn (2013, 2014a) predicting a magma sill below a cold lid in the case of efficient melt segregation.

Finally, our results indicate that the importance of melt segregation in planetesimal interiors may vary substantially, which generally affects the redistribution of heat-producing elements, such as ^{26}Al, during melt ascent. In the case of our *magma sill* end-member models, we also expect other incompatible elements to be preferentially segregated to shallow layers of a planetesimal. The crustal stripping paradigm of planetary accretion assumes that frequent impacts during planetary growth eroded and redistributed significant amounts of shallow materials between planetesimals. The strongly variable degree of melt segregation, and the resulting range of variably differentiated major, trace, and isotopic compositions of shallow planetesimal layers could result in compositional differences between forming planets and chondritic meteorites (Carter et al., 2018). Our simulations indicate that magma ascent governing material redistribution to the planetesimal crust occurs on a $\sim$Myr time scale, i.e., comparable to the collisional time scale of planetary accretion. This suggests that models quantifying compositional deviations between planets and chondrites should take into account the evolution of planetesimal interiors during planetary accretion.

5.5.4 *Limitations*

The main limitation of our models is the use of a 1D cartesian geometry, which incompletely captures the heating-to-cooling ratio of the spherical geometry of planetesimals. Here, we focus on planetesimal models of 60 km in radius that show a nearly isothermal evolution in the deep interior (cf. Figure 5.3), which is consistent with radially symmetric models (Castillo-Rogez and Young, 2017; Hunt et al., 2018). As a result of the column geometry, the amount of melt produced in the models is overestimated. Therefore, the lower boundary of the *magma sill* regime in Figure 5.6 is likely too low, because our higher early melt fractions increase melt migration speeds (Figure 5.1). However, because of the small planetesimal radius and the rapid heating during early times from ^{26}Al, the error introduced is minor.

Furthermore, the models presented in this work underestimate the vertical heat flux from turbulent mixing above the disaggregation limit (Golabek, Bourdon, and Gerya, 2014; Lichtenberg et al., 2018). This influences the cooling regime of planetesimals, but has no effect on the melt generation before magma ocean (or sill) phases are reached.

The melt in our *magma ocean* and *magma sill* models cannot breach the cold surface layers, as the temperature is too low for melt to exist in the porous medium. Our simulations cannot resolve potential melt transport through the upper lid by fracturing (Keller, May, and Kaus, 2013) or gravitational instability in the layered structure in Fig 5.5, which may bury the primitive lid (Wilson and Keil, 2012), and lead to efficient heat loss and magmatic resurfacing. This would affect the total retention of magma on the inside of planetesimals and the rate of magma transport on planetesimals. However, this does not affect our conclusions or any constraints on temperature inversions of planetesimals unless this transport is faster or comparable to the magma segregation in the interior.

Finally, our dry models neglect volatile-driven eruptions (Fu et al., 2017; Wilson and Keil, 2017), which may act as a catalyst for upward transport. If substantial volatile quantities could be retained, this mechanism would mainly affect the magma retention in the upper layers of planetesimals and potential chemical stratification upon crystallization of the silicate material. Also, the relatively low pressure at the planetesimal sizes we consider would not allow a high volatile solubility in silicate magma, and degassing would therefore be expected to be nearly complete in the earliest stages of melting and segregation.

5.6 SUMMARY & CONCLUSIONS

In this study we investigated magma genesis and redistribution in planetesimals during and shortly after the protoplanetary disk phase. Using scaling relations we demonstrated that the interior evolution of planetesimals sensitively depends on a variety of model parameters, with the grain size exerting the primary control on melt segregation. Based on average chondritic abundances of the most common mineral groups in meteorites, we calculated the composition for rock–melt aggregates comprised of idealized components using a reactive, multi-component melting model. We quantified the effects on ^{26}Al partitioning and magma ascent with a coupled, two-phase flow model. We defined the melt segregation number R_{seg} as the ratio between the heating and melt transport time scales in a planetesimal, which establishes the leading order parametric controls on the propensity for segregation to become important during the initial heating stage of planetesimal evolution. We predicted that the

primary two controls are the melt–rock density contrast and the mineral grain size.

Investigating the relative importance of model parameters for the evolution of planetesimals, we categorize model outcomes in terms of their melt segregation numbers R_{seg}, and their formation times t_{form}. Using this scheme, we find

- Planetesimal melt migration behavior can be classified in three general regimes:
  - The *magma ocean* regime with global interior magma oceans, where rapid melting overwhelms melt segregation.
  - The *magma sill* regime, where global interior magma oceans are prevented by rapid magma transport that concentrates melt in sills beneath the cool lid.
  - The *undifferentiated* regime with a low degree of melting, minor melt segregation, and therefore chemically primordial and largely undifferentiated interiors.
- *Magma sill* models crystallize to a compositionally stratified structure, with shallow depth layers dominantly enriched in the low melting point components, feldspar and pyroxene, and a paucity of high melting point components, such as olivine.
- *Magma ocean* and *magma sill* models show temperature inversions for high R_{seg} and early t_{form}, where the temperatures in the shallow- to mid-mantle are higher than at the center of the planetesimal.
- The *magma sill* regime can be achieved depending on a combination of a few key parameters:
  - The formation time t_{form} controls the total amount of energy available from ^{26}Al and restricts the regime for melt segregation to 0.5 $t_{1/2,^{26}\mathrm{Al}} \lesssim t_{\mathrm{form}} \lesssim 1.75\, t_{1/2,^{26}\mathrm{Al}}$, with a peak at $\sim$1 Myr after CAIs.
  - The grain size a_0 controls the rate of melt transport and thus whether a planetesimal with sufficient heating evolves toward a melt segregated structure. Below $a_0 \lesssim 0.1$ mm no segregation occurs, above $a_0 \gtrsim 1$ mm segregated structures form.
  - The solid-melt density contrast $\Delta\rho$ is of secondary importance, but can enhance melt segregation in the regime transition from a_0 = 0.1 mm to 1 mm.

In the mid-term, future spacecraft missions (A'Hearn, 2017) may be able to deliver further observational constraints on asteroid-belt objects. In conjunction with self-consistent evolutionary models of

metal-silicate and solid-melt segregation, these can help to further decipher the interior evolution of planetary bodies in the early Solar system and sharpen our understanding of terrestrial planet formation.

5.7 SUPPLEMENTARY MATERIAL

Supplementary material for this article is linked to at arXiv:1802.02157. The associated video file (arXiv version v1) shows a comparison between *magma ocean* and *magma sill* end-member models. Magma ocean stages are indicated in yellow. The *H3* annotation describes the heating value below which radiogenic heating from ^{26}Al is inefficient. Shown are various parameters for both models, from left to right: melt fraction φ, temperature T, radiogenic heating H, melt/liquid upwelling velocity w_{liq}, composition fraction of liquid $c^{\mathrm{i}}_{\mathrm{liq}}$, and composition fraction of solid $c^{\mathrm{i}}_{\mathrm{sol}}$. The composition is broken-down into the defined pseudo-components fsp, pxn, and olv. The model is started (= planetesimal formation time) at 0.9 Myr after CAIs.

ACKNOWLEDGMENTS TL was supported by ETH Zurich Research Grant ETH-17 13-1 and acknowledges partial financial support from the Swiss Society for Astrophysics and Astronomy trough a MERAC grant and from the National Center for Competence in Research PlanetS supported by the Swiss National Science Foundation. TK acknowledges financial support from Jenny Suckale, Stanford University. TK and RFK received funding from the European Research Council under the European Union's Seventh Framework Programme (FP7/2007–2013)/ERC grant agreement number 279925. The numerical simulations in this work were performed on the EULER computing cluster of ETH Zürich, and were analyzed using the open source software environments MATPLOTLIB[2] and SEABORN[3].

2 matplotlib.org (Hunter, 2007)
3 seaborn.pydata.org

Part III

IMPLICATIONS FOR PLANET FORMATION AND EVOLUTION

I use the derived SLR distribution across planetary systems and the time scales for planetesimal evolution from the previous chapters to constrain and predict planet formation in the Solar system and extrasolar systems. In particular, in combination with geochemical data from chondrites – the least altered meteorites – I constrain the accretion dynamics and reprocessing of the solid material during the first few million years of the Solar system. I find that the current major accretion paradigm of terrestrial planet growth is inconsistent with the chemical signature of chondritic meteorites. In particular, this suggests that the material in chondrites must be distinct from the material that accreted to form the terrestrial planets in the Solar system, which is in contrast with the classical idea of chondrites being the major building material of the planets. In addition, these inferences allow me to draw conclusions on the nature of precursor families to the asteroids that we observe today in the asteroid main belt and thus the planet formation dynamics in the early Solar system. As a final step, I model and predict the anticipated effects of the initial SLR abundances in planetary systems on the volatile budget in terrestrial planets in planetary systems in general. I show that the intense heat from SLRs dehydrates planetesimals during accretion, which substantially desiccates the rocky planets built from this material. These inferences establish that the planet formation process in planetary systems with and without substantial ($\gtrsim$ Solar) levels of SLRs should differ qualitatively. In particular, planetary systems with SLRs tend to form drier planets that are more closely Earth-like in composition, rather than with excess water abundances, which are predicted for planetary systems with negligible SLR abundances.

6

IMPACT SPLASH CHONDRULE FORMATION DURING PLANETESIMAL RECYCLING

The content of this section was published as: Lichtenberg, T., G. J. Golabek, C. P. Dullemond, M. Schönbächler, T. V. Gerya, and M. R. Meyer (2018). "Impact splash chondrule formation during planetesimal recycling." Icarus 302, 27–43. doi: 10.1016/j.icarus.2017.11.004. arXiv: 1711.02103.

ABSTRACT

Chondrules, mm-sized igneous-textured spherules, are the dominant bulk silicate constituent of chondritic meteorites and originate from highly energetic, local processes during the first million years after the birth of the Sun. So far, an astrophysically consistent chondrule formation scenario explaining major chemical, isotopic and textural features, in particular Fe,Ni metal abundances, bulk Fe/Mg ratios and intra-chondrite chemical and isotopic diversity, remains elusive. Here, we examine the prospect of forming chondrules from impact splashes among planetesimals heated by radioactive decay of short-lived radionuclides using thermomechanical models of their interior evolution. We show that intensely melted planetesimals with interior magma oceans became rapidly chemically equilibrated and physically differentiated. Therefore, collisional interactions among such bodies would have resulted in chondrule-like but basaltic spherules, which are not observed in the meteoritic record. This inconsistency with the expected dynamical interactions hints at an incomplete understanding of the planetary growth regime during the lifetime of the solar protoplanetary disk. To resolve this conundrum, we examine how the observed chemical and isotopic features of chondrules constrain the dynamical environment of accreting chondrite parent bodies by interpreting the meteoritic record as an impact-generated proxy of early Solar system planetesimals that underwent repeated collision and reaccretion cycles. Using a coupled evolution-collision model we demonstrate that the vast majority of collisional debris feeding the asteroid main belt must be derived from planetesimals that were partially molten at maximum. Therefore, the precursors of chondrite parent bodies either formed primarily small, from sub-canonical ^{26}Al reservoirs, or collisional destruction mechanisms were efficient enough to shatter planetesimals before they reached the magma ocean phase. Finally, we outline the window in parameter space for which chondrule formation from planetesimal collisions

can be reconciled with the meteoritic record and how our results can be used to further constrain early Solar system dynamics.

6.1 INTRODUCTION

Chondrules are igneous-textured spherules, typically 0.1–2 mm in diameter, and largely composed of the silicate minerals olivine and pyroxene. They are abundantly found in chondritic meteorites, together with other disk materials, such as CAIs and the fine-grained matrix that includes presolar grains and primitive organics (Scott and Krot, 2014). Chondrules are often surrounded by or close to beads of Fe,Ni metal (e.g., Wasson and Rubin, 2010; Jones, 2012) and show specific features, such as high abundances of moderately volatile elements like Na, K and S (Alexander et al., 2008; Scott and Krot, 2014; Connolly and Jones, 2016) and diverse chemical and isotopic signatures (Jones and Schilk, 2009; Hezel and Palme, 2010; Olsen et al., 2016). Their peak temperatures were $\sim$ 1900 K or higher (Alexander et al., 2008; Connolly and Jones, 2016) with subsequent cooling in minutes to days (e.g., Hewins, Zanda, and Bendersky, 2012; Desch et al., 2012; Wick and Jones, 2012). Most chondrules were formed during the earliest phases of the Solar system within the first 3–4 million years after the formation of CAIs (e.g., Villeneuve, Chaussidon, and Libourel, 2009; Connelly et al., 2012) and show clear evidence for multiple melting cycles (Rubin, 2017, and references therein).

Because of their enigmatic features coupled with high-energy processing, chondrule formation is considered to be intimately linked to the physical processes in the protoplanetary disk or planetary accretion and spawned a multitude of proposed formation mechanisms. The often underlying view of how chondrules are intertwined with the planet formation process is that they were formed before accretion and therefore represent the fundamental building materials of the planets and asteroids (Connolly and Jones, 2016). In this case, chondrules are formed before parent body accretion, either by melting dust aggregates by nebular shocks (Desch and Connolly, 2002; Morris and Desch, 2010; Morris, Weidenschilling, and Desch, 2016), for example related to global disk instabilities (Boss and Durisen, 2005; Lichtenberg and Schleicher, 2015), or condensation of melts and crystals (Blander et al., 2004; Nagahara et al., 2008). In contrast, if chondrules formed via processes involving already formed planetesimals, the interpretation of their role would shift to a 'by-product' of planet(esimal) formation (see discussion in Section 6.4).

Recently proposed chondrule formation scenarios considered melt spray from subsonic collisions ('splashes') between similar-sized planetesimals, which were fully melted by decay heat from ^{26}Al (Asphaug, Jutzi, and Movshovitz, 2011; Sanders and Scott, 2012) or impact 'jetting' via collisions of planetesimals with undifferentiated protoplan-

ets (Johnson et al., 2015; Hasegawa et al., 2016; Wakita et al., 2017). Collisional mechanisms were suggested previously and offer attractive solutions to many chondrule features (Krot et al., 2005; Sanders and Scott, 2012; Stammler and Dullemond, 2014; Dullemond, Stammler, and Johansen, 2014; Dullemond et al., 2016; Marrocchi et al., 2016). From a dynamical point-of-view, collisional interactions of planetesimals and embryos during accretion are inevitable and expected to create a vast amount of continuously reprocessed debris (Bottke et al., 2006; Carter et al., 2015; Jacobson and Walsh, 2015; Asphaug, 2017; Bottke and Morbidelli, 2017) that inherits the geochemical features from previous planetesimal generations.

Collisional models of chondrule formation considering fully-molten planetesimals, and thus highly energetic internal magma oceans with temperatures above the liquidus (Asphaug, Jutzi, and Movshovitz, 2011; Sanders and Scott, 2012), have the advantage that bodies interacting at low speeds ($\sim$ around the two-body escape velocity) can cause a melt spray ejection into the ambient disk medium that provides the inferred cooling regime for chondrules and the required solid densities to preserve primitive abundances of moderately volatile elements (Sanders and Scott, 2012; Dullemond, Stammler, and Johansen, 2014; Dullemond et al., 2016).

For consistency with the observed metal abundances in and around chondrules (Wasson and Rubin, 2010; Palme, Spettel, and Hezel, 2014; Connolly and Jones, 2016), droplet entrainment in a vigorously convecting magma ocean has been invoked to prevent efficient and complete metal-silicate segregation (Asphaug, Jutzi, and Movshovitz, 2011; Sanders and Scott, 2012; Asphaug, 2017). However, metal sequestration into the planetesimal core may have been rapid in magma ocean planetesimals as, for instance, supported by the old ages of iron meteorites (Kruijer et al., 2014). In this case, re-establishing post-collisional bulk Fe/Mg ratios and forming chondrites with metal beads would require a complicated and highly unlikely scenario of (i) partial oxidization of the metal cores of fully differentiated planetesimals and (ii) violent remixing of the remaining metal core material with mantle silicates during or after the collision (Palme, Hezel, and Ebel, 2015). Additionally, chemical (Jones, Grossman, and Rubin, 2005; Hezel and Palme, 2007; Palme, Spettel, and Hezel, 2014) and isotopic (Bauer et al., 2016; Olsen et al., 2016) heterogeneities between single chondrules of the same meteorite cannot be retained if vigorous convection at low silicate viscosities homogenized the bulk volume of primitive planetesimals down to chondrule-sized microscales.

However, it is well known that the interior evolution of planetesimals alone could create a diverse range of thermal histories and interior structures (e.g., Hevey and Sanders, 2006; Lichtenberg et al., 2016), where magma ocean planetesimals are only one end-member type. In addition, the structure and chemistry of planetary materials

was potentially further altered due to repeated collision–reaccretion cycles, which may generate varying thermal and chemical histories on a cm–m scale of planetary materials. Here, we probe the thermal and chemical evolution of such debris in a dynamical setting for the early Solar system, where small ($<$ 100 km) planetesimals were continuously formed over a given time frame during the lifetime of the circumstellar disk, evolved internally due to radiogenic heating, and were subsequently destroyed by collisions. To evaluate the thermal and chemical state of the debris over time, we quantify the processes governing metal-silicate segregation and chemical diversity within molten planetesimals and model their thermal histories dependent on their sizes and initial ^{26}Al abundances. To classify the parameter space that is (in-)consistent with chondrule formation from impact splashes among similar-sized planetesimals, we calculate the combined influence of interior evolution and collisional parameters in a simple Monte Carlo model. We describe our methodology in Section 6.2 and show the results from our scalings and computations in Section 6.3. We discuss our findings and the limits of our approach in Section 6.4, and draw conclusions in Section 6.5.

6.2 METHODS

6.2.1 *Scaling analysis*

This first part of our analysis aims to quantify the thermochemical processes governing the interior of planetesimals with high melt fractions above the rheological transition. The rheological transition of silicates describes the critical melt fraction $\varphi_{\mathrm{crit}} \sim$ 0.4–0.6 (Costa, Caricchi, and Bagdassarov, 2009) at which the silicate viscosity drops by orders of magnitude (from rock- to water-like behavior). At this range, the dynamic state of the system changes from solid-state creep processes to liquid-like convectional motions in an interior magma ocean. Here, we describe the processes in an idealized system that represents the end-member scenario of a planetesimal that has fully melted as a result of ^{26}Al decay.

6.2.1.1 *Metal-silicate segregation from Fe,Ni droplet rainfall*

For the case of a fully-molten planetesimal, we parameterize the rain-out of Fe,Ni metal droplets following the description by Solomatov (2015). The dynamic processes in the magma ocean are determined by its viscosity, which drops by orders of magnitude at the rheological transition $\varphi_{\mathrm{crit}} \sim$ 0.4–0.6 (Costa, Caricchi, and Bagdassarov, 2009), from $\eta \sim 10^{17}$ Pa s to 10^{-2} Pa s (Rubie et al., 2003; Liebske et al.,

Table 6.1: List of physical parameters used.

PARAMETER	SYMBOL	VALUE	UNIT	REF.
Density of uncompressed solid silicates	$\rho_{\mathrm{Si-sol}}$	3500	kg m^{-3}	(1,2)
Density of uncompressed molten silicates	$\rho_{\mathrm{Si-liq}}$	2900	kg m^{-3}	(1)
Density of uncompressed iron	ρ_{Fe}	7540	kg m^{-3}	(3)
Ambient temperature	T_0	290	K	(3,4)
Activation energy	E_{a}	470	kJ mol^{-1}	(5)
Dislocation creep onset stress	σ_0	$3 \cdot 10^7$	Pa	(6)
Power law exponent	n	4	non-dim.	(5)
Latent heat of silicate melting	L_{Si}	400	kJ kg^{-1}	(3,6)
Melt fraction at rheological transition	φ_{crit}	0.4	non-dim.	(8,9)
Silicate heat capacity	c_{P}	1000	J kg^{-1} K^{-1}	(6)
Thermal diffusivity	κ	$1 \cdot 10^{-6}$	m^2 s^{-1}	(6)
Thermal expansivity of solid silicates	$\alpha_{\mathrm{Si-sol}}$	$3 \cdot 10^{-5}$	K^{-1}	(2)
Thermal expansivity of molten silicates	$\alpha_{\mathrm{Si-liq}}$	$6 \cdot 10^{-5}$	K^{-1}	(2)
Thermal expansivity of iron	α_{Fe}	$1 \cdot 10^{-5}$	K^{-1}	(9)
Thermal conductivity of solid silicates	k	3	W m^{-1} K^{-1}	(10)
Thermal conductivity of molten silicates	k_{eff}	$\leq 10^6$	W m^{-1} K^{-1}	(11)
Min. unsintered silicate thermal conductivity	k_{low}	10^{-3}	W m^{-1} K^{-1}	(12,13)
Temperature at onset of hot sintering	T_{sint}	700	K	(12)
Peridotite solidus temperature	T_{sol}	1416	K	(14)
Peridotite liquidus temperature	T_{liq}	1973	K	(15)
Lower cut-off viscosity	η_{num}	10^{17}	Pa s	(16)
Silicate melt viscosity	η_{melt}	10^{-2}	Pa s	(17)
Droplet surface energy	σ	1	N m^{-1}	(18)
Chemical diffusivity of silicates	κ_{C}	10^{-8}	m^2 s^{-1}	(18)

References: (1) Stolper et al. (1981), (2) Suzuki, Ohtani, and Kato (1998), (3) Ghosh and McSween (1998), (4) Barshay and Lewis (1976), (5) Ranalli (1995), (6) Turcotte and Schubert (2014), (7) Costa, Caricchi, and Bagdassarov (2009), (8) Solomatov (2015), (9) Boehler, von Bargen, and Chopelas (1990), (10) Tarduno et al. (2012), (11) Golabek, Bourdon, and Gerya (2014), (12) Yomogida and Matsui (1984), (13) Henke et al. (2012b), (14) Herzberg, Raterron, and Zhang (2000), (15) Trønnes and Frost (2002), (16) Lichtenberg et al. (2016), (17) Liebske et al. (2005), (18) Rubie et al. (2003)

2005), as listed in Table 6.1. In melt regimes valid for planetesimals, the convective heat flux q of the magma ocean can be calculated via

$$q = 0.089k\frac{(T_{\mathrm{m}} - T_0)Ra^{1/3}}{D}, \tag{6.1}$$

with Rayleigh number

$$Ra = \alpha_{\mathrm{Si-liq}}g\rho_{\mathrm{ref}}\frac{(T_{\mathrm{m}} - T_0)D^3}{\kappa\eta}, \tag{6.2}$$

potential temperature T_{m}, ambient (and surface) temperature $T_0 = 290$ K, thermal diffusivity $\kappa = k/(\rho c_{\mathrm{p}})$, thermal conductivity of solid

silicates k, silicate heat capacity c_p, thermal expansivity of molten silicates $\alpha_\mathrm{Si-liq}$, depth of the magma ocean D, silicate densities

$$\rho_\mathrm{s} = \rho_\mathrm{sol} - (\rho_\mathrm{sol} - \rho_\mathrm{liq}) \cdot \varphi, \tag{6.3}$$

$$\rho_\mathrm{sol} = \rho_\mathrm{Si-sol} \cdot (1 - \alpha_\mathrm{Si-sol} \cdot [T - T_0]), \tag{6.4}$$

$$\rho_\mathrm{liq} = \rho_\mathrm{Si-liq} \cdot (1 - \alpha_\mathrm{Si-liq} \cdot [T - T_0]), \tag{6.5}$$

temperature T and thermal expansivity of solid silicates $\alpha_\mathrm{Si-sol}$. See Table 6.1 for the numerical values used. The convective velocities are then

$$v_\mathrm{s} \approx 0.6 \left(\frac{\alpha_\mathrm{Si-liq} g l q}{\rho_\mathrm{s} c_\mathrm{p}} \right)^{1/3}, \tag{6.6}$$

with gravity g, and mixing length $l \sim D \sim R_\mathrm{P}$. Based on laboratory experiments, it has been shown that droplets can be suspended (or re-entrained) by the convective flow if their diameter is

$$d \leq \frac{\rho_\mathrm{s} (v_\mathrm{s} / x_*)^2}{0.1 (\rho_\mathrm{m} - \rho_\mathrm{s}) g}, \tag{6.7}$$

with metal density

$$\rho_\mathrm{m} = \rho_\mathrm{Fe} \cdot (1 - \alpha_\mathrm{Fe} \cdot [T - T_0]), \tag{6.8}$$

thermal expansivity of iron α_Fe and constant factor $x_* = 60$ (Solomatov, 2015). Metal droplets suspended in the magma tend to be drawn together into spherical droplets, minimizing their surface area. Their stability is determined by the ratio between the stagnation pressure and the internal pressure caused by surface tension, given by the Weber number We, which can be used to estimate the expected sizes of droplet diameters

$$d = \frac{\sigma \cdot We}{(\rho_\mathrm{m} - \rho_\mathrm{s}) v_\mathrm{s}^2}, \tag{6.9}$$

with surface energy σ, where $We \leq 10$ is the stability threshold (Rubie et al., 2003). For a given depth of the magma ocean $D \sim R_\mathrm{P}$, melt fraction φ, and the numerical values listed in Table 6.1, we can determine the ratio of the expected droplet sizes and the upper limits for suspension (Section 6.3.1, Figure 6.3). The expected droplet size must be smaller than the upper limit for suspension for the droplets to be entrained in the flow and resist rain-out onto the planetesimal core.

6.2.1.2 *Chemical equilibration via turbulent diffusion*

Metal-silicate separation via the rainfall mechanism is not the only process that shapes the interior dynamics of a fully-molten planetesimal. Chemical and nucleosynthetic heterogeneities, inherited from the solar nebula prior to planetesimal formation, can be erased by

large-scale convective mixing once the silicate rheology transitions to fluid-like behavior. In addition to planetesimal-scale mixing, chemical diffusion (Rubie et al., 2003) from dissipation of turbulent energy down to the so-called Kolmogorov microscales affects chondrule- and grain-sized regions – the precursor material for chondrules in the splashing model. The time scale at which neighboring cells achieve such microscale chemical equilibration can be estimated via the local diffusion time scale

$$t_{\mathrm{eq}} = l_{\mathrm{K}}^2 / \kappa_{\mathrm{C}}, \tag{6.10}$$

with the Kolmogorov length scale l_{K} and the chemical diffusivity κ_{C} (Table 6.1). The Kolmogorov length scale is given as

$$l_{\mathrm{K}} = \left(\frac{\eta_{\mathrm{melt}}^3 D}{\rho_{\mathrm{Si-liq}}^3 v_{\mathrm{s}}^3} \right)^{1/4}, \tag{6.11}$$

with the viscosity of the magma ocean η_{melt}, the density of molten silicates $\rho_{\mathrm{Si-liq}}$ and v_{s} the convection velocity in the magma ocean calculated from Equation 6.6. Like in the section before, we choose to approximate the magma ocean length scale D with the planetesimal radius R_{P}, because in turbulent systems the dissipation rate at the smallest scales is primarily determined by the length scale of total kinetic energy in the turbulent motions; that is, the planetesimal radius in the case of a fully-molten magma ocean planetesimal. Using these scalings, we compute the time scales for diffusion, dependent on the radius of the planetesimal and the silicate viscosity.

In addition, we plot the time scales for collisions between similar-sized objects (Asphaug, 2010) in a planetesimal collision setting using

$$t_{\mathrm{coll}} = \frac{2R_{\mathrm{P}}}{\Delta v} \tag{6.12}$$

with the impact velocity Δv. Using the parameters given in Table 6.1, we derive scalings for various melt fractions, planetesimal radii and impact velocities, which are displayed in Figure 6.4 (Section 6.3.1).

6.2.2 *Thermomechanical evolution of planetesimals*

To bring the former calculations into context, we now consider the time-dependent interior evolution of planetesimals participating in potential chondrule-forming collisions in the early Solar system. To do so, we model their thermomechanical histories using two-dimensional fluid dynamics simulations employing a conservative finite-differences fully-staggered grid formulation (Gerya and Yuen, 2003, 2007). The numerical model is described in detail in Golabek, Bourdon, and Gerya (2014) and Lichtenberg et al. (2016, and references

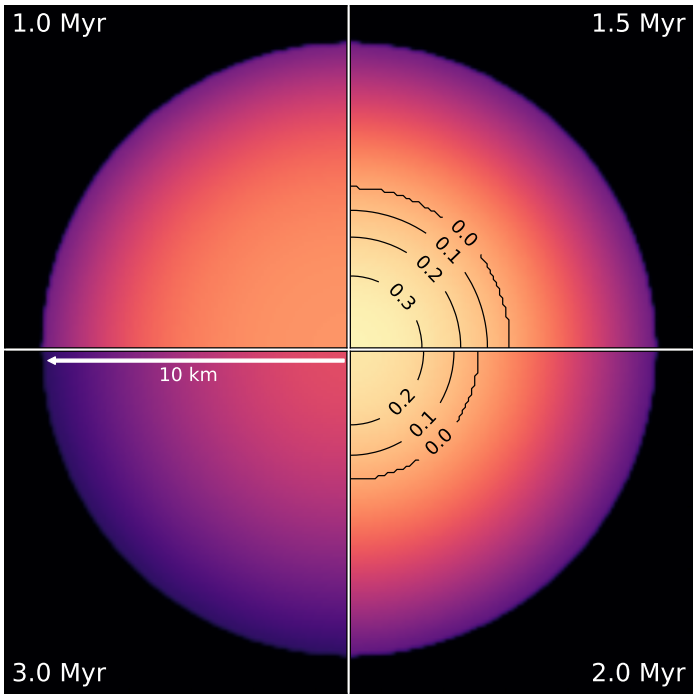

Figure 6.1: Thermal evolution of a planetesimal that is 10 km in radius and formed at 0.5 Myr after CAIs in our 2D cylinder geometry models. Silicate melt fractions are indicated with black isolines, and the temperature color scale ranges linearly from ∼290 K (black) to ∼1650 K (bright yellow).

therein), which is why we only briefly summarize its main characteristics here. The code solves the continuity, Stokes and location-dependent Poisson equation for self-gravity of material together with the energy equation, which includes source terms for radiogenic, shear and latent heat production. Physical properties are advanced using Lagrangian markers to minimize numerical diffusion and capture sharp viscosity and temperature gradients. To account for the Solar system-specific ^{26}Al heating term (Lichtenberg, Parker, and Meyer, 2016), the so-called 'canonical' abundance of $^{26}\mathrm{Al}/^{27}\mathrm{Al} = 5.25 \cdot 10^{-5}$ at CAI formation (Kita et al., 2013) is adopted.

The silicate melt is parameterized according to a peridotitic composition, taking into account both consumption and release of latent heat. For melt fractions $\varphi \geq 0.4$ the convective heat flux is approximated using the soft turbulence formulation (Kraichnan, 1962; Siggia, 1994). All our models incorporate an initial macroporosity (inverse filling-factor) of $\phi_{\mathrm{init}} = 0.3$, where sintering and compaction effects are parameterized using constraints from laboratory experiments (Henke et al., 2012b; Gail, Henke, and Trieloff, 2015).

The numerical models were run using a two-dimensional infinite cylinder geometry on a Cartesian grid, starting from ambient temperature of $T_0 = 290$ K, as for such small bodies accretionary heat

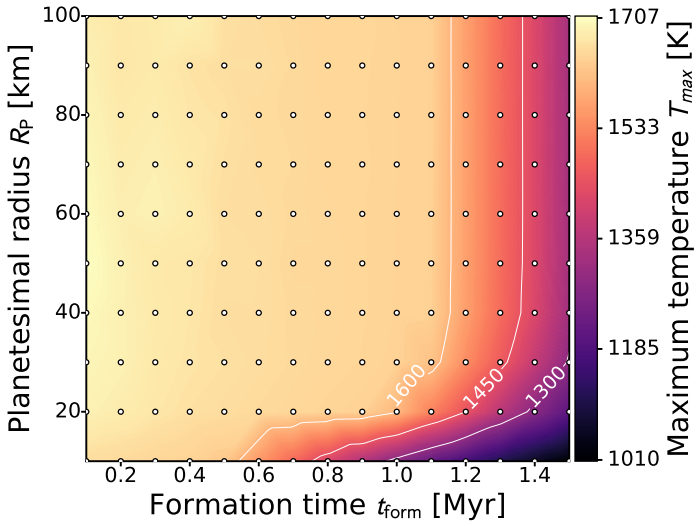

Figure 6.2: Maximum temperatures $T_{\max}$ reached within planetesimals of radius R_{P} and formation time t_{form}. Small planetesimals below 20–30 km in radius reach significantly lower temperatures than larger bodies for a given formation time.

is insignificant (Schubert, Spohn, and Reynolds, 1986; Elkins-Tanton, Weiss, and Zuber, 2011), and are surrounded by a low-density and low-viscosity layer of 'sticky air' that serves as heat sink (Schmeling et al., 2008; Crameri et al., 2012). The parameter space investigated spans the regime of R_{P} = 10–100 km in steps of 10 km, and t_{form} = 0.1–1.5 Myr after CAIs in steps of 0.1 Myr, the potential formation time interval of chondrule precursor material (Luu et al., 2015). Illustrations of the two-dimensional temperature and melt fraction evolution for a single simulation and the entire simulation grid are shown in Figure 6.1 and Figure 6.2, respectively. Further visualizations and analyses of the major qualitative regimes of the time-dependent thermal and density evolution are shown in Lichtenberg et al. (2016).

Importantly, our model utilizes a scaling for the cooling of a low-viscosity magma ocean, in which the effective thermal conductivity across finite-difference nodes is given as

$$k_{\mathrm{eff}} = (q/0.089)^{3/2} \cdot \frac{\alpha_{\mathrm{Si-liq}} g c_{\mathrm{p}}}{\Delta T^2 \rho_{\mathrm{s}} \eta_{\mathrm{num}}} \tag{6.13}$$

with the convective heat flux q, the temperature difference across the nodes ΔT, the silicate density ρ_{s}, the thermal expansivity $\alpha_{\mathrm{Si-liq}}$, gravity g, and the lower cut-off viscosity $\eta_{\mathrm{num}} = 10^{17}$ Pa s. This effective heat flux numerically approximates the increased heat flux during magma ocean stages and results in a more effective cooling of regions which are subject to the highest temperatures (Hevey and Sanders, 2006; Lichtenberg et al., 2016). We use these interior evolution models to determine the time-dependent thermal structure of the planetesimals together with the scalings from Section 6.2.1.1 and

6.2.1.2 to evaluate which parts of their interior can be eligible as chondrule precursor bodies at a given time after the formation of CAIs.

6.2.3 *Evolution-collision model*

The evolution of the precursor bodies is important to understand the energetic state and evolution of the silicates before the chondrule forming impact event. However, if the planetesimal body is not *fully* molten ($\varphi < \varphi_{\rm crit}$), the impact energy is necessary to elevate the silicate temperatures to above the chondrule formation temperature of $T_{\rm chondrule} \geq 1900$ K and eject the molten material from the two bodies. When material is freed from the colliding bodies during the impact, it is first compressed by the impact shock wave and then decompressed after ejection. By this process, fractions of the lithostatic/hydrostatic pressure within the planetesimal are converted into surface energy of magma (chondrule) droplets (Asphaug, Jutzi, and Movshovitz, 2011; Asphaug, 2017). In order to produce a melt spray that is consistent with the thermal histories of chondrules, at least parts of the material must have been heated to $T_{\rm chondrule} \geq 1900$ K (Alexander et al., 2008; Connolly and Jones, 2016) and subsequently cool down in an emerging droplet cloud of high density (Dullemond, Stammler, and Johansen, 2014; Dullemond et al., 2016).

In order to demonstrate the influence of the pre-collision state on chondrule thermal histories and the post-collision energy distribution, we have developed a Monte Carlo approach. The *a priori* assumption for this model is that planetesimals collide continuously during 0–5 Myr after CAI formation. Furthermore, when bodies collide, they generate debris and new planetesimals may be created from this material. For the moment, bodies from primordial and reaccreted material are treated the same, i.e., the material does not have a chemical 'memory' of prior generations. We discuss these and other assumptions in Section 6.4.

We start by randomly generating planetesimals in agreement with a radius power law

$$\mathrm{d}N/\mathrm{d}R_{\rm P} \propto R_{\rm P}^{-q}, \tag{6.14}$$

with the number of bodies N and power law index $q = 2.8$, consistent with shearing-box simulations of the streaming instability mechanism (Johansen et al., 2015; Simon et al., 2016, 2017). Using this power law, we generate integer radii $R_{\rm P} \geq R_{\rm P,min}$ according to

$$R_{\rm P} = ||R_{\rm P,min}(1 - x_{\rm rand})^{-1/(q-1)}||, \tag{6.15}$$

with the minimum planetesimal radius in our parameter space $R_{\rm P,min}$ = 10 km and pseudo-random number $x_{\rm rand}$ = 0–1. Depending on the regime chosen ($R_{\rm P,max}$ = 20, 30, 50, 100 km) we accept or reject radii

exceeding the upper limit value, resulting in an approximate power law distribution.

Following the approach of Wetherill and Stewart (1993) (as described in Morbidelli et al., 2009, Supplementary Material therein), we build a normalized collision probability distribution of pair-encounters for the generated planetesimals during a time step δt using

$$\hat{N}_{\mathrm{c,ij}} = N_{\mathrm{i}} N_{\mathrm{j}} F_{\mathrm{g,ij}} (R_{\mathrm{i}} + R_{\mathrm{j}})^2, \tag{6.16}$$

with bodies of different sizes i and j with their respective numbers N_{i} and N_{j} and radii R_{i} and R_{j} and gravitational focusing factor $F_{\mathrm{g,ij}} \approx 1$ for the velocity dispersions chosen here. Next, we sample the collision probability distribution using a linear alias method to return $N_{\mathrm{P,tot}}/2$ collision pairs ij, where $N_{\mathrm{P,tot}}$ is the total number of bodies in the generated planetesimal family.

Each planetesimal in each collision pair is randomly assigned a formation time t_{form} = [t_{min}, t_{max}], with t_{min} = 0.1 or 0.5 Myr, and t_{max} = 1.5 Myr. Additionally, we investigated a parameter space where t_{min} and t_{max} varied with collision time $t_{\mathrm{collision}}$, such that t_{min} = $t_{\mathrm{collision}}$ - Δt, where Δt = 0.5 or 0.7 Myr (but t_{min} = 0.1 Myr at minimum and t_{min} = 1.0/0.8 Myr at maximum) and t_{max} = 1.5 Myr. Naturally, the maximum formation time was limited to $t_{\mathrm{collision}}$ in case $t_{\mathrm{collision}} < t_{\mathrm{form,max}}$ = 1.5 Myr. The collision pair is assigned a randomized impact angle θ = [35, 55]$^\circ$ and a collision velocity Δv = 0.5, 1.0, 1.5 or 2.0 km/s, according to the specific setting. The different parameter choices are summarized in Table 6.2.

Table 6.2: Parameters for the Monte Carlo collision model with the maximum radius of a planetesimal family $R_{\mathrm{P,max}}$, the earliest formation $t_{\mathrm{form,min}}$, the latest formation $t_{\mathrm{form,max}}$, the maximum planetesimal dwell time Δt and the velocity dispersion Δv. See text for details on the assumptions.

Parameter	Unit	Values
$R_{\mathrm{P,max}}$	km	20, 30, 50, 100
$t_{\mathrm{form,min}}$	Myr	0.1, 0.5
$t_{\mathrm{form,max}}$	Myr	1.5
Δt	Myr	0.5, 0.7
Δv	km/s	0.5, 1.0, 1.5, 2.0

We evaluate each collision, depending on the sizes (and therefore masses, assuming constant initial densities of ρ = 3500 kg/m^3) R_{i} and R_{j}, angle θ and impact speed Δv, employing the EDACM model of Leinhardt and Stewart (2012). If the outcome is super-catastrophic, defined as the mass of the largest intact remnant block after the collision being less than 0.1 of the combined mass, we calculate the thermal effect on the remnant material as described further below. We

note that the model of Leinhardt and Stewart (2012) has recently been challenged regarding the catastrophic disruption threshold. Movshovitz et al. (2016) argue for a lower threshold value than Leinhardt and Stewart (2012), thus our estimate for super-catastrophic break-up using the EDACM scaling can be seen as a conservative approach so that we do not overestimate the number of super-catastrophic collisions, and thus potential chondrule material.

For categorizing the collisional debris, we evaluate the thermal state and material properties of each planetesimal in a collision pair before the impact using a two-dimensional bilinear interpolation from the initial R_P-t_{form} parameter grid (see Figure 6.2 and Section 6.3.1) of the time-dependent numerical models described in Section 6.2.2. The injected energy from body i to j, $\Delta E_{ij} = E_{kin,i} - E_{pot,j}$, with the kinetic energy of impactor i, $E_{kin,i}$, and potential energy of target j, $E_{pot,j}$, is homogenized over the target volume via $\Delta E_{j,k} = (E_{kin,k}/E_{pot,j})\Delta E_{ij}$, where the target volume is sub-divided into n shells with energy $E_{pot,k}$. If the injected energy $\Delta E_{j,k}$ into a sub-volume of the target is greater than the energy needed to heat it to above the chondrule formation temperature $T_{chondrule}$, the material is categorized as post-collision liquid $\hat{V}_{pc,chondrule}$ ($T_{post} > T_{chondrule}$, Figure 6.9), normalized by the total debris volume of the colliding family of planetesimals. The necessary energy is given by

$$\Delta E_{chondrule,k} = [(T_{chondrule} - T_k) \cdot c_p + L_{Si} \cdot (\varphi_{chondrule} - \varphi_k)] \cdot m_k \tag{6.17}$$

with temperature T_k, minimal chondrule formation peak melt fraction $\varphi_{chondrule}$, latent heat of silicate melt L_{Si}, melt fraction φ_k and mass m_k of the specific sub-volume. If it does not reach $T_{chondrule}$, it is counted as $\hat{V}_{pc,residual}$, further subdivided into partially melted ($T_{chondrule} > T_{post} > T_s$, Figure 6.9) and unmelted material ($T_{post} < T_s$, Figure 6.9). If the material exceeded the defined melt fraction threshold for metal loss φ_{crit} (0.4, 0.5 or 0.6) before the collision, the sub-volume is counted as $\hat{V}_{pc,loss}$ ($\varphi_{pre} > \varphi_{crit}$, Figure 6.9). We re-do these steps for each planetesimal of each collision pair for all timesteps starting from 0.1 Myr (or 0.5 Myr, Supplementary figures) until 5 Myr after CAIs, where for each timestep a new 'collision family' is generated. For instance, for model setting t_{form} = [0.1, 1.5] Myr at time t = 0.8 Myr, the planetesimals in the colliding family were randomly drawn from a formation time interval t_{form} = [0.1, 0.8] Myr; at time t = 2.3 Myr from a time interval t_{form} = [0.1, 1.5] Myr. For model setting t_{form} = [$t_{collision}$- 0.5, 1.5] Myr at time t = 0.8 Myr, the planetesimals in the colliding family were randomly drawn from a formation time interval t_{form} = [0.3, 0.8] Myr; at time t = 2.3 Myr from a time interval t_{form} = [1.0, 1.5] Myr.

The approach outlined above has several simplifications. First, the intrinsic collision probability for bodies in the sampled planetesimal orbit is chosen to be

$$P_{\mathrm{ij}} = (\alpha_{\mathrm{v}} v_{\mathrm{ij}}) / [4Ha(\delta a + 2ae_{\mathrm{i}})] = \mathrm{const.}, \tag{6.18}$$

with the average collision velocity Δv, a constant depending on Δv ranging from $0.57 \leq \alpha_{\mathrm{v}} \leq 0.855$ (Wetherill and Stewart, 1993), the symmetrical mutual scale height H, the semi-major axis and width a and δa of the annulus and the mean eccentricity of projectiles e_{i}, is chosen to be constant. Therefore, we do not simulate a global source system of generated planetesimals that collide randomly. Rather, we *ab initio* assume planetesimals that formed according to the power law slope described above and collide in pairs with a probability given by the mutual geometric factor. In other words, pairs of massive planetesimals are favored due to their larger geometrical cross-section, but eventually all planetesimals generated from the size frequency distribution of planetesimals (SFD) do collide. Second, we consider only the simple cases of super-catas-tro-phic interactions. In fact, catastrophic, hit-and-run, erosive and accretionary interactions could have an influence as well (Asphaug, 2010). However, for the low-mass regimes coupled with the chosen impact velocities shown here, super-catastrophic or catastrophic impacts are important and may create the majority of the debris. Third, the injected energy ΔE_{ij} is assumed to fully go into disruption and heating energy of the target material.

We use this model to demonstrate the qualitative imprint of the pre-collision interior evolution state of the planetesimals on the collisional debris in Section 6.3.2 and discuss its implications in Section 6.4.

6.3 RESULTS

In this section we present the results of our models of the thermomechanical history of colliding bodies before the impact event (Section 6.3.1) and the outcome of the coupled evolution-collision scenario (Section 6.3.2).

6.3.1 *Thermo-mechanical-chemical evolution before the collision event*

Figures 6.3 and 6.4 show the results of our scaling analysis of fully-molten planetesimals. Figure 6.3 demonstrates that the characteristic sizes of Fe,Ni metal droplets for the expected dynamics in a planetesimal magma ocean do not allow for droplet suspension. The droplets grow to sizes larger than can be suspended by convection and will thus rapidly rain out onto the planetesimal center. Therefore, fully-

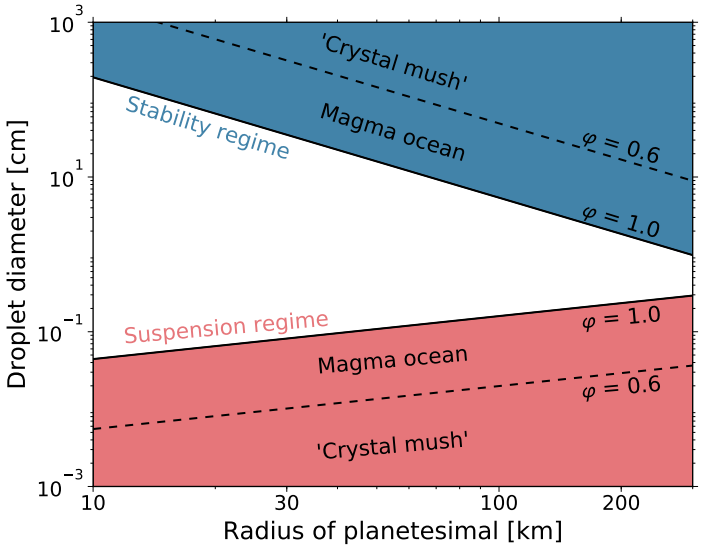

Figure 6.3: Droplet sizes of Fe,Ni metal versus planetesimal radius. The blue region ('stability'; Equation 6.9) shows the expected droplet sizes in fully-molten magma ocean planetesimals. The red region ('suspension'; Equation 6.7), in contrast, shows the maximum droplet sizes that can be entrained by vigorous convection for various melt fractions φ. Since the suspension limit never exceeds the stability criterion, metal droplets in fully-molten planetesimals efficiently segregate into the core. See text for details on the scalings. The considered planetesimal radius range here, and in Figure 6.4, corresponds to the birth-size frequency distribution of planetesimals (SFD) suggested by Johansen et al. (2015).

molten planetesimals rapidly evolved into a physically differentiated structure.

Figure 6.4 shows, first, that the time scale for chemical equilibration ($\sim$ hours to days) suggests a very fast homogenization of the material during magma ocean stages. In particular, it is much shorter than the lifetime of the protoplanetary disk (~ 3–$5 \cdot 10^6$ yr, Alexander et al., 2014), the thermo-mechanical evolution of planetesimal interiors ($\sim 10^5$–10^6 yr, Hevey and Sanders, 2006) and the collisional evolution of an accreting planetesimal swarm ($\sim 10^4$–10^5 yr, Wetherill and Stewart, 1993). Second, the chemical equilibration time scales for the cases we consider in this manuscript lie orders of magnitudes above the characteristic collision time scales. This suggests that the primordial chemical and isotopic heterogeneities inherited from prior to accretion were homogenized rapidly after reaching the magma ocean stage. However, the equilibration time scale is not fast enough to homogenize the interior during the collision if it remained below the rheological transition before the event, since the diffusion time scale is longer than the collision time scale by orders of magnitude.

Figures 6.5 and 6.6 show the time-dependent thermal structure of planetesimals due to their interior evolution from ^{26}Al heating. Fig-

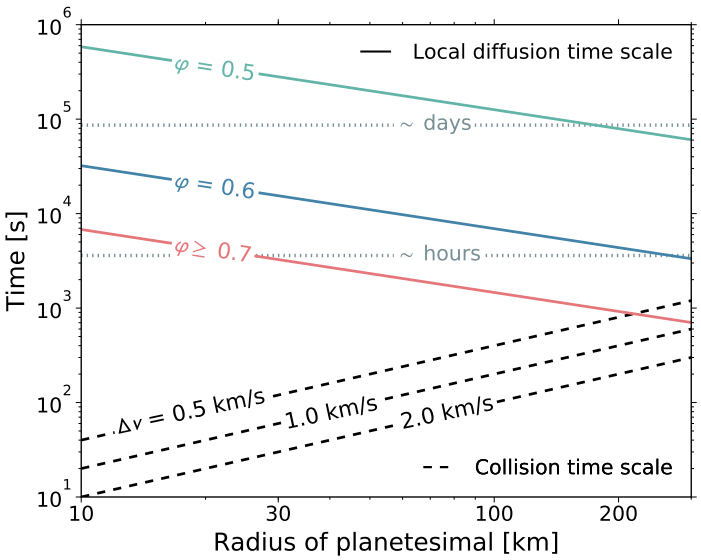

Figure 6.4: Radius of planetesimal versus time for either chemical equilibration (solid lines) or a planetesimal collision event (dashed lines). The solid lines ('local diffusion time scale', Equation 6.10) show the time scale for microscale chemical equilibration in a fully-molten magma ocean planetesimal for various silicate melt fractions φ. These are on the order of hours to days and thus demonstrate that fully-molten planetesimals rapidly chemically equilibrated. Therefore, any collisional debris from them would feature chemical signatures *unlike* chondrite material. The dashed lines ('collision time scale', Equation 6.12), in contrast, quantify the time it takes for an average collision of two similar-sized planetesimals to take place at various encounter velocities Δv. Up to several hundreds of km in radius, the diffusion (solid) and the collision (dashed) time scales differ by orders of magnitude. That means, if the planetesimal material was chemically unequilibrated (= *not fully-molten*) before a hypothetical impact splash event, the expanding magma plume could retain a chemically and isotopically heterogeneous signature – consistent with chondritic materials.

ure 6.5 shows the thermal evolution of one single model with internal melt fractions and in comparison the amount of melt produced within bodies of different sizes and formation times normalized to their total volume. In general, earlier formed and bigger planetesimals exhibited larger heating to cooling ratios, because the radiogenic heat source ^{26}Al decayed with $t_{1/2}$ = 0.72 Myr, and the surface-to-volume ratios shrank drastically with increasing size of the body. This means that the thermal evolution of the low-mass planetesimals was intrinsically time- and size-dependent. Importantly, a transient regime of silicate material with temperatures around the solidus (T_s = 1416 K) within planetesimals existed, which varied drastically with time and depth inside the bodies depending on the planetesimal sizes and formation times. Furthermore, low-mass bodies with radii

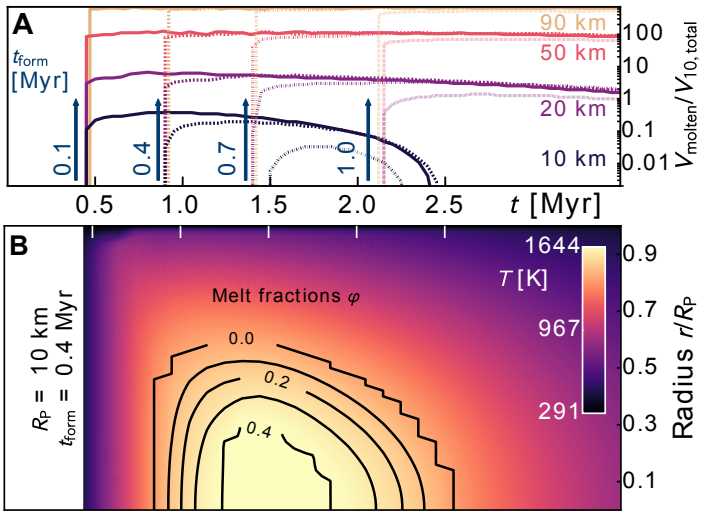

Figure 6.5: *(A)* Partially molten volume inside planetesimals over time, normalized by the total volume of a body with R_P = 10 km. The low-end mass tail of the planetesimals exhibited partially molten states only during a short time interval, e.g., from 0.5–2.5 Myr (R_P = 10 km). Arrows indicate formation times of associated lines. R_P = 10 km bodies did not exhibit any melt for $t_{form} \geq 1.2$ Myr. *(B)* Depth-dependent temperature structure for a planetesimal with R_P = 10 km and t_{form} = 0.4 Myr. Partial melt fractions (isolines) were sustained for a time period of $\Delta t \sim 1.7$ Myr after the initial heat-up phase.

$R_P \sim 10$ km exhibited partially molten states only during a narrow time interval $t \sim$ 0.5-2.5 Myr after CAIs.

Figure 6.6 shows the maximum fractional volumes of planetesimal models that exceeded the critical melt fraction threshold φ_{crit}. These planetesimal sub-volumes likely underwent magma ocean stages accompanied by rapid metal-silicate separation and chemical equilibration, as described in Figures 6.3 and 6.4. In particular, early formed massive planetesimals above $\geq$ 30 km radius with $t_{form} \leq 0.9$ Myr after CAIs were intensely heated and major parts of their total volume experienced pervasive melting periods. There is, however, a large transition regime with planetesimals mostly experiencing partial melting throughout their interiors (the transition band from black to bright yellow in Figure 6.6). Planetesimals that formed later than ~ 1.0 Myr, or alternatively formed with $^{26}Al/^{27}Al \leq 1.8 \cdot 10^{-5}$, experienced only minimal melting episodes within the innermost parts of their interior.

As a transition to the coupled evolution-collision scenario in Section 6.3.2, Figure 6.7 parameterizes the required impact energy for a collision in the super-catastrophic limit. In an idealized scenario, the injected energy must be sufficient to, first, heat at least parts of the target body to the required temperatures and, second, disrupt most of the target body into small pieces. In this idealized view, the most energetically favorable source of material for producing chondrules

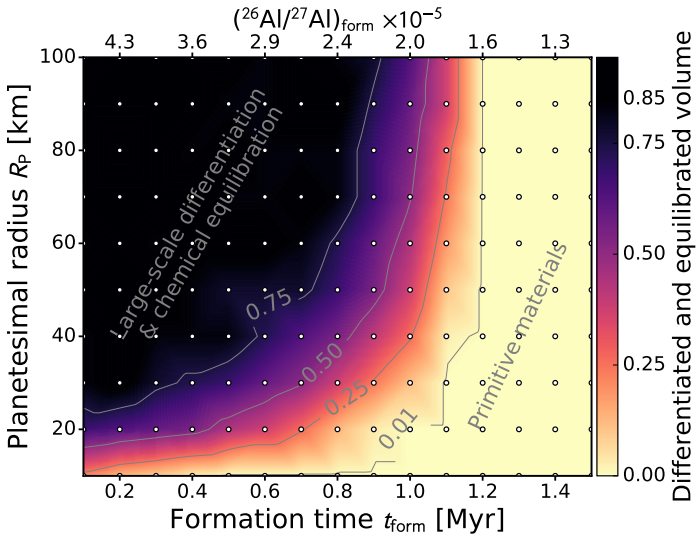

Figure 6.6: Volume of planetesimals that exceeded melt fractions of $\varphi \geq 0.4$ during the time interval t = 0.1–5 Myr after CAIs, normalized by the total volume of each body. The value at each dot represents the maximum volume fraction throughout a single numerical simulation with the indicated R_{P}-t_{form} combination. Especially planetesimals with $R_{\mathrm{P}} >$ 30 km and $t_{\mathrm{form}} \leq 0.9$ Myr after CAIs underwent large scale magma ocean periods and are therefore not eligible as chondrule precursor bodies. For reference, the ^{26}Al/^{27}Al ratio incorporated into a body at its formation time, for a disk-wide homogeneous ^{26}Al distribution, is shown at the top.

was the center of the target body, as it was hottest due to pre-heating from ^{26}Al.

Together with the melt fraction threshold for metal rain-out (φ_{crit}), this constrains the minimum required impact energy from a two-body encounter to produce chondrules in the collision (Figure 6.7). To give a simple example, under the assumption of perfect disruption and energy transfer between impactor and target, the minimal velocity necessary to achieve the critical chondrule formation temperature in the center of the target body is

$$\Delta v \geq \sqrt{\frac{2M_{\mathrm{tot}}}{m_{\mathrm{imp}}} \cdot \left(\Delta\varphi L_{\mathrm{Si}} + \Delta T c_{\mathrm{p}} - \frac{3GM_{\mathrm{tot}}}{5R_{\mathrm{tot}}} \right)},$$

with impactor mass m_{imp}, deviations from the required chondrule melt fraction $\varphi_{\mathrm{chondrule}} \sim$ 0.86 and temperature $T_{\mathrm{chondrule}}$ = 1900 K, $\Delta\varphi = \varphi_{\mathrm{chondrule}} - \varphi$ and $\Delta T = T_{\mathrm{chondrule}} - T_{\mathrm{center}}$, latent heat of silicate melting L_{Si} = 400 kJ/kg, pre-collisional material temperature at the target center T_{center}, silicate heat capacity c_{p} = 1000 J/(kg K), Newton's constant G, combined target-impactor mass M_{tot} and combined target-impactor radius R_{tot}. As an example, for the case of a super-catastrophic collision of two equally-sized planetesimals with R_{P} = 10 km and internal silicate temperature of T_{center} = 1600 K, which

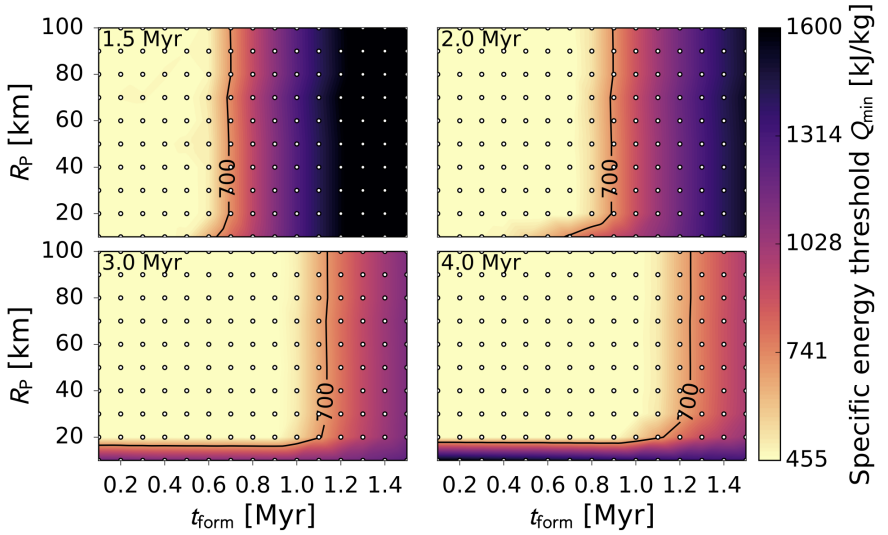

Figure 6.7: Evolution of the specific energy required at a given time t to raise the temperature in parts of the collisional debris to above the chondrule formation temperature: $T_{post} \geq T_{chondrule}$ = 1900 K. For this calculation, we assumed homogeneous energy injection across the entire target body. Importantly, the smallest bodies were sufficiently heated during the time interval $t \sim$ 1.5–3 Myr to require impact energies of $Q_{min} \sim$ 450 kJ per unit mass, after which they cooled down. The evolution of the 700 kJ/kg isocontour shows that until $\sim$ 2 Myr after CAIs small bodies required energies below this value, after 3 Myr after CAIs they required much higher energies to form chondrules.

translates to $\varphi = 1 - (T_{center} - T_{sol})/(T_{liq} - T_{sol}) \sim 0.33$, it would have required impact speeds of $\Delta v \sim$ 1.5 km/s to produce post-impact material with $T_{post} \geq T_{chondrule}$. With one of the two objects being more massive, the injected energy would have increased and thus lower impact speeds would have been sufficient to produce chondrule melt sprays. Still, this calculation and the required energies from Figure 6.7 define approximate estimates for the impact velocities required in our analytical expression in order to form chondrules from disruptive impacts. This yields roughly $\Delta v \sim$ 1 km/s and is thus presumably higher than the mutual velocities expected to arise from self-stirring of a small planetesimal swarm with radii of up to several tens of kilometers.

6.3.2 *Collisional processing*

To explore the effects of varying impact speeds on the planetesimal population, we developed a Monte Carlo approach to model the time-dependent influence of increased internal energies in the parent bodies on potential chondrule material in the collision aftermath (Section 6.2.3). The results from several simulation runs for planetesimal

swarms with R_{P} = 10–20 km are shown in Figure 6.8. In general, higher collision velocities increase the output of melt from the collision. For several cases (like in Figure 6.8A), the thermal evolution from ^{26}Al heating produced a peak in eligible chondrule material output for constant collision velocities at around $t \sim 2$ Myr. If planetesimals were allowed to form during the whole interval from t_{form} = 0.1–1.5 Myr (Figure 6.8A), the output of metal-free material became noticeable after $t \geq 0.7$ Myr. If the colliding families were preferentially formed at later time intervals, metal-free output became insignificant or virtually non-existent (Figure 6.8B,C and Supplementary figures). For bigger planetesimal regimes with radii up to 30, 50 or 100 km (Supplementary figures) this trend holds, while the output of chondrule forming material relative to material output with $T_{\mathrm{post}} < 1900$ K decreased.

It is important to note that the collisional debris showed a broad thermal distribution. Material from the inner parts of the body was heated to higher temperatures and thus higher melt fractions, whereas the outer parts of the colliding bodies may have remained cool and resulted in unmelted debris, which is not seen in chondritic meteorites. To address this issue, we have quantified the post-collisional thermal distribution for several parameter combinations and thus different collision families in Figure 6.9 (more in Supplementary figures). In order to 'suppress' the generation of a vast amount of differentiated material (which yields basaltic droplets unlike the chondrules observed in the meteoritic record, Asphaug, 2017) the make-up and dynamics of the colliding planetesimal swarm must be either (i) primarily composed of low-mass planetesimals, (ii) formed late, or (iii) feature a low dwell time before collisional recycling. The latter would correspond to a high encounter probability, which cools the material via total disruption, fragmentation or partial break-up (Ciesla et al., 2013).

The thermal distribution, and thus the ratios of melted, partially melted and unmelted debris, crucially depends on the localization of energy transfer during the collision. In our super-catastrophic model, however, in which the energy is distributed across the entire body, the pre-collision temperature solely determines the temperature deviations of the post-collision debris. Depending on the formation times, sizes and recycling efficiencies of the colliding planetesimals, the ratio of melted to unmelted debris may shift further (Supplementary figures).

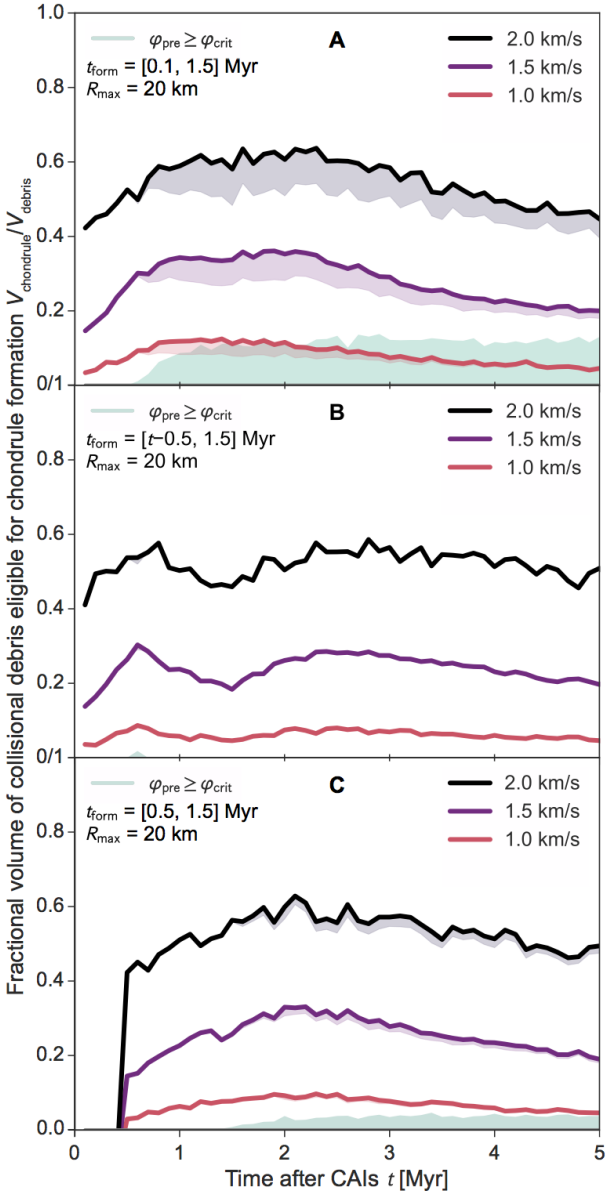

Figure 6.8: Output of chondrule-eligible collisional debris ($V_{\mathrm{chondrule}}$) with post-collision temperatures $T_{\mathrm{post}} \geq T_{\mathrm{chondrule}} = 1900$ K over time from randomized super-catastrophic collisions, normalized to the total volume of generated debris (V_{debris}). Each line in each subplot corresponds to a single Monte Carlo simulation with varying parameters. Black lines are runs with impact velocities $\Delta v =$ 2.0 km/s, purple lines $\Delta v =$ 1.5 km/s and red lines $\Delta v =$ 1.0 km/s. Shaded areas below these lines indicate the variation from using a different threshold for metal rain-out/chemical equilibration (φ_{crit}), with the lower bound φ_{crit} = 0.4 and the upper bound φ_{crit} = 0.5. Here, we consider bodies with R_{P} = 10–20 km and *(A)* t_{form} = 0.1–1.5 Myr, *(B)* t_{form} randomly drawn from the time interval Δt = 0.5 Myr before the collision time, and *(C)* t_{form} = 0.5–1.5 Myr. Green shaded areas show metal-depleted debris, that means, material originating from source regions with $\varphi \geq \varphi_{\mathrm{crit}}$ before the collision. The amount of metal-depleted material decreased significantly if collisional processing was efficient and the average dwell time of intact planetesimals was short *(B)*, or when planetesimal formation was suppressed during the early disk phase (*C*, Supplementary figures).

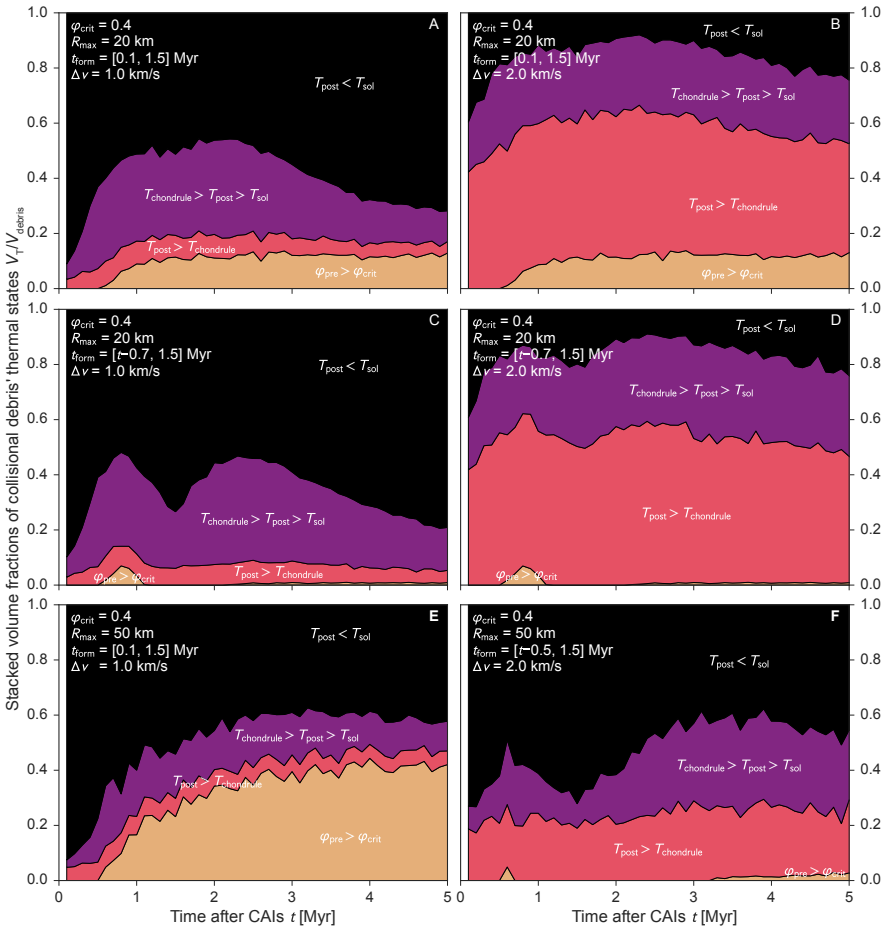

Figure 6.9: Thermal state of all post-collisional debris material over time for planetesimal swarms with R_P = 10–20 km *(A-D)* and R_P = 10–50 km *(E,F)*, metal preservation threshold criterion φ_{crit} = 0.4 and impact velocities of $\Delta v =$ 1 km/s *(A,C,E)* and $\Delta v = 2$ km/s *(B,D,F)*. Each subplot corresponds to a single Monte Carlo simulation. Different colors represent post-collisional material volume with varying thermal state, normalized to the volume of the total debris generated during continuous collisional recycling. The thermal distribution of the collision aftermath depended on the specific conditions during the impact, which can change the ratio of unmelted (black, $T_{post} < T_s$) to melted (purple, $T_{chondrule} > T_{post} > T_s$) debris and the output of chondrules (red, $T_{post} > T_{chondrule}$). Metal-depleted material (due to metal-silicate segregation prior to collision) is depicted in yellow ($\varphi_{pre} > \varphi_{crit}$). *(B,D,F)* all show eligible-chondrule material of $V_{chondrule}/V_{debris} =$ 0.2–0.5% throughout the time evolution. Subfigures *(C,D,F)* demonstrate the influence of a variable formation time interval in the model, representing an effective collisional grinding such that no bodies formed earlier than 0.7 Myr *(C,D)* or 0.5 Myr *(F)* before the collision time participate in the cycle. In the setting shown here, this generates some differentiated debris at $\sim$ 0.9 Myr *(C,D,F)*, but for the rest of the disk-phase prevented overheated material entering the debris cycles. *(E)* shows that larger planetesimal families readily reached debris states with a high fraction of differentiated debris (and potentially basaltic spherules as collision output). Importantly, we do not take the outcome from previous collision cycles into account, treating each time step as independent from the ones before. That implies that material labeled 'red' at $t =$ 1.0 Myr can become 'black' in the next time step and vice versa for all label mutations. See Supplementary figures for further parameter variations.

6.4 DISCUSSION

6.4.1 *Constraints from the interior evolution*

The scaling analysis performed in Section 6.3.1 (Figures 6.3 and 6.4) demonstrates that high melt fraction regions in radiogenically heated planetesimals rapidly evolve to physically differentiated and chemically equilibrated states. We note that the scalings used in this section are based on thermal driving forces and neglect potential other effects like magnetic fields (Scheinberg et al., 2015) or rotation (King et al., 2009; Maas and Hansen, 2015) that may alter the regimes. However, any potential changes to the convection regime within magma ocean planetesimals have two effects. If turbulence is less vigorous than derived here, Fe,Ni metal settling would be even more rapid, since the energy to suspend these droplets would decrease. In the opposite case, turbulence would be more vigorous and accelerates chemical equilibration, because the diffusion time scale derived from the Kolmogorov microscales diminishes. Therefore, we conclude that any planetesimals that can serve as eligible precursor bodies for chondrule formation in a collision event cannot have been fully-molten to above the rheological transition throughout a large fraction of their interior.

In general, it is important to note that the thermal evolution – and thus degree of differentiation and chemical homogenization – forms a continuum (Figures 6.5, 6.6 and 6.7; compare Lichtenberg et al., 2016). Therefore, the number of bodies that experienced substantial radiogenic preheating depends on the *local* planetesimal size frequency distribution, formation rate and recycling efficiency over time, in particular during the first 2 Myr after CAIs, during which the radiogenic heating from ^{26}Al was the predominant contributor to the internal evolution. From a thermomechanical point-of-view, the low-mass tail of planetesimals or bodies formed at sub-canonical ^{26}Al abundances (the transition region in Figure 6.6 and bodies labeled with 'primitive materials') barely incorporated enough ^{26}Al to reach temperatures near the solidus throughout most of their volume, and presumably never reached the rheological transition at melt fractions $\varphi_{\mathrm{crit}} \approx 0.4$–$0.6$ (Costa, Caricchi, and Bagdassarov, 2009) to develop an internal magma ocean (Lichtenberg et al., 2016).

Regarding the Fe,Ni metal abundances in and around chondrules, it is important to note that recent laboratory experiments demonstrated the trapping of metallic liquids in planetesimal mantles with low silicate melt fractions (Bagdassarov et al., 2009a; Rushmer and Petford, 2011; Holzheid, 2013; Cerantola, Walte, and Rubie, 2015; Todd et al., 2016). They showed that, first, in the regime below the silicate solidus, the high interfacial energy and wetting angle between metal-sulfide melts and solid silicate mantle minerals preclude ef-

ficient metallic core formation (Bagdassarov et al., 2009a; Rushmer and Petford, 2011). Second, it was shown that in the regime of modest silicate melt fractions, mobile basaltic melts reduce the interconnectivity and segregation of metal-sulfide liquids under deformation conditions with varying strain rates. This leaves some metallic liquid stranded in the olivine matrix until the rheological transition is reached (Holzheid, 2013; Cerantola, Walte, and Rubie, 2015; Todd et al., 2016). Above this threshold the silicate viscosity drops by orders of magnitudes and metal-silicate differentiation by gravitational settling becomes efficient (Figure 6.3 and Elkins-Tanton, 2012). From these experiments, we conclude that complete metal-silicate segregation in planetesimals required significant melt fractions, likely around and higher than the rheological transition. Therefore, small ($R_{\mathrm{P}} \sim$ 10–30 km) and/or late formed ($t_{\mathrm{form}} \geq$ 0.7–1.0 Myr after CAIs) planetesimals, with their presumably low melt fractions and thus incompletely differentiated interiors, can retain substantial metal abundances and chemical and isotopic heterogeneities distributed throughout most of the planetesimal volume. This qualifies these planetesimals as eligible chondrule precursor material.

Efficient collisional recycling of small or late-formed planetesimals is needed to produce large quantities of metal-bearing and chemically heterogeneous chondrules to populate the asteroid main belt with chondrite parent bodies. For that, planetesimals with modest internal melt fractions must have been abundant in the early Solar system. An additional source of chondrules may have come from larger planetesimals that experienced impacts in narrow time windows during their heat-up phase, when the radiogenic pre-heating was sufficient but before reaching the magma ocean phase. We have qualitatively summarized the thermomechanical planetesimal regime that may be capable of chondrule formation in the aftermath of a collision in Figure 6.10. The regime we propose as potential chondrule precursor bodies is highlighted in green. In general, small bodies or bodies with sub-canonical ^{26}Al abundances were more likely to be heated to suitable temperatures at around their thermal maxima and to not reach melt fractions above the rheological transition throughout most of their interiors. In comparison, larger bodies featured chondrule-eligible interior states only during their initial heat-up phases.

6.4.2 *Accretion and dynamical recycling*

The results from the evolution-collision model (Section 6.3.2, Figures 6.8, 6.9 and Supplementary figures) underline two points. First, planetesimals preheated by the decay of ^{26}Al require less energetic collisions than non-preheated bodies to produce chondrules in the collisional aftermath. If the bodies participating in the collision have not

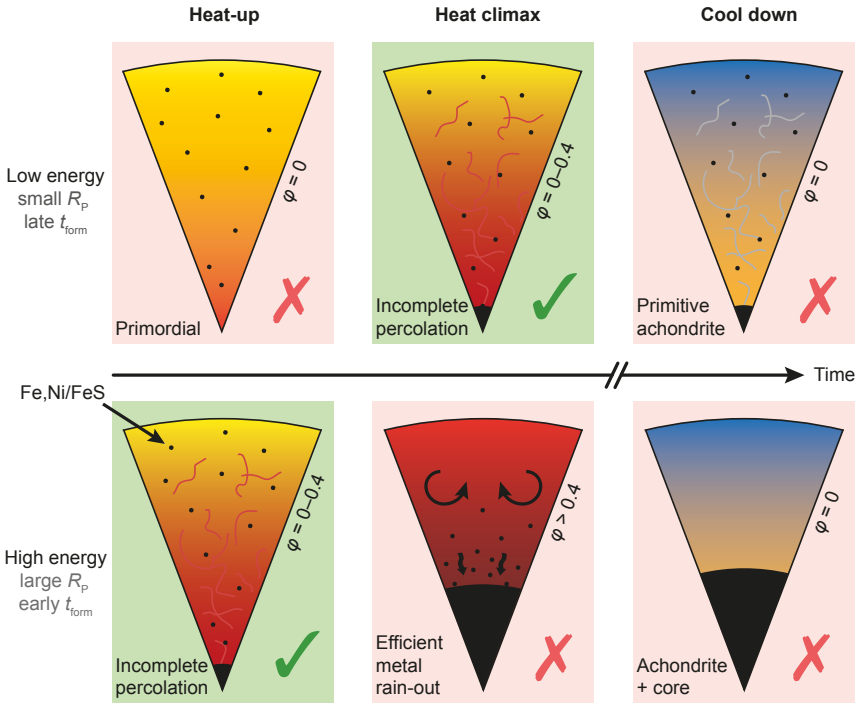

Figure 6.10: Schematic illustration of the qualitative thermomechanical planetesimal evolution regimes. *(Top)* Low-energy bodies with relatively small radii or late formation times, which were eligible chondrule precursor bodies (highlighted in green) around their heat climax (compare Figure 6.5 and Figure 6.7). *(Bottom)* High-energy bodies with either large radii or early formation times, which were eligible precursor bodies only during their brief initial heat-up phase. Models highlighted in red either do not feature high-enough radiogenic pre-heating (and thus would have needed implausible high impact velocities) or have lost their primordial metal abundances due to efficient metal-silicate segregation processes.

reached the magma ocean phase, droplets resulting from the impact can satisfy the constraints from chondrule textures, i.e., subsonic impact velocities in order to avoid shock textures in the resulting material (Asphaug, 2017). Therefore, we require velocities higher than the two-body escape speed but lower than for the case of cold planetesimals. Such velocities may be achieved during the gas disk phase (see further down). Second, Figure 6.9 and the additional figures for variable parameter regimes (Supplementary figures) demonstrate that the outcome of any collisional regime can be highly variable, depending on the local size frequency distribution (SFD), the internal state of the planetesimals and the dynamical regime of the swarm participating in the collisional processing. It underlines the necessity of simultaneously considering the *global* dynamical and *local* formation, growth and destruction mechanisms in astrophysical models of

planet formation in the early Solar system, which we therefore discuss here.

The first planetesimals likely formed according to a specific size frequency distribution (Johansen et al., 2007; Cuzzi, Hogan, and Shariff, 2008; Chambers, 2010; Simon et al., 2016). Recent planetesimal formation models can produce bodies via the streaming instability or turbulent concentration mechanisms within the first few million years in the solar nebula (Cuzzi, Hogan, and Shariff, 2008; Chambers, 2010; Carrera, Johansen, and Davies, 2015; Drążkowska, Alibert, and Moore, 2016; Schoonenberg and Ormel, 2017). Latest estimates of the initial SFD from the streaming instability mechanism (Johansen et al., 2015; Simon et al., 2016, 2017) converge on a power law $\mathrm{d}N/\mathrm{d}R_\mathrm{P} \sim R_\mathrm{P}^{-q}$, with the number of bodies N, the planetesimal radius R_P, index $q = 2.8$ and without an obvious lower cut-off. These estimates are consistent with the current distribution in the asteroid belt if accretionary growth of small bodies via collisions and/or pebble accretion is considered (Weidenschilling, 2011; Lithwick, 2014; Johansen et al., 2015; Morishima, 2017). In such a birth-SFD, the bulk of the mass resides in massive planetesimals, while the absolute number of low-mass planetesimals exceeds the number of massive bodies by orders of magnitude. Therefore, collisions among low-mass members of the SFD outnumber interactions with one or between two massive members, even if gravitational focusing is considered. This low-mass planetesimal collision regime was most vulnerable to disruption during collisions and thus presumably created much debris from hit-and-run, erosive or (super-)catastrophic interactions (Asphaug, 2010; Leinhardt and Stewart, 2012).

The collisional dynamics and, therefore, the prevailing impact parameters crucially depend on the ambient disk conditions and the nature of planet(esimal) growth (Wetherill and Stewart, 1989, 1993; Kokubo and Ida, 1996, 1998; Weidenschilling, 2011; Johansen et al., 2015). Importantly, in a growing planetesimal swarm the parameter dominating the mean impact velocity among bodies is the size of the largest body. The largest body stirs the velocity dispersion in the swarm to its own escape velocity and the smallest bodies reach the highest relative velocities (e.g., Schlichting and Sari, 2011). During the disk stage, the velocity dispersion can be highly reduced due to gas damping, which complicates reaching sufficient impact velocities to generate chondrule melts. This problem originally motivated the idea of chondrule formation from fully-molten planetesimals and the sole reliance on ^{26}Al as a heat source for chondrule formation (Asphaug, Jutzi, and Movshovitz, 2011; Sanders and Scott, 2012).

Therefore, producing chondrites as Nth generation planetesimals from the collisional recycling of radiogenically preheated but undifferentiated planetesimals required, first, continuous collisional reprocessing during the first few million years after the formation of

the Sun. Second, sufficient velocity dispersions above the mean two-body escape velocity of the lowest-mass members of the collisional planetesimal swarm ($v_{\rm esc} \lesssim 0.1$ km/s in the size regime evaluated here) must have been triggered. Potential stirring mechanisms to enable these enhanced mutual encounter velocities for low-mass planetesimals are manifold, for instance early formation of planetary embryos like Mars (Dauphas and Pourmand, 2011; Hasegawa et al., 2016), migration of giant planets (Walsh et al., 2011; Izidoro et al., 2016) and/or giant planets' forming cores (Raymond et al., 2016), resonant excitations (Weidenschilling, Marzari, and Hood, 1998) or implantation of planetesimals via scattering into the main belt region (Bottke et al., 2006). These mechanisms depend strongly on the ambient gas density and become more efficient as the solar nebula disperses over time, leading to decreased gas damping and allowing for higher mutual velocities.

The absolute volume of low-mass planetesimals in our Solar system was presumably minor compared to the material within massive bodies (Johansen et al., 2015; Simon et al., 2016). However, it was subject to most destructive collision events among planetesimals in terms of absolute numbers. Due to their larger cross-section and enhanced gravitational focusing, the largest bodies accreted the fastest and thus presumably accumulated to form the terrestrial planets in the inner Solar system (Wetherill and Stewart, 1989; Weidenschilling et al., 1997). The low-mass bodies were dynamically excited by the larger body-size population, which enhanced encounter rates. Depending on the planetesimal number and how they actually arrived at specific locations in the disk (for instance, in-situ formation versus implantation), the debris from low-mass collisions can dominate the total *local* solid density and provide the environment for the make-up of chondrite parent bodies as a result of collisionally recycled low-mass or sub-canonical-^{26}Al planetesimals.

Recent observations and theoretical considerations estimate that the solid pile-up within 'sweet spots' in inner disk regions facilitated planetesimal formation in confined bands (Drążkowska, Alibert, and Moore, 2016; Andrews et al., 2016; Isella et al., 2016; Schoonenberg and Ormel, 2017; Carrera et al., 2017). In such narrow planetesimal birth regions with high solid density, efficient collisional processing can be enhanced because of higher collisional cross-sections and average encounter rates compared to the classical picture of disk-wide planetesimal formation. In our model, collisions of chondrule-eligible planetesimals preferentially produced a chondrule formation peak at around $t \sim 2$ Myr after CAIs (Figure 6.8 and Supplementary figures). Although the exact timing depends on the parameter choice, this peak is in very good agreement with the radiogenic ages determined for chondrules in meteorites (Villeneuve, Chaussidon, and Libourel, 2009; Mishra and Chaussidon, 2014; Chaussidon and Liu, 2015,

see chondrule geochronology, Section 6.4.4). In our models, the peak reflects the temperature climax of planetesimals heated from ^{26}Al decay (as suggested in Sanders and Scott, 2012). Many chondrules may thus reflect collisional debris of low-mass and preheated planetesimals, whose material was not swept up by early oligarchs and survived in smaller bodies that comprise the asteroid belt today.

The asteroid belt today is significantly depleted in mass relative to the terrestrial and giant planet regions of the Solar system. Therefore, either the region was dynamically depleted early-on or the mass depletion must be primordial (Bottke et al., 2006; Walsh et al., 2011; Izidoro et al., 2016; Drążkowska, Alibert, and Moore, 2016; Morbidelli and Raymond, 2016). In the latter case, this may be a suitable environment for the kind of dynamical processing we propose here and the complex transition from S- to C-type asteroids (DeMeo et al., 2015). For instance, recent studies suggest early mixing of silicate and ice-rich planetesimals (Marrocchi et al., 2016). In this picture, planetesimals may either form in lower numbers in the asteroid belt region or can be implanted from inner and outer disk regions. Thus, they would originate from distinct source reservoirs, as was suggested for iron meteorites which may have formed pre-dominantly in the inner disk region (Bottke et al., 2006).

6.4.3 *Collision physics*

In general, a complicating issue for estimates of debris generation is that the effective amount of material excavated during the collision depends on a variety of impact parameters, such as the impact velocity, impact angle, mass ratio of the colliding bodies and material compositions (Leinhardt and Stewart, 2009; Asphaug, 2010; Leinhardt and Stewart, 2012; Movshovitz et al., 2016). In addition to the amount of material ejected during the collision, it is important to understand the energy distribution in the ejected fragments/droplets. This, in turn, determines the thermal histories of chondrules produced in the collision fragments (Figures 6.9 and Supplementary figures) and is crucially dependent on the energy localization during the impact, for which high-resolution three-dimensional numerical models are required. The derivation of scaling laws that account for the combined effects of ejecta size and energy distribution is a long-term goal of the impact modeling community (e.g., Ševeček et al., 2017). To our knowledge, at present there are no scaling laws that cover a large parameter space and can be used to couple the interior evolution of planetesimals prior to collision with the energy injection and material ejection during the collision.

Finally, we want to point out that, in the context of our semi-analytic evolution-collision model impacts usually require $\Delta v \gtrsim 0.5$ km/s to generate chondrule eligible material. However, using more advanced

numerical collision models utilizing more realistic energy localization together with a statistical or N-body growth model (e.g., Morbidelli et al., 2009; Schlichting and Sari, 2011; Carter et al., 2015; Johansen et al., 2015; Morishima, 2017) of the planetesimal swarm will enable much lower collision velocities. As demonstrated by Wakita et al. (2017), collisions among unheated planetesimals may already be close to generate chondrule eligible temperatures in the collision aftermath, therefore coupling both energy sources (collision and radiogenic heating) will be even more capable of producing the correct conditions.

6.4.4 *Geochemical perspective*

In this section we review some important geo- and cosmochemical constraints for the origin of chondrules and a potential collisional origin. Many interpretations of the chondrule record with respect to chondrule formation via collisions were already discussed in-depth by Sanders and Scott (2012) and partly in Connolly and Jones (2016). Even though these authors focused on fully-molten planetesimals as chondrule precursors, many of their interpretations also apply to the more moderate and realistic scenario of a radially heterogeneous interior evolution of colliding planetesimals that did not reach the magma ocean stage. Therefore, we will not repeat these arguments here, but instead focus on issues that emerged in recent years or are of direct consequence for our plead toward a more nuanced debate of collision models for chondrule formation.

Chondrule geochronology

Based on various radiometric dating techniques, chondrules formed during the first $\sim$ 4–6 Myr after CAIs (Scott and Krot, 2014; Chaussidon and Liu, 2015). The exact details, however, are debated. There is an on-going debate in the cosmochemical community as to whether ^{26}Al was heterogeneously distributed in the protoplanetary disk (Larsen et al., 2011; Schiller et al., 2015; Van Kooten et al., 2016; Kleine and Wadhwa, 2017). The consequences of a heterogeneous distribution are far reaching. In the following we discuss the implications for chondrule formation by collisions of preheated planetesimals for the case of (i) a homogeneous distribution, and (ii) a heterogeneous distribution.

(i) A homogeneous ^{26}Al distribution entails that precise Al-Mg ages of chondrules can be obtained and these indicate a time gap of Δt = 0.5–1.0 Myr between the formation of CAIs (at $t \sim 0$ Myr) and the onset of chondrule formation (Villeneuve, Chaussidon, and Libourel, 2009; Kita and Ushikubo, 2012; Nagashima et al., 2014; Chaussidon and Liu, 2015; Villeneuve, Libourel, and Soulié, 2015). In Section 6.4.2 we argued that the apparent peak in chondrule formation ages may be linked to the interior heat

climax of ^{26}Al-heated planetesimals. However, for some parameter combinations our models do not produce a gap during the first Myr after CAI formation. The apparent time gap between CAIs and chondrules could therefore reflect protracted planetesimal formation after CAIs (Figure 6.6) and thus reduced ^{26}Al inventories or alternatively insufficient debris ejection from collisions during the early phase of high gas-damping. Delayed planetesimal formation may be due to increasing dust-to-gas ratios with time due to photoevaporation (Johansen, Youdin, and Mac Low, 2009; Carrera et al., 2017). Decreasing ambient gas densities also allow for higher mutual velocities.

(ii) Based on a heterogeneous distribution of ^{26}Al in our Solar system, the cosmochemical record provides evidence for an extended period of chondrule formation, starting contemporaneously with CAI formation over 3–4 Myr (Larsen et al., 2011; Connelly et al., 2012; Schiller et al., 2015; Van Kooten et al., 2016; Connelly, Bollard, and Bizzarro, 2017). These results are inferred from Pb-Pb ages of individual chondrules. In this context, no gap needs to be reproduced, but the ^{26}Al inventory may be subcanonical everywhere in the disk except the CAI forming region. This would shift the thermomechanical regimes in Figure 6.6 but would still allow for substantial radiogenic preheating depending on the local inventory of ^{26}Al at the time of planetesimal formation or reaccretion.

Nucleosynthetic, chemical and petrographic constraints

Chemical and isotopic complementarity is a concept based on elemental and isotopic studies of chondrules and matrix. Various elemental and isotope compositions may be distinct in matrix and chondrules of a specific chondrite, but, when mixed together, complement each other to nearly CI-like composition (Bland et al., 2005; Hezel and Palme, 2008, 2010; Palme, Hezel, and Ebel, 2015; Ebel et al., 2016). This extends to W and Mo isotope variations derived from presolar carriers, which may also be complementary in 'matrix' (defined as fine-grained dust between chondrules) and chondrules (Becker et al., 2015; Budde et al., 2016a,b). These relations are often claimed to rule out particular chondrule formation mechanisms, such as a collisional origin of chondrules. Indeed, *if* complementarity of matrix and chondrules is real and indicates a genetic heritage linked by the chondrule formation process itself, this provides severe constraints on *every* chondrule formation mechanism suggested to date. The technical details and interpretations of the chondrule-matrix complementarity hypothesis are controversially debated in the community and out of the scope of this paper.

In recent years, it was found that terrestrial bodies in the Solar system exhibit distinct nucleosynthetic isotope signatures in, e.g., Zr (Schönbächler et al., 2011; Akram et al., 2015), Ni (Regelous, Elliott, and Coath, 2008; Steele et al., 2012), Cr (Trinquier, Birck, and Allègre, 2007; Trinquier et al., 2009; Olsen et al., 2016) and Mo (Burkhardt et al., 2011). How can this be reconciled with the collisional origin of chondrules we put forward in this manuscript? In any accretion scenario the most massive planetesimals and embryos preferentially served as the early precursors of the planets. Therefore, the most massive bodies were unavailable as meteorite parent bodies because they either seeded the planet formation processes themselves or preferentially interacted with the accreting protoplanets due to gravitational focusing and enhanced geometrical encounter rates. Since accretion mechanisms like planetesimal agglomeration or pebble accretion become less efficient for smaller bodies, debris from low-mass planetesimal collisions was presumably insufficient in mass to act as a seed for planet formation. In light of chondrule formation from collisions of low-mass planetesimals, chondrites can then be interpreted as left-over material, which did not end up in planets. Instead, it either formed small parent bodies by itself or was accreted onto other relatively low-mass bodies. This implies that the materials sampled in the meteoritic record were not important contributors to the chemical bulk planet compositions in the Solar system. Importantly, in this picture the chondrites sample qualitatively different material than represented in the Earth and the other terrestrial planets. This is consistent with nucleosynthetic signatures identified in meteorites, which are distinct from those of bulk Earth (Burkhardt et al., 2011; Akram et al., 2015; Palme and Zipfel, 2016).

In our model, age differences between chondrules of single chondrites can be attributed to, for instance, the storage of chondrules in outer parts of planetesimals, later liberation during disruption of the body and mixing with newly formed chondrules in the subsequent reaccretion of a new parent body. On the other hand, if age gaps in each chondrite group are narrow (as suggested by Alexander and Ebel, 2012) chondrule variability in a parent body can be obtained by mixing of debris ejecta from several chondrule-forming collisions in one annulus. Furthermore, most material eligible for chondrule formation, i.e., collisional debris, which is heated to $T_{\mathrm{post}} > 1900$ K (Connolly and Jones, 2016; Alexander et al., 2008; Villeneuve, Libourel, and Soulié, 2015) during one of the collisional cycles, not necessarily (fully) re-melts during the reprocessing. This allows chondrules to preserve relict grains – in agreement with the chondrule record (Jones, 2012) – and generates further chondrule diversity due to variable interaction of the ejected fragments with molten material and vapor in the impact plume (Villeneuve, Libourel, and Soulié, 2015). Moreover, each chondrite parent body sampled a distinct, isolated

reservoir without much mixing with those of other chondrite parent bodies (Jones, 2012). In the context of our model, this is a natural consequence if each chondrite parent body sampled a distinct band defined by the pile-up sweet spots for accretion (Drążkowska, Alibert, and Moore, 2016; Schoonenberg and Ormel, 2017; Carrera et al., 2017) or implantation (Bottke et al., 2006).

In our model, the ejection of material in the aftermath of the collision resulted in disconnected droplet clouds (Dullemond, Stammler, and Johansen, 2014; Dullemond et al., 2016). The collision time scale in Figure 6.4 (Section 6.3.1) is comparable to the time between the heat-up of a precursor body during the collision and the separation of single droplets in the collisional aftermath. As shown in Figure 6.4, this time scale is orders of magnitudes shorter than the local diffusion time scale of silicate material heated to high melt fractions, i.e., to the peak temperatures of chondrules. Therefore, the cooling droplets in the collisional aftermath preserved heterogeneous primordial nucleosynthetic signatures. Such distinct signatures are reported within chondrules of the same meteorite (Olsen et al., 2016; Bauer et al., 2016). As a further contribution, these variable chondrule signatures can also originate from different impact events, which were then mixed together during reaccretion in a subsequent accretion-collision cycle. Repeated thermal recycling of chondrules is also in line with recent studies of microchondrule formation (Bigolski et al., 2016).

In summary, we would like to emphasize that our results regarding the metal-silicate separation, chemical equilibration and the generation of variations among chondrules generally apply to both type I (FeO-poor) and type II (FeO-rich) chondrules. The presence of Fe,Ni metal varies between different chondrite groups (Davidson et al., 2014; Schrader et al., 2015) and the total amount of Fe,Ni metal within and in the vicinity of chondrules may be related to the oxygen and sulfur fugacity of the precursor body and the surrounding gaseous medium. Importantly, *any* Fe,Ni, FeS or chemical and isotopic heterogeneity present in precursor bodies before the chondrule-forming impact event would have been erased in planetesimals that experienced a magma ocean stage. As we have shown, however, it was possible to preserve these anomalies in (at maximum) partially molten precursor bodies that accreted from diverse nebular material.

6.4.5 *Further constraints and outlook*

Throughout this work we focused on geochemical and physical conditions for planetary materials *necessary* to retain abundant Fe,Ni metals, primordial isotopic and nucleosynthetic heterogeneities on a chondrule-size scale and to achieve the required peak temperatures for chondrule formation during planetesimal collisions. Further de-

tailed work – both from modelers and experimentalists – is needed to investigate the enigmatic nature of chondrules and its link to the environment in the early solar nebula. For instance, under which circumstances can the post-collision droplet clouds satisfy the thermal histories and moderately volatile element retention (e.g., Na and K) of chondrules (Alexander et al., 2008; Dullemond, Stammler, and Johansen, 2014; Dullemond et al., 2016), in case the thermal histories derived so far are reliable (Libourel and Portail, 2017)? Other important issues relate to, e.g., the prevalence of porphyritic textures among chondrules, varying chondrule distributions among different chondrite groups or the retention of relict grains. So far, there are only a few examples of chondrules that show strong experimental evidence for being generated by an impact (Krot et al., 2005; Marrocchi et al., 2016). More detailed work on the thermo-physical conditions during and after planetesimal impacts needs to be undertaken to compare theoretical expectations with experimental evidence with the goal of a *sufficient* set of evidence to either strengthen or rule out impacts as a formation mechanism for the majority of chondrules.

6.5 CONCLUSIONS

In this manuscript we examined the formation of chondrules from collisions of planetesimals, which were preheated from the radioactive decay of ^{26}Al. First, we investigated the end-member scenario of collisions between planetesimals heated to silicate melt fractions above the rheological transition, i.e., with interior magma oceans. Using well-studied scaling relations of the metal rainfall mechanism and the local diffusion time scale in convective silicate systems we determined that such planetesimals

(i) cannot suspend significant amounts of Fe,Ni metal and, therefore, evolve to a physically differentiated structure,

and

(ii) rapidly equilibrated primordial chemical and nucleosynthetic heterogeneities.

Therefore, we conclude that physically plausible impact splash interactions between such bodies would have resulted in chondrule-like but basaltic spherules, which are not observed in the meteoritic record. Contrary to Asphaug (2017), we argue that this is a telltale-sign that no such interactions took place in the early Solar system and that planetesimals with large-scale interior magma oceans were not abundant in the source reservoir of today's asteroid main belt. Potential reasons for this may be delayed planetesimal formation, sub-canonical ^{26}Al abundances in the planetesimal formation region, efficient heat source redistribution by migration of aluminum-rich

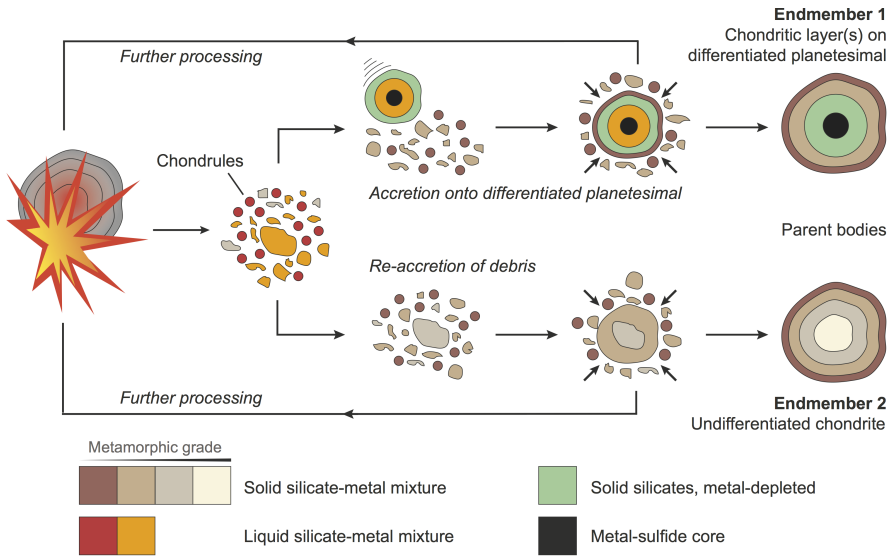

Figure 6.11: Schematic illustration of the accretion-collision cycles during which chondrules may form from impact splashes among radiogenically preheated planetesimals. The impacts launched expanding clouds of magma droplets (Dullemond, Stammler, and Johansen, 2014; Dullemond et al., 2016) in addition to melted and unmelted debris, which subsequently cooled. The debris then either re-accumulated or accreted onto a neighboring planetesimal. Before forming the final chondrite parent bodies the material could go through multiple cycles of liberation and re-accumulation with varying degrees of injected energy and accumulation time scales. Cold matrix material (not shown) from the surrounding disk environment is accreted together with chondrules into the final chondrite parent body.

melts to the surface (Wilson and Keil, 2017), or widespread collisional interactions of fully-molten bodies were prevented by environmental (disk conditions) or dynamical (collisional growth-related) mechanisms, for instance, efficient collisional recycling in the source reservoir of nowadays asteroid belt. Furthermore, it would imply that iron meteorites would have been primarily formed via incomplete metal-silicate differentiation or must originate from larger bodies than currently anticipated (Lyons et al., 2017). We suggest that these conclusions can help to achieve a better understanding of the early dynamical environment during the solar protoplanetary disk phase, because it excludes the part of the parameter space that leads to widespread generation of droplet-like and basaltic material feeding the asteroid main belt.

We argue that the debate of a collisional (or 'planetary') origin of chondrules needs to take into account the complications of the combined planetesimal evolution and recycling efficiency during accretion. The early formation and reaccretion of planetesimals of low mass and/or under sub-canonical ^{26}Al abundances opens the win-

dow to a vast collisional parameter space, which may satisfy many geo- and cosmochemical constraints derived from the meteoritic record. We have sketched one such accretion-collision cycle to generate chondrules in Figure 6.11. In the future, the dynamical feasibility and implications of our proposed chondrule formation scenario can be explored with astrophysical models that simultaneously solve for a global planetesimal source system and achieve sufficiently high mass resolution to resolve the low-mass bodies we focused on in this work (e.g., Levison, Duncan, and Thommes, 2012; Morishima, 2017).

In summary, we propose that the linkage of the initial planetesimal size frequency distribution, formation time, interior evolution and collisional recycling may be further used to constrain the formation of chondrules and subsequently the chondrite parent bodies. The collisional chondrule formation scenario links the chondrule origin to the formation of the terrestrial planets and the Solar system architecture we observe today. Details of the model – such as the exact disk conditions necessary to create such an environment and the thermo-physical processes and energy localization during collisions – demand detailed physical and chemical models on many spatial and temporal scales, which offer exciting new pathways for the study of planet formation. These models need to be further synchronized and tested against precise laboratory data and may ultimately lead the way to a better understanding of the earliest environment of the Solar nebula.

ACKNOWLEDGMENTS T.L. gratefully acknowledges insightful discussions with H. Palme, J. Zipfel, N. P. Walte, J. Drążkowska, S. N. Raymond and artistic advice from A. Rozel and C. Jain. The authors thank Z. M. Leinhardt and P. J. Carter for providing us a PYTHON-based script to evaluate planetesimal interactions on the basis of the EDACM scaling relations (Leinhardt and Stewart, 2012), C. M. O'D. Alexander and S. J. Desch for thorough and constructive reviews that considerably helped to improve the manuscript, A. Morbidelli for the editorial handling, and the organizers of the 2015 Gordon Research Conference 'Origins of Solar systems' for an inspiring and collaborative meeting that initiated this project. The models were analyzed using the open source software environment MATPLOTLIB (Hunter, 2007). T.L. was supported by ETH Research Grant ETH-17 13-1. The numerical simulations in this work were performed on the EULER computing cluster of ETH Zürich. Parts of this work have been carried out within the framework of the National Center for Competence in Research PlanetS supported by the Swiss National Science Foundation.

6.6 SUPPLEMENTARY FIGURES

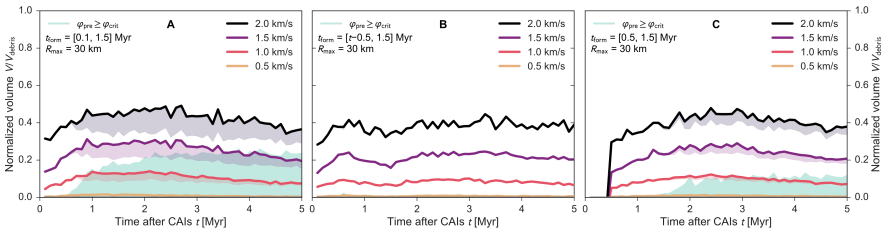

Figure 6.12: Simulation outputs for planetesimal families with radii $R_{\max}$ = 30 km and formation time regimes t_{form} = *(A)* [0.1, 1.5], *(B)* [t-0.5, 1.5] and *(C)* [0.5, 1.5] Myr. See Figure 6.8 for a detailed description.

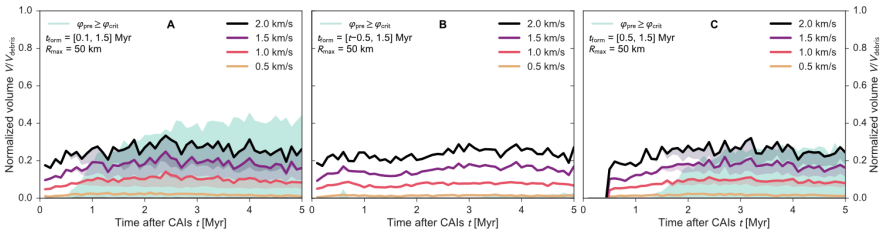

Figure 6.13: Simulation outputs for planetesimal families with radii $R_{\max}$ = 50 km and formation time regimes as in Figure 6.12.

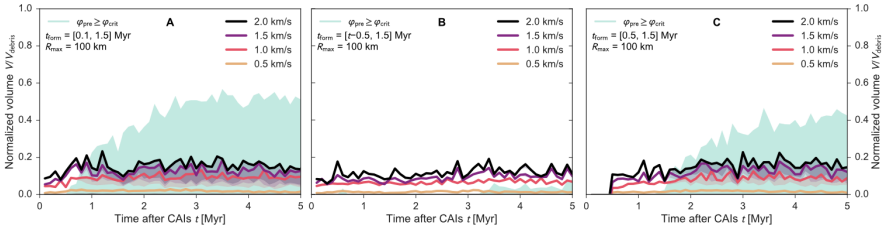

Figure 6.14: Simulation outputs for planetesimal families with radii $R_{\max}$ = 100 km and formation time regimes as in Figure 6.12.

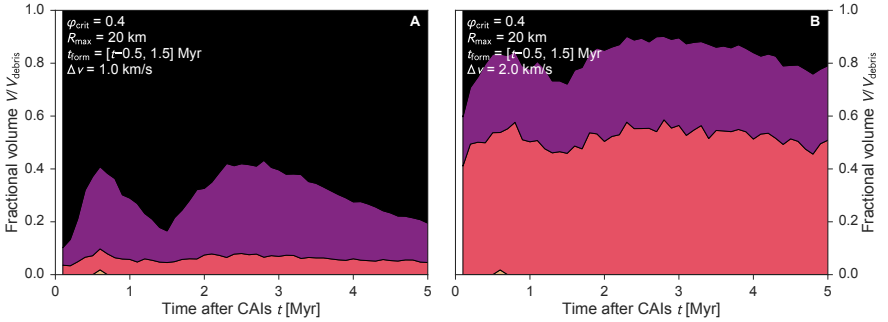

Figure 6.15: Thermal debris distribution for collision models with R_{max} = 20 km, t_{form} = [t-0.5, 1.5] Myr and collision velocities of *(A)* 1.0 km/s and *(B)* 2.0 km/s. Black represents unmelted, purple partially melted, red chondrule-eligible ($T_{\mathrm{post}} > T_{\mathrm{chondrule}}$) and yellow metal-depleted material. (Compare Figure 6.9.)

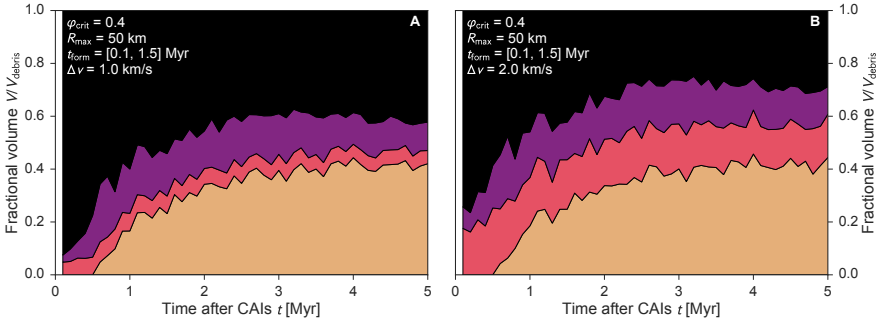

Figure 6.16: Thermal debris distribution for collision models with R_{max} = 50 km, t_{form} = [0.1, 1.5] Myr and collision velocities of *(A)* 1.0 km/s and *(B)* 2.0 km/s. Black represents unmelted, purple partially melted, red chondrule-eligible ($T_{\mathrm{post}} > T_{\mathrm{chondrule}}$) and yellow metal-depleted material. (Compare Figure 6.9.)

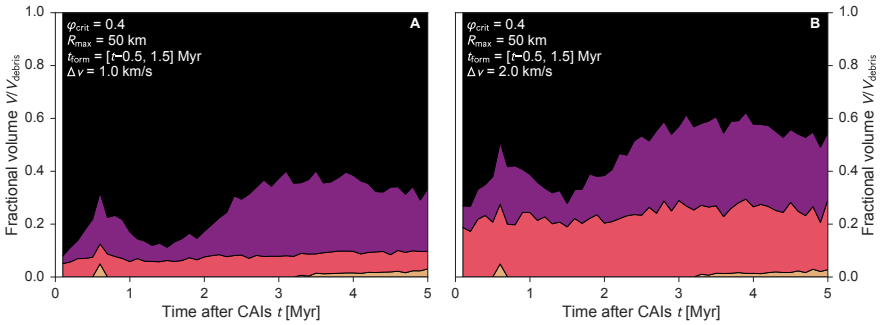

Figure 6.17: Thermal debris distribution for collision models with R_{max} = 50 km, t_{form} = [t-0.5, 1.5] Myr and collision velocities of *(A)* 1.0 km/s and *(B)* 2.0 km/s. Black represents unmelted, purple partially melted, red chondrule-eligible ($T_{\mathrm{post}} > T_{\mathrm{chondrule}}$) and yellow metal-depleted material. (Compare Figure 6.9.)

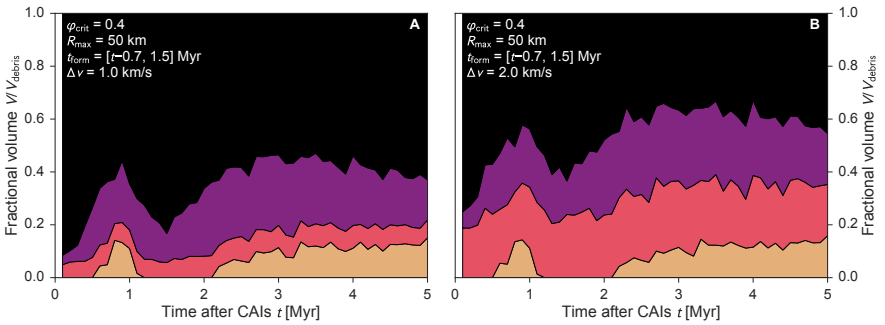

Figure 6.18: Thermal debris distribution for collision models with $R_{\max}$ = 50 km, t_{form} = [t-0.7, 1.5] Myr and collision velocities of *(A)* 1.0 km/s and *(B)* 2.0 km/s. Black represents unmelted, purple partially melted, red chondrule-eligible ($T_{\text{post}} > T_{\text{chondrule}}$) and yellow metal-depleted material. (Compare Figure 6.9.)

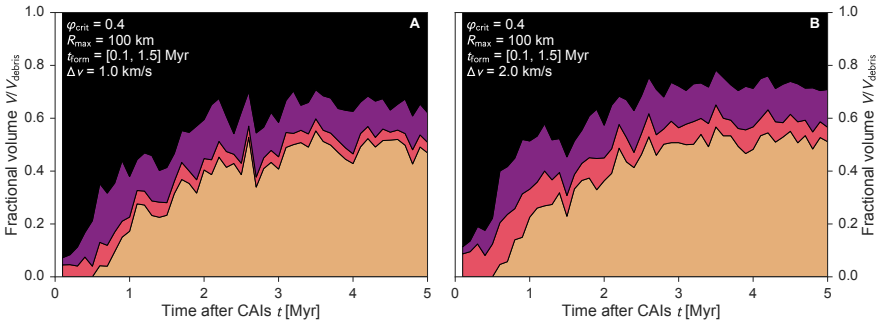

Figure 6.19: Thermal debris distribution for collision models with $R_{\max}$ = 100 km, t_{form} = [0.1, 1.5] Myr and collision velocities of *(A)* 1.0 km/s and *(B)* 2.0 km/s. Black represents unmelted, purple partially melted, red chondrule-eligible ($T_{\text{post}} > T_{\text{chondrule}}$) and yellow metal-depleted material. (Compare Figure 6.9.)

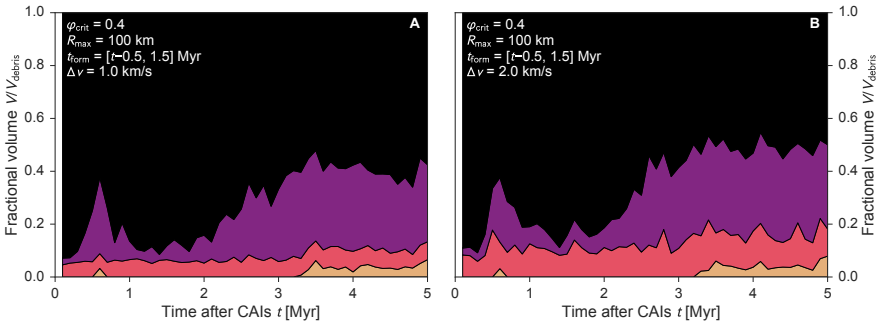

Figure 6.20: Thermal debris distribution for collision models with $R_{\max}$ = 100 km, t_{form} = [t-0.5, 1.5] Myr and collision velocities of *(A)* 1.0 km/s and *(B)* 2.0 km/s. Black represents unmelted, purple partially melted, red chondrule-eligible ($T_{\text{post}} > T_{\text{chondrule}}$) and yellow metal-depleted material. (Compare Figure 6.9.)

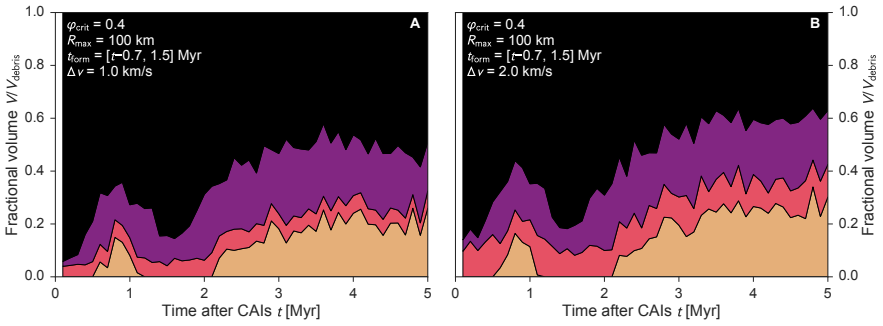

Figure 6.21: Thermal debris distribution for collision models with R_{max} = 100 km, t_{form} = [t-0.7, 1.5] Myr and collision velocities of *(A)* 1.0 km/s and *(B)* 2.0 km/s. Black represents unmelted, purple partially melted, red chondrule-eligible ($T_{\mathrm{post}} > T_{\mathrm{chondrule}}$) and yellow metal-depleted material. (Compare Figure 6.9.)

7

GRADUAL DESICCATION OF ROCKY PROTOPLANETS FROM ^{26}AL-HEATING

At the time of writing, June 19, 2018, the content of this section is under review for publication as: Lichtenberg, T., G. J. Golabek, R. Burn, M. R. Meyer, Y. Alibert, T. V. Gerya, C. A. Mordasini. "Gradual desiccation of rocky protoplanets from ^{26}Al-heating."

ABSTRACT

The formation and distribution of Earth-like planets remains poorly constrained. However, stochasticity during accretion (Raymond and Izidoro, 2017; Alibert and Benz, 2017) and the variety of exoplanet compositions (Kaltenegger, 2017; Millholland, Wang, and Laughlin, 2017) favor rocky worlds covered in thick volatile ice layers (Kuchner, 2003; Léger et al., 2004) as the dominant family of terrestrial analogues (Tian and Ida, 2015; Ramirez and Levi, 2018), deviating from the water-poor inner-Solar system planets. Here, we demonstrate the power of ^{26}Al, a short-lived radionuclide abundant in the early Solar system (Grimm and McSween, 1993), to control the water content of terrestrial exoplanets. Using numerical models of planet formation, evolution, and interior structure, we generate synthetic planet populations that are subject to a varying degree of ^{26}Al-heating during accretion. We show that planet bulk water fraction and radius are anti-correlated with the host system's ^{26}Al levels. This yields a system-wide correlation (Millholland, Wang, and Laughlin, 2017) of bulk abundances, and is consistent with the location-independent scarcity of water within the TRAPPIST-1 planets (Grimm et al., 2018). The generic sensitivity of exoplanet observables (Millholland, Wang, and Laughlin, 2017; Weiss et al., 2018) on primordial ^{26}Al inferred from our models suggests two distinct classes of rocky exoplanets: high-^{26}Al systems form small, water-depleted planets, those devoid of ^{26}Al form ocean worlds, with the mean planet radii deviating by up to $\sim$10%.

7.1 INTRODUCTION

Theoretical models of water content (Ciesla et al., 2015; Tian and Ida, 2015; Raymond and Izidoro, 2017; Alibert and Benz, 2017), and bulk abundances inferred for the extrasolar planet population (Kaltenegger, 2017; Dorn, Hinkel, and Venturini, 2017) consistently yield water fractions orders of magnitude higher than observed for Earth ($f_{\mathrm{H_2O,Earth}} \sim 10^{-3}$) Peslier et al., 2018. Because of the limited water solubility in

the interior of rocky planets, bulk water fractions on the order $f_{H_2O} \gtrsim \mathcal{O}$(wt%) result in a qualitatively different evolution compared to the Solar system terrestrial planets, including the absence of continents on the surface (Cowan and Abbot, 2014), deep global water oceans (Alibert, 2014; Noack, Snellen, and Rauer, 2017; Kite and Ford, 2018), and high-pressure ice layers that hinder interior-atmosphere exchange (Kuchner, 2003; Léger et al., 2004; Unterborn et al., 2018; Tian and Ida, 2015; Kite and Ford, 2018). However, the few exoplanets in the rocky regime ($R_P \lesssim 1.7\ R_{Earth}$, $M_P \lesssim 8\ M_{Earth}$) that are best characterized, most notably the TRAPPIST-1 planets, are consistent with $f_{H_2O} \lesssim 5$ wt% (Grimm et al., 2018). These compositions require a system-wide dehydration mechanism. During accretion, the total volatile inventory of planets may be sculpted by impacts (Marcus et al., 2010; Genda and Abe, 2003), but stochastically depends on the size, volatile fraction, and collision frequency of the impactors themselves. Later atmospheric loss processes are not efficient enough to systematically balance water abundances above a few to tens of Earth oceans, and become less efficient for $f_{H_2O} \gtrsim$ wt% (Kuchner, 2003; Tian and Ida, 2015; Luger and Barnes, 2015; Bourrier et al., 2017). Therefore, the system-wide magnitude of water supply during accretion primarily controls the bulk water mass fraction of planets.

Relative to exoplanets, the Solar system's accretion history is tightly constrained (Morbidelli et al., 2016; Raymond and Izidoro, 2017). Using geochemical evidence from meteorites, we can infer the thermochemical evolution of planetesimals, the building blocks of terrestrial planets, during accretion (Grimm and McSween, 1993; Monteux et al., 2018). The interior evolution of planetesimals during the first ∼2 Myr after the condensation of the oldest known solids, the Ca,Al-rich inclusions (CAIs), was dominated by radiogenic heating from ^{26}Al ($t_{1/2,^{26}Al} \sim 0.72$ Myr) and led to silicate melting, interior magma oceans (Fu and Elkins-Tanton, 2014; Lichtenberg et al., 2016, 2018), and degassing of primordial water ice abundances (Monteux et al., 2018). In general, water is delivered to rocky planets by the accretion of ice-rich planetesimals from beyond the water snowline that either enter the planetary feeding zone during migration or are scattered inwards by gas giants such as (proto-)Jupiter (Raymond and Izidoro, 2017).

7.2 METHODS

Here, we quantify the control of ^{26}Al-dehydration of planetesimals with radii 1–100 km on the water content of rocky exoplanets. We combine models of planet formation (Benz et al., 2014) with ^{26}Al-induced water loss from planetesimals during the main accretion phase (Monteux et al., 2018). From these we generate synthetic planet populations with internal structures defined by the planets' composition

(Mordasini et al., 2012), which relate the formation pathway to the planet radius (Extended methods).

In our models, initially Moon-sized protoplanets grow from planetesimals and gas within their local feeding zone in the protoplanetary disk. We consider G (1 $M_\odot$) and M-type (0.2 $M_\odot$) stars with appropriate disk masses and structures. Planetesimal orbits are influenced by self-interaction, stirring by nearby embryos and gas drag. The protoplanets migrate according to type I and II regimes, depending on their mass and physical structure of the disk. The initial location of the embryos and the starting disk structure and boundaries are randomized to reflect the diversity found in observed young planetary systems (Ansdell et al., 2016).

Planetesimals are icy beyond the static snowline and dry inside. The initial water mass fraction of planetesimals beyond the snowline in our models decreases in time due to dehydration from internal radiogenic heating, for which we compute the planetesimal interior and thermal evolution. During heat-up of a primordial water ice-rock mixture, ices melt and react with the ambient rock (Castillo-Rogez and Young, 2017). The liquid water undergoes pore water convection and escapes quickly once the gas phase is reached (Grimm and McSween, 1993), but a small fraction of water is trapped in hydrous silicate phases. Therefore, we numerically account for dehydration at even higher temperatures, when a planetesimal sub-volume in our models reaches temperatures above the amphibolite stability field (Fu and Elkins-Tanton, 2014), $T \geq T_{\mathrm{dry}}$ = 1223 K. At this point, even the most heat-resistant hydrous mineral phases break down, and the exsolved water vapor is lost quasi-instantaneously – planetesimals of this size cannot preserve an outgassed atmosphere. Such complete water-loss reduces the planetesimal bulk density and thus mass, and ultimately the surface density of solids available for embryos to accrete over time, which we account for in the dynamic accretion model (Extended methods).

The accretion dynamics of terrestrial planets depends on the initial size frequency distribution of planetesimals that accrete onto protoplanets. In addition, the average planetesimal radii influence water-loss due to internal heating because of less efficient heat-loss with larger body size (Lichtenberg et al., 2016, 2018; Castillo-Rogez and Young, 2017; Monteux et al., 2018). The dehydration efficiency from radiogenic heating is controlled by the amount of ^{26}Al incorporated upon planetesimal formation, which may vary substantially among planetary systems (Lichtenberg, Parker, and Meyer, 2016). We account for this potential variability by generating synthetic populations with different planetesimal radii, r_{plts} = 3, 10, 50 km, and initial ^{26}Al abundances between $^{26}\mathrm{Al}_0$ = [0.1, 10] $\times$ $^{26}\mathrm{Al}_\odot$, with $^{26}\mathrm{Al}_\odot$ the Solar system's 'canonical' ^{26}Al/^{27}Al at CAI formation (Extended methods), and compare them to the nominal case without ^{26}Al-heating.

7.3 RESULTS & DISCUSSION

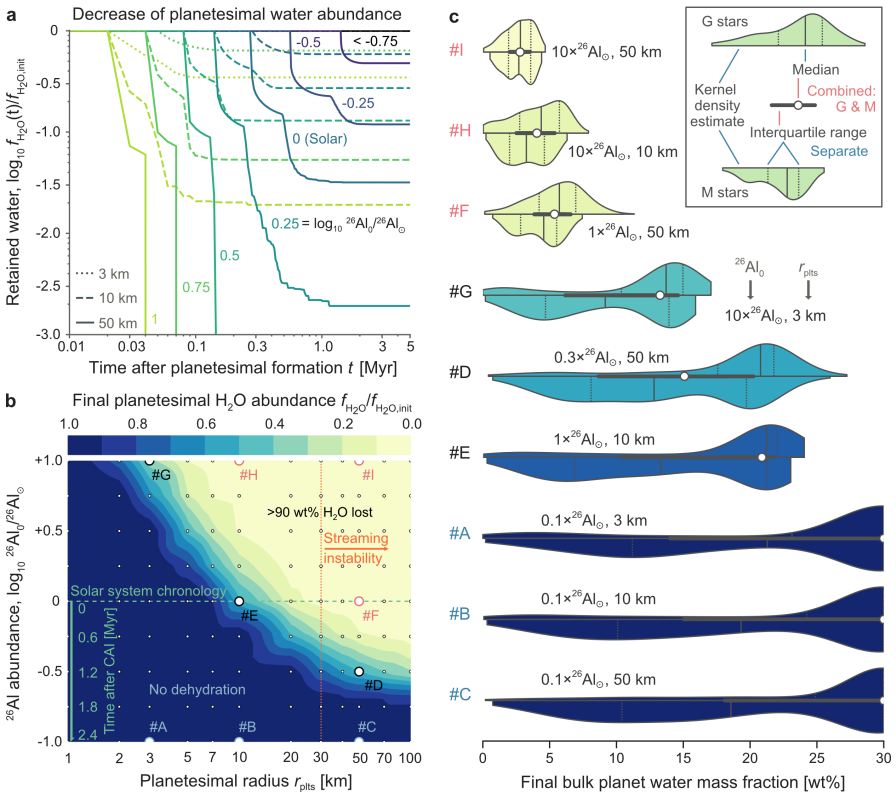

Figure 7.1: Dehydration of icy planetesimals from ^{26}Al-heating and resulting influence on planet water abundance. *(a)* Time-resolved water retention for planetesimals of 3, 10 and 50 km radius with $^{26}Al_0$ = [0.1, 10] $\times$ $^{26}Al_\odot$. Larger planetesimals with more ^{26}Al loose their water faster and to a greater degree. *(b)* Final state of water retention. $^{26}Al_0$ at planetesimal formation can be translated into planetesimal formation time after CAIs for Solar system objects. The orange line depicts the lowest mass planetesimals inferred for the early Solar system planetesimal population (Delbo et al., 2017). *(c)* Shift in planet bulk water abundances for specific planetesimal configurations from *a* and *b*, for planet masses M_P = [0.1, 10] $\times$ M_{Earth}, and $f_{H_2O} > 0$. The water retention in planetesimals from *a* and *b* is correlated with the final retained water in *c* (color scales in *b* and *c* are equal). Thus, planetary systems tend to reflect the water lost from planetesimals during accretion due to ^{26}Al-heating.

The control of $^{26}Al_0$ and r_{plts} on the retention of water within planetesimals and resulting planet populations from a given set of initial conditions are shown in Figure 7.1. Planetesimals with larger r_{plts} and higher $^{26}Al_0$ dehydrate faster and up to 100% for extreme values. Rooted in our conservative choice for dehydration, the total water loss divides the parameter range into two distinct regimes. The first consists of almost pristine water-rock ratios for small planetesimals

with low $^{26}Al_0$. However, for $^{26}Al_0 \gtrsim {}^{26}Al_\odot$ and planetesimals with $r_{plts} \gtrsim$ 10 km, water loss is nearly complete (Figure 7.1a,b).

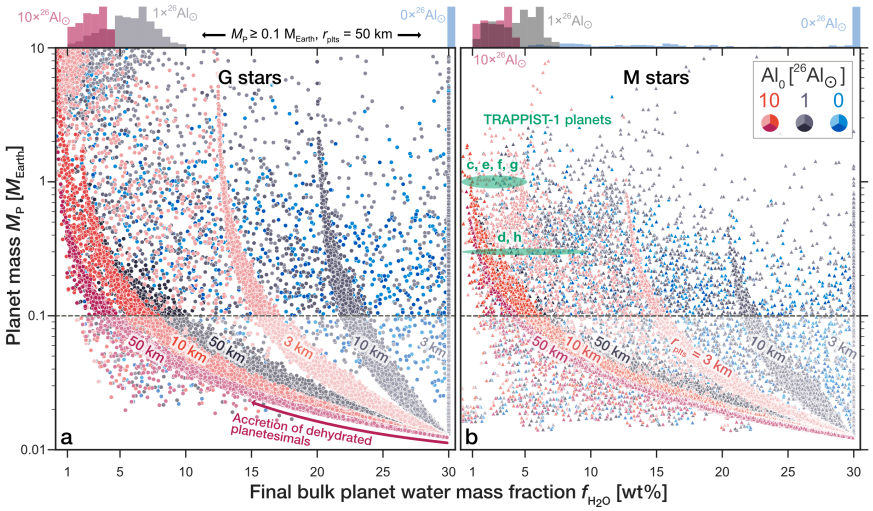

Figure 7.2: Gradual desiccation as a function of $^{26}Al_0$ for planets with $f_{H_2O} > 0$. For increasing $^{26}Al_0$ and r_{plts}, the bulk planet water fraction f_{H_2O} decreases systematically. For $M_P \geq 0.1\ M_{Earth}$ and r_{plts} = 50 km, the f_{H_2O} histogram on top shows approximately one order of magnitude deviation between planets formed devoid of ^{26}Al and with $^{26}Al \gtrsim {}^{26}Al_\odot$. Only the latter cases increasingly populate the terrestrial planet regime with $f_{H_2O} \lesssim$ wt%. The blue points from the populations with zero $^{26}Al_0$ only rarely and stochastically form planets with low water mass fractions, which are all due to rapid inward migration. The clustering for $^{26}Al_0$ = 0 at the maximum water mass fraction is inherited from our chosen initial composition of planetesimals beyond the snowline (Extended methods). It is important to note that the areas of clustering locate the *maximum* water mass fractions for a given planet mass within a synthetic population, i.e., planets that are formed entirely beyond the snowline. For example, all planets from the synthetic population with r_{plts} = 3 km, and $^{26}Al_0 = 10 \times {}^{26}Al_\odot$, show water mass fractions $f_{H2O} \lesssim$ 15 wt% for $M_P \geq 0.1\ M_{Earth}$. M stars (*b*) on average form lower mass planets because of lower disk masses. The TRAPPIST-1 planets, as inferred by Grimm et al. (2018), are consistent with being formed in a planetary system with $^{26}Al_0 \gtrsim {}^{26}Al_\odot$ and $r_{plts} \gtrsim$ 10 km.

For distinct combinations of $^{26}Al_0$ and r_{plts}, we simulate the influence on the expected planet population for planet masses M_P = [0.1, 10] $\times\ M_{Earth}$ (Figure 7.1c). Because the timescale for water-loss caused by ^{26}Al-heating is shorter than the accretion timescale by up to an order of magnitude, most planetesimals sufficiently ^{26}Al-enriched are dry when they accrete onto protoplanets. Therefore, the final planet water mass fractions are correlated with the retained water fraction in planetesimals due to ^{26}Al heating.

Planet desiccation caused by the accretion of ever-more dehydrated planetesimals reduces the inherent scatter and range in f_{H_2O} in the synthetic planet populations (cf. Figure 7.1c and Figure 7.2a,b). For fixed planetesimal radius and increasing $^{26}Al_0$, accreting planets receive more relative mass contribution from dry objects and end up water-depleted relative to nominal conditions.

In the Solar system, the initial planetesimal size frequency distribution is expected to have been dominated by bodies with $r_{plts} \gtrsim$ 30–50 km (Delbo et al., 2017). For such bodies and larger, the equilibrium between radiogenic heating and surface cooling stabilizes internal temperatures for an extended timespan at spatially isothermal conditions (Lichtenberg et al., 2016; Castillo-Rogez and Young, 2017). Therefore, the fractional dehydration in Figure 7.1b converges above $r_{plts} \gtrsim$ 50 km and becomes nearly independent of planetesimal size. In the 50 km cases, dehydration is dominantly controlled by $^{26}Al_0$ and generates a dichotomy between planets in not-enriched systems (blue histogram on top in Figure 7.2) and systems that are enriched with $^{26}Al_0 \gtrsim {}^{26}Al_\odot$ (black and red histograms on top in Figure 7.2). M and G stars overall display the same trend, but M stars form smaller planets on average, due to smaller and less massive disks.

The emerging trend from our simulations is illustrated in Figure 7.3, with a clear distinction between planetary systems that are significantly enriched ($^{26}Al_0 \gtrsim {}^{26}Al_\odot$), and those that are not. In general, ^{26}Al is expected to be abundant in the galaxy (Adams, 2010) but likely inhomogeneously distributed (Kuffmeier et al., 2016), with the Sun at the higher-end tail of the distribution (Lichtenberg, Parker, and Meyer, 2016). According to our simulations, planets in enriched systems grow from ever-more dehydrated planetesimals and form desiccated planets in their terrestrial planet zone. Depending on the initial planetesimal sizes, final planet water fractions are up to two orders of magnitude below the initial planetesimal water mass fractions, and are strongly correlated with the efficiency of dehydration during accretion (Figure 7.1).

Because the absolute volatile mass fraction of a planet has a disproportionate influence on the internal structure of a planet (Dorn, Hinkel, and Venturini, 2017; Noack, Snellen, and Rauer, 2017; Unterborn et al., 2018), we anticipate the resulting smaller radii for lower water mass fraction to be reflected in the global exoplanet population. For deviations in planet water fractions predicted here, the thickness of the volatile layer on top of the silicate mantle constitutes several per cent of the radius (Kuchner, 2003; Léger et al., 2004; Alibert, 2014; Noack, Snellen, and Rauer, 2017). We calculate this deviation in our synthetic populations by translating the derived planetary masses and compositions into a mean radius in a given mass bin (Figure 7.3b, top) using interior structure models that are sensitive to the total planet mass, its water and (captured) hydrogen/helium mass

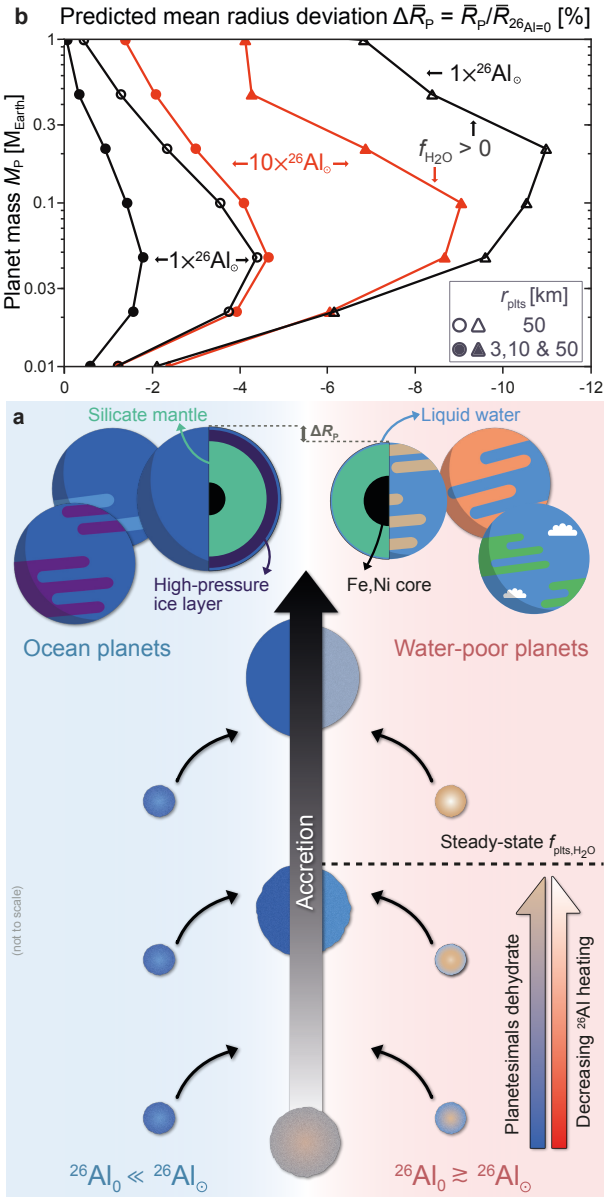

Figure 7.3: Qualitative sketch of the effects of ^{26}Al enrichment on planetary accretion and mean-radius shift for varying $^{26}Al_0$. *(a, bottom)* Planetary systems devoid of ^{26}Al tend to accrete from water-rich planetesimals that result in global oceans and potentially high-pressure ice layers that separate interior and atmosphere. Planetary systems with $^{26}Al_0 \gtrsim {}^{26}Al_\odot$ accrete from dehydrating planetesimals and acquire moderate water abundances relative to systems devoid of ^{26}Al. The arrows indicate proceeding accretion (middle), planetesimal water content (bottom right, blue-brown), and live ^{26}Al (bottom right, red-white). *(b, top)* Quantitative predictions for planetary mean transit radii (Extended methods) for given mass bins in planetary systems with ^{26}Al, normalized to the case completely devoid of ^{26}Al. Empty symbols indicate radius deviations for planets with $f_{H_2O} > 0$, filled symbols include also completely dry planets that formed entirely inside of the water snow-line. For varying selection criteria, the planet radii per mass bin among the high-end tail of ^{26}Al-enriched systems deviate from not-enriched systems by up to ∼10 %.

fraction, and the surface pressure (Mordasini et al., 2012) (Extended methods). For the entire populations of planets among G and M stars, the radius deviation reaches up to 2% for $1 \times {}^{26}\mathrm{Al}_{\odot}$, and with $10 \times {}^{26}\mathrm{Al}_{\odot}$ or r_{plts} = 50 km goes to ∼4% deviation for Mars-sized planets. If we only consider planets that accrete a minimum amount of water (planets that receive some mass contribution from beyond the ice-line), with $10 \times {}^{26}\mathrm{Al}_{\odot}$, or $1 \times {}^{26}\mathrm{Al}_{\odot}$ with r_{plts} = 50 km, the mean-radius shift can reach up to ∼10%. Planetary systems with high ${}^{26}\mathrm{Al}_0$ (${}^{26}\mathrm{Al}_0 \gtrsim 1$–$10 \times {}^{26}\mathrm{Al}_{\odot}$) form water-depleted planets and with system-wide smaller radii compared to the not-enriched population.

Such deviations are measurable by ESA's PLATO mission (Rauer et al., 2014), which will aim to detect a statistical ensemble of planetary radii within the rocky planet regime. However, the intrinsic compositional scatter in the inferred mean densities from known exoplanets suggests a large stochastic component in the planet formation process. Yet, recent analyses of data based on Kepler multi-planet systems provided strong evidence for intra-system correlation between planetary radii (Millholland, Wang, and Laughlin, 2017; Weiss et al., 2018). Therefore, the fate and long-term structure of planets seems to be dominated by physical and chemical effects on a system-to-system level, rather than emerging from intra-system stochasticity during accretion, such as impact stripping. As a result, with access to a statistical ensemble of low-mass planet radii, the high-end tail of ${}^{26}\mathrm{Al}$-enriched systems, where planetary radii deviate by several per cent, may stick out from the mean of the population.

For example, the system-wide water depletion of the TRAPPIST-1 planets, all featuring $f_{\mathrm{H_2O}} \lesssim 5\%$ (Grimm et al., 2018), is consistent with $\gtrsim$ Solar ${}^{26}\mathrm{Al}$-induced desiccation (Figure 7.2). The atmospheres of the TRAPPIST-1 planets seem to be secondary (de Wit et al., 2018), and may have lost several Earth ocean equivalents of water (Luger and Barnes, 2015; Bourrier et al., 2017). However, to account for the consistency of the outermost planets *e*-*h* with Earth-like volatile abundances, and near-uniformity of their water mass fractions, an order of magnitude depletion mechanism, such as suggested here, must affect all of the planets independent of their incident stellar fluxes. Therefore, the retrieved water mass fractions of the TRAPPIST-1 planets are unexpected from formation and evolution models for ultra-cool M stars (Tian and Ida, 2015; Luger and Barnes, 2015; Ciesla et al., 2015; Ormel, Liu, and Schoonenberg, 2017; Alibert and Benz, 2017; Unterborn et al., 2018), and present a severe challenge for current planet formation scenarios. The ${}^{26}\mathrm{Al}$-desiccation mechanism we put forward achieves system-wide water depletion for G and M stars without the need to fit specific accretion dynamics, as it has been proposed (Ormel, Liu, and Schoonenberg, 2017; Unterborn et al., 2018).

7.4 SUMMARY & CONCLUSIONS

In summary, our models suggest that the level of ^{26}Al-enrichment of planetary systems fundamentally shapes the efficiency of water delivery during accretion, and thus the structure and long-term fate of terrestrial planets. We demonstrate that planetary systems with ^{26}Al abundances similar to or higher than the Solar system generically form terrestrial planets with low water mass fractions $f_{\mathrm{H_2O}} \lesssim \mathcal{O}(\mathrm{wt\%})$. Not-enriched systems, which may comprise the majority of planetary systems in the galaxy (Lichtenberg, Parker, and Meyer, 2016), tend to be dominated by water mass fractions $\gtrsim$ tens of wt%. This effect is more pronounced for more distant planets, as embryos in these regions grow preferentially from initially water-rich planetesimals, and are unlikely to be affected by atmospheric loss processes.

For a non-uniform distribution of ^{26}Al in Milky Way star-forming regions, our models suggest that ^{26}Al-desiccation of protoplanets creates two qualitatively distinct classes of planetary systems: water-poor (^{26}Al-enriched) and water-rich (^{26}Al-poor) systems. We predict a systematic mean-radius deviation for sub-Earth terrestrial planets between these classes, which can be statistically detected with future transit surveys.

7.5 EXTENDED METHODS

7.5.1 *Planetesimal dehydration*

We model water loss from instantaneously-formed planetesimals composed of a rock-ice mixture using numerical models that employ a conservative finite-differences, fully-staggered grid method coupled to a marker-in-cell approach (Gerya and Yuen, 2007; Golabek, Bourdon, and Gerya, 2014). The thermo-chemical evolution of planetesimals is computed in a 2D infinite cylinder geometry on a cartesian grid, solving the Poisson, continuity, Stokes and energy conservation equations. We assume the planetesimals to be accreted with the temperature of the protoplanetary disk beyond the water snowline, $T_0 = 150$ K, which is kept constant during the evolution of the planetesimal utilizing the free-surface 'sticky-air' method (Crameri et al., 2012). Heating is provided by the decay of ^{26}Al, which defines the radiogenic heat source term over time

$$H_{^{26}\mathrm{Al}}(t) = f_{\mathrm{Al}} \cdot (^{26}\mathrm{Al}/^{27}\mathrm{Al})_0 \cdot E_{^{26}\mathrm{Al}} \cdot \exp(-t/\tau_{^{26}\mathrm{Al}})/\tau_{^{26}\mathrm{Al}}, \qquad (7.1)$$

with the chondritic abundance of aluminum, f_{Al} (Lodders, 2003), the ratio of ^{26}Al to stable ^{27}Al at the time of planetesimal formation, $^{26}\mathrm{Al}_0$ = $(^{26}\mathrm{Al}/^{27}\mathrm{Al})_0$, the decay energy, $E_{^{26}\mathrm{Al}} = 3.12$ MeV (Castillo-Rogez et al., 2009), and the mean lifetime, $\tau_{^{26}\mathrm{Al}} = 1.03$ Myr. We ignore any potential heat contribution from ^{60}Fe, which may further boost radiogenic

heating rates in extrasolar systems (Lichtenberg, Parker, and Meyer, 2016; Nicholson and Parker, 2017). If the planetesimal interior reaches temperatures beyond the rock disaggregation threshold at a silicate melt fraction of $\phi \gtrsim 0.4$ Costa, Caricchi, and Bagdassarov, 2009, where the rock viscosity drops by more than ten orders or magnitude, we approximate the thermal conductivity in the soft turbulence limit (Siggia, 1994) with

$$k_{\mathrm{eff}} = (q/0.89)^{3/2} \cdot \alpha_{\mathrm{liq}} g c_{\mathrm{p}} / (\Delta T^2 \rho_{\mathrm{s}} \eta_{\mathrm{num}}), \tag{7.2}$$

with the convective heat flux, q, the temperature difference across nodes, ΔT, silicate density, ρ_{s}, thermal expansivity of silicates, α_{liq}, silicate heat capacity, c_{p}, local gravity, $g(x,y)$, and lower cut-off viscosity, η_{num}. For numerical values used and further details and references on the code see Lichtenberg et al. (2016). The initial planetesimal water fraction beyond the snowline is expected to be between ∼5 wt% (Ciesla et al., 2015; O'Brien et al., 2018), the water content of carbonaceous chondrites, and ∼50 wt%, as suggested by equilibrium condensation calculations (Lodders, 2003). Here, we adopt a value closer to the upper estimate, $f_{\mathrm{H_2O}}$ = 30 wt%, but our calculations only marginally depend on the adopted value.

We assume complete dehydration of the planetesimal (sub-)volume if its temperature rises above $T_{\mathrm{dry}} = 1223$ K (Fu and Elkins-Tanton, 2014), the upper limit of the amphibolite stability field, which are the most heat-resistant hydrous silicate phases. Doing so, we do not resolve potential earlier water-loss from degassing (Castillo-Rogez and Young, 2017), or residual volatiles above T_{dry} (Fu et al., 2017). Using these assumptions, we compute the expected volume ratio of dehydrated to primordial water-rock mixture, $f_{\mathrm{H_2O}}(t) = 1 - V_{\mathrm{dry}}(t)/V_{\mathrm{plts}}$, with the dry volume, V_{dry}, and the total planetesimal volume, V_{plts}, at a given time t.

7.5.2 *Planet formation*

We compute the formation of planets and generate our synthetic planet populations using an updated version of the model of Alibert et al. (2005). The computer code numerically treats the structure and evolution of the protoplanetary disk, the dynamical properties and accretion rate of planetesimals onto accreting protoplanets, the planetary envelope structure and disk-planet interactions Mordasini, Alibert, and Benz, 2009; Mordasini et al., 2009; Mordasini et al., 2015; Benz et al., 2014. Here, we provide a brief summary of the most important code modules used in this work.

The protoplanetary disk model relies on the Shakura-Sunyaev (Shakura and Sunyaev, 1973) disk viscosity approximation ($\alpha_{\mathrm{disk}} = 2 \times$

10^{-3}) and computes the surface density evolution over time by solving the radial diffusion equation

$$\frac{\mathrm{d}\Sigma}{\mathrm{d}t} = \frac{3}{r}\frac{\partial}{\partial r}\left[r^{1/2}\frac{\partial}{\partial r}\tilde{\nu}\Sigma r^{1/2}\right] + \dot{\Sigma}_{\mathrm{w}} + \dot{Q}_{\mathrm{planet}}, \tag{7.3}$$

with the surface density, Σ, orbital radius, r, effective viscosity, $\tilde{\nu}$, and gas accretion onto embryos, $\dot{Q}_{\mathrm{planet}}$, calculated from removing gas in an annulus centered on the embryo with a width of one Hill radius,

$$R_{\mathrm{H}} = a_{\mathrm{planet}}\left[M_{\mathrm{planet}}/(3M_{\mathrm{star}})\right]^{1/3}, \tag{7.4}$$

with the planet semi-major axis, a_{planet}, planet mass, M_{planet}, and star mass, M_{star}. Mass loss due to internal (EUV) photoevaporation $\dot{\Sigma}_{\mathrm{w}}$ (Clarke, Gendrin, and Sotomayor, 2001) is set $\propto r^{-5/2}$ outside of a gravitational radius of ≈ 5 au and external (FUV) photoevaporation (Matsuyama, Johnstone, and Hartmann, 2003) is constant outside of ≈ 140 au, with the total mass loss being a free model parameter. The model used to represent the planetesimal disk relies on the initial central temperature and pressure from the disk model to compute the location of the water snowline, thereby neglecting radial drift of planetesimals (Sasselov and Lecar, 2000) and that of the snowline. Drift timescales for planetesimals larger than 1 km exceed the disk lifetime by orders of magnitude (Weidenschilling, 1977).

We consider rocky planetesimals ($\overline{\rho}_{\mathrm{plts}} = \rho_{\mathrm{rock}}$ = 3200 kg/m^3) inside, and rock-ice aggregates ($\overline{\rho}_{\mathrm{plts}} = \rho_{\mathrm{H2O}} f_{\mathrm{H2O}} + \rho_{\mathrm{rock}}[1 - f_{\mathrm{H2O}}]$) beyond the snowline, which accrete onto planetary embryos. The residual water mass fraction $f_{\mathrm{H_2O}}(t)$ computed from the internal evolution (Section 7.5.1) is translated into a decreasing planetesimal density $\overline{\rho}_{\mathrm{plts}}$ and disk surface density Σ_{plts} by reducing the planetesimal density as $\overline{\rho}_{\mathrm{plts}}(t) = f_{\mathrm{H_2O/rock}}(0)\rho_{\mathrm{H_2O}}(t) + \rho_{\mathrm{rock}}[1 - f_{\mathrm{H_2O/rock}}(0)]$, where $f_{\mathrm{H_2O/rock}}(0) = 0.3$ is the initial total water-to-rock ratio. The solid surface density available for embryos to accrete thus changes with

$$\Sigma_s(t) = \Sigma_s(0) \cdot \left(f_{\mathrm{H_2O/rock}}(0) \cdot f_{\mathrm{H_2O}}(t) + [1 - f_{\mathrm{H_2O/rock}}(0)]\right). \tag{7.5}$$

In our nominal model, a single embryo of initially lunar mass, $M = 0.0123\ M_{\mathrm{Earth}}$, is placed randomly between an inner and outer orbit (see Table 7.1), with a dry composition inside the snowline, and wet outside. It starts accreting solids and gas, and may migrate in the type I and II regime, depending on the embryo mass and physical structure of the disk at a given orbit (Dittkrist et al., 2014). The solid accretion rate (Inaba et al., 2001; Inaba and Ikoma, 2003) takes into account the captured atmosphere. Planetesimal excitation and damping is computed by taking into account self interactions and damping by gas drag (Fortier et al., 2013). Gas accretion due to planetary contraction is considered using a dust opacity reduction factor of 0.01 compared to interstellar values (Pollack et al., 1996; Alibert et al., 2013).

G star settings are identical to the Sun's values. The properties for the M star runs are scaled down. We choose a fixed mass of $M_{\rm star} = 0.2\ M_\odot$ for the M stars. The radius of the star is set to

$$R_{\rm star} = (M_{\rm star}/M_\odot)^{0.945} R_\odot, \tag{7.6}$$

with luminosity (Demircan and Kahraman, 1991)

$$L_{\rm star} = 0.628 (M_{\rm star}/M_\odot)^{2.62} L_\odot, \tag{7.7}$$

and temperature

$$T_{\rm star} = \sqrt[4]{L_{\rm star}/(4\pi R_{\rm star}^2 \sigma)}, \tag{7.8}$$

with stellar radius, $R_{\rm star}$, stellar mass, $M_{\rm star}$, and Stefan-Boltzmann constant, σ. The disk dimensions, exponential cut-off radius and the embryo placement boundaries (Table 7.1) are reduced to account for the lower masses and sizes of M star disks. Thus, initially all embryos form closer to the star compared to the G star populations. The initial disk mass follows the scaling law (Alibert, Mordasini, and Benz, 2011)

$$M_{\rm disk} \propto (M_{\rm star}/M_\odot)^{1.2}, \tag{7.9}$$

with the internal photoevaporation rate adapted to match similar mean lifetimes compared to the G star simulations. In reality, these could be longer for M stars, which would increase the efficiency of the ^{26}Al-dehydration mechanism further.

7.5.3 *Interior structure & evolution*

The interior structure and the long-term evolution of the planets is calculated as described in Mordasini et al. (2012) by solving the classical 1-dimensional radially symmetric interior structure equations of mass conservation, hydrostatic equilibrium, and energy transport (Bodenheimer and Pollack, 1986)

$$\frac{\partial m}{\partial r} = 4\pi r^2 \rho, \tag{7.10}$$

$$\frac{\partial P}{\partial r} = -\frac{Gm}{r^2}\rho, \tag{7.11}$$

$$\frac{\partial T}{\partial r} = \frac{T}{P}\frac{\partial P}{\partial r}\nabla(T,P), \tag{7.12}$$

where r is the radial distance from the planet's center, m the enclosed mass, P the pressure, ρ the density, and G the gravitational constant. The intrinsic luminosity of a planet is assumed to be constant as a function of the planet radius. The gradient ∇ depends on the process by which the energy is transported (radiative diffusion or convection).

These calculations yield the radii of the planets given their mass and bulk composition, namely the mass fractions of iron, silicates,

water, and H/He. These quantities are yielded by the planet formation and planetesimal dehydration models. For the H/He envelope, the equation of state of Saumon, Chabrier, and Horn (1995) is used to solve the structure equations, while for the solid part of the planet, including the water content, the modified polytropic equations of state of Seager et al. (2007) are employed. The transit radius is estimated as in Guillot (2010).

The loss of the primordial H/He envelope by atmospheric escape is considered in the energy- and radiation-recombination-limited approximation as described in Jin et al. (2014) and results in the loss of the H/He for low-mass planets at smaller orbital distances. For such planets without H/He, the radius depends strongly on the water mass fraction (Jin and Mordasini, 2018) and thus reveals the dehydration caused by different contents of ^{26}Al.

7.5.4 *Parameter space*

From gamma-ray observations (Smith, 2003) and the compositional inventory of planetary debris around white dwarfs (Jura, Xu, and Young, 2013; Jura and Young, 2014) there is evidence for a widespread distribution of ^{26}Al in the galaxy. Because ^{26}Al can only be produced in a massive star with $M_{\text{star}} \gtrsim 20 M_{\odot}$, the stellar initial mass function in conjunction with the dynamics in young star-forming regions suggests a strongly non-uniform enrichment pattern (Adams, 2010; Adams, Fatuzzo, and Holden, 2014; Gounelle, 2015; Pfalzner et al., 2015; Lichtenberg, Parker, and Meyer, 2016; Kuffmeier et al., 2016; Parker, Lichtenberg, and Quanz, 2017; Nicholson and Parker, 2017; Dwarkadas et al., 2017) with order of magnitude deviations from the Solar system's 'canonical' ^{26}Al value of $^{26}\text{Al}_{\odot} = {}^{26}\text{Al}/{}^{27}\text{Al} = 5.25 \times 10^{-5}$ (Kita et al., 2013). To account for these variations, we consider values in the range $^{26}\text{Al}_0$ = [0.1, 10] $\times$ $^{26}\text{Al}_{\odot}$. In addition to initial ^{26}Al abundance, the radii of planetesimals during accretion yield different thermal evolutionary sequences and thus dehydration patterns (Lichtenberg et al., 2016; Monteux et al., 2018). Here, we test values in the range r_{plts} = [1, 100] km. However, we note that from asteroid-belt inferences and numerical studies of the streaming instability mechanism, radii larger than $\gtrsim$ 30–50 km (Johansen et al., 2015; Klahr and Schreiber, 2016; Simon et al., 2017; Delbo et al., 2017; Tsirvoulis et al., 2018) are expected. The most important parameters for this study are listed in Table 7.1, all others are identical to Lichtenberg et al. (2016) and Monteux et al. (2018).

The innermost radius of the disk is of the order 0.1 au and can vary over time. Disk lifetimes are distributed around 5 Myr, which is controlled via the photoevaporation rate (Fortier et al., 2013) and in agreement with current disk surveys (Meng et al., 2017; Kral, Clarke, and Wyatt, 2017). We vary in a Monte Carlo fashion (Mordasini, Alibert,

Parameter	Value/Range	Unit
^{26}Al abundance $^{26}\mathrm{Al}_0$	[0.1, 10]	$^{26}\mathrm{Al}_\odot$
Planetesimal radii r_{plts}	[1, 100]	km
Helium fraction	0.24	non-dim.
Planetesimal water fraction	0.3	non-dim.
α_{disk}-viscosity	2×10^{-3}	non-dim.
Initial embryo mass	0.0123	M_{Earth}
G-star embryo range	[0.05, 40]	au
M-star embryo range	[0.00855, 23.4]	au

Table 7.1: Parameters for the planetesimal interior and planet formation model.

and Benz, 2009) the disk mass, lifetime, dust-to-gas ratio and the exponential cut-off radius (Mordasini et al., 2012) to represent the diversity found in nature Andrews et al., 2010; Ansdell et al., 2016.

ACKNOWLEDGMENTS The authors thank Edwin Kite and Richard Parker for comments that improved the manuscript. TL was supported by ETH Zürich Research Grant ETH-17 13-1, and acknowledges partial financial support from the Swiss Society for Astrophysics and Astronomy trough a MERAC grant. YA acknowledges support from the Swiss National Science Foundation. The numerical simulations in this work were partially performed on the EULER computing cluster of ETH Zürich, and were analyzed using the open source software environments MATPLOTLIB[1] and SEABORN[2]. Parts of this work have been carried out within the framework of the National Center for Competence in Research PlanetS supported by the Swiss National Science Foundation.

1 matplotlib.org (Hunter, 2007)
2 seaborn.pydata.org

Part IV

CONCLUSIONS & FUTURE RESEARCH

What did I learn and find out over the course of this thesis? In this final part I summarize the main conclusions from each of the sections. I point out the linking elements and how each of the separate topics are connected in a grand view. Finally, I draw general conclusions, interpret my findings in light of the exoplanet population, and offer possible avenues for future research.

8

SUMMARY & CONCLUSIONS

8.1 GRAND CONTEXT

Where is everyone? Did the cosmic party of all life happen without us?[1] Or was never anyone else around? If there is a bottleneck, is it before or behind us (Chopra and Lineweaver, 2016; Nicholson et al., 2018)?

Sometime between ∼4.5–3.9 Gyr ago, life emerged on planet Earth (Pearce et al., 2018). Compared to this 200–800 million year timespan for the origin of life on one planet with suitable environmental conditions, the age of the universe of ∼13.8 Gyr multiplied by the probably vast number of planets seems to offer infinite opportunity for a cosmic neighborhood teeming with life. In the grand view of things, the Solar system appears to be just one iteration of the zillions of planetary systems in our home galaxy. However, it is the place we happen to originate from and spend our entire lives. Compared to cosmic scales, we are confined to see the spectacle out there through the narrow perspective of a water-filled, oxygen-addicted mammal that partly disengaged from its primary procreative destiny just the fraction of a second ago. Naturally, our understanding grows slowly and follows the patterns we find around us, the ones we can understand the best.

The work I presented in this thesis tried to contribute to the – first slow, now ever-more rapid – broadening of our cosmic horizon. Rocky planets, the only places where we are sure life can exist, are complex entities. All four rocky planets in the Solar system – Mercury, Venus, Earth and Mars – are strikingly different from each other in structural and compositional properties, and so must be their histories. Luckily, since the beginning of the exoplanet revolution we are *not* confined anymore to our tiny speckle of stellar debris in the Solar system. We can peek out to check what else is there, and compare it with our home planet and its siblings. We can eventually find out whether Earth really is a special place out there, or if we find, once again, that it is not as special as we deemed it to be. As I pointed out in Chapter 1, we are just at the very beginning of placing the Solar system into the wider context of exoplanetary systems. At the time of writing, June 19, 2018, the global race to detect Earth-like worlds is ongoing. Despite frequent media headlines about a postulated detection of *Earth 2.0*, we still did not find an exoplanet that matches Earth in the most

1 Perhaps that would be best for everyone involved, since *homo 'sapiens'* showcased a devastating record in dealing with other beings so far.

important basic characteristics, such as mass, radius, distance to its central star, similar stellar mass and age, and finally, composition; not even considering characteristics that are currently impossible to probe, like tectonic mode (Tackley et al., 2013; Noack and Breuer, 2014; Stamenković and Seager, 2016).

This is where I want to position the work of this thesis. Even with ever-increasing observational capabilities, our knowledge surrounding extrasolar planets will *always* remain limited compared to the Solar system planets. The best we can work toward in the next several years is to collect data as precise as possible on mass and radius, and if we are lucky enough and can allocate enough telescope time, a glimpse of the atmospheric composition, possibly only the uppermost layers at most (Kreidberg et al., 2014; Sing et al., 2016). Therefore, an in-depth analysis of the exoplanet population needs to make use of the entirety of resources and knowledge we can lay our hands on. This means we must aim to understand as much as possible of the entire life cycle and evolutionary regimes of planets.

A planet's current thermo-physical state depends on how it evolved to this certain point. Take Earth as an example: there is now ample evidence for multiple periods of extended glaciation over Earth's history, so-called *snowball* episodes (Hoffman et al., 2017), during which its *habitability*[2] may have been severely limited. Therefore, the current atmospheric regime and surface conditions of a planet do not necessarily constrain its entire life cycle. On a planetary system level, dynamic instabilities may or may not lead to episodes of frequent bombardment (Boehnke and Harrison, 2016; Morbidelli et al., 2018) and render rocky planets' surfaces hellish wastelands for extended periods of time. As a result of this, we need to strategically invest into a *planetary systems science* approach (Pierrehumbert, 2013; Scharf, Fischer, and Meadows, 2018; Apai et al., 2018) that draws synergies from relevant disciplines in order to gain a holistic understanding of planetary growth and evolution. In the following section, I will outline how the collective findings of this thesis contribute to this long-term goal.

8.2 CHAPTER SUMMARY

8.2.1 *Part i*

CHAPTER 2 I started out with modeling the isotope enrichment of forming planetary systems with ^{26}Al and ^{60}Fe, the two most crucial SLRs in terms of internal heating of rocky bodies. My work here focused on intermediate to dense star-forming regions, which are expected to be the nurseries of the majority of stars in the Milky Way

2 Which I define in this context as the propensity of a planet for biogenesis, or support of already existing life forms.

galaxy. While the stars form, the most massive stars go supernova and eject the material that was fused inside them to the surroundings, enriching the disks of lower-mass stars that are actively forming planets. I calculated the effectiveness of this process and derived a distribution function for maximum SLR enrichment. I found a distribution dichotomy between planetary systems, where disks are either strongly enriched to Solar system-like levels with ^{26}Al, or not enriched at all. The relative fraction of these two regimes varies depending on the morphology of the star-forming region, but typically yields fractions of enriched systems on the order of $\sim$5–10%.

CHAPTER 3 Motivated by the recent developments in the astronomical community – the hypothesized existence of a formerly unknown super-Earth-sized planet ('Planet 9') in the outer Solar system, we calculated the odds that it was captured from the Sun's star-forming region instead of having formed within the Solar system. Because of its distant orbit, the potential origin of Planet 9 is under heavy debate and may either give us further clues on early Solar system accretion dynamics, or reveal some interaction with the Sun's environment during planet growth. We found the chances for a capture of a free-floating planet to be relatively low for a typical environment of a young star, less than a few per cent. In addition, when taking into account that the Solar system must have passed by a massive star to become enriched in SLRs, this chance drops further, to literally astronomically low numbers. This may either mean that Planet 9 formed in the inner Solar system, or that it simply does not exist. At the time of writing, June 19, 2018, no direct observational signature of Planet 9 has been found, but surveys are on-going.

8.2.2 *Part ii*

CHAPTER 4 The formation mechanism of terrestrial planets' seeds in the disk, planetesimals, is still debated: they likely formed from some sort of rapid gravitational collapse of dense dust grain clouds. In this part of the thesis, I investigated the thermal evolution of rapidly formed planetesimals resulting from the presence of short-lived radionuclides, in particular ^{26}Al. Formerly it was hypothesized that the macroporosity of the material that is acquired during collapse would critically alter the thermal regime of the planetesimals and therefore influence their chemical evolution. Here, I showed that macroporosity is only of secondary importance and presented evolutionary regimes for planetesimals of various sizes and formation times. The timing of the formation and the subsequent evolution of the silicate material, including the formation of internal magma oceans, yields critical insights for forming planets and on-going planetary science missions to asteroid belt objects.

CHAPTER 5 On a bulk scale, the chemical differentiation of planetesimals reveals insights into the origin of meteorites and therefore about how early planetary materials in the Solar system were processed. This, in turn, helps us to distinguish between different models of planetary formation. In this project, I followed-up on the evolution of the silicate melt that arises in planetesimals during internal silicate melting phases using a novel computational method from petrological sciences. I found that during the first ∼1 Myr after CAIs internal magma oceans were prevalent in planetesimals. In bodies formed at ∼1 Myr after CAIs, incipient melts would ascent rapidly to the surface, perhaps resulting in extensive volcanism on the surface of planetesimals. These findings suggest qualitatively distinct evolutionary paths for rocky planetesimals in the early solar system, and may represent two different regimes of core formation in early protoplanets.

8.2.3 *Part iii*

CHAPTER 6 The internal chemical evolution of planetesimals is altered during planet growth by frequent mutual collisions. It is thought that the the world's meteorite collection represents the remnants of the planet building materials. The most pristine of them display peculiar signs of silicate melt droplet inclusions – chondrules. In this chapter, I connected the thermal planetesimal evolution to the debris created in planetesimal collision events. Namely, if and how the debris itself may be consistent with forming the melt droplets in space following reaccretion onto the parent bodies of the meteorites. I found that the materials within early-formed planetesimals undergo the aforementioned magma ocean stages, resulting in rapid metal-silicate separation and isotopic equilibration. The chemical signatures found in chondritic meteorites are inconsistent with this kind of thermochemical processing. This finding puts tight constraints on the source material for meteorites because in the classical accretion paradigm collisions are a generic outcome of planet growth and should populate the Solar system solid material with vast amounts of such chondrule-inconsistent material. Because of the complete absence of material created from magma ocean planetesimal collisions, the real chondrite material must come from a different source than the material that formed the planets. Interaction between these reservoirs must have been limited and separated by either time, space, or both.

CHAPTER 7 In the final chapter, I related the evolution of planetesimals during planet formation to the compositional properties of extrasolar planets in a general framework. Planetesimals that form beyond the water snowline in the disk deliver water to the growing planets during accretion. When the host system of a planet is enriched in SLRs to a certain degree, the internal heating dehydrated

the planetesimals rapidly. In this chapter, I calculate upper limits for planetesimals to retain their water during accretion and relate the efficiency of dehydration to the final bulk water fractions of planets. I showed that in planetesimal-based accretion settings the resulting planet's water fractions are strongly correlated with the dehydration of planetesimals and are therefore anti-correlated with initial SLR abundances. Combining these outcomes with interior structure models of the planets, I derived predictions for planet populations subject to various degrees of radiogenic heating and showed that populations with Solar system-like or higher SLR levels are substantially depleted in water relative to not-enriched planetary systems. The anticipated shift in mean planet radii due to the lack of extended surface water layers for Moon- to Earth-sized planets can be up to several per cent. With the near-future arrival of transit surveys that are sensitive to this planet regime, we may be able to find a statistical trace of SLR-dehydration in the exoplanet population. This will enable us to disentangle planetary systems that are strongly enriched and harbor relatively dry planets from not-enriched planet systems that dominantly form ocean worlds.

8.3 GENERAL CONCLUSIONS

To summarize, this thesis spanned several orders of magnitudes in space and time throughout planet formation: from parsec scales in star-forming regions down to mm-cm scales during chondrule-forming events in the early Solar nebula, from a broad perspective of accretion disks to the dynamical interactions among forming protoplanets. Having investigated details of the accretion process in the Solar system, I then extended the regime to the exoplanet population. Taken at face value, what is the outcome from all these projects combined?

In Chapter 2, I calculated that ^{26}Al and ^{60}Fe should show a dichotomous distribution among planetary systems. Therefore, the potential for heating in exo-planetesimals, and therefore internal differentiation and volatile loss, should follow this picture if the formation of planetesimals can be expected to be rapid, as in the Solar system (cf. Chapter 9). That means that the thermochemical evolution and growth in planetary systems can be divided into two regimes:

Type I planetary systems that are strongly enriched ($\sim$ Solar system levels and higher in integrated SLR heating, including ^{60}Fe) are populated with planetesimals that are strongly heated from within. Simplified, these systems tend to form cores on smaller bodies, and dehydrate from intense radiogenic heating. As a result, these systems form lower-mass planets with lower volatile fractions in the terrestrial planet region.

Type II not-enriched systems form extended metallic cores only when the accretion energy is sufficient to allow internal melting to segregate silicates and metal. Small planetesimals always retain their primordial water abundances and the resulting terrestrial planets acquire substantial amounts of water, exceeding the storage capacity of silicate mantles by orders of magnitude – ocean worlds.

Deviations on this level between the two classes yield striking implications for the propensity of planetary systems to form Earth-like planets. In particular, the bulk chemistry of the rocky material would be altered during the accretion stage. Changes in the bulk composition of planets on the order of magnitude level, as suggested here, predicts different evolutionary paths in planetary systems depending on the presence and level of SLRs at the time of planetesimal formation and planet accretion. On a more detailed level, the anticipated changes between the two planetary system types can be more subtle and require a closer discussion of the accretion physics and redistribution of material. Therefore, I will connect a discussion of these processes with limitations of the results presented in this thesis and suggestions for future research in the next and final chapter.

9 OUTLOOK

To conclude, I discuss critical issues of the projects I carried out in a general framework, and suggest avenues for future research that can help to sharpen our understanding of planet formation and evolution. The grouping here deviates slightly from the thesis section, in order to allow for a more natural flow of the argumentation.

9.1 ENVIRONMENT OF PLANET-FORMING SYSTEMS

In Chapter 2 and 3, I covered two general topics. The first is the star-forming environment of planet-forming disks and the planets that form in them. The second is the relation of the Solar system to the general initial conditions of protoplanetary disks and their distribution, which is of particular importance in relation to the Solar system's abundances in SLRs. As discussed by Nittler and Ciesla (2016), the Solar system enrichment channel is debated in the literature, with authors leaning either toward a single late-stage event after formation of the protoplanetary disk (as put forward in this thesis) or a pre-enrichment of the Solar system material in a triggering scenario. Recent literature focused on the discrepancy in the initial ^{26}Al/^{60}Fe value as measured in meteorites versus predicted rates from stellar evolution models. As pointed out by Adams, Fatuzzo, and Holden (2014), however, the uncertainties in the predicted ^{60}Fe production rates are significant and may attenuate the problem. On the other hand, the enhanced ^{26}Al abundances in stellar winds, as pointed out by Young (2014), were neglected in former literature. Because ^{26}Al and ^{60}Fe are formed at different depths within Wolf-Rayet stars, the ^{26}Al carried away by the winds therefore decouple the ^{26}Al abundances from the ^{26}Al/^{60}Fe ratio predicted from supernova models. However, for their interstellar material mixing models, Young (2014) assumed that Wolf-Rayet stars do not expel material into the surrounding interstellar medium in a supernova event, for which there may be opposing observations (Gal-Yam et al., 2014).

In general, the late-stage enrichment of young planetary systems regions requires complex models that take into account a multitude of physical effects that are complex to treat in conjunction. In this thesis work, I expanded on the direct disk-injection model with N-body simulations that can handle the substructure of star-forming regions. However, I did not take into account the additional contamination with winds, as described above. In addition to the winds, which may shift the regimes derived here toward more enriched systems (with

perhaps varying ^{26}Al/^{60}Fe ratios), the potential age spreads in young clusters (Reggiani et al., 2011; Cottaar, Meyer, and Parker, 2012) may shift the timing of disk-enrichment to be in better consistency with evidence for rapid planetesimal formation in the early Solar nebula (Dauphas and Pourmand, 2011; Kruijer et al., 2014).

From the perspective of the Solar system meteoritic record, these parameters are crucial for the early and brief formation time interval of CAIs, the abundance of FUN-CAIs without ^{26}Al, the (in-)homogeneity of ^{26}Al in the disk and its outer truncation radius, and thus absolute mass budget (Portegies Zwart et al., 2018). In relation to the compositional budget for planets stored in planetesimals, SLRs may contribute significantly to the ionization rate in disks, and therefore the chemical evolution of volatiles before accretion onto planetesimals (Eistrup, Walsh, and van Dishoeck, 2016), which may alter the expected abundances for exoplanet atmospheres with and without ^{26}Al in the host planetary system.

9.2 EVOLUTION OF ROCKY PLANETS' BUILDING BLOCKS

The internal evolution of accreting rocky planets is inherently limited by the assumptions about their growth history. In this work, in chapters 4, 5 and 6, I followed the currently favored scenario of rapid planetesimal formation with limited subsequent growth, which is justified in a scenario dominated by planetesimal formation from the streaming instability mechanism (Johansen et al., 2015; Simon et al., 2017). However, since the accretion physics of pebbles and the guiding parameters are still uncertain, it will be beneficial in the future to investigate how the interior evolution of planetesimals responds to steady growth from accreting dust particles (Visser and Ormel, 2016; Hughes and Boley, 2017; Ormel, 2017).

As an additional step, smaller or larger impacts need to be taken into account, which can alter the planetesimal thermal regime, if it survives the impact (Ciesla et al., 2013). In Chapter 6, I have used a minimalistic treatment of these effects, which in the future requires renewed efforts to couple internal evolution with impacts and additional pebble growth to deliver us a more complete picture of the thermal and chemical evolution of accreting and growing planetesimals.

From a purely petrological and geophysical perspective, all thermal models employed to date suffered from severe methodological shortcomings when dealing with chemical differentiation, both for core-mantle segregation and the exsolution of volatiles such as water. In chapter 4, I did the first step toward having a more petrologically robust model of chemical differentiation by introducing several phases (liquid-solid) that are subdivided into various components. Ideally an updated model should consider both solid and liquid sil-

icates and iron/nickel, and volatile phases. As to the last issue, in Chapter 7, I employed a simplified dehydration criterion, which enabled me to calculate upper limits for water retention. In fact, dehydration of planetesimals should commence at much lower temperatures, where part of the melting water ice is lost via pore water convection and outgassing, and parts react with the ambient rock to form phyllosilicates. However, investigating a more complete picture relevant for planetary accretion requires combining the aforementioned growth and destruction mechanisms with a thermochemically consistent treatment of water-rock reaction kinetics and gas escape from the planetesimals (Castillo-Rogez and Young, 2017).

9.3 PLANETARY ACCRETION, COMPOSITION & LONG-TERM EVOLUTION

From a planet formation perspective, Chapter 6 expanded on the current knowledge surrounding the earliest planetesimal families and the accretion dynamics in the Solar protoplanetary disk. We need to understand when planetesimals form, how their size frequency distribution is constructed and how they interact dynamically with each other in order to draw an ever-complete picture of planetary growth (Benz et al., 2014; Johansen et al., 2015; Drążkowska and Alibert, 2017; Alibert, 2017; Chambers, 2016; Chambers, 2017). Unraveling the Solar system planets' accretion in extreme detail (relative to extrasolar systems) is imperative to be able to predict global patterns in the exoplanet census. Vice versa, the exoplanet census will refine our picture of Solar system accretion once we will be able to probe the terrestrial exoplanet regime.

Planets are formed and evolve through the complex interplay of physics and chemistry (Foley and Driscoll, 2016). Understanding universal trends in the exoplanet population will require a global and transdisciplinary endeavor into the unknown. In the upcoming years, with increasing numbers of characterized rocky planets, we may find and understand currently unknown parametric controls and interplays, such as the shift in planet water abundances as suggested in Chapter 7. Trends in composition, and perhaps accretion dynamics, in addition to the orbital parameters and system architecture will be guiding our understanding in the years to come. Probing planetary systems as a whole will require refinements of planet formation and evolution theory and can be tested against in-depth characterization of planetary archetypes (Jontof-Hutter et al., 2015; Demory et al., 2016; Gillon et al., 2017; Santerne et al., 2018) in conjunction with statistical analysis of the complete exoplanet census (Fulton et al., 2017; Weiss et al., 2018; Millholland, Wang, and Laughlin, 2017) to usher into the era of comparative statistical exoplanetology.

How are the earliest surface environments on rocky planets constructed? What are the primary atmospheric and interior dynamics regimes? How frequent are giant impacts such as the Moon-forming impact in Earth's history? With the forthcoming era of exciting new ground- and space-based observatories, such as TESS, CHEOPS, WFIRST, JWST, OSIRIS-REx, the ELTs, PLATO, Lucy, Psyche, and ARIEL, we are at the edge to unravel ever-deeper mysteries of planetary environments in the universe.

If we are lucky and continue to educate ourselves and keep our home planet intact, perhaps what we find will not only bring a scientific revolution, but also a revolution of our self-perception.

Tim Lichtenberg
June 19, 2018, Zurich

BIBLIOGRAPHY

A'Hearn, M. F. (2017). "The future of NASA's missions." *Nat. Astron.* 1, 0095. DOI: 10.1038/s41550-017-0095.

ALMA Partnership et al. (2015). "The 2014 ALMA Long Baseline Campaign: First Results from High Angular Resolution Observations toward the HL Tau Region." *Astrophys. J. Lett.* 808, L3. DOI: 10.1088/2041-8205/808/1/L3. arXiv: 1503.02649 [astro-ph.SR].

Aarseth, S. J., M. Henon, and R. Wielen (1974). "A comparison of numerical methods for the study of star cluster dynamics." *Astron. Astrophys.* 37, 183–187.

Abbot, D. S., N. B. Cowan, and F. J. Ciesla (2012). "Indication of Insensitivity of Planetary Weathering Behavior and Habitable Zone to Surface Land Fraction." *Astrophys. J.* 756, 178. DOI: 10.1088/0004-637X/756/2/178. arXiv: 1208.1760 [astro-ph.EP].

Abe, Y. (1993). "Physical state of the very early Earth." *Lithos* 30, 223–235. DOI: 10.1016/0024-4937(93)90037-D.

Abe, Y. and T. Matsui (1985). "The formation of an impact-generated H_2O atmosphere and its implications for the early thermal history of the Earth." *J. Geophys. Res.* 90, C545–C560. DOI: 10.1029/JB090iS02p0C545.

Abramov, O. and S. J. Mojzsis (2011). "Abodes for life in carbonaceous asteroids?" *Icarus* 213, 273–279. DOI: 10.1016/j.icarus.2011.03.003.

Adams, E. R., S. Seager, and L. Elkins-Tanton (2008). "Ocean Planet or Thick Atmosphere: On the Mass-Radius Relationship for Solid Exoplanets with Massive Atmospheres." *Astrophys. J.* 673, 1160–1164. DOI: 10.1086/524925. arXiv: 0710.4941.

Adams, F. C. (2010). "The Birth Environment of the Solar System." *Annu. Rev. Astron. Astrophys.* 48, 47–85. DOI: 10.1146/annurev-astro-081309-130830. arXiv: 1001.5444 [astro-ph.SR].

Adams, F. C., M. Fatuzzo, and L. Holden (2014). "Distributions of Short-lived Radioactive Nuclei Produced by Young Embedded Star Clusters." *Astrophys. J.* 789, 86. DOI: 10.1088/0004-637X/789/1/86. arXiv: 1405.5142 [astro-ph.SR].

Adams, F. C., D. Hollenbach, G. Laughlin, and U. Gorti (2004). "Photoevaporation of Circumstellar Disks Due to External Far-Ultraviolet Radiation in Stellar Aggregates." *Astrophys. J.* 611, 360–379. DOI: 10.1086/421989. eprint: astro-ph/0404383.

Ahrens, James, Berk Geveci, and Charles Law (2005). "ParaView: An End-User Tool for Large-Data Visualization." *Elsevier, ISBN-13: 978-0123875822*, 2005.

Akram, W., M. Schönbächler, S. Bisterzo, and R. Gallino (2015). "Zirconium isotope evidence for the heterogeneous distribution of s-process materials in the solar system." *Geochim. Cosmochim. Acta* 165, 484–500. DOI: 10.1016/j.gca.2015.02.013.

Alexander, C. M. O. and D. S. Ebel (2012). "Questions, questions: Can the contradictions between the petrologic, isotopic, thermodynamic, and astrophysical constraints on chondrule formation be resolved?" *Meteorit. Planet. Sci.* 47, 1157–1175. DOI: 10.1111/j.1945-5100.2011.01308.x.

Alexander, C. M. O., J. N. Grossman, D. S. Ebel, and F. J. Ciesla (2008). "The Formation Conditions of Chondrules and Chondrites." *Science* 320, 1617. DOI: 10.1126/science.1156561.

Alexander, R., I. Pascucci, S. Andrews, P. Armitage, and L. Cieza (2014). "The Dispersal of Protoplanetary Disks." *Protostars and Planets VI*, 475–496. DOI: 10.2458/azu_uapress_97808165-31240-ch021. arXiv: 1311.1819 [astro-ph.EP].

Alibert, Y. (2014). "On the radius of habitable planets." *Astron. Astrophys.* 561, A41. DOI: 10.1051/0004-6361/201322293. arXiv: 1311.3039 [astro-ph.EP].

— (2017). "Maximum mass of planetary embryos that formed in core-accretion models." *Astron. Astrophys.* 606, A69. DOI: 10.1051/0004-6361/201630051. arXiv: 1705.06008 [astro-ph.EP].

Alibert, Y. and W. Benz (2017). "Formation and composition of planets around very low mass stars." *Astron. Astrophys.* 598, L5. DOI: 10.1051/0004-6361/201629671. arXiv: 1610.03460 [astro-ph.EP].

Alibert, Y., C. Mordasini, and W. Benz (2011). "Extrasolar planet population synthesis. III. Formation of planets around stars of different masses." *Astron. Astrophys.* 526, A63. DOI: 10.1051/0004-6361/201014760. arXiv: 1101.0513 [astro-ph.EP].

Alibert, Y., C. Mordasini, W. Benz, and C. Winisdoerffer (2005). "Models of giant planet formation with migration and disc evolution." *Astron. Astrophys.* 434, 343–353. DOI: 10.1051/0004-6361:20042032. eprint: astro-ph/0412444.

Alibert, Y., F. Carron, A. Fortier, S. Pfyffer, W. Benz, C. Mordasini, and D. Swoboda (2013). "Theoretical models of planetary system formation: mass vs. semi-major axis." *Astron. Astrophys.* 558, A109. DOI: 10.1051/0004-6361/201321690. arXiv: 1307.4864 [astro-ph.EP].

Allison, R. J., S. P. Goodwin, R. J. Parker, S. F. Portegies Zwart, and R. de Grijs (2010). "The early dynamical evolution of cool, clumpy star clusters." *Mon. Not. R. Astron. Soc.* 407, 1098–1107. DOI: 10.1111/j.1365-2966.2010.16939.x. arXiv: 1004.5244.

Amari, S., R. S. Lewis, and E. Anders (1994). "Interstellar grains in meteorites. I - Isolation of SiC, graphite, and diamond; size distributions of SiC and graphite. II - SiC and its noble gases." *Geochim. Cosmochim. Acta* 58, 459. DOI: 10.1016/0016-7037(94)90477-4.

André, P. et al. (2010). "From filamentary clouds to prestellar cores to the stellar IMF: Initial highlights from the Herschel Gould Belt Survey." *Astron. Astrophys.* 518, L102. DOI: 10.1051/0004-6361/201014666. arXiv: 1005.2618.

André, P., J. Di Francesco, D. Ward-Thompson, S.-I. Inutsuka, R. E. Pudritz, and J. E. Pineda (2014). "From Filamentary Networks to Dense Cores in Molecular Clouds: Toward a New Paradigm for Star Formation." *Protostars and Planets VI*, 27–51. DOI: 10.2458/azu_uapress_97808165-31240-ch002. arXiv: 1312.6232.

Andrews, S. M., D. J. Wilner, A. M. Hughes, C. Qi, and C. P. Dullemond (2010). "Protoplanetary Disk Structures in Ophiuchus. II. Extension to Fainter Sources." *Astrophys. J.* 723, 1241–1254. DOI: 10.1088/0004-637X/723/2/1241. arXiv: 1007.5070 [astro-ph.SR].

Andrews, S. M. et al. (2016). "Ringed Substructure and a Gap at 1 au in the Nearest Protoplanetary Disk." *Astrophys. J. Lett.* 820, L40. DOI: 10.3847/2041-8205/820/2/L40. arXiv: 1603.09352 [astro-ph.EP].

Ansdell, M. et al. (2016). "ALMA Survey of Lupus Protoplanetary Disks. I. Dust and Gas Masses." *Astrophys. J.* 828, 46. DOI: 10.3847/0004-637X/828/1/46. arXiv: 1604.05719 [astro-ph.EP].

Apai, D. et al. (2018). "A comprehensive understanding of planet formation is required for assessing planetary habitability and for the search for life." arXiv: 1803.08682 [astro-ph.EP].

Arney, G., S. D. Domagal-Goldman, V. S. Meadows, E. T. Wolf, E. Schwieterman, B. Charnay, M. Claire, E. Hébrard, and M. G. Trainer (2016). "The Pale Orange Dot: The Spectrum and Habitability of Hazy Archean Earth." *Astrobiology* 16, 873–899. DOI: 10.1089/ast.2015.1422. arXiv: 1610.04515 [astro-ph.EP].

Asphaug, E. (2010). "Similar-sized collisions and the diversity of planets." *Chemie der Erde / Geochemistry* 70, 199–219. DOI: 10.1016/j.chemer.2010.01.004.

Asphaug, E., M. Jutzi, and N. Movshovitz (2011). "Chondrule formation during planetesimal accretion." *Earth Planet. Sci. Lett.* 308, 369–379. DOI: 10.1016/j.epsl.2011.06.007.

Asphaug, Erik (2017). "Signatures of Hit-and-run Collisions." *Planetesimals: Early Differentiation and Consequences for Planets*. Ed. by Linda T. Elkins-Tanton and Benjamin P. Weiss. Cambridge: Cambridge University Press, pp. 7–37. DOI: 10.1017/9781316339794.002.

Bagdassarov, N., G. Solferino, G. J. Golabek, and M. W. Schmidt (2009a). "Centrifuge assisted percolation of Fe-S melts in partially molten peridotite: Time constraints for planetary core formation." *Earth Planet. Sci. Lett.* 288, 84–95. DOI: 10.1016/j.epsl.2009.09.010.

Bagdassarov, N., G. J. Golabek, G. Solferino, and M. W. Schmidt (2009b). "Constraints on the Fe-S melt connectivity in mantle silicates from electrical impedance measurements." *Phys. Earth Planet. Inter.* 177, 139–146. DOI: 10.1016/j.pepi.2009.08.003.

Balay, S., W. D. Gropp, L. Curfman McInnes, and B. F. Smith (1997). "Efficient Management of Parallelism in Object Oriented Numerical Software Libraries." *Modern Software Tools in Scientific Computing*. Ed. by E. Arge, A. M. Bruaset, and H. P. Langtangen. Birkhäuser Press, pp. 163–202.

Balbus, S. A. and J. F. Hawley (1991). "A powerful local shear instability in weakly magnetized disks. I - Linear analysis. II - Nonlinear evolution." *Astrophys. J.* 376, 214–233. DOI: 10.1086/170270.

Bally, J., A. Ginsburg, H. Arce, J. Eisner, A. Youngblood, L. Zapata, and H. Zinnecker (2017). "The ALMA View of the OMC1 Explosion in Orion." *Astrophys. J.* 837, 60. DOI: 10.3847/1538-4357/aa5c8b. arXiv: 1701.01906 [astro-ph.SR].

Barr, A. C. and R. M. Canup (2008). "Constraints on gas giant satellite formation from the interior states of partially differentiated satellites." *Icarus* 198, 163–177. DOI: 10.1016/j.icarus.2008.07.004.

Barshay, S. S. and J. S. Lewis (1976). "Chemistry of primitive solar material." *Annu. Rev. Astron. Astrophys.* 14, 81–94. DOI: 10.1146/annurev.aa.14.090176.000501.

Batygin, K. and M. E. Brown (2016a). "Evidence for a Distant Giant Planet in the Solar System." *Astron. J.* 151, 22. DOI: 10.3847/0004-6256/151/2/22. arXiv: 1601.05438 [astro-ph.EP].

— (2016b). "Generation of Highly Inclined Trans-Neptunian Objects by Planet Nine." *Astrophys. J. Lett.* 833, L3. DOI: 10.3847/2041-8205/833/1/L3. arXiv: 1610.04992 [astro-ph.EP].

Bauer, K. K., M. Schönbächler, M. A. Fehr, T. Vennemann, N. Chaumard, and B. Zanda (2016). "Titanium and Oxygen Isotope Compositions of Individual Chondrules from Ordinary Chondrites." *LPI Contributions* 1921, 6503.

Becker, M., D. C. Hezel, T. Schulz, B.-M. Elfers, and C. Münker (2015). "Formation timescales of CV chondrites from component specific Hf-W systematics." *Earth Planet. Sci. Lett.* 432, 472–482. DOI: 10.1016/j.epsl.2015.09.049.

Bell, C. P. M., T. Naylor, N. J. Mayne, R. D. Jeffries, and S. P. Littlefair (2013). "Pre-main-sequence isochrones - II. Revising star and planet formation time-scales." *Mon. Not. R. Astron. Soc.* 434, 806–831. DOI: 10.1093/mnras/stt1075. arXiv: 1306.3237 [astro-ph.SR].

Benz, W., S. Ida, Y. Alibert, D. Lin, and C. Mordasini (2014). "Planet Population Synthesis." *Protostars and Planets VI*, 691–713. DOI: 10.2458/azu_uapress_9780816531240-ch030. arXiv: 1402.7086 [astro-ph.EP].

Benz, Willy, Shigeru Ida, Yann Alibert, D. N.C. Lin, and Christoph Mordasini (2014). "Planet Population Synthesis." *Protostars and Planets VI*. Ed. by Henrik Beuther, Ralf S. Klessen, C. P. Dullemond, and Thomas Henning. Tucson: University of Arizona Press, pp. 697–713. DOI: 10.2458/azu_uapress_9780816531240-ch030. URL: https://arxiv.org/pdf/1402.7086.pdf.

Bigolski, J. N., M. K. Weisberg, H. C. Connolly, and D. S. Ebel (2016). "Microchondrules in three unequilibrated ordinary chondrites." *Meteorit. Planet. Sci.* 51, 235–260. DOI: 10.1111/maps.12585.

Birnstiel, T., M. Fang, and A. Johansen (2016). "Dust Evolution and the Formation of Planetesimals." *Space Sci. Rev.* 205, 41–75. DOI: 10.1007/s11214-016-0256-1. arXiv: 1604.02952 [astro-ph.SR].

Bizzarro, M., D. Ulfbeck, A. Trinquier, K. Thrane, J. N. Connelly, and B. S. Meyer (2007). "Evidence for a Late Supernova Injection of ^{60}Fe into the Protoplanetary Disk." *Science* 316, 1178. DOI: 10.1126/science.1141040.

Bland, P. A., O. Alard, G. K. Benedix, A. T. Kearsley, O. N. Menzies, L. E. Watt, and N. W. Rogers (2005). "Volatile fractionation in the early solar system and chondrule/matrix complementarity." *Proc. Natl. Acad. Sci.* 102, 13755–13760. DOI: 10.1073/pnas.0501885102.

Blander, M., A. D. Pelton, I.-H. Jung, and R. Weber (2004). "Non-equilibrium concepts lead to a unified explanation of the formation of chondrules and chondrites." *Meteorit. Planet. Sci.* 39, 1897–1910. DOI: 10.1111/j.1945-5100.2004.tb00085.x.

Bodenheimer, P. and J. B. Pollack (1986). "Calculations of the accretion and evolution of giant planets The effects of solid cores." *Icarus* 67, 391–408. DOI: 10.1016/0019-1035(86)90122-3.

Boehler, R., N. von Bargen, and A. Chopelas (1990). "Melting, thermal expansion, and phase transitions of iron at high pressures." *J. Geophys. Res.* 95, 21731–21736. DOI: 10.1029/JB095iB13p21731.

Boehnke, P. and T. M. Harrison (2016). "Illusory Late Heavy Bombardments." *Proceedings of the National Academy of Science* 113, 10802–10806. DOI: 10.1073/pnas.1611535113.

Bonnell, I. A., M. R. Bate, and S. G. Vine (2003). "The hierarchical formation of a stellar cluster." *Mon. Not. R. Astron. Soc.* 343, 413–418. DOI: 10.1046/j.1365-8711.2003.06687.x. eprint: astro-ph/0305082.

Bonsor, A., Z. M. Leinhardt, P. J. Carter, T. Elliott, M. J. Walter, and S. T. Stewart (2015). "A collisional origin to Earth's non-chondritic composition?" *Icarus* 247, 291–300. DOI: 10.1016/j.icarus.2014.10.019. arXiv: 1410.3421 [astro-ph.EP].

Boss, A. P. (2007). "Evolution of the Solar Nebula. VIII. Spatial and Temporal Heterogeneity of Short-lived Radioisotopes and Stable Oxygen Isotopes." *Astrophys. J.* 660, 1707–1714. DOI: 10.1086/513184. eprint: astro-ph/0702069.

— (2017). "Triggering Collapse of the Presolar Dense Cloud Core and Injecting Short-lived Radioisotopes with a Shock Wave. V. Nonisothermal Collapse Regime." *Astrophys. J.* 844, 113. DOI: 10.3847/1538-4357/aa7cf4. arXiv: 1706.09840 [astro-ph.SR].

Boss, A. P. and R. H. Durisen (2005). "Chondrule-forming Shock Fronts in the Solar Nebula: A Possible Unified Scenario for Planet and Chondrite Formation." *Astrophys. J. Lett.* 621, L137–L140. DOI: 10.1086/429160. eprint: astro-ph/0501592.

Boss, A. P. and S. A. Keiser (2015). "Triggering Collapse of the Presolar Dense Cloud Core and Injecting Short-lived Radioisotopes with a Shock Wave. IV. Effects of Rotational Axis Orientation." *Astrophys. J.* 809, 103. DOI: 10.1088/0004-637X/809/1/103. arXiv: 1507.03956 [astro-ph.EP].

Bottinga, Yan and Daniel F Weill (1972). "The viscosity of magmatic silicate liquids: a model calculation." *Am. J. Sci.* 272, 438–475.

Bottke, W. F., D. Nesvorný, R. E. Grimm, A. Morbidelli, and D. P. O'Brien (2006). "Iron meteorites as remnants of planetesimals formed in the terrestrial planet region." *Nature* 439, 821–824. DOI: 10.1038/nature04536.

Bottke, W. and A. Morbidelli (2017). "Using the Main Asteroid Belt to Constrain Planetesimal and Planet Formation." *Planetesimals: Early Differentiation and Consequences for Planets*. Ed. by Linda T. Elkins-Tanton and Benjamin P. Weiss. Cambridge: Cambridge University Press, pp. 38–68. DOI: 10.1017/9781316339794.003.

Bourrier, V. et al. (2017). "Temporal Evolution of the High-energy Irradiation and Water Content of TRAPPIST-1 Exoplanets." *Astron. J.* 154, 121. DOI: 10.3847/1538-3881/aa859c. arXiv: 1708.09484 [astro-ph.EP].

Bressert, E. et al. (2010). "The spatial distribution of star formation in the solar neighbourhood: do all stars form in dense clusters?" *Mon. Not. R. Astron. Soc.* 409, L54–L58. DOI: 10.1111/j.1745-3933.2010.00946.x. arXiv: 1009.1150 [astro-ph.SR].

Brett, R. and M. Sato (1984). "Intrinsic oxygen fugacity measurements on seven chondrites, a pallasite, and a tektite and the redox state of meteorite parent bodies." *Geochim. Cosmochim. Acta* 48, 111–120. DOI: 10.1016/0016-7037(84)90353-3.

Brown, M. E. and K. Batygin (2016). "Observational Constraints on the Orbit and Location of Planet Nine in the Outer Solar System." *Astrophys. J. Lett.* 824, L23. DOI: 10.3847/2041-8205/824/2/L23. arXiv: 1603.05712 [astro-ph.EP].

Budde, G., C. Burkhardt, G. A. Brennecka, M. Fischer-Gödde, T. S. Kruijer, and T. Kleine (2016a). "Molybdenum isotopic evidence for the origin of chondrules and a distinct genetic heritage of carbonaceous and non-carbonaceous meteorites." *Earth Planet. Sci. Lett.* 454, 293–303. DOI: 10.1016/j.epsl.2016.09.020.

Budde, G., T. Kleine, T. S. Kruijer, C. Burkhardt, and K. Metzler (2016b). "Tungsten isotopic constraints on the age and origin of chondrules." *Proc. Natl. Acad. Sci.* 113, 2886–2891. DOI: 10.1073/pnas.1524980113.

Burbine, Thomas H., Francesca E. Demeo, Andrew S. Rivkin, and Vishnu Reddy (2017). "Evidence for Differentiation among Asteroid Families." *Planetesimals: Early Differentiation and Consequences for Planets*. Ed. by Linda T. Elkins-Tanton and Benjamin P. Weiss. Cambridge: Cambridge University Press, pp. 298–320. DOI: 10.1017/9781316339794.014.

Burkhardt, C., T. Kleine, F. Oberli, A. Pack, B. Bourdon, and R. Wieler (2011). "Molybdenum isotope anomalies in meteorites: Constraints on solar nebula evolution and origin of the Earth." *Earth Planet. Sci. Lett.* 312, 390–400. DOI: 10.1016/j.epsl.2011.10.010.

Cameron, A. G. W. and J. W. Truran (1977). "The supernova trigger for formation of the solar system." *Icarus* 30, 447–461. DOI: 10.1016/0019-1035(77)90101-4.

Carpenter, J. M., E. E. Mamajek, L. A. Hillenbrand, and M. R. Meyer (2006). "Evidence for Mass-dependent Circumstellar Disk Evolution in the 5 Myr Old Upper Scorpius OB Association." *Astrophys. J. Lett.* 651, L49–L52. DOI: 10.1086/509121. eprint: astro-ph/0609372.

Carporzen, L., B. P. Weiss, L. T. Elkins-Tanton, D. L. Shuster, D. Ebel, and J. Gattacceca (2011). "Magnetic evidence for a partially differentiated carbonaceous chondrite parent body." *Proc. Natl. Acad. Sci. U.S.A.* 108, 6386–6389. DOI: 10.1073/pnas.1017165108.

Carrera, D., A. Johansen, and M. B. Davies (2015). "How to form planetesimals from mm-sized chondrules and chondrule aggregates." *Astron. Astrophys.* 579, A43. DOI: 10.1051/0004-6361/201425120. arXiv: 1501.05314 [astro-ph.EP].

Carrera, D., U. Gorti, A. Johansen, and M. B. Davies (2017). "Planetesimal Formation by the Streaming Instability in a Photoevaporating Disk." *Astrophys. J.* 839, 16. DOI: 10.3847/1538-4357/aa6932. arXiv: 1703.07895 [astro-ph.EP].

Carter, P. J., Z. M. Leinhardt, T. Elliott, M. J. Walter, and S. T. Stewart (2015). "Compositional Evolution during Rocky Protoplanet Accretion." *Astrophys. J.* 813, 72. DOI: 10.1088/0004-637X/813/1/72. arXiv: 1509.07504 [astro-ph.EP].

Carter, P. J., Z. M. Leinhardt, T. Elliott, S. T. Stewart, and M. J. Walter (2018). "Collisional stripping of planetary crusts." *Earth Planet. Sci. Lett.* 484, 276–286. DOI: 10.1016/j.epsl.2017.12.012. arXiv: 1712.02790 [astro-ph.EP].

Cartwright, A. and A. P. Whitworth (2004). "The statistical analysis of star clusters." *Mon. Not. R. Astron. Soc.* 348, 589–598. DOI: 10.1111/j.1365-2966.2004.07360.x. eprint: astro-ph/0403474.

Castillo-Rogez, J. and E. D. Young (2017). "Origin and Evolution of Volatile-rich Asteroids." *Planetesimals: Early Differentiation and Consequences for Planets*. Ed. by L. T. Elkins-Tanton and B. P. Weiss. Cambridge: Cambridge University Press, pp. 92–114. DOI: 10.1017/9781316339794.005.

Castillo-Rogez, J., T. V. Johnson, M. H. Lee, N. J. Turner, D. L. Matson, and J. Lunine (2009). "^{26}Al decay: Heat production and a revised age for Iapetus." *Icarus* 204, 658–662. DOI: 10.1016/j.icarus.2009.07.025.

Cerantola, V., N. P. Walte, and D. C. Rubie (2015). "Deformation of a crystalline olivine aggregate containing two immiscible liquids: Implications for early core-mantle differentiation." *Earth Planet. Sci. Lett.* 417, 67–77. DOI: 10.1016/j.epsl.2015.02.014.

Chabrier, G. (2003). "Galactic Stellar and Substellar Initial Mass Function." *PASP* 115, 763–795. DOI: 10.1086/376392. eprint: astro-ph/0304382.

Chambers, J. E. (2010). "Planetesimal formation by turbulent concentration." *Icarus* 208, 505–517. DOI: 10.1016/j.icarus.2010.03.004.

— (2016). "Pebble Accretion and the Diversity of Planetary Systems." *Astrophys. J.* 825, 63. DOI: 10.3847/0004-637X/825/1/63. arXiv: 1604.06362 [astro-ph.EP].

Chambers, J. (2017). "Steamworlds: Atmospheric Structure and Critical Mass of Planets Accreting Icy Pebbles." *Astrophys. J.* 849, 30. DOI: 10.3847/1538-4357/aa91d0. arXiv: 1710.03134 [astro-ph.EP].

Chaussidon, M. and M.-C. Liu (2015). "Timing of Nebula Processes That Shaped the Precursors of the Terrestrial Planets." *The Early Earth: Accretion and Differentiation*. Ed. by J. Badro and M. Walter. New Jersey: John Wiley & Sons, Inc., Hoboken, pp. 1–26. DOI: 10.1002/9781118860359.ch1.

Chevalier, R. A. (2000). "Young Circumstellar Disks near Evolved Massive Stars and Supernovae." *Astrophys. J. Lett.* 538, L151–L154. DOI: 10.1086/312814. eprint: astro-ph/0006029.

Chopra, A. and C. H. Lineweaver (2016). "The Case for a Gaian Bottleneck: The Biology of Habitability." *Astrobiology* 16, 7–22. DOI: 10.1089/ast.2015.1387.

Ciesla, F. J. (2007). "Outward Transport of High-Temperature Materials Around the Midplane of the Solar Nebula." *Science* 318, 613. DOI: 10.1126/science.1147273.

Ciesla, F. J. and J. N. Cuzzi (2006). "The evolution of the water distribution in a viscous protoplanetary disk." *Icarus* 181, 178–204. DOI: 10.1016/j.icarus.2005.11.009. eprint: astro-ph/0511372.

Ciesla, F. J., T. M. Davison, G. S. Collins, and D. P. O'Brien (2013). "Thermal consequences of impacts in the early solar system." *Meteorit. Planet. Sci.* 48, 2559–2576. DOI: 10.1111/maps.12236.

Ciesla, F. J., G. D. Mulders, I. Pascucci, and D. Apai (2015). "Volatile Delivery to Planets from Water-rich Planetesimals around Low Mass Stars." *Astrophys. J.* 804, 9. DOI: 10.1088/0004-637X/804/1/9. arXiv: 1502.07412 [astro-ph.EP].

Cieza, L. A. et al. (2016). "Imaging the water snow-line during a protostellar outburst." *Nature* 535, 258–261. DOI: 10.1038/nature18612. arXiv: 1607.03757 [astro-ph.SR].

Clarke, C. J., A. Gendrin, and M. Sotomayor (2001). "The dispersal of circumstellar discs: the role of the ultraviolet switch." *MNRAS* 328.2, 485–491. ISSN: 0035-8711. DOI: 10.1046/j.1365-8711.2001.04891.x. URL: https://academic.oup.com/mnras/article-lookup/doi/10.1046/j.1365-8711.2001.04891.x.

Clayton, D. D. (1977). "Solar system isotopic anomalies - Supernova neighbor or presolar carriers." *Icarus* 32, 255–269. DOI: 10.1016/0019-1035(77)90001-X.

Cleeves, L. I., F. C. Adams, E. A. Bergin, and R. Visser (2013). "Radionuclide Ionization in Protoplanetary Disks: Calculations of Decay Product Radiative Transfer." *Astrophys. J.* 777, 28. DOI: 10.1088/0004-637X/777/1/28. arXiv: 1309.0018 [astro-ph.SR].

Clenet, H., M. Jutzi, J.-A. Barrat, E. I. Asphaug, W. Benz, and P. Gillet (2014). "A deep crust-mantle boundary in the asteroid 4 Vesta." *Nature* 511, 303–306. DOI: 10.1038/nature13499.

Cloutier, R., T. Currie, G. H. Rieke, S. J. Kenyon, Z. Balog, and R. Jayawardhana (2014). "A Deep Spitzer Survey of Circumstellar Disks in the Young Double Cluster, h and χ Persei." *Astrophys. J.* 796, 127. DOI: 10.1088/0004-637X/796/2/127. arXiv: 1408.1724 [astro-ph.SR].

Cobb, A. K. and R. E. Pudritz (2014). "Nature's Starships. I. Observed Abundances and Relative Frequencies of Amino Acids in Meteorites." *Astrophys. J.* 783, 140. DOI: 10.1088/0004-637X/783/2/140. arXiv: 1402.2281 [astro-ph.EP].

Cobb, A. K., R. E. Pudritz, and B. K. D. Pearce (2015). "Nature's Starships. II. Simulating the Synthesis of Amino Acids in Meteorite Parent Bodies." *Astrophys. J.* 809, 6. DOI: 10.1088/0004-637X/809/1/6. arXiv: 1506.06740 [astro-ph.EP].

Connelly, J. N., J. Bollard, and M. Bizzarro (2017). "Pb-Pb chronometry and the early Solar System." *Geochim. Cosmochim. Acta* 201, 345–363. DOI: 10.1016/j.gca.2016.10.044.

Connelly, J. N., M. Bizzarro, A. N. Krot, Å. Nordlund, D. Wielandt, and M. A. Ivanova (2012). "The Absolute Chronology and Thermal Processing of Solids in the Solar Protoplanetary Disk." *Science* 338, 651. DOI: 10.1126/science.1226919.

Connolly, H. C. and R. H. Jones (2016). "Chondrules: The canonical and noncanonical views." *J. Geophys. Res. Planets* 121, 1885–1899. DOI: 10.1002/2016JE005113.

Consolmagno, G. J., G. J. Golabek, D. Turrini, M. Jutzi, S. Sirono, V. Svetsov, and K. Tsiganis (2015). "Is Vesta an intact and pristine protoplanet?" *Icarus* 254, 190–201. DOI: 10.1016/j.icarus.2015.03.029.

Costa, A., L. Caricchi, and N. Bagdassarov (2009). "A model for the rheology of particle-bearing suspensions and partially molten rocks." *Geochem. Geophys. Geosys* 10, 3010. DOI: 10.1029/2008GC002138.

Cottaar, M., M. R. Meyer, and R. J. Parker (2012). "Characterizing a cluster's dynamic state using a single epoch of radial velocities." *Astron. Astrophys.* 547, A35. DOI: 10.1051/0004-6361/201219673. arXiv: 1209.2623 [astro-ph.SR].

Cournede, C., J. Gattacceca, M. Gounelle, P. Rochette, B. P. Weiss, and B. Zanda (2015). "An early solar system magnetic field recorded in CM chondrites." *Earth Planet. Sci. Lett.* 410, 62–74. DOI: 10.1016/j.epsl.2014.11.019.

Cowan, N. B. and D. S. Abbot (2014). "Water Cycling between Ocean and Mantle: Super-Earths Need Not Be Waterworlds." *Astrophys. J.* 781, 27. DOI: 10.1088/0004-637X/781/1/27. arXiv: 1401.0720 [astro-ph.EP].

Crameri, F., H. Schmeling, G. J. Golabek, T. Duretz, R. Orendt, S. J. H. Buiter, D. A. May, B. J. P. Kaus, T. V. Gerya, and P. J. Tackley (2012). "A comparison of numerical surface topography

calculations in geodynamic modelling: an evaluation of the 'sticky air' method." *Geophys. J. Int.* 189, 38–54. DOI: 10.1111/j.1365-246X.2012.05388.x.

Cuzzi, J. N., R. C. Hogan, and K. Shariff (2008). "Toward Planetesimals: Dense Chondrule Clumps in the Protoplanetary Nebula." *Astrophys. J.* 687, 1432–1447. DOI: 10.1086/591239. arXiv: 0804.3526.

Daemgen, S., M. Bonavita, R. Jayawardhana, D. Lafrenière, and M. Janson (2015). "Sub-stellar Companions and Stellar Multiplicity in the Taurus Star-forming Region." *Astrophys. J.* 799, 155. DOI: 10.1088/0004-637X/799/2/155. arXiv: 1411.7031 [astro-ph.SR].

Dale, J. E., B. Ercolano, and I. A. Bonnell (2012a). "Ionization-induced star formation - IV. Triggering in bound clusters." *Mon. Not. R. Astron. Soc.* 427, 2852–2865. DOI: 10.1111/j.1365-2966.2012.22104.x. arXiv: 1208.4486.

— (2012b). "Ionizing feedback from massive stars in massive clusters - II. Disruption of bound clusters by photoionization." *Mon. Not. R. Astron. Soc.* 424, 377–392. DOI: 10.1111/j.1365-2966.2012.21205.x. arXiv: 1205.0360.

Dale, J. E., T. J. Haworth, and E. Bressert (2015). "The dangers of being trigger-happy." *Mon. Not. R. Astron. Soc.* 450, 1199–1211. DOI: 10.1093/mnras/stv396. arXiv: 1502.05865.

Dauphas, N. and A. Pourmand (2011). "Hf-W-Th evidence for rapid growth of Mars and its status as a planetary embryo." *Nature* 473, 489–492. DOI: 10.1038/nature10077.

Davidson, J., D. L. Schrader, C. M. O. Alexander, D. S. Lauretta, H. Busemann, I. A. Franchi, R. C. Greenwood, H. C. Connolly, K. J. Domanik, and A. Verchovsky (2014). "Petrography, stable isotope compositions, microRaman spectroscopy, and presolar components of Roberts Massif 04133: A reduced CV3 carbonaceous chondrite." *Meteorit. Planet. Sci.* 49, 2133–2151. DOI: 10.1111/maps.12377.

Davis, A. M., C. M. O. '. Alexander, F. J. Ciesla, M. Gounelle, A. N. Krot, M. I. Petaev, and T. Stephan (2014). "Samples of the Solar System: Recent Developments." *Protostars and Planets VI*, 809–831. DOI: 10.2458/azu_uapress_9780816531240-ch035.

Davison, T. M., D. P. O'Brien, F. J. Ciesla, and G. S. Collins (2013). "The early impact histories of meteorite parent bodies." *Meteorit. Planet. Sci.* 48, 1894–1918. DOI: 10.1111/maps.12193. arXiv: 1307.7549 [astro-ph.EP].

DeMeo, F. E., C. M. O. Alexander, K. J. Walsh, C. R. Chapman, and R. P. Binzel (2015). "The Compositional Structure of the Asteroid Belt." *Asteroids IV*. Ed. by P. Michel, F. E. DeMeo, and W. F. Bottke. University of Arizona Press, pp. 13–41. DOI: 10.2458/azu_uapress_9780816532131-ch002.

Delbo, M., K. Walsh, B. Bolin, C. Avdellidou, and A. Morbidelli (2017). "Identification of a primordial asteroid family constrains the original planetesimal population." *Science* 357, 1026–1029. DOI: 10.1126/science.aam6036.

Demircan, O. and G. Kahraman (1991). "Stellar mass-luminosity and mass-radius relations." *Astrophys. Space Sci.* 181, 313–322. DOI: 10.1007/BF00639097.

Demory, B.-O. et al. (2016). "A map of the large day-night temperature gradient of a super-Earth exoplanet." *Nature* 532, 207–209. DOI: 10.1038/nature17169. arXiv: 1604.05725 [astro-ph.EP].

Desch, S. J. and H. C. Connolly Jr. (2002). "A model of the thermal processing of particles in solar nebula shocks: Application to the cooling rates of chondrules." *Meteorit. Planet. Sci.* 37, 183–207. DOI: 10.1111/j.1945-5100.2002.tb01104.x.

Desch, S. J., M. A. Morris, H. C. Connolly, and A. P. Boss (2012). "The importance of experiments: Constraints on chondrule formation models." *Meteorit. Planet. Sci.* 47, 1139–1156. DOI: 10.1111/j.1945-5100.2012.01357.x.

Dittkrist, K.-M., C. Mordasini, H. Klahr, Y. Alibert, and T. Henning (2014). "Impacts of planet migration models on planetary populations. Effects of saturation, cooling and stellar irradiation." *Astron. Astrophys.* 567, A121. DOI: 10.1051/0004-6361/201322506. arXiv: 1402.5969 [astro-ph.EP].

Dorn, C., N. R. Hinkel, and J. Venturini (2017). "Bayesian analysis of interiors of HD 219134b, Kepler-10b, Kepler-93b, CoRoT-7b, 55 Cnc e, and HD 97658b using stellar abundance proxies." *Astron. Astrophys.* 597, A38, A38. DOI: 10.1051/0004-6361/201628749.

Doyle, P. M., K. Jogo, K. Nagashima, A. N. Krot, S. Wakita, F. J. Ciesla, and I. D. Hutcheon (2015). "Early aqueous activity on the ordinary and carbonaceous chondrite parent bodies recorded by fayalite." *Nat. Commun.* 6, 7444. DOI: 10.1038/ncomms8444.

Drążkowska, J. and Y. Alibert (2017). "Planetesimal formation starts at the snow line." *Astron. Astrophys.* 608, A92. DOI: 10.1051/0004-6361/201731491. arXiv: 1710.00009 [astro-ph.EP].

Drążkowska, J., Y. Alibert, and B. Moore (2016). "Close-in planetesimal formation by pile-up of drifting pebbles." *Astron. Astrophys.* 594, A105. DOI: 10.1051/0004-6361/201628983. arXiv: 1607.05734 [astro-ph.EP].

Dullemond, C. P., S. M. Stammler, and A. Johansen (2014). "Forming Chondrules in Impact Splashes. I. Radiative Cooling Model." *Astrophys. J.* 794, 91–103. DOI: 10.1088/0004-637X/794/1/91. arXiv: 1501.05791 [astro-ph.EP].

Dullemond, C. P., D. Harsono, S. M. Stammler, and A. Johansen (2016). "Forming Chondrules in Impact Splashes II Volatile Retention." *Astrophys. J.* 832, 91. DOI: 10.3847/0004-637X/832/1/91.

Dunn, T. L., G. Cressey, H. Y. McSween Jr., and T. J. McCoy (2010). "Analysis of ordinary chondrites using powder X-ray diffraction: 1. Modal mineral abundances." *Meteorit. Planet. Sci.* 45, 123–134. DOI: 10.1111/j.1945-5100.2009.01011.x.

Dwarkadas, V. V., N. Dauphas, B. Meyer, P. Boyajian, and M. Bojazi (2017). "Triggered Star Formation inside the Shell of a Wolf-Rayet Bubble as the Origin of the Solar System." *Astrophys. J.* 851, 147. DOI: 10.3847/1538-4357/aa992e. arXiv: 1712.10053 [astro-ph.SR].

Ebel, D. S. and L. Grossman (2000). "Condensation in dust-enriched systems." *Geochim. Cosmochim. Acta* 64, 339–366. DOI: 10.1016/S0016-7037(99)00284-7.

Ebel, D. S., C. Brunner, K. Konrad, K. Leftwich, I. Erb, M. Lu, H. Rodriguez, E. J. Crapster-Pregont, J. M. Friedrich, and M. K. Weisberg (2016). "Abundance, major element composition and size of components and matrix in CV, CO and Acfer 094 chondrites." *Geochim. Cosmochim. Acta* 172, 322–356. DOI: 10.1016/j.gca.2015.10.007.

Eistrup, C., C. Walsh, and E. F. van Dishoeck (2016). "Setting the volatile composition of (exo)planet-building material. Does chemical evolution in disk midplanes matter?" *Astron. Astrophys.* 595, A83. DOI: 10.1051/0004-6361/201628509. arXiv: 1607.06710 [astro-ph.EP].

Elkins-Tanton, L. T. (2008). "Linked magma ocean solidification and atmospheric growth for Earth and Mars." *Earth Planet. Sci. Lett.* 271, 181–191. DOI: 10.1016/j.epsl.2008.03.062.

— (2011). "Formation of early water oceans on rocky planets." *Astrophys. Space Sci.* 332, 359–364. DOI: 10.1007/s10509-010-0535-3. arXiv: 1011.2710 [astro-ph.EP].

— (2012). "Magma Oceans in the Inner Solar System." *Annu. Rev. Earth Planet. Sci.* 40, 113–139. DOI: 10.1146/annurev-earth-042711-105503.

Elkins-Tanton, L. T. and S. Seager (2008). "Ranges of Atmospheric Mass and Composition of Super-Earth Exoplanets." *Astrophys. J.* 685, 1237–1246. DOI: 10.1086/591433. arXiv: 0808.1909.

Elkins-Tanton, L. T., B. P. Weiss, and M. T. Zuber (2011). "Chondrites as samples of differentiated planetesimals." *Earth Planet. Sci. Lett.* 305, 1–10. DOI: 10.1016/j.epsl.2011.03.010.

Elmegreen, B. G. (2000). "Star Formation in a Crossing Time." *Astrophys. J.* 530, 277–281. DOI: 10.1086/308361. eprint: astro-ph/9911172.

Elmegreen, B. G. and D. M. Elmegreen (2001). "Fractal Structure in Galactic Star Fields." *Astron. J.* 121, 1507–1511. DOI: 10.1086/319416. eprint: astro-ph/0012184.

Elser, S., M. R. Meyer, and B. Moore (2012). "On the origin of elemental abundances in the terrestrial planets." *Icarus* 221, 859–874. DOI: 10.1016/j.icarus.2012.09.016. arXiv: 1209.3635 [astro-ph.EP].

Facchini, S., C. J. Clarke, and T. G. Bisbas (2016). "External photoevaporation of protoplanetary discs in sparse stellar groups: the impact of dust growth." *Mon. Not. R. Astron. Soc.* 457, 3593–3610. DOI: 10.1093/mnras/stw240. arXiv: 1601.07562 [astro-ph.SR].

Fischer, D. A. and J. Valenti (2005). "The Planet-Metallicity Correlation." *Astrophys. J.* 622, 1102–1117. DOI: 10.1086/428383.

Flaherty, K. M., A. M. Hughes, K. A. Rosenfeld, S. M. Andrews, E. Chiang, J. B. Simon, S. Kerzner, and D. J. Wilner (2015). "Weak Turbulence in the HD 163296 Protoplanetary Disk Revealed by ALMA CO Observations." *Astrophys. J.* 813, 99. DOI: 10.1088/0004-637X/813/2/99. arXiv: 1510.01375 [astro-ph.SR].

Foley, B. J. and P. E. Driscoll (2016). "Whole planet coupling between climate, mantle, and core: Implications for rocky planet evolution." *Geochem. Geophys. Geosys.* 17, 1885–1914. DOI: 10.1002/2015GC006210.

Fortier, A., Y. Alibert, F. Carron, W. Benz, and K.-M. Dittkrist (2013). "Planet formation models: the interplay with the planetesimal disc." *Astron. Astrophys.* 549, A44. DOI: 10.1051/0004-6361/201220241. arXiv: 1210.4009 [astro-ph.EP].

Fu, R. R. and L. T. Elkins-Tanton (2014). "The fate of magmas in planetesimals and the retention of primitive chondritic crusts." *Earth Planet. Sci. Lett.* 390, 128–137. DOI: 10.1016/j.epsl.2013.12.047.

Fu, R. R., E. D. Young, R. C. Greenwood, and L. T. Elkins-Tanton (2017). "Silicate Melting and Volatile Loss During Differentiation in Planetesimals." *Planetesimals: Early Differentiation and Consequences for Planets*. Ed. by Linda T. Elkins-Tanton and Benjamin P. Weiss. Cambridge: Cambridge University Press, pp. 115–135. DOI: 10.1017/9781316339794.006.

Fu, R., R. J. O'Connell, and D. D. Sasselov (2010). "The Interior Dynamics of Water Planets." *Astrophys. J.* 708, 1326–1334. DOI: 10.1088/0004-637X/708/2/1326. arXiv: 1001.2890 [astro-ph.EP].

Fulton, B. J. et al. (2017). "The California-Kepler Survey. III. A Gap in the Radius Distribution of Small Planets." *Astron. J.* 154, 109. DOI: 10.3847/1538-3881/aa80eb. arXiv: 1703.10375 [astro-ph.EP].

Gaidos, E., A. N. Krot, J. P. Williams, and S. N. Raymond (2009). "^{26}Al and the Formation of the Solar System from a Molecular Cloud Contaminated by Wolf-Rayet Winds." *Astrophys. J.* 696, 1854–1863. DOI: 10.1088/0004-637X/696/2/1854. arXiv: 0901.3364 [astro-ph.EP].

Gail, H.-P., S. Henke, and M. Trieloff (2015). "Thermal evolution and sintering of chondritic planetesimals. II. Improved treatment of the compaction process." *Astron. Astrophys.* 576, A60. DOI: 10.1051/0004-6361/201424278. arXiv: 1411.2850 [astro-ph.EP].

Gal-Yam, A. et al. (2014). "A Wolf-Rayet-like progenitor of SN 2013cu from spectral observations of a stellar wind." *Nature* 509, 471–474. DOI: 10.1038/nature13304. arXiv: 1406.7640 [astro-ph.HE].

Genda, H. and Y. Abe (2003). "Survival of a proto-atmosphere through the stage of giant impacts: the mechanical aspects." *Icarus* 164, 149–162. DOI: 10.1016/S0019-1035(03)00101-5.

Gerya, T. V. and D. A. Yuen (2003). "Characteristics-based marker-in-cell method with conservative finite-differences schemes for modeling geological flows with strongly variable transport properties." *Phys. Earth Planet. Int.* 140, 293–318. DOI: 10.1016/j.pepi.2003.09.006.

— (2007). "Robust characteristics method for modelling multiphase visco-elasto-plastic thermo-mechanical problems." *Phys. Earth Planet. Inter.* 163, 83–105. DOI: 10.1016/j.pepi.2007.04.015.

Gerya, T. V., R. J. Stern, M. Baes, S. V. Sobolev, and S. A. Whattam (2015). "Plate tectonics on the Earth triggered by plume-induced subduction initiation." *Nature* 527, 221–225. DOI: 10.1038/nature15752.

Getman, K. V., E. D. Feigelson, and M. A. Kuhn (2014). "Core-Halo Age Gradients and Star Formation in the Orion Nebula and NGC 2024 Young Stellar Clusters." *Astrophys. J.* 787, 109. DOI: 10.1088/0004-637X/787/2/109. arXiv: 1403.2742 [astro-ph.SR].

Ghosh, A. and H. Y. McSween (1998). "A Thermal Model for the Differentiation of Asteroid 4 Vesta, Based on Radiogenic Heating." *Icarus* 134, 187–206. DOI: 10.1006/icar.1998.5956.

Gillon, M. et al. (2016). "Temperate Earth-sized planets transiting a nearby ultracool dwarf star." *Nature* 533, 221–224. DOI: 10.1038/nature17448. arXiv: 1605.07211 [astro-ph.EP].

Gillon, M. et al. (2017). "Seven temperate terrestrial planets around the nearby ultracool dwarf star TRAPPIST-1." *Nature* 542, 456–460. DOI: 10.1038/nature21360. arXiv: 1703.01424 [astro-ph.EP].

Girichidis, P., C. Federrath, R. Allison, R. Banerjee, and R. S. Klessen (2012). "Importance of the initial conditions for star formation - III. Statistical properties of embedded protostellar clusters." *Mon. Not. R. Astron. Soc.* 420, 3264–3280. DOI: 10.1111/j.1365-2966.2011.20250.x. arXiv: 1111.5440 [astro-ph.SR].

Golabek, G. J., B. Bourdon, and T. V. Gerya (2014). "Numerical models of the thermomechanical evolution of planetesimals: Application to the acapulcoite-lodranite parent body." *Meteorit. Planet. Sci.* 49, 1083–1099. DOI: 10.1111/maps.12302.

Golabek, G. J., T. Keller, T. V. Gerya, G. Zhu, P. J. Tackley, and J. A. D. Connolly (2011). "Origin of the martian dichotomy and Tharsis from a giant impact causing massive magmatism." *Icarus* 215, 346–357. DOI: 10.1016/j.icarus.2011.06.012.

Goldreich, P., Y. Lithwick, and R. Sari (2004). "Planet Formation by Coagulation: A Focus on Uranus and Neptune." *Annu. Rev. Astron. Astrophys.* 42, 549–601. DOI: 10.1146/annurev.astro.42.053102.134004. eprint: astro-ph/0405215.

Goodwin, S. P. and A. P. Whitworth (2004). "The dynamical evolution of fractal star clusters: The survival of substructure." *Astron. Astrophys.* 413, 929–937. DOI: 10.1051/0004-6361:20031529. eprint: astro-ph/0310333.

Gounelle, M. (2015). "The abundance of ^{26}Al-rich planetary systems in the Galaxy." *Astron. Astrophys.* 582, A26. DOI: 10.1051/0004-6361/201526174.

Gounelle, M. and A. Meibom (2008). "The Origin of Short-lived Radionuclides and the Astrophysical Environment of Solar System Formation." *Astrophys. J.* 680, 781–792. DOI: 10.1086/587613.

Gounelle, M. and G. Meynet (2012). "Solar system genealogy revealed by extinct short-lived radionuclides in meteorites." *Astron. Astrophys.* 545, A4. DOI: 10.1051/0004-6361/201219031. arXiv: 1208.5879 [astro-ph.SR].

Greenberg, R., W. K. Hartmann, C. R. Chapman, and J. F. Wacker (1978). "Planetesimals to planets - Numerical simulation of collisional evolution." *Icarus* 35, 1–26. DOI: 10.1016/0019-1035(78)90057-X.

Grimm, R. E. and H. Y. McSween (1993). "Heliocentric zoning of the asteroid belt by aluminum-26 heating." *Science* 259, 653–655.

Grimm, R. E. and H. Y. McSween Jr. (1989). "Water and the thermal evolution of carbonaceous chondrite parent bodies." *Icarus* 82, 244–280. DOI: 10.1016/0019-1035(89)90038-9.

Grimm, S. L. et al. (2018). "The nature of the TRAPPIST-1 exoplanets." *Astron. Astrophys., in press.* arXiv: 1802.01377 [astro-ph.EP].

Gritschneder, M., D. N. C. Lin, S. D. Murray, Q.-Z. Yin, and M.-N. Gong (2012). "The Supernova Triggered Formation and Enrichment of Our Solar System." *Astrophys. J.* 745, 22. DOI: 10.1088/0004-637X/745/1/22. arXiv: 1111.0012 [astro-ph.SR].

Guillot, T. (2010). "On the radiative equilibrium of irradiated planetary atmospheres." *Astron. Astrophys.* 520, 27.

Hacar, A., M. Tafalla, J. Kauffmann, and A. Kovács (2013). "Cores, filaments, and bundles: hierarchical core formation in the L1495/B213 Taurus region." *Astron. Astrophys.* 554, A55. DOI: 10.1051/0004-6361/201220090. arXiv: 1303.2118.

Haisch Jr., K. E., E. A. Lada, and C. J. Lada (2001). "Disk Frequencies and Lifetimes in Young Clusters." *Astrophys. J. Lett.* 553, L153–L156. DOI: 10.1086/320685. eprint: astro-ph/0104347.

Hamano, K., Y. Abe, and H. Genda (2013). "Emergence of two types of terrestrial planet on solidification of magma ocean." *Nature* 497, 607–610. DOI: 10.1038/nature12163.

Hartmann, L. (2009). *Accretion Processes in Star Formation: Second Edition*. Cambridge University Press.

Hasegawa, Y., S. Wakita, Y. Matsumoto, and S. Oshino (2016). "Chondrule Formation via Impact Jetting Triggered by Planetary Accretion." *Astrophys. J.* 816, 8–22. DOI: 10.3847/0004-637X/816/1/8. arXiv: 1511.03344 [astro-ph.EP].

Henke, S., H.-P. Gail, M. Trieloff, W. H. Schwarz, and T. Kleine (2012a). "Thermal evolution and sintering of chondritic planetesimals." *Astron. Astrophys.* 537, A45. DOI: 10.1051/0004-6361/201117177. arXiv: 1110.4818 [astro-ph.EP].

— (2012b). "Thermal history modelling of the H chondrite parent body." *Astron. Astrophys.* 545, A135. DOI: 10.1051/0004-6361/201219100. arXiv: 1208.4633 [astro-ph.EP].

Henshaw, J. D., I. Jiménez-Serra, S. N. Longmore, P. Caselli, J. E. Pineda, A. Avison, A. T. Barnes, J. C. Tan, and F. Fontani (2017). "Unveiling the early-stage anatomy of a protocluster hub with ALMA." *Mon. Not. R. Astron. Soc.* 464, L31–L35. DOI: 10.1093/mnrasl/slw154. arXiv: 1608.00009.

Herzberg, C., P. Raterron, and J. Zhang (2000). "New experimental observations on the anhydrous solidus for peridotite KLB-1." *Geochem. Geophys. Geosyst.* 1, 1051–14. DOI: 10.1029/2000GC000089.

Hevey, P. J. and I. S. Sanders (2006). "A model for planetesimal meltdown by ^{26}Al and its implications for meteorite parent bodies." *Meteorit. Planet. Sci.* 41, 95–106. DOI: 10.1111/j.1945-5100.2006.tb00195.x.

Hewins, R. H., B. Zanda, and C. Bendersky (2012). "Evaporation and recondensation of sodium in Semarkona Type II chondrules." *Geochim. Cosmochim. Acta* 78, 1–17. DOI: 10.1016/j.gca.2011.11.027.

Hezel, D. C. and H. Palme (2007). "The conditions of chondrule formation, Part I: Closed system." *Geochim. Cosmochim. Acta* 71, 4092–4107. DOI: 10.1016/j.gca.2007.06.035.

— (2008). "Constraints for chondrule formation from Ca-Al distribution in carbonaceous chondrites." *Earth Planet. Sci. Lett.* 265, 716–725. DOI: 10.1016/j.epsl.2007.11.003.

— (2010). "The chemical relationship between chondrules and matrix and the chondrule matrix complementarity." *Earth Planet. Sci. Lett.* 294, 85–93. DOI: 10.1016/j.epsl.2010.03.008.

Hillenbrand, L. A., S. E. Strom, N. Calvet, K. M. Merrill, I. Gatley, R. B. Makidon, M. R. Meyer, and M. F. Skrutskie (1998). "Circumstellar Disks in the Orion Nebula Cluster." *Astron. J.* 116, 1816–1841. DOI: 10.1086/300536.

Hiraga, T., C. Tachibana, N. Ohashi, and S. Sano (2010). "Grain growth systematics for forsterite ± enstatite aggregates: Effect of lithology on grain size in the upper mantle." *Earth Planet. Sci. Lett.* 291, 10–20. DOI: 10.1016/j.epsl.2009.12.026.

Hirschmann, M. M., A. C. Withers, P. Ardia, and N. T. Foley (2012). "Solubility of molecular hydrogen in silicate melts and consequences for volatile evolution of terrestrial planets." *Earth Planet. Sci. Lett.* 345, 38–48. DOI: 10.1016/j.epsl.2012.06.031.

Hirth, G. and D. Kohlstedt (2003). "Rheology of the upper mantle and the mantle wedge: A view from the experimentalists." *Inside the subduction Factory*, 83–105.

Hoffman, P. F. et al. (2017). "Snowball Earth climate dynamics and Cryogenian geology-geobiology." *Sci. Adv.* 3, e1600983. DOI: 10.1126/sciadv.1600983.

Holman, M. J. and M. J. Payne (2016a). "Observational Constraints on Planet Nine: Astrometry of Pluto and Other Trans-Neptunian Objects." *Astron. J.* 152, 80. DOI: 10.3847/0004-6256/152/4/80. arXiv: 1603.09008 [astro-ph.EP].

— (2016b). "Observational Constraints on Planet Nine: Cassini Range Observations." *Astron. J.* 152, 94. DOI: 10.3847/0004-6256/152/4/94. arXiv: 1604.03180 [astro-ph.EP].

Holzheid, Astrid (2013). "Sulphide melt distribution in partially molten silicate aggregates: implications to core formation scenarios in terrestrial planets." *Eur. J. Mineral.* 25, 267–277.

Howard, L. N. (1964). "Convection at high Rayleigh number." Ed. by H. Gørtler. Proceedings of the 11th International Congress in Applied Mechanics. Springer, Berlin, pp. 1109–1115.

Hughes, A. G. and A. C. Boley (2017). "Simulations of small solid accretion on to planetesimals in the presence of gas." *Mon. Not. R. Astron. Soc.* 472, 3543–3553. DOI: 10.1093/mnras/stx1964. arXiv: 1708.00450 [astro-ph.EP].

Hunt, A. C., D. L. Cook, T. Lichtenberg, P. M. Reger, M. Ek, G. J. Golabek, and M. Schönbächler (2018). "Late metal-silicate separation on the IAB parent asteroid: Constraints from combined W

and Pt isotopes and thermal modelling." *Earth and Planetary Science Letters* 482, 490–500. DOI: 10.1016/j.epsl.2017.11.034. arXiv: 1802.10421 [astro-ph.EP].

Hunter, John D. (2007). "Matplotlib: A 2D graphics environment." *Computing In Science & Engineering* 9, 90–95.

Hutchison, R. (2004). *Meteorites, Cambridge University Press*, p. 520.

Hwang, U. and J. M. Laming (2012). "A Chandra X-Ray Survey of Ejecta in the Cassiopeia A Supernova Remnant." *Astrophys. J.* 746, 130. DOI: 10.1088/0004-637X/746/2/130. arXiv: 1111.7316 [astro-ph.HE].

Inaba, S. and M. Ikoma (2003). "Enhanced collisional growth of a protoplanet that has an atmosphere." *Astron. Astrophys.* 410, 711–723. DOI: 10.1051/0004-6361:20031248.

Inaba, S., H. Tanaka, K. Nakazawa, G. W. Wetherill, and E. Kokubo (2001). "High-Accuracy Statistical Simulation of Planetary Accretion: II. Comparison with N-Body Simulation." *Icarus* 149, 235–250. DOI: 10.1006/icar.2000.6533.

Isella, A. et al. (2016). "Ringed Structures of the HD 163296 Protoplanetary Disk Revealed by ALMA." *Phys. Rev. Lett.* 117.25, 251101. DOI: 10.1103/PhysRevLett.117.251101.

Izidoro, A., S. N. Raymond, A. Pierens, A. Morbidelli, O. C. Winter, and D. Nesvorny' (2016). "The Asteroid Belt as a Relic from a Chaotic Early Solar System." *Astrophys. J.* 833, 40–58. DOI: 10.3847/1538-4357/833/1/40. arXiv: 1609.04970 [astro-ph.EP].

Jacobsen, B., Q.-Z. Yin, F. Moynier, Y. Amelin, A. N. Krot, K. Nagashima, I. D. Hutcheon, and H. Palme (2008). "^{26}Al- ^{26}Mg and ^{207}Pb- ^{206}Pb systematics of Allende CAIs: Canonical solar initial ^{26}Al/ ^{27}Al ratio reinstated." *Earth Planet. Sci. Lett.* 272, 353–364. DOI: 10.1016/j.epsl.2008.05.003.

Jacobson, S. A. and K. J. Walsh (2015). "Earth and Terrestrial Planet Formation." *The Early Earth: Accretion and Differentiation*. Ed. by J. Badro and M. Walter. John Wiley & Sons, Inc., Hoboken, pp. 49–70. DOI: 10.1002/9781118860359.ch3.

Jeffries, R. D., S. P. Littlefair, T. Naylor, and N. J. Mayne (2011). "No wide spread of stellar ages in the Orion Nebula Cluster." *Mon. Not. R. Astron. Soc.* 418, 1948–1958. DOI: 10.1111/j.1365-2966.2011.19613.x. arXiv: 1108.2052 [astro-ph.SR].

Jin, S. and C. Mordasini (2018). "Compositional Imprints in Density-Distance-Time: A Rocky Composition for Close-in Low-mass Exoplanets from the Location of the Valley of Evaporation." *Astrophys. J.* 853, 163. DOI: 10.3847/1538-4357/aa9f1e. arXiv: 1706.00251 [astro-ph.EP].

Jin, S., C. Mordasini, V. Parmentier, R. van Boekel, T. Henning, and J. Ji (2014). "Planetary Population Synthesis Coupled with Atmospheric Escape: A Statistical View of Evaporation." *Astrophys. J.* 795, 65. DOI: 10.1088/0004-637X/795/1/65. arXiv: 1409.2879 [astro-ph.EP].

Johansen, A., A. Youdin, and M.-M. Mac Low (2009). "Particle Clumping and Planetesimal Formation Depend Strongly on Metallicity." *Astrophys. J. Lett.* 704, L75–L79. DOI: 10.1088/0004-637X/704/2/L75. arXiv: 0909.0259 [astro-ph.EP].

Johansen, A., J. S. Oishi, M.-M. Mac Low, H. Klahr, T. Henning, and A. Youdin (2007). "Rapid planetesimal formation in turbulent circumstellar disks." *Nature* 448, 1022–1025. DOI: 10.1038/nature06086. arXiv: 0708.3890.

Johansen, A., M.-M. Mac Low, P. Lacerda, and M. Bizzarro (2015). "Growth of asteroids, planetary embryos, and Kuiper belt objects by chondrule accretion." *Sci. Adv.* 1, 1500109. DOI: 10.1126/sciadv.1500109. arXiv: 1503.07347 [astro-ph.EP].

Johnson, B. C., D. A. Minton, H. J. Melosh, and M. T. Zuber (2015). "Impact jetting as the origin of chondrules." *Nature* 517, 339–341. DOI: 10.1038/nature14105.

Johnstone, D., D. Hollenbach, and J. Bally (1998). "Photoevaporation of Disks and Clumps by Nearby Massive Stars: Application to Disk Destruction in the Orion Nebula." *Astrophys. J.* 499, 758–776.

Jones, R. H. (2012). "Petrographic constraints on the diversity of chondrule reservoirs in the protoplanetary disk." *Meteorit. Planet. Sci.* 47, 1176–1190. DOI: 10.1111/j.1945-5100.2011.01327.x.

Jones, R. H., J. N. Grossman, and A. E. Rubin (2005). "Chemical, Mineralogical and Isotopic Properties of Chondrules: Clues to Their Origin." *Chondrites and the Protoplanetary Disk*. Ed. by A. N. Krot, E. R. D. Scott, and B. Reipurth. Vol. 341. Astronomical Society of the Pacific Conference Series, p. 251.

Jones, R. H. and A. J. Schilk (2009). "Chemistry, petrology and bulk oxygen isotope compositions of chondrules from the Mokoia CV3 carbonaceous chondrite." *Geochim. Cosmochim. Acta* 73, 5854–5883. DOI: 10.1016/j.gca.2009.06.029.

Jontof-Hutter, D., J. F. Rowe, J. J. Lissauer, D. C. Fabrycky, and E. B. Ford (2015). "The mass of the Mars-sized exoplanet Kepler-138 b from transit timing." *Nature* 522, 321–323. DOI: 10.1038/nature14494. arXiv: 1506.07067 [astro-ph.EP].

Jura, M., S. Xu, and E. D. Young (2013). "^{26}Al in the Early Solar System: Not So Unusual after All." *Astrophys. J. Lett.* 775, L41. DOI: 10.1088/2041-8205/775/2/L41. arXiv: 1308.6325 [astro-ph.EP].

Jura, M. and E. D. Young (2014). "Extrasolar Cosmochemistry." *Annu. Rev. Earth Planet. Sci.* 42, 45–67. DOI: 10.1146/annurev-earth-060313-054740.

Jutzi, Martin, Willy Benz, and Patrick Michel (2008). "Numerical simulations of impacts involving porous bodies: I. Implementing sub-resolution porosity in a 3D SPH hydrocode." *Icarus* 198, 242–255.

Jutzi, Martin, Patrick Michel, Kensuke Hiraoka, Akiko M Nakamura, and Willy Benz (2009). "Numerical simulations of impacts involving porous bodies: II. Comparison with laboratory experiments." *Icarus* 201, 802–813.

Kaltenegger, L. (2017). "How to Characterize Habitable Worlds and Signs of Life." *Annu. Rev. Astron. Astrophys.* 55, 433–485. DOI: 10.1146/annurev-astro-082214-122238.

Kataoka, A., H. Tanaka, S. Okuzumi, and K. Wada (2013). "Fluffy dust forms icy planetesimals by static compression." *Astron. Astrophys.* 557, L4. DOI: 10.1051/0004-6361/201322151. arXiv: 1307.7984 [astro-ph.EP].

Kataoka, A. et al. (2016). "Submillimeter Polarization Observation of the Protoplanetary Disk around HD 142527." *Astrophys. J. Lett.* 831, L12. DOI: 10.3847/2041-8205/831/2/L12. arXiv: 1610.06318 [astro-ph.EP].

Katz, R. F., M. Knepley, B. Smith, M. Spiegelman, and E. Coon (2007). "Numerical simulation of geodynamic processes with the Portable Extensible Toolkit for Scientific Computation." *Phys. Earth Planet. Inter.* 163, 52–68.

Kauffmann, J., T. Pillai, and P. F. Goldsmith (2013). "Low Virial Parameters in Molecular Clouds: Implications for High-mass Star Formation and Magnetic Fields." *Astrophys. J.* 779, 185. DOI: 10.1088/0004-637X/779/2/185. arXiv: 1308.5679.

Keller, T. and R. F. Katz (2016). "The Role of Volatiles in Reactive Melt Transport in the Asthenosphere." *J. Petrol.* 57, 1073–1108. DOI: 10.1093/petrology/egw030.

Keller, T., R. F. Katz, and M. M. Hirschmann (2017). "Volatiles beneath mid-ocean ridges: Deep melting, channelised transport, focusing, and metasomatism." *Earth Planet. Sci. Lett.* 464, 55–68. DOI: 10.1016/j.epsl.2017.02.006. arXiv: 1608.03841 [physics.geo-ph].

Keller, T., D. A. May, and B. J. P. Kaus (2013). "Numerical modelling of magma dynamics coupled to tectonic deformation of lithosphere and crust." *Geophys. J. Int.* 195, 1406–1442. DOI: 10.1093/gji/ggt306.

King, E. M., S. Stellmach, J. Noir, U. Hansen, and J. M. Aurnou (2009). "Boundary layer control of rotating convection systems." *Nature* 457, 301–304. DOI: 10.1038/nature07647.

King, I. R. (1966). "The structure of star clusters. III. Some simple dynamical models." *Astron. J.* 71, 64. DOI: 10.1086/109857.

King, R. R., R. J. Parker, J. Patience, and S. P. Goodwin (2012). "Testing the universality of star formation - I. Multiplicity in nearby star-forming regions." *Mon. Not. R. Astron. Soc.* 421, 2025–2042. DOI: 10.1111/j.1365-2966.2012.20437.x. arXiv: 1201.1311 [astro-ph.SR].

Kita, N. T. and T. Ushikubo (2012). "Evolution of protoplanetary disk inferred from ^{26}Al chronology of individual chondrules." *Meteorit. Planet. Sci.* 47, 1108–1119. DOI: 10.1111/j.1945-5100.2011.01264.x.

Kita, N. T., Q.-Z. Yin, G. J. MacPherson, T. Ushikubo, B. Jacobsen, K. Nagashima, E. Kurahashi, A. N. Krot, and S. B. Jacobsen (2013). "^{26}Al-^{26}Mg isotope systematics of the first solids in the early solar system." *Meteorit. Planet. Sci.* 48, 1383–1400. DOI: 10.1111/maps.12141.

Kite, E. S. and E. B. Ford (2018). "Habitability of exoplanet waterworlds." *ArXiv e-prints*. arXiv: 1801.00748 [astro-ph.EP].

Klahr, H. and A. Schreiber (2016). "Linking the Origin of Asteroids to Planetesimal Formation in the Solar Nebula." *Asteroids: New Observations, New Models*. Ed. by S. R. Chesley, A. Morbidelli, R. Jedicke, and D. Farnocchia. Vol. 318. IAU Symposium, pp. 1–8. DOI: 10.1017/S1743921315010406.

Kleine, T. and M. Wadhwa (2017). "Chronology of Planetesimal Differentiation." *Planetesimals: Early Differentiation and Consequences for Planets*. Ed. by Linda T. Elkins-Tanton and Benjamin P. Weiss. Cambridge: Cambridge University Press, pp. 224–245. DOI: 10.1017/9781316339794.011.

Kleine, T., M. Touboul, B. Bourdon, F. Nimmo, K. Mezger, H. Palme, S. B. Jacobsen, Q.-Z. Yin, and A. N. Halliday (2009). "Hf-W chronology of the accretion and early evolution of asteroids and terrestrial planets." *Geochim. Cosmochim. Acta* 73, 5150–5188. DOI: 10.1016/j.gca.2008.11.047.

Kokubo, E. and S. Ida (1996). "On Runaway Growth of Planetesimals." *Icarus* 123, 180–191. DOI: 10.1006/icar.1996.0148.

— (1998). "Oligarchic Growth of Protoplanets." *Icarus* 131, 171–178. DOI: 10.1006/icar.1997.5840.

Kouwenhoven, M. B. N., S. P. Goodwin, R. J. Parker, M. B. Davies, D. Malmberg, and P. Kroupa (2010). "The formation of very wide binaries during the star cluster dissolution phase." *Mon. Not. R. Astron. Soc.* 404, 1835–1848. DOI: 10.1111/j.1365-2966.2010.16399.x. arXiv: 1001.3969.

Kraichnan, R. H. (1962). "Turbulent Thermal Convection at Arbitrary Prandtl Number." *Physics of Fluids* 5, 1374–1389. DOI: 10.1063/1.1706533.

Kral, Q., C. Clarke, and M. Wyatt (2017). "Circumstellar discs: What will be next?" *Handbook of Exoplanets, Edited by Hans J. Deeg and Juan Antonio Belmonte. Springer Living Reference Work, ISBN: 978-3-319-30648-3, id. 165*.

Kreidberg, L., J. L. Bean, J.-M. Désert, B. Benneke, D. Deming, K. B. Stevenson, S. Seager, Z. Berta-Thompson, A. Seifahrt, and D. Homeier (2014). "Clouds in the atmosphere of the super-Earth exoplanet GJ1214b." *Nature* 505, 69–72. DOI: 10.1038/nature12888. arXiv: 1401.0022 [astro-ph.EP].

Krot, A. N., Y. Amelin, P. Cassen, and A. Meibom (2005). "Young chondrules in CB chondrites from a giant impact in the early Solar System." *Nature* 436, 989–992. DOI: 10.1038/nature03830.

Krot, A. N. et al. (2009). "Origin and chronology of chondritic components: A review." *Geochim. Cosmochim. Acta* 73, 4963–4997. DOI: 10.1016/j.gca.2008.09.039.

Krot, A. N., K. Makide, K. Nagashima, G. R. Huss, R. C. Ogliore, F. J. Ciesla, L. Yang, E. Hellebrand, and E. Gaidos (2012). "Heterogeneous distribution of ^{26}Al at the birth of the solar system: Evidence from refractory grains and inclusions." *Meteorit. Planet. Sci.* 47, 1948–1979. DOI: 10.1111/maps.12008.

Kroupa, P. (1995). "Inverse dynamical population synthesis and star formation." *Mon. Not. R. Astron. Soc.* 277. DOI: 10.1093/mnras/277.4.1491. eprint: astro-ph/9508117.

Kruijer, T. S., M. Touboul, M. Fischer-Gödde, K. R. Bermingham, R. J. Walker, and T. Kleine (2014). "Protracted core formation and rapid accretion of protoplanets." *Science* 344, 1150–1154. DOI: 10.1126/science.1251766.

Kuchner, M. J. (2003). "Volatile-rich Earth-Mass Planets in the Habitable Zone." *Astrophys. J. Lett.* 596, L105–L108. DOI: 10.1086/378397. eprint: astro-ph/0303186.

Kuffmeier, M., T. Frostholm Mogensen, T. Haugbølle, M. Bizzarro, and Å. Nordlund (2016). "Tracking the Distribution of 26Al and 60Fe during the Early Phases of Star and Disk Evolution." *Astrophys. J.* 826, 22. DOI: 10.3847/0004-637X/826/1/22. arXiv: 1605.05008 [astro-ph.SR].

Lada, C. J. and E. A. Lada (2003). "Embedded Clusters in Molecular Clouds." *Annu. Rev. Astron. Astrophys.* 41, 57–115. DOI: 10.1146/annurev.astro.41.011802.094844. eprint: astro-ph/0301540.

Larsen, K. K., A. Trinquier, C. Paton, M. Schiller, D. Wielandt, M. A. Ivanova, J. N. Connelly, Å. Nordlund, A. N. Krot, and M. Bizzarro (2011). "Evidence for Magnesium Isotope Heterogeneity in the Solar Protoplanetary Disk." *Astrophys. J. Lett.* 735, L37. DOI: 10.1088/2041-8205/735/2/L37.

Larson, R. B. (1981). "Turbulence and star formation in molecular clouds." *Mon. Not. R. Astron. Soc.* 194, 809–826. DOI: 10.1093/mnras/194.4.809.

Lee, T., D. A. Papanastassiou, and G. J. Wasserburg (1976a). "Correction to [Demonstration of ^{26}Mg excess in Allende and evidence for ^{26}Al]." *Geophys. Res. Lett.* 3, 109–112. DOI: 10.1029/GL003i002p00109.

— (1976b). "Demonstration of Mg-26 excess in Allende and evidence for Al-26." *Geophys. Res. Lett.* 3, 41–44. DOI: 10.1029/GL003i001p00041.

Léger, A. et al. (2004). "A new family of planets? "Ocean-Planets"." *Icarus* 169, 499–504. DOI: 10.1016/j.icarus.2004.01.001. eprint: astro-ph/0308324.

Leinhardt, Z. M. and S. T. Stewart (2009). "Full numerical simulations of catastrophic small body collisions." *Icarus* 199, 542–559. DOI: 10.1016/j.icarus.2008.09.013. arXiv: 0811.0175.

— (2012). "Collisions between Gravity-dominated Bodies. I. Outcome Regimes and Scaling Laws." *Astrophys. J.* 745, 79. DOI: 10.1088/0004-637X/745/1/79. arXiv: 1106.6084.

Levison, H. F., M. J. Duncan, and E. Thommes (2012). "A Lagrangian Integrator for Planetary Accretion and Dynamics (LIPAD)." *Astron. J.* 144, 119. DOI: 10.1088/0004-6256/144/4/119. arXiv: 1207.0754 [astro-ph.EP].

Li, G. and F. C. Adams (2016). "Interaction Cross Sections and Survival Rates for Proposed Solar System Member Planet Nine." *Astrophys. J. Lett.* 823, L3. DOI: 10.3847/2041-8205/823/1/L3. arXiv: 1602.08496 [astro-ph.EP].

Libourel, G. and M. Portail (2017). "Overlooked Chondrules: A High Resolution Cathodoluminscence Survey." *Chondrules and the Protoplanetary Disk*. Vol. 1963. LPI Contrib. P. 2008.

Lichtenberg, T., R. J. Parker, and M. R. Meyer (2016). "Isotopic enrichment of forming planetary systems from supernova pollution." *Mon. Not. R. Astron. Soc.* 462, 3979–3992. DOI: 10.1093/mnras/stw1929. arXiv: 1608.01435 [astro-ph.EP].

Lichtenberg, T. and D. R. G. Schleicher (2015). "Modeling gravitational instabilities in self-gravitating protoplanetary disks with adaptive mesh refinement techniques." *Astron. Astrophys.* 579, A32. DOI: 10.1051/0004-6361/201424528.

Lichtenberg, T., G. J. Golabek, T. V. Gerya, and M. R. Meyer (2016). "The effects of short-lived radionuclides and porosity on the early thermo-mechanical evolution of planetesimals." *Icarus* 274, 350–365. DOI: 10.1016/j.icarus.2016.03.004. arXiv: 1603.05979 [astro-ph.EP].

Lichtenberg, T., G. J. Golabek, C. P. Dullemond, M. Schönbächler, T. V. Gerya, and M. R. Meyer (2018). "Impact splash chondrule formation during planetesimal recycling." *Icarus* 302, 27–43. DOI: 10.1016/j.icarus.2017.11.004. arXiv: 1711.02103 [astro-ph.EP].

Liebske, C., B. Schmickler, H. Terasaki, B. T. Poe, A. Suzuki, K.-I. Funakoshi, R. Ando, and D. C. Rubie (2005). "Viscosity of peridotite liquid up to 13 GPa: Implications for magma ocean viscosities." *Earth Planet. Sci. Lett.* 240, 589–604. DOI: 10.1016/j.epsl.2005.10.004.

Limongi, M. and A. Chieffi (2006). "The Nucleosynthesis of ^{26}Al and ^{60}Fe in Solar Metallicity Stars Extending in Mass from 11 to 120 M_{solar}: The Hydrostatic and Explosive Contributions." *Astrophys. J.* 647, 483–500. DOI: 10.1086/505164. eprint: astro-ph/0604297.

Limongi, M., O. Straniero, and A. Chieffi (2000). "Massive Stars in the Range 13-25 M_{solar}: Evolution and Nucleosynthesis. II. The Solar Metallicity Models." *Astrophys. J. Suppl.* 129, 625–664. DOI: 10.1086/313424. eprint: astro-ph/0003401.

Lithwick, Y. (2014). "After Runaway: The Trans-Hill Stage of Planetesimal Growth." *Astrophys. J.* 780, 22. DOI: 10.1088/0004-637X/780/1/22. arXiv: 1303.3890 [astro-ph.EP].

Lodders, K. (2003). "Solar System Abundances and Condensation Temperatures of the Elements." *Astrophys. J.* 591, 1220–1247. DOI: 10.1086/375492.

Lopez, L. A., E. Ramirez-Ruiz, D. A. Pooley, and T. E. Jeltema (2009). "Tools for Dissecting Supernova Remnants Observed with Chandra: Methods and Application to the Galactic Remnant W49B." *Astrophys. J.* 691, 875–893. DOI: 10.1088/0004-637X/691/1/875. arXiv: 0810.0009.

Luger, R. and R. Barnes (2015). "Extreme Water Loss and Abiotic O^2Buildup on Planets Throughout the Habitable Zones of M Dwarfs." *Astrobiology* 15, 119–143. DOI: 10.1089/ast.2014.1231. arXiv: 1411.7412 [astro-ph.EP].

Luu, T.-H., E. D. Young, M. Gounelle, and M. Chaussidon (2015). "Short time interval for condensation of high-temperature silicates in the solar accretion disk." *Proc. Natl. Acad. Sci.* 112, 1298–1303. DOI: 10.1073/pnas.1414025112.

Lynden-Bell, D. (1967). "Statistical mechanics of violent relaxation in stellar systems." *Mon. Not. R. Astron. Soc.* 136, 101. DOI: 10.1093/mnras/136.1.101.

Lyons, R. J., T. J. Bowling, F. J. Ciesla, T. M. Davison, and G. S. Collins (2017). "Impact Effects on Cooling Rates of Iron Meteorites." *Lunar and Planetary Science Conference*. Vol. 48. Lunar and Planetary Inst. Technical Report, p. 2433.

Maas, C. and U. Hansen (2015). "Effects of Earth's rotation on the early differentiation of a terrestrial magma ocean." *J. Geophys. Res. Solid Earth* 120, 7508–7525. DOI: 10.1002/2015JB012053.

Mackwell, S. J. (1991). "High-temperature rheology of enstatite: Implications for creep in the mantle." *Geophys. Res. Lett.* 18, 2027–2030. DOI: 10.1029/91GL02492.

Makide, K., K. Nagashima, A. N. Krot, G. R. Huss, F. J. Ciesla, E. Hellebrand, E. Gaidos, and L. Yang (2011). "Heterogeneous Distribution of ^{26}Al at the Birth of the Solar System." *Astrophys. J. Lett.* 733, L31. DOI: 10.1088/2041-8205/733/2/L31. arXiv: 1105.2620 [astro-ph.EP].

Mamajek, E. E. (2009). "Initial Conditions of Planet Formation: Lifetimes of Primordial Disks." *AIP Conference Series 1158*, pp. 3–10. DOI: 10.1063/1.3215910.

Mandler, B. E. and L. T. Elkins-Tanton (2013). "The origin of eucrites, diogenites, and olivine diogenites: Magma ocean crystallization and shallow magma chamber processes on Vesta." *Meteorit. Planet. Sci.* 48, 2333–2349. DOI: 10.1111/maps.12135.

Marcus, R. A., D. Sasselov, S. T. Stewart, and L. Hernquist (2010). "Water/Icy Super-Earths: Giant Impacts and Maximum Water Content." *Astrophys. J. Lett.* 719, L45–L49. DOI: 10.1088/2041-8205/719/1/L45. arXiv: 1007.3212 [astro-ph.EP].

Marrocchi, Y., M. Chaussidon, L. Piani, and G. Libourel (2016). "Early scattering of the solar protoplanetary disk recorded in meteoritic chondrules." *Sci. Adv.* 2, e1601001–e1601001. DOI: 10.1126/sciadv.1601001.

Maschberger, T. (2013). "On the function describing the stellar initial mass function." *Mon. Not. R. Astron. Soc.* 429, 1725–1733. DOI: 10.1093/mnras/sts479. arXiv: 1212.0939.

Mathis, J. S., W. Rumpl, and K. H. Nordsieck (1977). "The size distribution of interstellar grains." *Astrophys. J.* 217, 425–433. DOI: 10.1086/155591.

Matsuura, M. et al. (2011). "Herschel Detects a Massive Dust Reservoir in Supernova 1987A." *Science* 333, 1258. DOI: 10.1126/science.1205983. arXiv: 1107.1477 [astro-ph.SR].

Matsuyama, Isamu, Doug Johnstone, and Lee Hartmann (2003). "Viscous Diffusion and Photoevaporation of Stellar Disks." *Astrophys. J.* 582.2, 893–904. ISSN: 0004-637X. DOI: 10.1086/344638. URL: http://stacks.iop.org/0004-637X/582/i=2/a=893.

Mayor, M. and D. Queloz (1995). "A Jupiter-mass companion to a solar-type star." *Nature* 378, 355–359. DOI: 10.1038/378355a0.

McKenzie, D. (1984). "The generation and compaction of partially molten rock." *J. Petrol.* 5, 713–765.

McSween, H. Y., M. E. Bennett, and E. Jarosewich (1991). "The mineralogy of ordinary chondrites and implications for asteroid spectrophotometry." *Icarus* 90, 107–116. DOI: 10.1016/0019-1035(91)90072-2.

Mei, S., W. Bai, T. Hiraga, and D. L. Kohlstedt (2002). "Influence of melt on the creep behavior of olivine-basalt aggregates under hydrous conditions." *Earth Planet. Sci. Lett.* 201, 491–507. DOI: 10.1016/S0012-821X(02)00745-8.

Meng, H. Y. A., G. H. Rieke, K. Y. L. Su, and A. Gáspár (2017). "The First 40 Million Years of Circumstellar Disk Evolution: The Signature of Terrestrial Planet Formation." *Astrophys. J.* 836, 34. DOI: 10.3847/1538-4357/836/1/34. arXiv: 1701.01786 [astro-ph.SR].

Meyer, B. S. and D. D. Clayton (2000). "Short-Lived Radioactivities and the Birth of the sun." *Space Sci. Rev.* 92, 133–152. DOI: 10.1023/A:1005282825778.

Meyer, M. R., K. Flaherty, J. L. Levine, E. A. Lada, B. P. Bowler, and R. Kandori (2008). "Star Formation in NGC 2023, NGC 2024, and Southern L1630." *Handbook of Star Forming Regions, Volume I*. Ed. by B. Reipurth, p. 662.

Millholland, S., S. Wang, and G. Laughlin (2017). "Kepler Multi-planet Systems Exhibit Unexpected Intra-system Uniformity in Mass and Radius." *Astrophys. J. Lett.* 849, L33. DOI: 10.3847/2041-8213/aa9714. arXiv: 1710.11152 [astro-ph.EP].

Mishra, R. K. and M. Chaussidon (2014). "Fossil records of high level of ^{60}Fe in chondrules from unequilibrated chondrites." *Earth Planet. Sci. Lett.* 398, 90–100. DOI: 10.1016/j.epsl.2014.04.032.

Mishra, R. K., K. K. Marhas, and Sameer (2016). "Abundance of ^{60}Fe inferred from nanoSIMS study of QUE 97008 (L3.05) chondrules." *Earth Planet. Sci. Lett.* 436, 71–81. DOI: 10.1016/j.epsl.2015.12.007.

Moeckel, N. and M. R. Bate (2010). "On the evolution of a star cluster and its multiple stellar systems following gas dispersal." *Mon. Not. R. Astron. Soc.* 404, 721–737. DOI: 10.1111/j.1365-2966.2010.16347.x. arXiv: 1001.3417 [astro-ph.SR].

Moeckel, N. and C. J. Clarke (2011). "The formation of permanent soft binaries in dispersing clusters." *Mon. Not. R. Astron. Soc.* 415, 1179–1187. DOI: 10.1111/j.1365-2966.2011.18731.x. arXiv: 1103.2306 [astro-ph.SR].

Monteux, J., G. J. Golabek, D. C. Rubie, G. Tobie, and E. D. Young (2018). "Water and the Interior Structure of Terrestrial Planets and Icy Bodies." *Space Sci. Rev.* 214, 39. DOI: 10.1007/s11214-018-0473-x.

Morbidelli, A. and S. N. Raymond (2016). "Challenges in planet formation." *J. Geophys. Res. Planet.* 121, 1962–1980. DOI: 10.1002/2016JE005088. arXiv: 1610.07202 [astro-ph.EP].

Morbidelli, A., W. F. Bottke, D. Nesvorný, and H. F. Levison (2009). "Asteroids were born big." *Icarus* 204, 558–573. DOI: 10.1016/j.icarus.2009.07.011. arXiv: 0907.2512 [astro-ph.EP].

Morbidelli, A., M. Lambrechts, S. Jacobson, and B. Bitsch (2015). "The great dichotomy of the Solar System: Small terrestrial embryos and massive giant planet cores." *Icarus* 258, 418–429. DOI: 10.1016/j.icarus.2015.06.003. arXiv: 1506.01666 [astro-ph.EP].

Morbidelli, A., B. Bitsch, A. Crida, M. Gounelle, T. Guillot, S. Jacobson, A. Johansen, M. Lambrechts, and E. Lega (2016). "Fossilized condensation lines in the Solar System protoplanetary disk." *Icarus* 267, 368–376. DOI: 10.1016/j.icarus.2015.11.027. arXiv: 1511.06556 [astro-ph.EP].

Morbidelli, A., D. Nesvorny, V. Laurenz, S. Marchi, D. C. Rubie, L. Elkins-Tanton, M. Wieczorek, and S. Jacobson (2018). "The timeline of the lunar bombardment: Revisited." *Icarus* 305, 262–276. DOI: 10.1016/j.icarus.2017.12.046. arXiv: 1801.03756 [astro-ph.EP].

Mordasini, C., Y. Alibert, and W. Benz (2009). "Extrasolar planet population synthesis. I. Method, formation tracks, and mass-distance distribution." *Astron. Astrophys.* 501, 1139–1160. DOI: 10.1051/0004-6361/200810301. arXiv: 0904.2524 [astro-ph.EP].

Mordasini, C., Y. Alibert, W. Benz, and D. Naef (2009). "Extrasolar planet population synthesis. II. Statistical comparison with observations." *Astron. Astrophys.* 501, 1161–1184. DOI: 10.1051/0004-6361/200810697. arXiv: 0904.2542 [astro-ph.EP].

Mordasini, C., Y. Alibert, C. Georgy, K.-M. Dittkrist, H. Klahr, and T. Henning (2012). "Characterization of exoplanets from their formation. II. The planetary mass-radius relationship." *Astron. Astrophys.* 547, A112. DOI: 10.1051/0004-6361/201118464. arXiv: 1206.3303 [astro-ph.EP].

Mordasini, C., P. Mollière, K.-M. Dittkrist, S. Jin, and Y. Alibert (2015). "Global models of planet formation and evolution." *Int. J. Astrobiol.* 14.02, 201–232. ISSN: 1473-5504. DOI: 10.1017/S1473550414000263.

Morishima, R. (2017). "Onset of oligarchic growth and implication for accretion histories of dwarf planets." *Icarus* 281, 459–475. DOI: 10.1016/j.icarus.2016.07.019. arXiv: 1608.00043 [astro-ph.EP].

Morris, M. A. and S. J. Desch (2010). "Thermal Histories of Chondrules in Solar Nebula Shocks." *Astrophys. J.* 722, 1474–1494. DOI: 10.1088/0004-637X/722/2/1474. arXiv: 1008.2741 [astro-ph.EP].

Morris, M. A., S. J. Weidenschilling, and S. J. Desch (2016). "The effect of multiple particle sizes on cooling rates of chondrules produced in large-scale shocks in the solar nebula." *Meteorit. Planet. Sci.* 51, 870–883. DOI: 10.1111/maps.12631. arXiv: 1603.03711 [astro-ph.EP].

Moskovitz, N. and E. Gaidos (2011). "Differentiation of planetesimals and the thermal consequences of melt migration." *Meteorit. Planet. Sci.* 46, 903–918. DOI: 10.1111/j.1945-5100.2011.01201.x. arXiv: 1101.4165 [astro-ph.EP].

Movshovitz, N., F. Nimmo, D. G. Korycansky, E. Asphaug, and J. M. Owen (2016). "Impact disruption of gravity-dominated bodies: New simulation data and scaling." *Icarus* 275, 85–96. DOI: 10.1016/j.icarus.2016.04.018.

Mróz, P. et al. (2017). "No large population of unbound or wide-orbit Jupiter-mass planets." *Nature* 548, 183–186. DOI: 10.1038/nature23276. arXiv: 1707.07634 [astro-ph.EP].

Mulders, G. D., F. J. Ciesla, M. Min, and I. Pascucci (2015). "The Snow Line in Viscous Disks around Low-mass Stars: Implications for Water Delivery to Terrestrial Planets in the Habitable Zone." *Astrophys. J.* 807, 9. DOI: 10.1088/0004-637X/807/1/9. arXiv: 1505.03516 [astro-ph.EP].

Mustill, A. J., S. N. Raymond, and M. B. Davies (2016). "Is there an exoplanet in the Solar system?" *Mon. Not. R. Astron. Soc.* 460, L109–L113. DOI: 10.1093/mnrasl/slw075. arXiv: 1603.07247 [astro-ph.EP].

Nagahara, H., N. T. Kita, K. Ozawa, and Y. Morishita (2008). "Condensation of major elements during chondrule formation and its implication to the origin of chondrules." *Geochim. Cosmochim. Acta* 72, 1442–1465. DOI: 10.1016/j.gca.2007.12.020.

Nagashima, K., A. Krot, N. Alexander, and G. R. Huss (2014). "^{26}Al in chondrules from CR2 chondrites." *Geochem. J.* 48, 561–570.

Natta, A., V. Grinin, and V. Mannings (2000). "Properties and Evolution of Disks around Pre-Main-Sequence Stars of Intermediate Mass." *Protostars and Planets IV*, 559–588.

Nesvorný, D., D. Vokrouhlický, L. Dones, H. F. Levison, N. Kaib, and A. Morbidelli (2017). "Origin and Evolution of Short-period Comets." *Astrophys. J.* 845, 27. DOI: 10.3847/1538-4357/aa7cf6. arXiv: 1706.07447 [astro-ph.EP].

Neumann, W., D. Breuer, and T. Spohn (2013). "The thermo-chemical evolution of Asteroid 21 Lutetia." *Icarus* 224, 126–143. DOI: 10.1016/j.icarus.2013.02.025.

— (2014a). "Differentiation of Vesta: Implications for a shallow magma ocean." *Earth Planet. Sci. Lett.* 395, 267–280. DOI: 10.1016/j.epsl.2014.03.033. arXiv: 1402.3103 [astro-ph.EP].

— (2014b). "Modelling of compaction in planetesimals." *Astron. Astrophys.* 567, A120. DOI: 10.1051/0004-6361/201423648.

Nicholson, A. E., D. M. Wilkinson, H. T. P. Williams, and T. M. Lenton (2018). "Gaian bottlenecks and planetary habitability maintained by evolving model biospheres: The ExoGaia model." *Mon. Not. R. Astron. Soc.* DOI: 10.1093/mnras/sty658. arXiv: 1803.08063 [astro-ph.EP].

Nicholson, R. B. and R. J. Parker (2017). "Supernova enrichment of planetary systems in low-mass star clusters." *Mon. Not. R. Astron. Soc.* 464, 4318–4324. DOI: 10.1093/mnras/stw2682. arXiv: 1610.05303 [astro-ph.EP].

Nittler, L. R. and F. Ciesla (2016). "Astrophysics with Extraterrestrial Materials." *Annu. Rev. Astron. Astrophys.* 54, 53–93. DOI: 10.1146/annurev-astro-082214-122505.

Noack, L. and D. Breuer (2014). "Plate tectonics on rocky exoplanets: Influence of initial conditions and mantle rheology." *Planet. Space Sci.* 98, 41–49. DOI: 10.1016/j.pss.2013.06.020.

Noack, L., I. Snellen, and H. Rauer (2017). "Water in Extrasolar Planets and Implications for Habitability." *Space Sci. Rev.* 212, 877–898. DOI: 10.1007/s11214-017-0413-1.

Noack, L., D. Höning, A. Rivoldini, C. Heistracher, N. Zimov, B. Journaux, H. Lammer, T. Van Hoolst, and J. H. Bredehöft (2016). "Water-rich planets: How habitable is a water layer deeper than on Earth?" *Icarus* 277, 215–236. DOI: 10.1016/j.icarus.2016.05.009.

O'Brien, D. P., A. Izidoro, S. A. Jacobson, S. N. Raymond, and D. C. Rubie (2018). "The Delivery of Water During Terrestrial Planet Formation." *Space Sci. Rev.* 214, 47. DOI: 10.1007/s11214-018-0475-8. arXiv: 1801.05456 [astro-ph.EP].

O'Neill, H. S. C. and H. Palme (2008). "Collisional erosion and the non-chondritic composition of the terrestrial planets." *Philosophical Transactions of the Royal Society of London Series A* 366, 4205–4238. DOI: 10.1098/rsta.2008.0111.

Öberg, K. I., R. Murray-Clay, and E. A. Bergin (2011). "The Effects of Snowlines on C/O in Planetary Atmospheres." *Astrophys. J. Lett.* 743, L16. DOI: 10.1088/2041-8205/743/1/L16. arXiv: 1110.5567.

Olsen, M. B., D. Wielandt, M Schiller, E. M. M. E. Van Kooten, and M. Bizzarro (2016). "Magnesium and ^{54}Cr isotope compositions of carbonaceous chondrite chondrules–insights into early disk processes." *Geochim. Cosmochim. Acta* 191, 118–138. DOI: 10.1016/j.gca.2016.07.011.

Ormel, C. W., B. Liu, and D. Schoonenberg (2017). "Formation of TRAPPIST-1 and other compact systems." *Astron. Astrophys.* 604, A1. DOI: 10.1051/0004-6361/201730826. arXiv: 1703.06924 [astro-ph.EP].

Ormel, Chris W (2017). "The Emerging Paradigm of Pebble Accretion." *Pessah M., Gressel O. (Eds.) Formation, Evolution, and Dynamics of Young Solar Systems. Astrophysics and Space Science Library, vol 445. Springer*.

Ouellette, N., S. J. Desch, and J. J. Hester (2007). "Interaction of Supernova Ejecta with Nearby Protoplanetary Disks." *Astrophys. J.* 662, 1268–1281. DOI: 10.1086/518102. arXiv: 0704.1652.

— (2010). "Injection of Supernova Dust in Nearby Protoplanetary Disks." *Astrophys. J.* 711, 597–612. DOI: 10.1088/0004-637X/711/2/597.

Ouellette, N., S. J. Desch, M. Bizzarro, A. P. Boss, F. Ciesla, and B. Meyer (2009). "Injection mechanisms of short-lived radionuclides and their homogenization." *Geochim. Cosmochim. Acta* 73, 4946–4962. DOI: 10.1016/j.gca.2008.10.044.

Palme, H., D. C. Hezel, and D. S. Ebel (2015). "The origin of chondrules: Constraints from matrix composition and matrix-chondrule complementarity." *Earth Planet. Sci. Lett.* 411, 11–19. DOI: 10.1016/j.epsl.2014.11.033.

Palme, H., B. Spettel, and D. Hezel (2014). "Siderophile elements in chondrules of CV chondrites." *Chemie der Erde / Geochemistry* 74, 507–516. DOI: 10.1016/j.chemer.2014.06.003.

Palme, H. and J. Zipfel (2016). "The Earth Contains a Large Fraction of Material not Represented by Meteorites." *Lunar and Planetary Science Conference*. Vol. 47. Lunar and Planetary Science Conference, p. 2252.

Pan, L., S. J. Desch, E. Scannapieco, and F. X. Timmes (2012). "Mixing of Clumpy Supernova Ejecta into Molecular Clouds." *Astrophys. J.* 756, 102. DOI: 10.1088/0004-637X/756/1/102. arXiv: 1206.6516 [astro-ph.SR].

Parker, R. J. and J. E. Dale (2016). "Did the Solar system form in a sequential triggered star formation event?" *Mon. Not. R. Astron. Soc.* 456, 1066–1072. DOI: 10.1093/mnras/stv2765. arXiv: 1511.06763 [astro-ph.EP].

Parker, R. J. and S. P. Goodwin (2007). "Do O-stars form in isolation?" *Mon. Not. R. Astron. Soc.* 380, 1271–1275. DOI: 10.1111/j.1365-2966.2007.12179.x. arXiv: 0707.0605.

— (2012). "The same, but different: stochasticity in binary destruction." *Mon. Not. R. Astron. Soc.* 424, 272–281. DOI: 10.1111/j.1365-2966.2012.21190.x. arXiv: 1204.6037.

Parker, R. J., T. Lichtenberg, and S. P. Quanz (2017). "Was Planet 9 captured in the Sun's natal star-forming region?" *Mon. Not. R. Astron. Soc.* 472, L75–L79. DOI: 10.1093/mnrasl/slx141. arXiv: 1709.00418 [astro-ph.EP].

Parker, R. J. and M. R. Meyer (2012). "Characterizing the dynamical state of star clusters from snapshots of their spatial distributions." *Mon. Not. R. Astron. Soc.* 427, 637–650. DOI: 10.1111/j.1365-2966.2012.21851.x. arXiv: 1208.0335.

Parker, R. J. and S. P. Quanz (2012). "The effects of dynamical interactions on planets in young substructured star clusters." *Mon. Not. R. Astron. Soc.* 419, 2448–2458. DOI: 10.1111/j.1365-2966.2011.19911.x. arXiv: 1109.6007 [astro-ph.EP].

Parker, R. J., N. J. Wright, S. P. Goodwin, and M. R. Meyer (2014a). "Dynamical evolution of star-forming regions." *Mon. Not. R. Astron. Soc.* 438, 620–638. DOI: 10.1093/mnras/stt2231. arXiv: 1311.3639.

Parker, R. J., R. P. Church, M. B. Davies, and M. R. Meyer (2014b). "Supernova enrichment and dynamical histories of solar-type stars in clusters." *Mon. Not. R. Astron. Soc.* 437, 946–958. DOI: 10.1093/mnras/stt1957. arXiv: 1310.3270 [astro-ph.EP].

Pätzold, M. et al. (2011). "Asteroid 21 Lutetia: Low Mass, High Density." *Science* 334, 491. DOI: 10.1126/science.1209389.

Pearce, B. K. D., A. S. Tupper, R. E. Pudritz, and P. G. Higgs (2018). "Constraining the Time Interval for the Origin of Life on Earth." *Astrobiology* 18, 343–364. DOI: 10.1089/ast.2017.1674.

Perets, H. B. and M. B. N. Kouwenhoven (2012). "On the Origin of Planets at Very Wide Orbits from the Recapture of Free Floating Planets." *Astrophys. J.* 750, 83. DOI: 10.1088/0004-637X/750/1/83. arXiv: 1202.2362 [astro-ph.EP].

Peretto, N., P. André, and A. Belloche (2006). "Probing the formation of intermediate- to high-mass stars in protoclusters. A detailed millimeter study of the NGC 2264 clumps." *Astron. Astrophys.* 445, 979–998. DOI: 10.1051/0004-6361:20053324. eprint: astro-ph/0508619.

Pérez, L. M. et al. (2016). "Spiral density waves in a young protoplanetary disk." *Science* 353, 1519–1521. DOI: 10.1126/science.aaf8296. arXiv: 1610.05139.

Peslier, A., M. Schönbächler, H. Busemann, and S.-I. Karato (2018). "Water in the Earth's interior: Distribution and origin." *Space Sci. Rev.* 212, 743–810.

Pfalzner, S., M. B. Davies, M. Gounelle, A. Johansen, C. Münker, P. Lacerda, S. Portegies Zwart, L. Testi, M. Trieloff, and D. Veras (2015). "The formation of the solar system." *Phys. Scr* 90.6, 068001. DOI: 10.1088/0031-8949/90/6/068001. arXiv: 1501.03101 [astro-ph.EP].

Pfalzner, S., H. Kirk, A. Sills, J. S. Urquhart, J. Kauffmann, M. A. Kuhn, A. Bhandare, and K. M. Menten (2016). "Observational constraints on star cluster formation theory. I. The mass-radius relation." *Astron. Astrophys.* 586, A68. DOI: 10.1051/0004-6361/201527449. arXiv: 1512.00334 [astro-ph.SR].

Pierrehumbert, R. T. (2013). "Strange news from other stars." *Nat. Geo.* 6, 81–83. DOI: 10.1038/ngeo1711.

Pinkerton, H. and R. J. Stevenson (1992). "Methods of determining the rheological properties of magmas at sub-liquidus temperatures." *J. Volcanol. Geotherm. Res.* 53, 47–66. DOI: 10.1016/0377-0273(92)90073-M.

Plummer, H. C. (1911). "On the problem of distribution in globular star clusters." *Mon. Not. R. Astron. Soc.* 71, 460–470. DOI: 10.1093/mnras/71.5.460.

Pollack, J. B., O. Hubickyj, P. Bodenheimer, J. J. Lissauer, M. Podolak, and Y. Greenzweig (1996). "Formation of the Giant Planets by Concurrent Accretion of Solids and Gas." *Icarus* 124, 62–85. DOI: 10.1006/icar.1996.0190.

Porras, A., M. Christopher, L. Allen, J. Di Francesco, S. T. Megeath, and P. C. Myers (2003). "A Catalog of Young Stellar Groups and Clusters within 1 Kiloparsec of the Sun." *Astron. J.* 126, 1916–1924. DOI: 10.1086/377623. eprint: astro-ph/0307510.

Portegies Zwart, S. F. (2009). "The Lost Siblings of the Sun." *Astrophys. J. Lett.* 696, L13–L16. DOI: 10.1088/0004-637X/696/1/L13. arXiv: 0903.0237 [astro-ph.GA].

Portegies Zwart, S. F. and F. Verbunt (1996). "Population synthesis of high-mass binaries." *Astron. Astrophys.* 309, 179–196.

— (2012). *SeBa: Stellar and binary evolution*. Astrophysics Source Code Library. ascl: 1201.003.

Portegies Zwart, S. F., J. Makino, S. L. W. McMillan, and P. Hut (1999). "Star cluster ecology. III. Runaway collisions in young compact star clusters." *Astron. Astrophys.* 348, 117–126. eprint: astro-ph/9812006.

Portegies Zwart, S. F., S. L. W. McMillan, P. Hut, and J. Makino (2001). "Star cluster ecology - IV. Dissection of an open star cluster: photometry." *Mon. Not. R. Astron. Soc.* 321, 199–226. DOI: 10.1046/j.1365-8711.2001.03976.x. eprint: astro-ph/0005248.

Portegies Zwart, S., I. Pelupessy, A. van Elteren, T. Wijnen, and M. Lugaro (2018). "The consequences of a nearby supernova on the early Solar System." *ArXiv e-prints*. arXiv: 1802.04360 [astro-ph.SR].

Qin, L., N. Dauphas, M. Wadhwa, J. Masarik, and P. E. Janney (2008). "Rapid accretion and differentiation of iron meteorite parent bodies inferred from ^{182}Hf-^{182}W chronometry and thermal modeling." *Earth Planet. Sci. Lett.* 273, 94–104. DOI: 10.1016/j.epsl.2008.06.018.

Quanz, S. P., D. Lafrenière, M. R. Meyer, M. M. Reggiani, and E. Buenzli (2012). "Direct imaging constraints on planet populations detected by microlensing." *Astron. Astrophys.* 541, A133. DOI: 10.1051/0004-6361/201118320. arXiv: 1203.3647.

Quitté, G., A. N. Halliday, B. S. Meyer, A. Markowski, C. Latkoczy, and D. Günther (2007). "Correlated Iron 60, Nickel 62, and Zirconium 96 in Refractory Inclusions and the Origin of the Solar System." *Astrophys. J.* 655, 678–684. DOI: 10.1086/509771.

Quitté, G., A. Markowski, C. Latkoczy, A. Gabriel, and A. Pack (2010). "Iron-60 Heterogeneity and Incomplete Isotope Mixing in the Early Solar System." *Astrophys. J.* 720, 1215–1224. DOI: 10.1088/0004-637X/720/2/1215.

Ramirez, R. M. and A. Levi (2018). "The Ice Cap Zone: A Unique Habitable Zone for Ocean Worlds." *Mon. Not. R. Astron. Soc.* DOI: 10.1093/mnras/sty761.

Ranalli, G. (1995). *Rheology of the Earth*. Chapman and Hall, New York.

Rauer, H. et al. (2014). "The PLATO 2.0 mission." *Exp. Astron.* 38, 249–330. DOI: 10.1007/s10686-014-9383-4. arXiv: 1310.0696 [astro-ph.EP].

Rauscher, T., A. Heger, R. D. Hoffman, and S. E. Woosley (2002). "Nucleosynthesis in Massive Stars with Improved Nuclear and Stellar Physics." *Astrophys. J.* 576, 323–348. DOI: 10.1086/341728. eprint: astro-ph/0112478.

Raymond, S. N. and A. Izidoro (2017). "Origin of water in the inner Solar System: Planetesimals scattered inward during Jupiter and Saturn's rapid gas accretion." *Icarus* 297, 134–148. DOI: 10.1016/j.icarus.2017.06.030. arXiv: 1707.01234 [astro-ph.EP].

Raymond, S. N., P. J. Armitage, A. Moro-Martín, M. Booth, M. C. Wyatt, J. C. Armstrong, A. M. Mandell, F. Selsis, and A. A. West (2011). "Debris disks as signposts of terrestrial planet formation." *Astron. Astrophys.* 530, A62. DOI: 10.1051/0004-6361/201116456. arXiv: 1104.0007 [astro-ph.EP].

Raymond, S. N., A. Izidoro, B. Bitsch, and S. A. Jacobson (2016). "Did Jupiter's core form in the innermost parts of the Sun's protoplanetary disc?" *Mon. Not. R. Astron. Soc.* 458, 2962–2972. DOI: 10.1093/mnras/stw431. arXiv: 1602.06573 [astro-ph.EP].

Regelous, M., T. Elliott, and C. D. Coath (2008). "Nickel isotope heterogeneity in the early Solar System." *Earth Planet. Sci. Lett.* 272, 330–338. DOI: 10.1016/j.epsl.2008.05.001.

Reggiani, M., M. Robberto, N. Da Rio, M. R. Meyer, D. R. Soderblom, and L. Ricci (2011). "Quantitative evidence of an intrinsic luminosity spread in the Orion nebula cluster." *Astron. Astrophys.* 534, A83. DOI: 10.1051/0004-6361/201116946. arXiv: 1108.1015.

Roberts, P. H. (1967). "Convection in horizontal layers with internal heat generation. Theory." *Fluid Mech.* 30, 33–49. DOI: 10.1017/S0022112067001284.

Rozel, A., Y. Ricard, and D. Bercovici (2011). "A thermodynamically self-consistent damage equation for grain size evolution during dynamic recrystallization." *Geophys. J. Int.* 184, 719–728. DOI: 10.1111/j.1365-246X.2010.04875.x.

Rubie, D. C., H. J. Melosh, J. E. Reid, C. Liebske, and K. Righter (2003). "Mechanisms of metal-silicate equilibration in the terrestrial magma ocean." *Earth Planet. Sci. Lett.* 205, 239–255. DOI: 10.1016/S0012-821X(02)01044-0.

Rubie, D. C., S. A. Jacobson, A. Morbidelli, D. P. O'Brien, E. D. Young, J. de Vries, F. Nimmo, H. Palme, and D. J. Frost (2015). "Accretion and differentiation of the terrestrial planets with implications for the compositions of early-formed Solar System bodies and accretion of water." *Icarus* 248, 89–108. DOI: 10.1016/j.icarus.2014.10.015. arXiv: 1410.3509 [astro-ph.EP].

Rubin, A. E. (2017). "Multiple Indicators for Multiple Melting of Chondrules." *Chondrules and the Protoplanetary Disk*. Vol. 1963. LPI Contributions, p. 2006.

Rudge, J. F., D. Bercovici, and M. Spiegelman (2011). "Disequilibrium melting of a two phase multicomponent mantle." *Geophys. J. Int.* 184, 699–718. DOI: 10.1111/j.1365-246X.2010.04870.x.

Rushmer, T. and N. Petford (2011). "Microsegregation rates of liquid Fe-Ni-S metal in natural silicate-metal systems: A combined experimental and numerical study." *Geochem. Geophys. Geosys.* 12, Q03014. DOI: 10.1029/2010GC003413.

Sahijpal, S, P Soni, and G Gupta (2007). "Numerical simulations of the differentiation of accreting planetesimals with ^{26}Al and ^{60}Fe as the heat sources." *Meteorit. Planet. Sci.* 42, 1529–1548.

Salpeter, E. E. (1955). "The Luminosity Function and Stellar Evolution." *Astrophys. J.* 121, 161. DOI: 10.1086/145971.

Sánchez, N. and E. J. Alfaro (2009). "The Spatial Distribution of Stars in Open Clusters." *Astrophys. J.* 696, 2086–2093. DOI: 10.1088/0004-637X/696/2/2086. arXiv: 0902.1071 [astro-ph.SR].

Sanders, I. S. and E. R. D. Scott (2012). "The origin of chondrules and chondrites: Debris from low-velocity impacts between molten planetesimals?" *Meteorit. Planet. Sci.* 47, 2170–2192. DOI: 10.1111/maps.12002.

Sanders, I. S. and G. J. Taylor (2005). "Implications of ^{26}Al in Nebular Dust: Formation of Chondrules by Disruption of Molten Planetesimals." *Chondrites and the Protoplanetary Disk*. Ed. by A. N. Krot, E. R. D. Scott, and B. Reipurth. Vol. 341. Astronomical Society of the Pacific Conference Series, pp. 915–932.

Santerne, A., B. Brugger, D. J. Armstrong, V. Adibekyan, J. Lillo-Box, H. Gosselin, J. M. Aguichine, and et al. (2018). "An Earth-sized exoplanet with a Mercury-like composition." *Nat. Astron.* 2.

Sasselov, D. D. and M. Lecar (2000). "On the Snow Line in Dusty Protoplanetary Disks." *Astrophys. J.* 528, 995–998. DOI: 10.1086/308209. eprint: astro-ph/9911390.

Sato, T., S. Okuzumi, and S. Ida (2016). "On the water delivery to terrestrial embryos by ice pebble accretion." *Astron. Astrophys.* 589, A15. DOI: 10.1051/0004-6361/201527069. arXiv: 1512.02414 [astro-ph.EP].

Saumon, D., G. Chabrier, and H. M van Horn (1995). "An Equation of State for Low-Mass Stars and Giant Planets." *Astrophys. J. Suppl.* 99, 713.

Scally, A. and C. Clarke (2001). "Destruction of protoplanetary discs in the Orion Nebula Cluster." *Mon. Not. R. Astron. Soc.* 325, 449–456. DOI: 10.1046/j.1365-8711.2001.04274.x. eprint: astro-ph/0012098.

Schaefer, L. and D. Sasselov (2015). "The Persistence of Oceans On Earth-like Planets: Insights from the Deep-water Cycle." *Astrophys. J.* 801, 40. DOI: 10.1088/0004-637X/801/1/40. arXiv: 1501.00735 [astro-ph.EP].

Scharf, C., D. Fischer, and V. Meadows (2018). "Exoplanet science 2.0." *Nature* 553, 149–151. DOI: 10.1038/d41586-018-00108-3.

Scheinberg, A., R. R. Fu, L. T. Elkins-Tanton, and B. P. Weiss (2015). "Asteroid Differentiation: Melting and Large-Scale Structure." *Asteroids IV*. Ed. by P. Michel, F. E. DeMeo, and W. F. Bottke, pp. 533–552. DOI: 10.2458/azu_uapress_9780816532131-ch028.

Schiller, M., C. Paton, and M. Bizzarro (2015). "Evidence for nucleosynthetic enrichment of the protosolar molecular cloud core by multiple supernova events." *Geochim. Cosmochim. Acta* 149, 88–102. DOI: 10.1016/j.gca.2014.11.005.

Schiller, M., J. N. Connelly, A. C. Glad, T. Mikouchi, and M. Bizzarro (2015). "Early accretion of protoplanets inferred from a reduced inner solar system ^{26}Al inventory." *Earth Planet. Sci. Lett.* 420, 45–54. DOI: 10.1016/j.epsl.2015.03.028.

Schlichting, H. E. and R. Sari (2011). "Runaway Growth During Planet Formation: Explaining the Size Distribution of Large Kuiper Belt Objects." *Astrophys. J.* 728, 68. DOI: 10.1088/0004-637X/728/1/68. arXiv: 1011.0201 [astro-ph.EP].

Schmeling, H. et al. (2008). "A benchmark comparison of spontaneous subduction models-Towards a free surface." *Phys. Earth Planet. Int.* 171, 198–223. DOI: 10.1016/j.pepi.2008.06.028.

Schönbächler, M., W. M. Akram, N. H. Williams, and I. Leya (2011). "Nucleosynthetic Heterogeneities of Neutron-Rich Isotopes in Calcium Aluminum-Rich Inclusions and Bulk Solar System Materials." *Workshop on Formation of the First Solids in the Solar System*. Vol. 1639. LPI Contributions, p. 9085.

Schoonenberg, D. and C. W. Ormel (2017). "Planetesimal formation near the snowline: in or out?" *Astron. Astrophys.* 602, A21. DOI: 10.1051/0004-6361/201630013. arXiv: 1702.02151 [astro-ph.EP].

Schrader, D. L., H. C. Connolly, D. S. Lauretta, T. J. Zega, J. Davidson, and K. J. Domanik (2015). "The formation and alteration of the Renazzo-like carbonaceous chondrites III: Toward understanding the genesis of ferromagnesian chondrules." *Meteorit. Planet. Sci.* 50, 15–50. DOI: 10.1111/maps.12402.

Schubert, G., T. Spohn, and R. T Reynolds (1986). "Thermal histories, compositions and internal structures of the moons of the solar system." *Satellites*. Arizona University Press, pp. 224–292.

Scott, E. R. D. and A. N. Krot (2014). "Chondrites and Their Components." *Treatise on Geochemistry* 2nd ed. Ed. by A. M. Davis, 65–137.

Seager, S., M. Kuchner, C. A. Hier-Majumder, and B. Militzer (2007). "Mass-Radius Relationships for Solid Exoplanets." *Astrophys. J.* 669, 1279–1297. DOI: 10.1086/521346. arXiv: 0707.2895.

Shakura, N. I. and R. A. Sunyaev (1973). "Black holes in binary systems. Observational appearance." *Astron. Astrophys.* 24, 337–355.

Shankman, C. et al. (2017). "OSSOS. VI. Striking Biases in the Detection of Large Semimajor Axis Trans-Neptunian Objects." *Astron. J.* 154, 50. DOI: 10.3847/1538-3881/aa7aed. arXiv: 1706.05348 [astro-ph.EP].

Sierks, H., P. Lamy, C. Barbieri, D. Koschny, H. Rickman, R. Rodrigo, M. F A'Hearn, and et al. (2011). "Images of Asteroid 21 Lutetia: A Remnant Planetesimal from the Early Solar System." *Science* 334, 487. DOI: 10.1126/science.1207325.

Siggia, E. D. (1994). "High rayleigh number convection." *Annu. Rev. Fluid Mech.* 26, 137–168. DOI: 10.1146/annurev.fl.26.010194.001033.

Simon, J. B., P. J. Armitage, R. Li, and A. N. Youdin (2016). "The Mass and Size Distribution of Planetesimals Formed by the Streaming Instability. I. The Role of Self-gravity." *Astrophys. J.* 822, 55. DOI: 10.3847/0004-637X/822/1/55. arXiv: 1512.00009 [astro-ph.SR].

Simon, J. B., P. J. Armitage, A. N. Youdin, and R. Li (2017). "Evidence for Universality in the Initial Planetesimal Mass Function." *Astrophys. J. Lett.* 847, L12. DOI: 10.3847/2041-8213/aa8c79. arXiv: 1705.03889 [astro-ph.EP].

Sing, D. K. et al. (2016). "A continuum from clear to cloudy hot-Jupiter exoplanets without primordial water depletion." *Nature* 529, 59–62. DOI: 10.1038/nature16068. arXiv: 1512.04341 [astro-ph.EP].

Smith, D. M. (2003). "The Reuven Ramaty High Energy Solar Spectroscopic Imager Observation of the 1809 keV Line from Galactic ^{26}Al." *Astrophys. J. Lett.* 589, L55–L58. DOI: 10.1086/375795. eprint: astro-ph/0304508.

Soderblom, D. R., L. A. Hillenbrand, R. D. Jeffries, E. E. Mamajek, and T. Naylor (2014). "Ages of Young Stars." *Protostars and Planets VI*, 219–241. DOI: 10.2458/azu_uapress_97808165-31240-ch010. arXiv: 1311.7024 [astro-ph.SR].

Solomatov, V. S. (2015). "Magma oceans and primordial mantle differentiation." *Treatise on Geophysics* 2nd ed. pp. 81–104.

Sotin, C., O. Grasset, and A. Mocquet (2007). "Mass radius curve for extrasolar Earth-like planets and ocean planets." *Icarus* 191, 337–351. DOI: 10.1016/j.icarus.2007.04.006.

Sotin, C. and S. Labrosse (1999). "Three-dimensional thermal convection in an iso-viscous, infinite Prandtl number fluid heated from within and from below: applications to the transfer of heat through planetary mantles." *Phys. Earth Planet. Inter.* 112, 171–190. DOI: 10.1016/S0031-9201(99)00004-7.

Stamenković, V. and S. Seager (2016). "Emerging Possibilities and Insuperable Limitations of Exogeophysics: The Example of Plate Tectonics." *Astrophys. J.* 825, 78. DOI: 10.3847/0004-637X/825/1/78.

Stammler, S. M. and C. P. Dullemond (2014). "A critical analysis of shock models for chondrule formation." *Icarus* 242, 1–10. DOI: 10.1016/j.icarus.2014.07.024. arXiv: 1408.4651 [astro-ph.EP].

Steele, R. C. J., C. D. Coath, M. Regelous, S. Russell, and T. Elliott (2012). "Neutron-poor Nickel Isotope Anomalies in Meteorites." *Astrophys. J.* 758, 59. DOI: 10.1088/0004-637X/758/1/59.

Stevenson, D. J. (1990). "Fluid dynamics of core formation." *Origin of the Earth*. Ed. by H. E. Newsom and J. H. Jones, pp. 231–249.

Stolper, E., B. H. Hager, D. Walker, and J. F. Hays (1981). "Melt segregation from partially molten source regions - The importance of melt density and source region size." *J. Geophys. Res.* 86, 6261–6271. DOI: 10.1029/JB086iB07p06261.

Störzer, H. and D. Hollenbach (1999). "Photodissociation Region Models of Photoevaporating Circumstellar Disks and Application to the Proplyds in Orion." *Astrophys. J.* 515, 669–684. DOI: 10.1086/307055.

Sumi, T. et al. (2011). "Unbound or distant planetary mass population detected by gravitational microlensing." *Nature* 473, 349–352. DOI: 10.1038/nature10092. arXiv: 1105.3544 [astro-ph.EP].

Suzuki, A., E. Ohtani, and T. Kato (1998). "Density and thermal expansion of a peridotite melt at high pressure." *Phys. Earth Planet. Inter.* 107, 53–61. DOI: 10.1016/S0031-9201(97)00123-4.

Tachibana, S. and G. R. Huss (2003). "The Initial Abundance of ^{60}Fe in the Solar System." *Astrophys. J. Lett.* 588, L41–L44. DOI: 10.1086/375362.

Tackley, P. J., G. Schubert, G. A. Glatzmaier, P. Schenk, J. T. Ratcliff, and J.-P. Matas (2001). "Three-Dimensional Simulations of Mantle Convection in Io." *Icarus* 149, 79–93. DOI: 10.1006/icar.2000.6536.

Tackley, P. J., M. Ammann, J. P. Brodholt, D. P. Dobson, and D. Valencia (2013). "Mantle dynamics in super-Earths: Post-perovskite rheology and self-regulation of viscosity." *Icarus* 225, 50–61. DOI: 10.1016/j.icarus.2013.03.013. arXiv: 1204.3539 [astro-ph.EP].

Tang, H. and N. Dauphas (2012). "Abundance, distribution, and origin of ^{60}Fe in the solar protoplanetary disk." *Earth Planet. Sci. Lett.* 359, 248–263. DOI: 10.1016/j.epsl.2012.10.011. arXiv: 1212.1490 [astro-ph.EP].

— (2015). "Low ^{60}Fe Abundance in Semarkona and Sahara 99555." *Astrophys. J.* 802, 22–31. DOI: 10.1088/0004-637X/802/1/22. arXiv: 1502.05611 [astro-ph.EP].

Tarduno, J. A., R. D. Cottrell, F. Nimmo, J. Hopkins, J. Voronov, A. Erickson, E. Blackman, E. R. D. Scott, and R. McKinley (2012). "Evidence for a Dynamo in the Main Group Pallasite Parent Body." *Science* 338, 939. DOI: 10.1126/science.1223932.

Tatischeff, V., J. Duprat, and N. de Séréville (2010). "A Runaway Wolf-Rayet Star as the Origin of ^{26}Al in the Early Solar System." *Astrophys. J. Lett.* 714, L26–L30. DOI: 10.1088/2041-8205/714/1/L26. arXiv: 1003.3856 [astro-ph.SR].

Telus, M., G. R. Huss, K. Nagashima, R. C. Ogliore, and S. Tachibana (2018). "In situ^{60}Fe-^{60}Ni systematics of chondrules from unequilibrated ordinary chondrites." *Geochim. Cosmochim. Acta* 221, 342–357. DOI: 10.1016/j.gca.2017.06.013.

Thrane, K., M. Bizzarro, and J. A. Baker (2006). "Extremely Brief Formation Interval for Refractory Inclusions and Uniform Distribution of ^{26}Al in the Early Solar System." *Astrophys. J. Lett.* 646, L159–L162. DOI: 10.1086/506910.

Thrane, K., K. Nagashima, A. N. Krot, and M. Bizzarro (2008). "Discovery of a New FUN CAI from a CV Carbonaceous Chondrite: Evidence for Multistage Thermal Processing in the Protoplanetary Disk." *Astrophys. J. Lett.* 680, L141. DOI: 10.1086/589972.

Tian, F. and S. Ida (2015). "Water contents of Earth-mass planets around M dwarfs." *Nat. Geo.* 8, 177–180. DOI: 10.1038/ngeo2372.

Tkalcec, B. J. and F. E. Brenker (2014). "Plastic deformation of olivine-rich diogenites and implications for mantle processes on the diogenite parent body." *Meteorit. Planet. Sci.* 49, 1202–1213. DOI: 10.1111/maps.12324.

Tkalcec, B. J., G. J. Golabek, and F. E. Brenker (2013). "Solid-state plastic deformation in the dynamic interior of a differentiated asteroid." *Nat. Geo.* 6, 93–97. DOI: 10.1038/ngeo1710.

Todd, K. A., H. C. Watson, T. Yu, and Y. Wang (2016). "The effects of shear deformation on planetesimal core segregation: Results from in-situ X-ray micro-tomography." *Am. Mineral.* 101, 1996–2004. DOI: 10.2138/am-2016-5474.

Trinquier, A., J.-L. Birck, and C. J. Allègre (2007). "Widespread ^{54}Cr Heterogeneity in the Inner Solar System." *Astrophys. J.* 655, 1179–1185. DOI: 10.1086/510360.

Trinquier, A., T. Elliott, D. Ulfbeck, C. Coath, A. N. Krot, and M. Bizzarro (2009). "Origin of Nucleosynthetic Isotope Heterogeneity in the Solar Protoplanetary Disk." *Science* 324, 374. DOI: 10.1126/science.1168221.

Trønnes, R. G. and D. J. Frost (2002). "Peridotite melting and mineral-melt partitioning of major and minor elements at 22-24.5 GPa." *Earth Planet. Sci. Lett.* 197, 117–131. DOI: 10.1016/S0012-821X(02)00466-1.

Trujillo, C. A. and S. S. Sheppard (2014). "A Sedna-like body with a perihelion of 80 astronomical units." *Nature* 507, 471–474. DOI: 10.1038/nature13156.

Tsirvoulis, G., A. Morbidelli, M. Delbo, and K. Tsiganis (2018). "Reconstructing the size distribution of the primordial Main Belt." *Icarus* 304, 14–23. DOI: 10.1016/j.icarus.2017.05.026. arXiv: 1706.02091 [astro-ph.EP].

Turcotte, D. L. and G. Schubert (2014). *Geodynamics, 3rd ed.* Cambridge University Press, p. 636.

Unterborn, C. T., S. J. Desch, N. Hinkel, and A. Lorenzo (2018). "Constraining the Compositions of the TRAPPIST-1 Planets to Trace Snow Lines and Migration in M Dwarf Disks." *Nat. Astron.* 1. arXiv: 1706.02689 [astro-ph.EP].

Valencia, D., R. J. O'Connell, and D. Sasselov (2006). "Internal structure of massive terrestrial planets." *Icarus* 181, 545–554. DOI: 10.1016/j.icarus.2005.11.021. eprint: astro-ph/0511150.

Van Kooten, E. M. M. E., D. Wielandt, M. Schiller, K. Nagashima, A. Thomen, K. K. Larsen, M. B. Olsen, Å. Nordlund, A. N. Krot, and M. Bizzarro (2016). "Isotopic evidence for primordial molecular cloud material in metal-rich carbonaceous chondrites." *Proc. Natl. Acad. Sci.* 113, 2011–2016. DOI: 10.1073/pnas.1518183113.

Vasileiadis, A., Å. Nordlund, and M. Bizzarro (2013). "Abundance of ^{26}Al and ^{60}Fe in Evolving Giant Molecular Clouds." *Astrophys. J. Lett.* 769, L8. DOI: 10.1088/2041-8205/769/1/L8. arXiv: 1302.0843 [astro-ph.EP].

Vázquez-Semadeni, E., A. González-Samaniego, and P. Colín (2017). "Hierarchical star cluster assembly in globally collapsing molecular clouds." *Mon. Not. R. Astron. Soc.* 467, 1313–1328. DOI: 10.1093/mnras/stw3229. arXiv: 1611.00088.

Villeneuve, J., M. Chaussidon, and G. Libourel (2009). "Homogeneous Distribution of ^{26}Al in the Solar System from the Mg Isotopic Composition of Chondrules." *Science* 325, 985. DOI: 10.1126/science.1173907.

Villeneuve, J., G. Libourel, and C. Soulié (2015). "Relationships between type I and type II chondrules: Implications on chondrule formation processes." *Geochim. Cosmochim. Acta* 160, 277–305. DOI: 10.1016/j.gca.2015.03.033.

Visser, R. G. and C. W. Ormel (2016). "On the growth of pebble-accreting planetesimals." *Astron. Astrophys.* 586, A66. DOI: 10.1051/0004-6361/201527361. arXiv: 1511.03903 [astro-ph.EP].

Wade, J. and B. J. Wood (2005). "Core formation and the oxidation state of the Earth." *Earth Planet. Sci. Lett.* 236, 78–95. DOI: 10.1016/j.epsl.2005.05.017.

Wahlberg Jansson, K. and A. Johansen (2017). "Radially resolved simulations of collapsing pebble clouds in protoplanetary discs." *Mon. Not. R. Astron. Soc.* 469, 149–157. DOI: 10.1093/mnras/stx1470. arXiv: 1706.03655 [astro-ph.EP].

Wakita, S., Y. Matsumoto, S. Oshino, and Y. Hasegawa (2017). "Planetesimal Collisions as a Chondrule Forming Event." *Astrophys. J.* 834, 125. DOI: 10.3847/1538-4357/834/2/125. arXiv: 1611.05511 [astro-ph.EP].

Wallner, A., M. Bichler, K. Buczak, R. Dressler, L. K. Fifield, D. Schumann, J. H. Sterba, S. G. Tims, G. Wallner, and W. Kutschera (2015). "Settling the Half-Life of ^{60}Fe: Fundamental for a Versatile Astrophysical Chronometer." *Phys. Rev. Lett.* 114.4, 041101. DOI: 10.1103/PhysRevLett.114.041101.

Walsh, K. J., A. Morbidelli, S. N. Raymond, D. P. O'Brien, and A. M. Mandell (2011). "A low mass for Mars from Jupiter's early gas-driven migration." *Nature* 475, 206–209. DOI: 10.1038/nature10201. arXiv: 1201.5177 [astro-ph.EP].

Wang, H., B. P. Weiss, B. G. Downey, J. Wang, Y. K. Chen-Wiegart, J. Wang, C. R. Suavet, R. R. Fu, E. A. Lima, and M. E. Zucolotto (2015). "Onset of a Planetesimal Dynamo and the Lifetime of the Solar Nebular Magnetic Field." *Lunar and Planetary Science Conference*. Vol. 46, p. 2516.

Wasserburg, G. J., T. Lee, and D. A. Papanastassiou (1977). "Correlated O and MG isotopic anomalies in Allende inclusions. II - Magnesium." *Geophys. Res. Lett.* 4, 299–302. DOI: 10.1029/GL004i007p00299.

Wasson, J. T. (1990). "Ungrouped iron meteorites in Antarctica - Origin of anomalously high abundance." *Science* 249, 900–902. DOI: 10.1126/science.249.4971.900.

Wasson, J. T. and A. E. Rubin (2010). "Metal in CR chondrites." *Geochim. Cosmochim. Acta* 74, 2212–2230. DOI: 10.1016/j.gca.2010.01.014.

Weidenschilling, S. J. (1977). "Aerodynamics of solid bodies in the solar nebula." *Mon. Not. R. Astron. Soc.* 180, 57–70. DOI: 10.1093/mnras/180.1.57.

— (2011). "Initial sizes of planetesimals and accretion of the asteroids." *Icarus* 214, 671–684. DOI: 10.1016/j.icarus.2011.05.024.

Weidenschilling, S. J. and J. N. Cuzzi (2006). "Accretion Dynamics and Timescales: Relation to Chondrites." *Meteorites and the Early Solar System II*. Ed. by D. S. Lauretta and H. Y. McSween, pp. 473–485.

Weidenschilling, S. J., F. Marzari, and L. L. Hood (1998). "The Origin of Chondrules at Jovian Resonances." *Science* 279, 681. DOI: 10.1126/science.279.5351.681.

Weidenschilling, S. J., D. Spaute, D. R. Davis, F. Marzari, and K. Ohtsuki (1997). "Accretional Evolution of a Planetesimal Swarm." *Icarus* 128, 429–455. DOI: 10.1006/icar.1997.5747.

Weidner, C., P. Kroupa, and I. A. D. Bonnell (2010). "The relation between the most-massive star and its parental star cluster mass." *Mon. Not. R. Astron. Soc.* 401, 275–293. DOI: 10.1111/j.1365-2966.2009.15633.x. arXiv: 0909.1555 [astro-ph.SR].

Weiss, B. P. and L. T. Elkins-Tanton (2013). "Differentiated Planetesimals and the Parent Bodies of Chondrites." *Annu. Rev. Earth Planet. Sci.* 41, 529–560. DOI: 10.1146/annurev-earth-040610-133520.

Weiss, B. P. et al. (2012). "Possible evidence for partial differentiation of asteroid Lutetia from Rosetta." *Planet. Space Sci.* 66, 137–146. DOI: 10.1016/j.pss.2011.09.012.

Weiss, L. M. et al. (2018). "The California-Kepler Survey. V. Peas in a Pod: Planets in a Kepler Multi-planet System Are Similar in Size and Regularly Spaced." *Astron. J.* 155, 48. DOI: 10.3847/1538-3881/aa9ff6. arXiv: 1706.06204 [astro-ph.EP].

Wetherill, G. W. and G. R. Stewart (1989). "Accumulation of a swarm of small planetesimals." *Icarus* 77, 330–357. DOI: 10.1016/0019-1035(89)90093-6.

— (1993). "Formation of planetary embryos - Effects of fragmentation, low relative velocity, and independent variation of eccentricity and inclination." *Icarus* 106, 190. DOI: 10.1006/icar.1993.1166.

Wick, M. J. and R. H. Jones (2012). "Formation conditions of plagioclase-bearing type I chondrules in CO chondrites: A study of natural samples and experimental analogs." *Geochim. Cosmochim. Acta* 98, 140–159. DOI: 10.1016/j.gca.2012.09.027.

Williams, J. P. and L. A. Cieza (2011). "Protoplanetary Disks and Their Evolution." *Annu. Rev. Astron. Astrophys.* 49, 67–117. DOI: 10.1146/annurev-astro-081710-102548. arXiv: 1103.0556 [astro-ph.GA].

Williams, J. P. and E. Gaidos (2007). "On the Likelihood of Supernova Enrichment of Protoplanetary Disks." *Astrophys. J. Lett.* 663, L33–L36. DOI: 10.1086/519972. arXiv: 0705.3459.

Wilson, L. and K. Keil (2012). "Volcanic activity on differentiated asteroids: A review and analysis." *Chemie der Erde / Geochemistry* 72, 289–321. DOI: 10.1016/j.chemer.2012.09.002.

Wilson, L. and K. Keil (2017). "Arguments for the Non-existence of Magma Oceans in Asteroids." *Planetesimals: Early Differentiation and Consequences for Planets*. Ed. by Linda T. Elkins-Tanton and Benjamin P. Weiss. Cambridge Planetary Science. Cambridge University Press, pp. 159–179.

Winn, J. N. and D. C. Fabrycky (2015). "The Occurrence and Architecture of Exoplanetary Systems." *Annu. Rev. Astron. Astrophys.* 53, 409–447. DOI: 10.1146/annurev-astro-082214-122246. arXiv: 1410.4199 [astro-ph.EP].

Woosley, S. E. and A. Heger (2007). "Nucleosynthesis and remnants in massive stars of solar metallicity." *Phys. Rep.* 442, 269–283. DOI: 10.1016/j.physrep.2007.02.009. eprint: astro-ph/0702176.

Woosley, S. E. and T. A. Weaver (1995). "The Evolution and Explosion of Massive Stars. II. Explosive Hydrodynamics and Nucleosynthesis." *Astrophys. J. Suppl.* 101, 181. DOI: 10.1086/192237.

Yomogida, K. and T. Matsui (1984). "Multiple parent bodies of ordinary chondrites." *Earth Planet. Sci. Lett.* 68, 34–42. DOI: 10.1016/0012-821X(84)90138-9.

Young, E. D. (2014). "Inheritance of solar short- and long-lived radionuclides from molecular clouds and the unexceptional nature of the solar system." *Earth Planet. Sci. Lett.* 392, 16–27. DOI: 10.1016/j.epsl.2014.02.014. arXiv: 1403.0832 [astro-ph.EP].

Young, E. D., R. D. Ash, P. England, and D. Rumble III (1999). "Fluid flow in chondritic parent bodies: deciphering the compositions of planetesimals." *Science* 286, 1331–1335. DOI: 10.1126/science.286.5443.1331.

Zahnle, K. J., J. F. Kasting, and J. B. Pollack (1988). "Evolution of a steam atmosphere during earth's accretion." *Icarus* 74, 62–97. DOI: 10.1016/0019-1035(88)90031-0.

Zsom, A., C. W. Ormel, C. Güttler, J. Blum, and C. P. Dullemond (2010). "The outcome of protoplanetary dust growth: pebbles, boulders, or planetesimals? II. Introducing the bouncing barrier." *Astron. Astrophys.* 513, A57. DOI: 10.1051/0004-6361/200912976. arXiv: 1001.0488 [astro-ph.EP].

de Wit, J. et al. (2018). "Atmospheric reconnaissance of the habitable-zone Earth-sized planets orbiting TRAPPIST-1." *Nat. Astron.* 2, 214–219. DOI: 10.1038/s41550-017-0374-z. arXiv: 1802.02250 [astro-ph.EP].

Ševeček, P., M. Brož, D. Nesvorný, B. Enke, D. Durda, K. Walsh, and D. C. Richardson (2017). "SPH/N-Body simulations of small (D = 10km) asteroidal breakups and improved parametric relations for Monte-Carlo collisional models." *Icarus* 296, 239–256. DOI: 10.1016/j.icarus.2017.06.021.

Šrámek, O., L. Milelli, Y. Ricard, and S. Labrosse (2012). "Thermal evolution and differentiation of planetesimals and planetary embryos." *Icarus* 217, 339–354. DOI: 10.1016/j.icarus.2011.11.021.

van Boekel, R. et al. (2004). "The building blocks of planets within the 'terrestrial' region of protoplanetary disks." *Nature* 432, 479–482. DOI: 10.1038/nature03088.

DECLARATION OF ORIGINALITY

I hereby confirm that I am the sole author of the written work here enclosed and that I have compiled it in my own words. Parts excepted are corrections of form and content by the supervisors.

Title of work: Thermal Evolution of Forming Planets: Isotope Enrichment, Differentiation & Volatile Retention

With my signature I confirm that I have committed none of the forms of plagiarism described in the 'Citation etiquette' information sheet; I have documented all methods, data and processes truthfully; I have not manipulated any data; I have mentioned all persons who were significant facilitators of the work. I am aware that the work may be screened electronically for plagiarism.

Zurich, June 19, 2018

Tim Lichtenberg

ACKNOWLEDGMENTS

I understand that I find myself in an extraordinary and privileged position. Being fortunate enough to be born at all, rather than not being born, in a developed country, at a time when the health status and personal well-being of humans all over the world reaches historic highs is remarkable enough. Even more, I am in the incredibly lucky position to be allowed to freely choose a profession that gives meaning to my life, and that I find enriching and motivating. This is so extraordinarily rare that I cannot find proper words for it. I am truly thankful for it and in particular to the people around me who supported and helped me during my life, and who continue to do so until this day. Without you I could not do this. Without you – all of you — nothing of it would be possible.

I want to thank Lola, my partner in life, for your never-ending support, intimateness and companionship. You keep me functioning, you give my life stability, and – quite important when thinking about supernovae, extrasolar planets, and alien life all day long – you keep me rooted in reality when I may lose myself in it sometimes. I love you.
Oh, and Lola, thanks for the financial support, much appreciated.

Thank you to my loving parents, Margit and Fred. You let me choose what I wanted to do, where I wanted to go. You supported me in finding a path on my own and when I tried something new once again. I am thankful for my sheltered and happy childhood that you provided me, and that gave me a kickstart into the life I opt for. Thank you for your love and for everything you gave me.

Thank you to Marianne, for your support, and for never objecting about the places so far away we go to. Thank you to Claudio, for introducing me to the most important person in my life.

Thank you to Gregor, Michael, Taras, and Richard, who conceived this amazing idea of an interdisciplinary PhD, and who trusted in my abilities and supported me for three and a half years to perform such a crazy out-of-this-world research project; or better, this mammoth of research endeavor, which kept me in constant amazement and wonder. It was an epic tale, a never-ending one. There is more to come, *so much* more out there.

Thanks to Gregor, for always being available to talk, for replying to e-mails in less than 5 minutes (that's the spirit!), and for the myriads of comma errors and reference corrections; to Michael, for the many uplifting discussions, I always come out of them a bit taller than before; to Taras, for the uncomplicated chats and the immediate help

when it was needed, and for the tea (great tea!); and to Richard, for showing me how to get things done, now.

Thank you to Charitra, Antoine, Lisbeth, Patrick (1823 m!), Jana, Dan, Danny, Vojta, Maxim, Silke, Suzanne, Krisztina, Stefano, Jessica, Diogo, Frank, Daniela, Antonio, Monika, and everyone else from GFD, Geophysics, and Geochemistry, who welcomed the 'astronomer' in their middle; and to the people from ETH Astronomy, Sascha, Lia, Federica, Hans Martin, and many others, who allowed the 'geologist' to talk with them about 'stones' in the computer.

A huge thanks to CJ for helping me proofreading this thesis and the deep discussions about style, color, movies, and life.

Thank you to Toby and Rich, who slowly explained the basics of petrology to an 'astronomer'; to Paul, for supporting my stay in his research group and for the pink air guitar; to Maria, for having patience with me while I continuously kept mixing up meteorite classes; to Fred, for his inspiring work and setting an example how a inter(trans-?)disciplinary scientist can thrive; to Audra Baleisis, for opening my eyes toward my own privilege; to my friends from UZH, Tom Hands (1823 m!), Joanna (ąż≠az!), Miles, Caro, and Julia, for the weekly Astrotime in the separata, and the successful water workshop. Thank you to Uli, Kerstin, Gillian, and Michael, for the wonderful comic strip from the beginning of the thesis.

Thank you to my friends from Göttingen's 42nd Institute, Andre, Daniel, Flori, Uli, Philipp, Alex, Ina, Nina, Mattias, and Stefan, for an amazing time. Just to be clear: I truly hate exercise sheets, even with stupefying horse songs in the background. Already 8 years now since this bedeviled 'history of analysis' lecture, wow.

To all the ambassadors of science communication, whose books and films inspired me to pursue a career in science. And last but not least, I want to thank the Swiss people for financing a world class science hub, including the NCCR PlanetS platform for an inspiring community that opens doors and connects curious people to each other.

Humans always depended on curiosity and acumen. We will continue to need it in an ever-more complex world, more than ever. Reason and thought are the *only* difference between us and amoebas. Let's give it a *real* chance.

So long, and thanks for all the fish

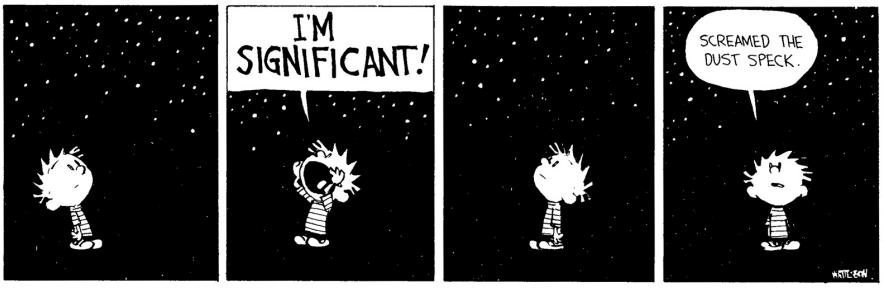
I'M SIGNIFICANT!
SCREAMED THE DUST SPECK.
WATTERSON